Large Scale Growth of MoS_2 Monolayers by Low Pressure Chemical Vapor Deposition

Omar Salih Omar

Doctor of Philosophy

University of York

Physics

March 2018

Abstract

Monolayers of molybdenum disulphide MoS_2, a two dimensional (2D) semiconductor with a direct band gap of 1.9 eV, have been proposed as a candidate for next generation nanoscale electronic and opto-electronic devices. Controlled synthesis of MoS_2 monolayers is critically important since the thickness uniformity and grain size are major concerns for the fabrication of opto-electronic devices.

In this study, we demonstrated the growth of wafer scale uniform MoS_2 monolayers on SiO_2 covered silicon wafers, at a range of growth temperatures (650 ^oC-850 ^oC) with optimum grain sizes as large as 400 μm, using low pressure chemical vapor deposition (LPCVD). By controlling the partial pressure of the reactant species at the growth surface and the limiting time, we can achieve prefered monolayer growth over multilayer growth.

The MoS_2 monolayer crystals follow a lognormal size distribution, consistent with random crystal nucleation, with single crystal domains as large as 400 μm. We estimated the thermal expansion coefficient to be (2.5±1.2) $\times 10^{-6}$ /^oC, which is at least double that of the bulk.

We have found film growth can be clearly classified into the reaction limited, feed limited and desorption limited regimes. With the help of COMSOL simulations, we have related the local growth environment such as growth temperature, MoO_2 concentration, sulphur chemical potential and growth time with the macroscopic growth parameters such as Ar flux. In the feed limited regions, it is the supply of Mo that is the rate limiting factor. In the desorption regions, the growth is controlled by thermal stability of MoS_2 monolayers. The growth modes also can be used to tune the grain morphology from perfect triangles to hexagons.

Finally, we have also compared our approach with an LPCVD approach based on MoO_3 as the Mo source. MoO_3 has a higher vapor pressure than MoO_2 which was used in the previous approach. By tuning the the S:MoO_3 ratio, we could grow controllably planar MoS_2 monolayers, vertically aligned MoS_2/MoO_2 and planar MoO_2 crystals.

Table of Contents

List of figures

Acknowledgements

I would like to thank all those that helped me complete this PhD project. A special thanks goes to my supervisor professor Jun Yuan for his supervision , helpful discussions ,invaluable feedbacks and encouragement. Without his guidance and persistent help this thesis would not have been possible.

I am particularly grateful to Ben Dudson,my thesis advisor panel,advice and comments given by Ben has been a great help in completing this project.

A special thank you to York nanocenter staff: Ian Wright, Leonardo Lari and Jon Barnard for doing a brilliant job in keeping the microscopes working, for teaching to use many of the research tools used during my PhD work.

I am particularly grateful for the assistance given by Dr. Andrew Pratt for X-ray photoelectron spectroscopy measurements and data analysis.

Special thanks also to professor Kevin O'Grady and his group for XRD measurements.

My sincerely thank Dr. Stuart Cavill and to diamond light source beam 107 staff for the in-plane XRD measurements.

Special thanks to professor Chuanhong and his his group in China for the Raman and photoluminescence measurements and data analysis.

I would like to thank the technicians Dave Coulthard, Mark Laughton, Adam Stroughair and Neil Johnson for helping to assemble the CVD system and keep it in working order.

My deepest thanks to the Kurdistan regional government for the financial support.

A final thank to my beloved parents, brothers, sisters and my wife Awaz Badry who have been supportive all times and have always encouraged me to aim high.

Dedication

To my beloved parents, brothers, sisters and my wife Awaz Badry

Declaration

I declare that this thesis is a presentation of original work and I am the sole author. This work has not previously been presented for an award at this, or any other, University. All sources are acknowledged as References

Chapter 1: Introduction

Two dimensional materials can be defined as the “materials in which the atomic organization and bond strength along two dimensions are similar and much stronger than along a third dimension”[1]. With recent advanced techniques almost all layered three dimensional materials can be exfoliated to make atomically thin layers. Particularly, the family of van der Waals solids is one of the most popular sources of 2D materials, in which the strong in plane bonds provide stability for atomically thin layers and weak interlayer van der Waals forces offer the feasibility of exfoliation [1], [2].

Silicon is the most common material that has been employed in the electronics devices industry. However, in the era of Nanoelectronics devices, silicon is facing size limitations. This motivated researchers to quest for novel materials that could overcome those shortcomings. The family of 2D materials could have a range of electronic properties; they could be metals, semimetals, insulators and semiconductors with a band gap from ultraviolet to infrared. This makes 2D materials a good candidate to replace silicon [2]. Due to the high mechanical strength, carrier mobility and thermal conductivity, graphene appeared to be one of the most promising 2D materials that might have potential applications in nanoelectronics, optoelectronics, energy harvesting, and biosensing fields [3]. However, graphene, as a semimetal, has a zero band gap, limiting its applications in nanoelectronics [4], [5]. With this consideration, other graphene-like materials such as transition metal dichalcogenides (TMDs) have recently emerged and differently to graphene, many of them have the advantage of being semiconductors and have a sizable band gap, thus making them appealing for nanoelectronics applications [6], [7].

1.1 Transition metal dichalcogenides (TMDs)

Layered transition metal dichalcogenides have the stoichiometry formula MX_2. The letter M stands for the transitional metal atom and X is the chalcogen atom (for example, M = Ti, Zr, Hf, V, Nb, Ta, Re; X = S, Se, Te (see figure 1:1). These materials belong to family of van der Waals solids with the transition metal atoms sandwiched between two chalcogen layers. M-X are strongly bonded by covalent

bonds, while the sheets are held together by weak van der Waals forces which make these materials easy to be exfoliated to a single and few layers [8].

Different transition metal dichalcogenides possess very different electrical properties depending on polytype and number of electrons in the d-shell of the transitional metal atom: some are insulators such as HfS_2, while the others could be semiconductors such as MoS_2, WS_2, $MoSe_2$ and WSe_2, or semimetals such as WTe_2 and $TiSe_2$, or even true metals such as NbS_2 and VSe_2. Among 2D transition metal dichalcogenides, MoS_2, WS_2, $MoSe_2$ and WSe_2 are most widely studied in nanoelectronic applications since they are semiconductors with a sizable band gap, and have a high chemical and thermal stability [2], [6], [8].

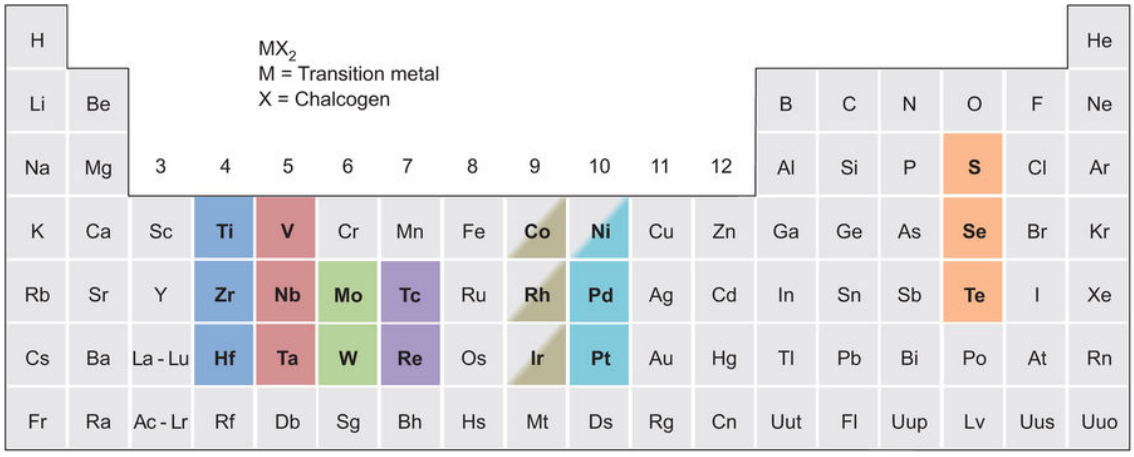

Fig. (1:1): The transition metals and the three chalcogens that are highlighted have a layered structure. Partial highlights for Co, Rh, Ir and Ni refer to some of the dichalcogenides that form layered structures [6].

Bulk MoS_2 can be found in different polytypes (different stacking sequences). The most identified polytypes are 2H which is mostly found in naturally grown material and 3R found in synthetic material where the letters represent hexagonal and rhombohedral respectively, and the numbers represent the number of layers in the stacking sequence. The 2H phase has a AbA BaB (capital letter stands for the sulphur atoms and the lower-case letters for molybdenum atoms) stacking sequence with trigonal prismatic coordination and the 3R phase follows a AbA CaC BcB stacking sequence with trigonal prismatic coordination [8]. A 1T phase with stacking ABC ABC has been found in other TMDs such as TiS_2 [6], [8]. Figure 1:2 represents different stacking sequences in TMD materials.

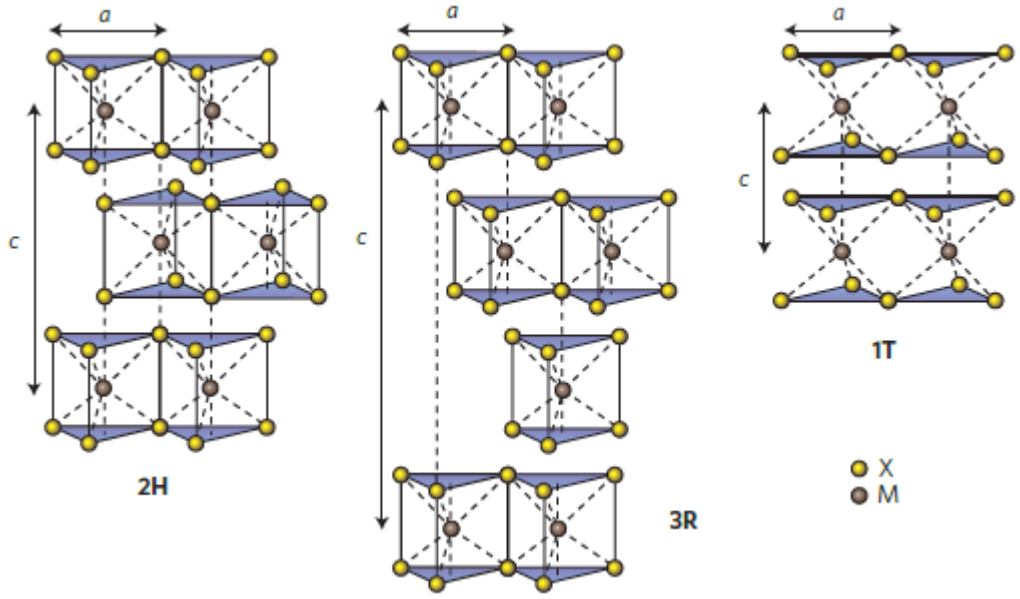

Fig. (1:2): Schematics of the structural polytypes: 2H, 3R and 1T stacking sequences in TMD materials. The chalcogen atoms (X) are yellow and the metal atoms (M) are grey [9].

Monolayer of MoS_2, a sheet of S-Mo-S sandwich layer, has two phases: 1T with stacking AbC and 1H with stacking sequence AbA. It has been found more stable than 1T [10].

For MoS_2 monolayers, 1H has trigonal prismatic coordination that belongs D_3h point group and the 1T has octahedral coordination belongs to the D_3d point group. Figure 1:3 shows both monolayer polytopes [6].

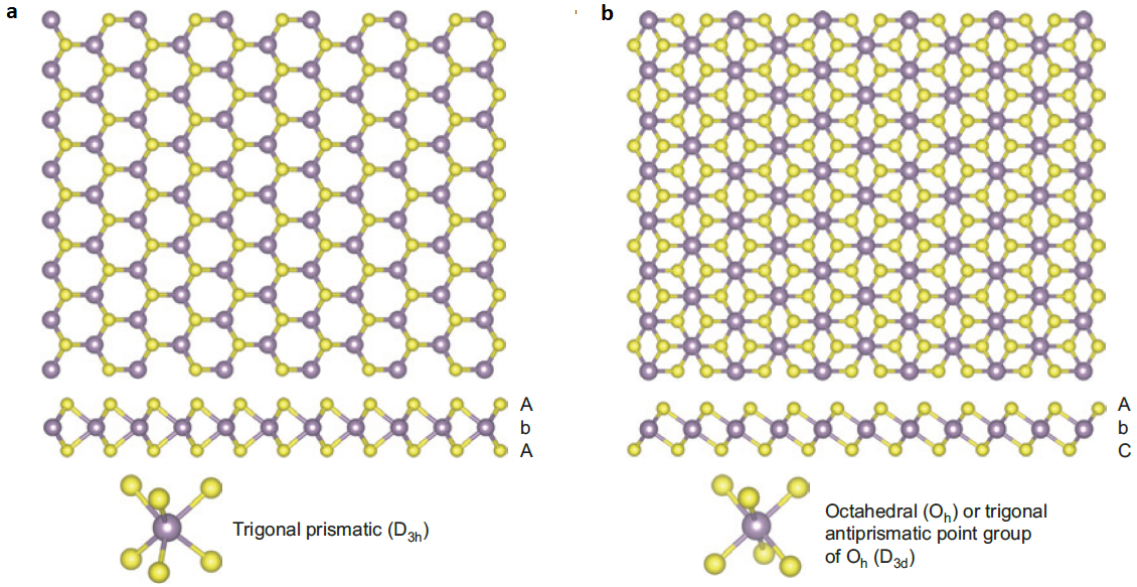

Fig. (1:3): (a,b) Atomic models showing 1H and 1T phases of monolayer MoS_2 respectively [6].

The crystallographic orientations of MoS_2 monolayers are depicted in figure 1:4a and the primitive unit cell is shown in figure 1:4b. Figure 1:5 a,b shows a bright-field TEM image and diffraction patterns of a single-crystal triangle grown by CVD. As seen in the schematic in figure 1:5b, the lattice of monolayer MoS_2 is divided into molybdenum and sulphur sublattices, which reduces the hexagonal lattice from six-fold to three-fold symmetry. As a result, the six $[\bar{1}100]$ diffraction spots belong to two distinct families $k_a = \{(\bar{1}100), (10\bar{1}0), (0\bar{1}10)\}$ and $k_b = -k_a$ [11].

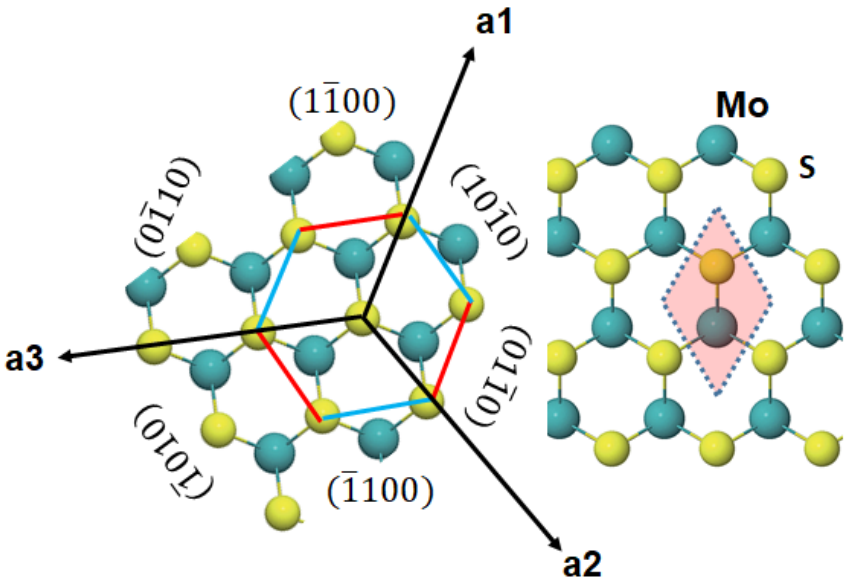

Fig.(1:4): (a): Crystallographic orientations of a MoS_2 monolayer (b): The shaded region bounded by dashed lines corresponds to one primitive cell.

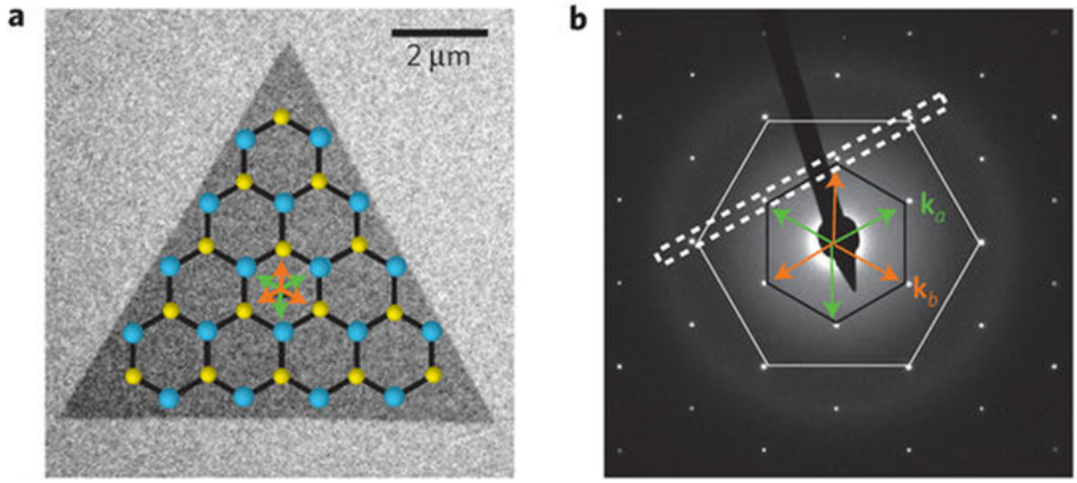

Fig. (1:5): (a) Bright-field TEM image of a single-crystal triangle with a Mo-zigzag edge orientation. (b) Diffraction patterns from a. The asymmetry of the Mo and S sublattices separates the $[\bar{1}100]$ diffraction spots into two families: $k_a = \{(\bar{1}100), (10\bar{1}0), (0\bar{1}10)\}$ and $k_b = -k_a$ [11].

1.2 Why MoS_2 monolayers are interesting

As bulk MoS_2 is thinned down, the band structure changes with the number of layers. The sizable band gap of MoS_2 is one of the most important features that make MoS_2 to be a promising candidate for 2D electronic devices. The MoS_2 band gap size varies from 1.2 eV which is an indirect band gap associated with bulk MoS_2 to a 1.9 eV direct band gap for a single layer [12]. An example of the calculated band structure of MoS_2 is shown figure 1:6 [13]. In bulk MoS_2, the indirect band gap occurs at the Γ-point. The conduction band states at the Γ-point arise from the hybridization between p_z orbitals on S atoms and the d orbitals on the Mo atoms. The conduction band states at the K-point mainly occur due to the localized d orbitals on Mo atoms. The Mo atoms are sandwiched in the middle of S-Mo-S layers and they are fairly isolated from the interlayer coupling therefore the K-point is not influenced by a decreasing layer number. However, the Γ-point is strongly affected by interlayer coupling effect since the stats at this point are due to combinations of the p_z orbitals on the S atoms and the d orbitals of the Mo atoms. Thus, when the layer number decreases, the energy at the Γ-point increases, while the conduction band at the K-point remains stable as shown in figure 1:6 [13].

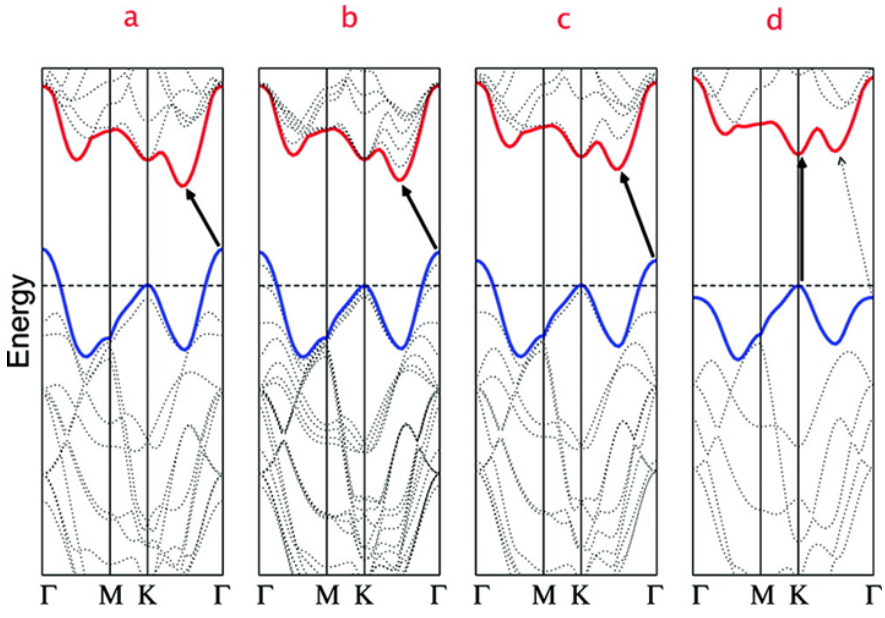

Fig. (1:6): Calculated band structure of (a) bulk MoS_2 (b) 4 layers (c) 2 layers and (d) 1 layer [13].

Such a transition from an indirect to a direct band gap semiconductor has been confirmed by photoluminescence (PL) measurements. Bulk and multilayer MoS_2 exhibit a negligible photoluminescence peak due to the indirect band gap.

However, a bright photoluminescence peak has been detected from direct band gap (1.9) eV single layer MoS_2 as shown in figure 1:7. This emerging PL in the monolayers in the visible range make them a promising candidates for future photodiodes [14].

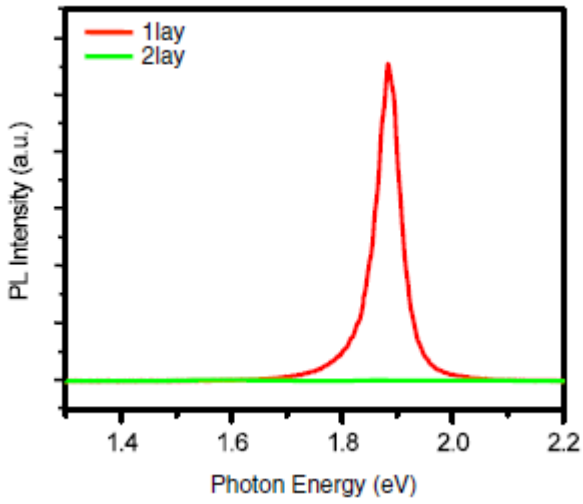

Fig. (1:7): Photoluminescence of single and bilayer MoS_2 [12].

With the band gap in the visible range, the monolayers can also be used for solar energy harvesting. MoS_2 monolayers as active layers have been integrated with silicon to make MoS_2-Si heterostructures. A maximum efficiency of 5.23% has been achieved from such heterostructures [15].

MoS_2 monolayers and 3R bulk material have broken inversion symmetry (figure 1:2) and they exhibit spin orbit splitting at the top of the valence band. These two properties make them favorable candidates for spin based devices. The band structure of the first Brillouin zone of a MoS_2 monolayer is shown in figure 1:8. The points (valleys) located at the corners (K and -K) have equal energies and different well separated momentums. This makes selective excitation of carriers with various combinations of valley and spin index possible [16], [17].

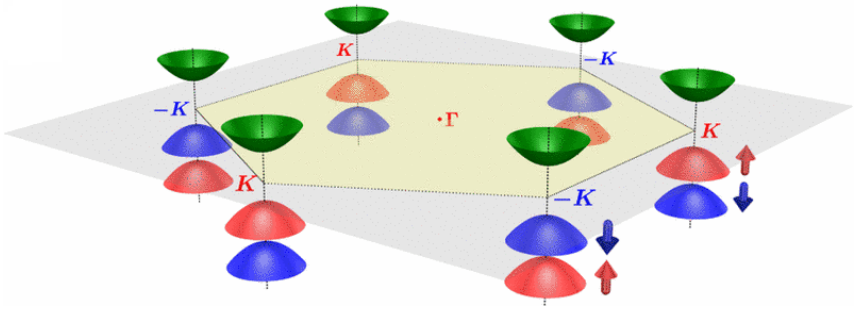

Fig. (1:8): Band structure of the first Brillouin zone. Green cones represent the conduction band, blue and red cones are the spin-orbit split valence band, and the arrows are spin up and down of the carriers [16].

The broken inversion symmetry in MoS_2 monolayers can also be used for converting mechanical energy to electricity. A measured piezoelectric coefficient of $e_{11} = 2.9 \times 10^{-10}$ C m^{-1} of the monolayers makes them an excellent material for atomically thin piezoelectric devices [18].

Another promising application of MoS_2 monolayers is expected to be in the field of electronics. The calculated room temperature phonon limited mobility in the MoS_2 monolayer is found to be ~410 cm^2 V^{-1}s^{-1} [19]. Field effect transistors (FET) fabricated from single layer MoS_2 exhibit a room temperature on/off ratio of 10^8, and a mobility over 200 cm^{2}V^{-1}s^{-1} with very low standby power dissipation [7].

Mechanically, MoS_2 monolayers are flexible, with a Young's modulus of 270±100 GPa, which is comparable to that of steel. Such exceptional mechanical properties make this material suitable to be integrated in flexible electronic devices [20].

1.3 Outline of the structure of the thesis

The aim of this thesis is to develop a reliable chemical vapor deposition approach for growing high quality, uniform wafer scale MoS_2 monolayers with the largest possible grain size and exploring their intrinsic optical, electrical and structural properties.

Chapter one covers a brief introduction of two dimensional materials with special attention given to the structural, electrical and optical intrinsic properties of molybdenum disulphide monolayers.

In chapter two, we mainly focus on the synthesis approaches established for 2D materials. It includes top-down approaches such as mechanical exfoliation, chemical exfoliation and electrochemical exfoliation. The bottom up approaches cover chemical vapor deposition, physical vapor deposition, atomic layer deposition and molecular beam epitaxy.

In chapter three, we present the characterization and simulation tools that have been employed in this project. We introduce X-ray photoelectron spectroscopy (XPS) that has been used for chemical analysis of MoS_2 monolayers. Microscopic tools such as scanning electron microscopy (SEM), transmission electron microscopy (TEM), scanning transmission electron microscopy (STEM) and atomic force microscopy (AFM) that have been used in monolayer imaging, studying the crystalline nature of the monolayer and their thickness measurements are discussed. We also covers Raman spectroscopy for

qualitative thickness measurements and evaluating growth induced strain in the monolayers. Second harmonic generation (SHG) was used for confirming the uniformity of the monolayers and studying the grain size distribution of the monolayers as function of growth conditions. X-ray diffractometry (XRD) and in-plane grazing incidence angle X-ray are presented for studying the crystalline nature of the monolayers. Finally, the CVD simulation software COMSOL is presented and the fluid dynamics module, chemical engineering, and heat transfer module are outlined.

Chapter four presents a low pressure chemical vapor deposition method for growing MoS_2 monolayers on SiO_2 covered Si. In this chapter we took advantage of the low vapor pressure of molybdenum dioxide as the Mo source to establish an approach for producing uniform MoS_2 monolayers on a wafer scale. The production of such large scale monolayers is essential in the practical world of optoelectronic devices. Under optimized conditions, we grew a uniform wafer scale polycrystalline monolayer film with a grain size up to 400 μm. Different techniques such as XPS, AFM, TEM, PL, Raman spectroscopy, SHG and XRD were used for studying the chemical composition, thickness measurements, uniformity and intrinsic structural, optical and electrical properties of the as grown monolayers.

In chapter five we further modified the growth conditions of the approach presented in chapter four. We report the dependence of MoS_2 film growth as a function of growth conditions such as temperature, MoO_2 concentration, sulphur flux and carrier gas flow rate. We also studied the grain size distribution as a function of growth temperatures to optimize the growth of largest possible grains within a continuous polycrystalline film. We employed COMSOL software to simulate the concentration distribution at the surface of the substrate with a view to understanding the reaction conditions at the growth front under different growth conditions. We also investigated the growth rate of isolated grains for better optimizing the growth regimes in our CVD process. Finally, we present an approach for tuning the morphology of the grains as a function of growth temperatures.

In chapter six, another approach based on using MoO_3 as a Mo source is presented. MoO_3 has a much higher vapor pressure than MoO_2 at the same growth temperature. As a result of this, different structures such as laterally aligned MoS_2 monolayers, vertically aligned MoS_2/MoO_2 crystals and laterally

aligned MoO_2 are produced. COMSOL is used for fluid dynamics simulations and the ratio of Mo/S for each growth regime is comprehensively analysed and the growth mechanisms of the film growth is discussed.

Finally, chapter seven summarizes the conclusion for the whole project as well as an outlook of potential future research.

Chapter 2: Preparation of 2D materials

2.1 Overview

The fabrication methods of transition metal dichalcogenides (TMDs) can be classified into two types of general approaches: top-down and bottom-up. In top-down approaches, techniques such as mechanical exfoliation, liquid exfoliation and electrochemical exfoliation are used to thin down bulk crystals to few layers and monolayers. In bottom-up approaches, starting materials in the form of gases and powders are used to grow multilayers and monolayers using chemical vapor deposition CVD, physical vapor deposition, atomic layer deposition and molecular beam epitaxy.

2.2 Top-down approaches

2.2.1 Mechanical exfoliation

The nature of bulk layered materials has been studied for more than 150 years [21]. Isolation of monolayers dates back at least to a few years ago (2004) when A. Geim, and his colleagues isolated graphene (a monolayer of graphite) using mechanical exfoliation by Scotch tape. This technique is the starting point for much monolayer research in the world [22].

In mechanical exfoliation, an adhesive tape is used to peel off a thin layer of graphite from the bulk crystal. Then the freshly cleaved nanosheet is brought into contact with an appropriate substrate (SiO_2) for further thinning and investigation [22]. As well as exfoliation of graphene, the technique has also been widely used in exfoliating other layered materials such as transition metal dichalcogenides [7], hexagonal boron nitride [23] and black phosphorus [24]. What makes the isolation of a monolayer possible is that the adhesion between the substrate and the bottom layer of the bulk material can be stronger than the interlayer coupling of the bulk material. Therefore, for exfoliation, of different materials different substrates can be used [25]. For example, the flake size of MoS_2 using SiO_2 as a substrate is about one order of magnitude smaller than the graphene size exfoliated using the same substrate. To overcome this problem, gold is being used instead of SiO_2 for

producing MoS_2, as the sulphur's affinity to gold is higher and MoS_2 strongly binds to gold [25].

The exfoliation technique is straightforward, inexpensive and reliable for producing high quality monolayers for research purposes (for studying optical, electrical and structural properties), however, the exfoliation technique is time consuming and the lateral size of flakes is very small, in the range of a few microns. Also, the number of layers in the exfoliated material cannot be precisely controlled, as the exfoliation yield comprised of monolayers, multilayers and even bulk material. Finally the technique is unreliable for mass production [22]. Figure 2:1 shows the micro cleavage technique used for graphene exfoliation [26]. Figure 2:2 shows optical images of monolayers and few layer of MoS_2 deposited on a SiO_2/Si substrate using Scotch tape together with their corresponding thickness measurements using AFM [27].

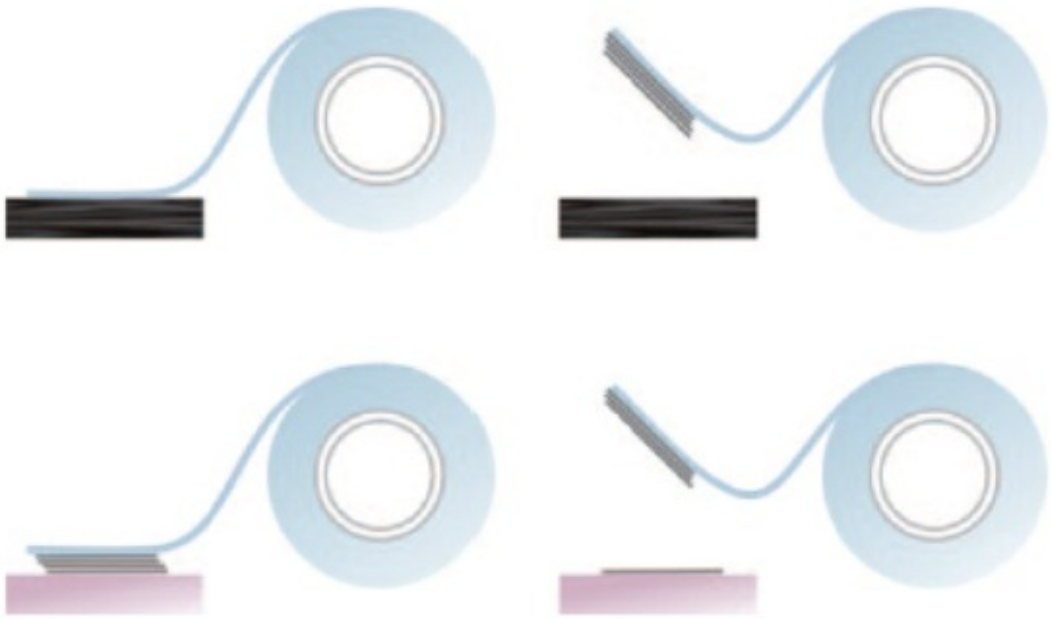

Fig (2:1): The micromechanical cleavage technique ("Scotch tape" method) for producing graphene. Top: Adhesive tape is used to cleave the top few layers of graphite from a bulk crystal of the material. Bottom left: The tape with graphitic flakes is then pressed against the substrate of choice. Bottom right: Some flakes stay on the substrate, even on removal of the tape [26].

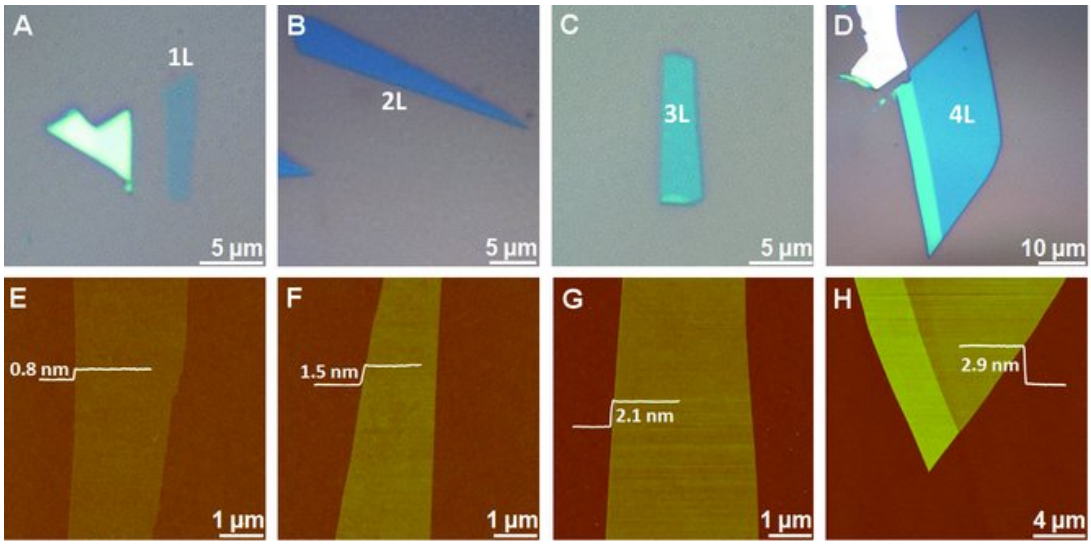

Fig. (2:2): Mechanically exfoliated single layer and multilayer MoS_2 films on SiO_2/Si substrate. Optical microscope images of single-layer (1L), bilayer (2L), trilayer (3L), and quadrilayer (4L) MoS_2 films (A–D). Panels E–H show the corresponding AFM images of the 1L (thickness ≈ 0.8 nm), 2L (thickness ≈ 1.5 nm), 3L (thickness ≈ 2.1 nm), and 4L (thickness ≈ 2.9 nm) MoS_2 films shown in (A–D) [27].

2.2.2 Liquid exfoliation

The liquid exfoliation of 2D materials can be categorized into direct and ion intercalated sonication of bulk 2D crystals in an appropriate liquid. Figure 2:3 represents the schematic of the two approaches [28]. In a direct sonication, a bulk crystal or powder of the 2D material is dispersed into a solvent with surface tension in certain ranges, then the mixture is sonicated to produce dispersed mono and multilayers, finally the product is centrifuged to remove unexfoliated residues [29].

The suitability of many solvents for liquid exfoliation of TMDs has been evaluated and it has been found that only solvents with a surface tension close to 40 mJ/m^2 are suitable for exfoliation of monolayers and multilayers. Several TMDs such as MoS_2, $MoSe_2$, WS_2 and NbS_2 have been exfoliated by direct sonication and the two solvents, N-methyl-pyrrolidone (NMP) and isopropanol (IPA), resulted in better yields [29]. TMDs have also been exfoliated in water and in this case a surfactant such as sodium cholate is added to the mixture to prevent the re-aggregation of the exfoliated material, as the water does not provide enough surface energy to keep the exfoliated material dispersed [30].

In the ion intercalation approach, atomically thin TMDs layers can be prepared by intercalating bulk TMDs crystal with ions such as lithium and then

exposing them to water [31]. Typically, a bulk TMD is first submerged in lithium for more than 24 hours and then the intercalated TMD is exposed to water [32]. The water strongly reacts with lithium between the layers to release hydrogen and separate bulk the TMD into layers [32]. Such methods can be employed to produce relatively large quantities (grams) of single layer TMDs [33]. However, only small size flakes up to a fraction of a micrometer could be produced. Moreover, the structural change (in the case of MoS_2) (from trigonal prismatic 2H-MoS_2 to octahedral 1T-MoS_2) can result from the lithium interaction. This could make MoS_2 lose its pristine semiconducting properties. To reverse the phase change and restore semiconducting properties of chemically exfoliated MoS_2, the samples need to be annealed at 300 ^oC [31], [33].

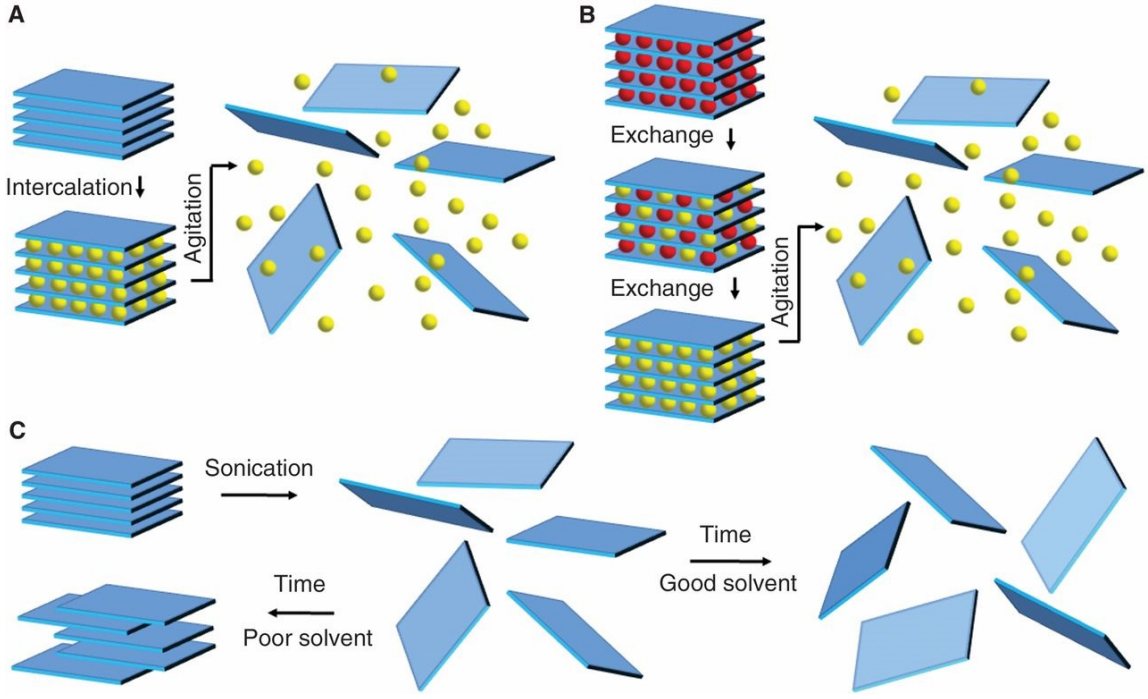

Fig. (2:3): Schematic illustration of the most widely used liquid exfoliation methods. (A) Ion intercalation. Ions represented by (yellow spheres) are intercalated between the TMD crystal layers in a liquid environment causing crystal swelling and resulting a decrease in the interlayer attraction. Adding energy such as shear, ultrasonication, or thermal to the system causes bulk TMD to exfoliate into a dispersed layers. (B) Some TMDs have ions between their layers, these ions are represented by (red spheres). In a liquid environment, these ions can be replaced by larger ions (yellow spheres) weakening the interlayer attraction. After Ion exchange, an external perturbation can exfoliate bulk TMD crystal to layers. (C) Sonication-assisted exfoliation. A bulk TMD crystal can be exfoliated into separated layers by sonication in a solvent with an appropriate surface energy. The solvent stabilize the exfoliated layers against re-aggregation and sedimentation [28].

2.2.3 Electrochemical Exfoliation

Two dimensional materials nanosheets can also be prepared by electrochemical exfoliation in which a DC bias voltage is applied between a 2D crystal and a Pt electrode in an electrolyte (Na_2SO_4) solution. Initially, the 2D crystal is wetted by applying a small voltage, and then the voltage is increased for exfoliation. Flakes can be dissociated from the bulk material and become suspended in the electrolyte [34]. The mechanisms of this technique can be understood as follow: when applying positive voltage to the working electrodes, radicals OH^- and O^- or SO_4^{-2} are produced around the 2D crystal as a result of water oxidation. Such radicals intercalate the 2D crystal and weaken the van der Waals forces between the layers. Gases such as O_2 and SO_2 are released as a result of second oxidation causing more weakening in the interlayer forces and finally flakes are detached from the bulk crystal by the erupting gas bubble [34]. Figure 2:4 summarizes the schematic production and mechanisms of this technique [34].

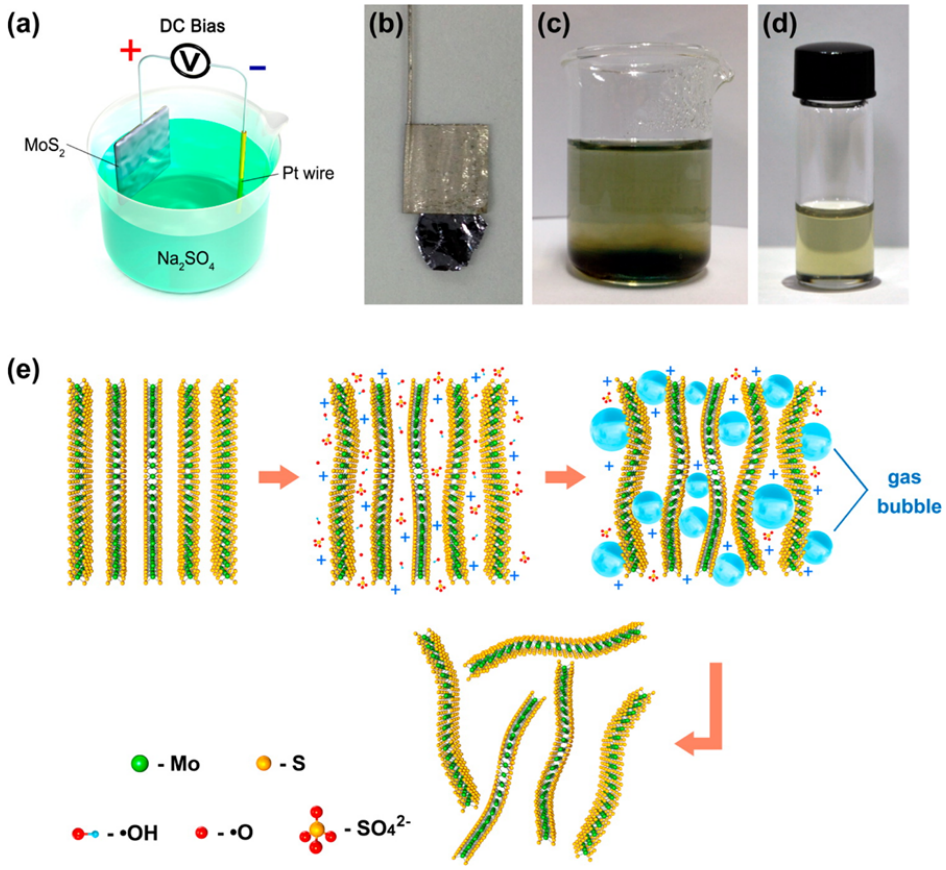

Figure (2:4): (a) The electrochemical circuit used for exfoliation of bulk MoS_2 crystal. (b) Bulk MoS_2 crystal held by a Pt clamp (c) Dispersed MoS_2 layers in Na_2SO_4 solution (d) Dispersed MoS_2 layers in N-methyl-2-pyrrolidone (NMP) solution. (e) Schematic description summarizing the electrochemical exfoliation mechanisms of bulk MoS_2 crystal [34].

2.3 Bottom-up approaches

2.3.1 Chemical vapor deposition

For mass production and integrating the 2D materials into industrial applications, new techniques that enable control over the layer number, crystal quality, lateral size of grains, etc. must be introduced. For this purpose, many bottom up techniques such as CVD, PVD, ALD, MBE…, etc. have been proposed [35]. Such processes utilize one or two starting materials to grow two dimensional materials. In the case of TMDs the starting materials in form of the powder are vaporized, carried by a carrier gas to the substrate where the reaction takes places and the film grows. Through optimization of growth parameters such as temperature of starting materials and their concentrations, reactor design, the species can be uniformly delivered to the substrate which in principle permits uniform growth [35].

The most adopted scenarios for the CVD growth of TMDs are summarized in figure 2:5. We will now focus on the growth of MoS_2 as the most widely grown TMD using approaches shown in figure 2:5. In the case of (a) the chalcogen powder, mostly sulphur with high purity is placed at the upstream of a furnace tube in a region where the temperature reaches above its melting point. The Mo source is also in the form of powder such as molybdenum trioxide MoO_3. It is placed at the center of the heating zone where the temperature is high enough for Mo source sublimation. The S and MoO_3 vapors are carried by an inert gas (Ar or N_2) to the substrate placed downstream a few centimeters away from the Mo container. On the substrate, and sometimes within the carrier gas atmosphere, the reaction takes place and a film grows, with the reaction byproducts carried by the carrier gas out of the furnace. The most common substrates used are insulating materials such as SiO_2/Si, quartz, mica or noble metals such as gold foils [34], [36]–[41]. Using this method, films up to centimeter scale as well as isolated crystals with edge length up to few hundreds of microns can be grown as shown in figure 2:6 [11]. Figure 2:7 is an optical image of continuous monolayers and bilayers with their corresponding AFM thickness measurements, grown using $MoCl_5$ and sulphur as the starting materials [41].

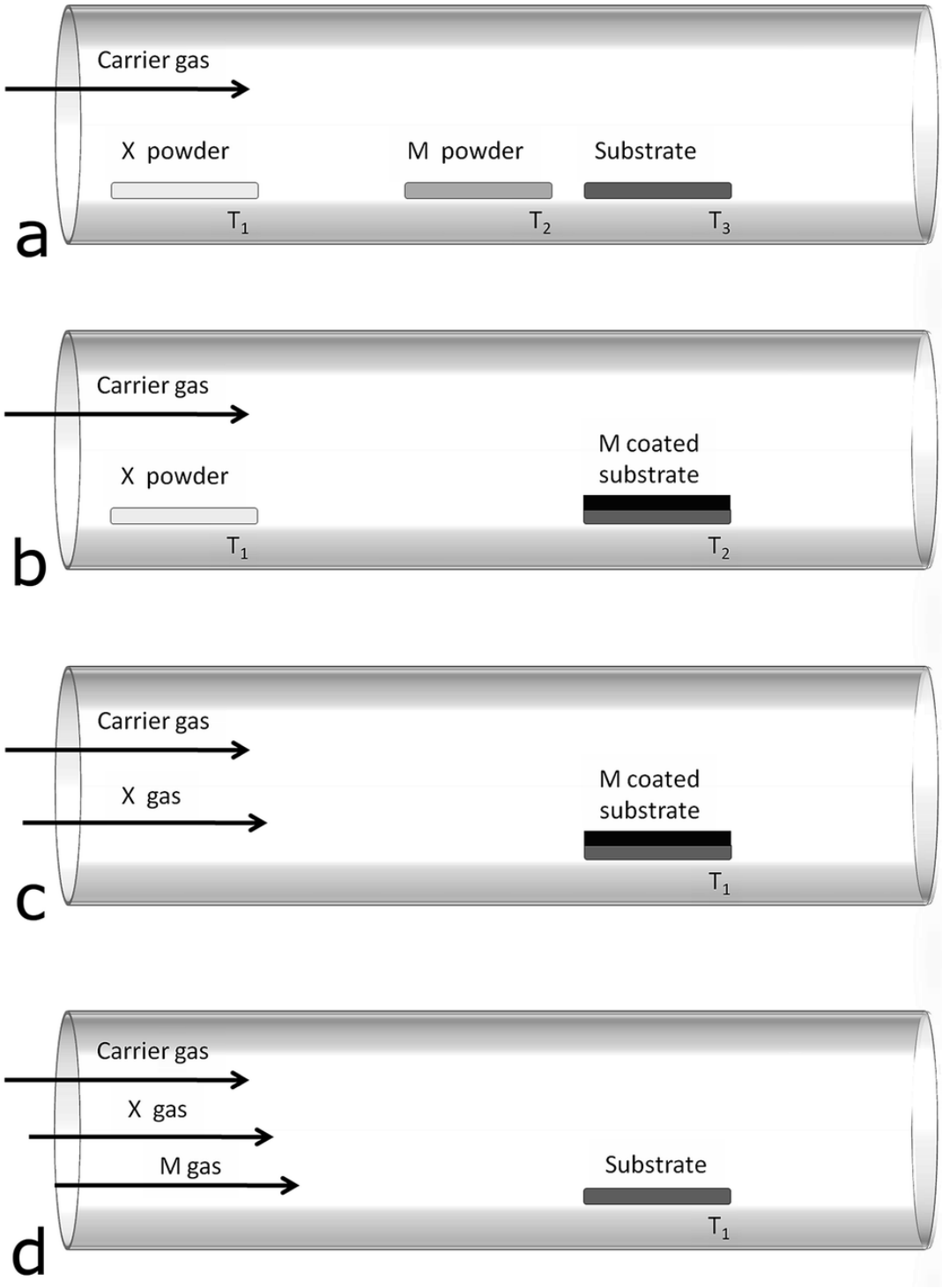

Fig. (2:5): Schematics of the most common methods used to deposit TMD from vapor phase. (a) Metal (M) and chalcogen (X) powders. (b) Metal or metal oxides deposited on substrate and chalcogen powders. (c) Metal or metal oxides deposited on substrate and chalcogen supplied as gaseous precursor. (d) Metal and chalcogen compounds supplied by gaseous precursors [35].

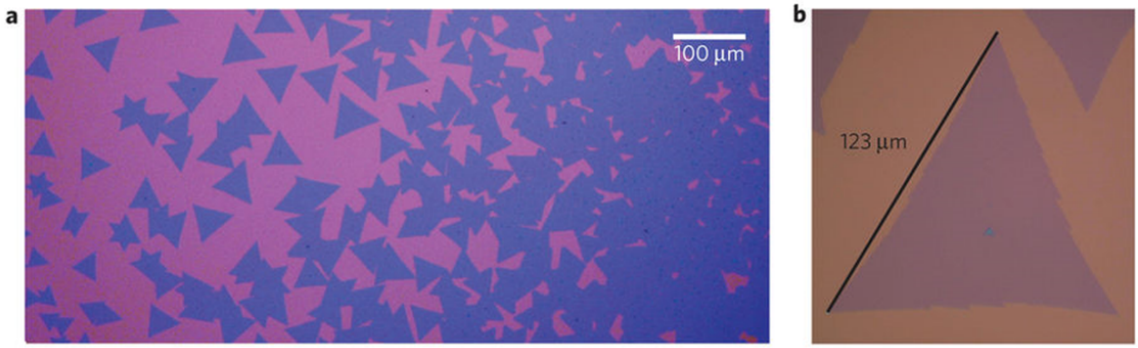

Fig. (2:6): a, Optical image of CVD growth of typical large-grain MoS_2 on a SiO_2 (285 nm)/Si substrate. The image contrast has been increased for visibility; magenta is the bare substrate, and violet represents monolayer MoS_2. b, Optical image of a monolayer MoS_2 triangle. The triangle is 123 µm from tip to tip [11].

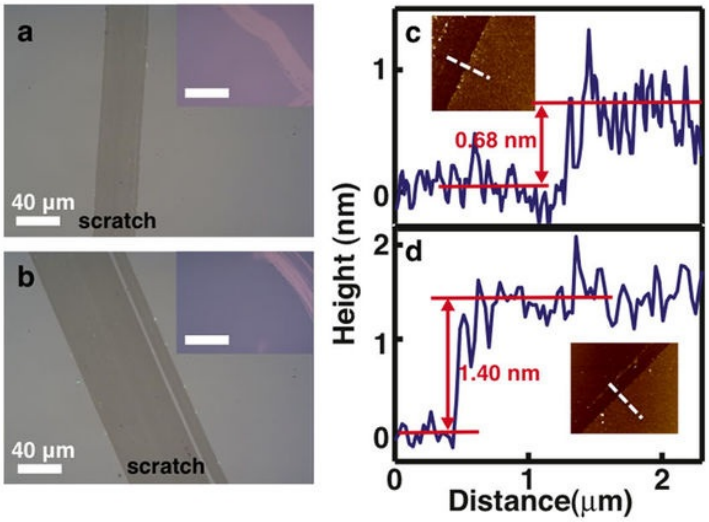

Fig. (2:7): (a) and (b), Optical images of the MoS_2 monolayer and bilayer films, respectively. The insets are optical micrographs of the MoS_2 monolayer and bilayer films grown on SiO_2/Si substrates. The scale bars in the insets are 80 µm. (c) and (d), AFM height profiles for typical MoS_2 monolayer and bilayer films grown on sapphire, respectively [41].

Cases (b) and (c) in figure 2.5 are a two-step process CVD, in which MoO_3 film with the required thickness is first deposited on the substrate using physical vapor deposition techniques such as e-beam evaporation and then sulfurized at high temperature using sulphur powder or H_2S gas. Employing this approach, one can grow wafer scale MoS_2 thin films, however the uniformity of the grown films is still an issue, monolayer, bilayer and trilayers coexist on the substrate of the same growth run [42], [43]. Similarly, instead of MoO_3, Mo metal has been predeposited on the substrate and sulfurized to get MoS_2 films. Despite large scale films that can be prepared using this method, some residual Mo atoms tend not to react with sulphur affecting the semiconducting properties of the final product. Additionally,

as Mo metal has a much higher melting point (2610 °C) compared to MoS_2 growth temperatures (typically 650-850 °C), Mo atom migration is suppressed at these growth temperatures which in turn affects the grain size of the grown film [44]–[46]. An example of two step growth using MoO_3 is summarized in figure 2:8; the same growth process can be applied to Mo-based growth as well.

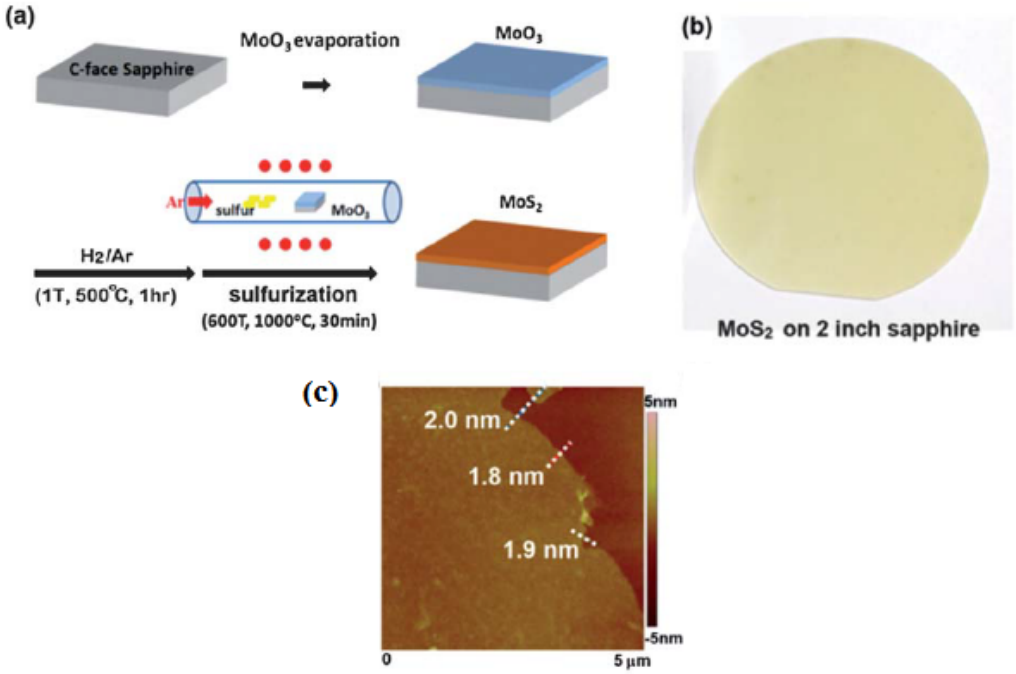

Fig. (2:8): (a) Schematic illustration for growing MoS_2 layers by MoO_3 sulfurization. A MoO_3 film (~3.6 nm) was thermally evaporated on the sapphire substrate. The MoO_3 was then converted to a MoS_2 by a two-step thermal process. (b) MoS_2 layer grown on a sapphire wafer. (c) AFM thickness measurements [42].

The Mo and S sources can also be supplied in the form of gas precursors at the furnace inlet as in the example of metalorganic chemical vapor deposition (MOCVD) (see Fig. 2:5, case d). In this approach, molybdenum hexacarbonyl (MHC) as Mo source and diethyl sulphide (DES) as sulphur source are diluted in H_2 and Ar carrier gases. Wafer scale films with a controlled number of layers can be produced. The disadvantage of this approach is the growth time is quite long time (26 hrs) for each run and the grain size is very small (about 10 microns) as well as that the precursors are highly toxic and they need special precaution during the growth [47].

Dip coating is another MoS_2 CVD growth method that has been used. The process starts by immersing an insulating substrate in ammonium thiomolybdate $(NH_4)_2MoS_4$ diluted in dimethylformamide (DMF). Then the substrate coated with $(NH_4)_2MoS_4$) is annealed at 500 °C in an Ar-H_2 mixture to remove the residual

solvent, NH_3 molecules, and other byproducts are dissociated from the precursors. Finally, by sulfurization in 1000 °C, MoS_2 film is obtained. The approach can be used to grow large scale multilayer MoS_2 films, however the uniformity of the film is not under control because of the difficulties of coating uniform $(NH_4)_2MoS_4$) films at the beginning of the process [48]. Additionally, the self-assembly of the precursor on the substrate during dip-coating could lead to the growth of different morphologies such as MoS_2 nanowires rather than films [49]. A typical procedure of the dip coating approach is shown in figure 2:9 [48].

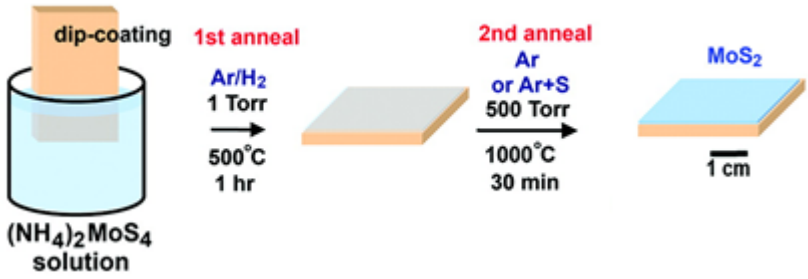

Fig. (2:9): Schematic illustration of the two-step thermolysis process for the synthesis of MoS_2 thin layers on insulating substrates. The precursor $(NH_4)_2MoS_4$ was dip-coated on SiO_2/Si or sapphire substrates followed by the two-step annealing process [48].

2.3.2 Physical vapor deposition

The growth of MoS_2 monolayers using physical vapor deposition has also been reported in a few works. This is a single component process in which high purity MoS_2 powder is evaporated in a thermal system at high temperature (900 °C) with the vapor carried away by an inert gas to the substrate placed in a cooler region (600 °C) on which the physical deposition happens and an MoS_2 film grow. The technique has successfully been used to produce micron-sized monolayers. However, there is no reports about scaling up the method as further work is needed for optimization of the process [50].

2.3.3 Atomic layer deposition (ALD)

ALD is also one of the common techniques that has been used for growing TMDs. The technique has multiple steps as shown in figure 2:10. The steps are as follows: (1) introducing a sublimed Mo source to the reaction chamber where the substrate is placed; (2) purging the chamber with an inert gas; (3) introducing the sulphur source to the reaction chamber; (4) purging the chamber again by an inert

gas to remove the reaction byproducts. The mentioned steps represent one cycle of ALD. Such cycles are repeated based on the required thickness to be deposited [51].

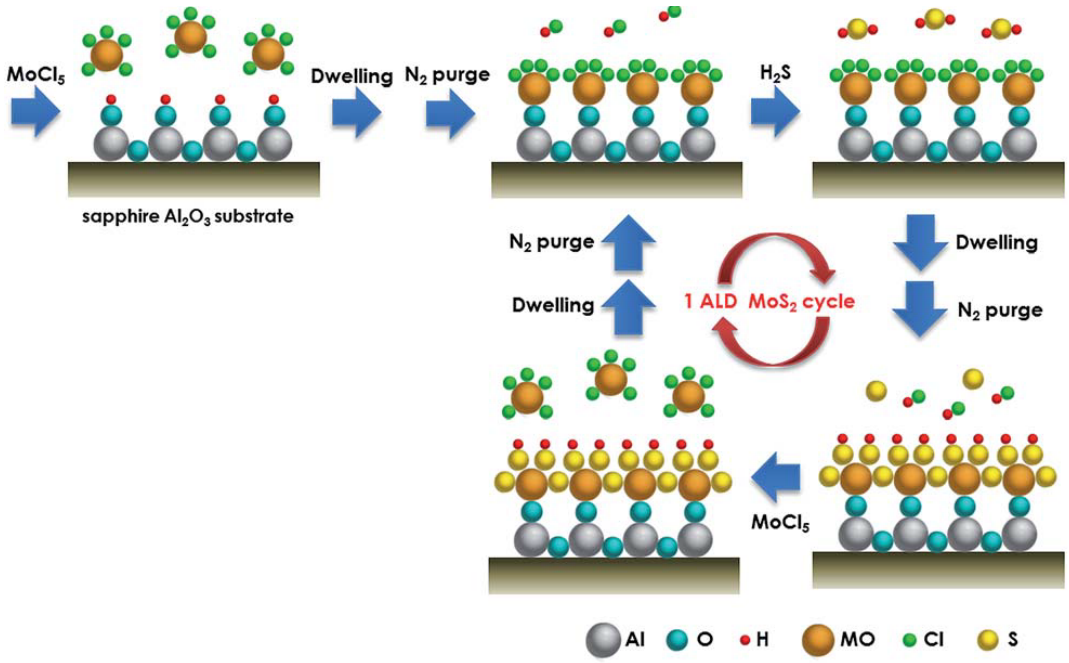

Fig. (2:10): Schematic illustration of one growth cycle of an ALD MoS_2 film [51].

Although the technique can be used to grow large scale MoS_2 films, the uniformity of the continuous monolayers on a wafer scale has not been reported yet. Beside the ALD grown MoS_2 films exhibit poor optical properties attributed to the amorphous nature of the as-grown films. To improve the crystalline quality of the as-grown films, further annealing in a sulphur rich environment is needed [51].

2.3.4 Molecular beam epitaxy (MBE)

The MBE technique has been widely used in growing TMD monolayers such MoS_2 [52], $MoSe_2$ [53] and WS_2 [54] as well as TMD heterostructures like MoS_2/h-BN [55], $MoTe_2/MoS_2$ [56] and $HfSe_2/MoS_2$ [57].

In this technique the transitional metal source and chalcogen are co-evaporated on a heated substrate using Knudsen effusion cells and e-beam evaporators [53]. The growth rate and the morphology of the grown 2D material is determined by source material fluxes [56].

There are several advantages of MBE over other deposition techniques, it can control the elemental deposition rates, and switch easily from one source material to another during deposition which enables the technique to have precise

composition control for heterostructure growth [56]. Another advantage of MBE is that the growth of the films can be in-situ monitored using tools such as reflection high energy electron diffraction (RHEED) [53].

However, the challenge in using MBE for growth of TMD heterostructures is that the chalcogens are volatile either in elemental form or as small molecules. This causes a low sticking coefficient on the growth-substrate, especially on inert van der Waals substrates. Therefore, MBE generally requires low growth temperature regimes and chalcogen rich conditions [56]. Finally, as the films are grown in low temperature regimes, the grains have a limited grain size (<200 nm) [54].

2.4 Conclusion

We have presented the main techniques that have been employed in the deposition of TMDs and TMDs heterostructures.

Initially, researchers focused on depositing TMDs using top-down techniques for fundamental research purposes and studying the intrinsic opto-electronic and structural properties. The field of 2D TMDs was started by micromechanical exfoliation of graphene in 2004 and then this technique become one of the most widely used in exfoliating other 2D materials such as MoS_2, WS_2, h-BN ...etc. The technique is simple and does not need sophisticated tools to produce monolayers and multilayers. However, it is time consuming and for mass production it is not reliable.

To scale up the production, other exfoliation techniques such as liquid exfoliation have been tried. Beside the success that has been achieved in producing large amount of 2D materials, the technique failed to produce pure monolayers and there is always a mixture of monolayers and multilayers in the yield. The problem of reaggregation of the produced monolayers still needs to be tackled.

Top-down techniques, such as CVD, PVD, ALD and MBE, are offering an alternative for growing 2D materials on large scales that are essential for industrial applications. Rapid development in the deposition of 2D materials, driven by optimizing the growth conditions and using different starting materials, has been reviewed.

Graphene and other 2D materials with grain sizes of several hundreds of microns have been grown using CVD. Continuous films on relatively large areas

have been achieved. Heterostructures of different kinds are successfully grown using MBE.

Although remarkable successes have been achieved in depositing 2D materials, the grown films are polycrystalline with relatively small grain size, and there is a lot of grain boundaries that affect the opto-electronic and mechanical properties of the film. The growth of films with large grain size is still a challenge. More understanding about the film growth mechanisms and optimum growth conditions still need further investigations.

The continuity and uniformity of the grown films will also affect the potential applications of the films. More work is needed to produce continuous uniform wafer scale films. This can be done through more investigations about the nature of the starting materials, substrates and trying different growth regimes.

All in all, the 2D materials are becoming more and more interesting and potential applications in future microdevices have already appeared on the horizon. Through the available techniques, a variety of monolayers and heterostructures have been produced. However, despite the intense research work towards controlled deposition of 2D materials, wafer scale growth, uniformity and grain size remain challenging issues. The chemical vapor deposition (CVD) technique has shown great potential to grow large area TMDs. Nevertheless, mass production for industrial applications is still at the very early stages which requires more efforts to achieve the goal.

Chapter 3:Experimental and Simulation Techniques

In this chapter we introduce the characterization and simulation tools that have been employed during the course of this project. Different techniques have been used for characterization of MoS_2 mono and multilayers. The following is a list of techniques: optical microscopy, X-Ray photoelectron spectroscopy (XPS), photoluminescence spectroscopy (PL), atomic force microscopy (AFM), Raman spectroscopy, second harmonic generation (SHG) microscopy, scanning electron microscopy (SEM), transmission electron microscopy (TEM) and X-ray diffractometry (XRD). For CVD simulations we used COMSOL multiphysics 5.2a.

3.1 Characterization techniques

3.1.1 Optical microscope

Optical microscopes are inexpensive, rapid and nondestructive tools for characterization large areas of 2D materials. As a result of light interference between the 2D layer and underlying substrate, even single layer of graphene on SiO_2 covered Si show detectable contrast under optical microscope [58]. Figure 3:1 is a depiction of 2D/SiO_2/Si stacking [59].

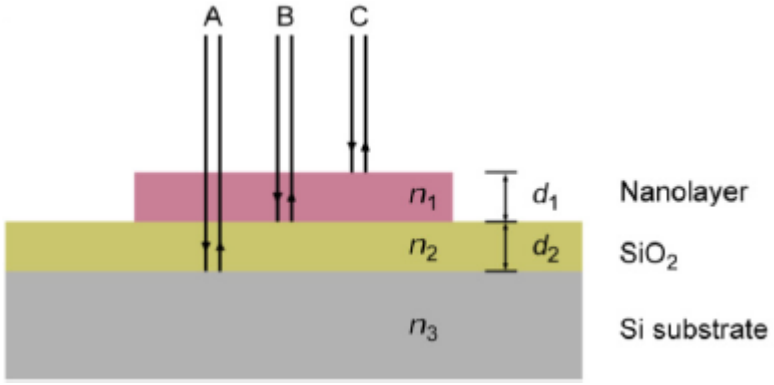

Fig. (3:1): Schematic depiction of optical reflection and transmission for a nanolayer with thickness d_1 and complex index of refraction n_1 deposited on an SiO_2 layer characterized by thickness d_2 and index of refraction n_2 that is grown on top of a Si substrate. Nanolayers deposited on SiO_2 are visible due to interference between light rays A, B and C reflected at various interfaces in the stack [59].

Under normal incidence the intensity of the reflected light from 2D/SiO_2/Si stacking can be calculated as follow [59]:

$$R(n) = \left| \frac{r1e^{i(\varphi 1+\varphi 2)} + r2e^{-i(\varphi 1-\varphi 2)} + r3e^{-i(\varphi 1+\varphi 2)} + r1r2r3e^{i(\varphi 1-\varphi 2)}}{e^{i(\varphi 1+\varphi 2)} + r1r2e^{-i(\varphi 1-\varphi 2)} + r1r3e^{-i(\varphi 1+\varphi 2)} + r2r2r3e^{i(\varphi 1-\varphi 2} \right|^2 \qquad 3:1$$

where

$$r1 = \frac{n_o - n_1}{n_o + n_1}\ ,\ r2 = \frac{n_1 - n_2}{n_1 + n_2}\ ,\ r3 = \frac{n_2 - n_3}{n_2 + n_3} \qquad 3:2$$

are the relative indices of refraction and $\varphi_i = \frac{2\pi d_i n_i}{\lambda}$ are the phase shifts induced by changes in the optical path. n_o, n_1, n_2 and n_3 are the refractive indices of air, 2D material, SiO_2 and Si respectively.

The reflectivity of the bare substrate is given by:

$$R(n1 = 1) = \left| \frac{r'2e^{i(\varphi 2)} + r3e^{-i(\varphi 2)}}{e^{i(\varphi 2)} + r'2r3e^{-i(\varphi 2)}} \right|^2 \qquad 3:3$$

where $r'2 = \frac{n_o - n_2}{n_o + n_2}$ is the relative index of refraction at the interface between air and the dielectric thin film.

Then the contrast between the the substrate and 2D material is given by:

$$Contrast = \frac{R(n=1) - R(n)}{R(n=1)} \qquad 3:4$$

Using optical microscopy, the contrast of the 2D material depends on the thickness of the underlying SiO_2, 2D material thickness and camera filter used for imaging. Therefore, optical microscopy is a rapid tool for distinguishing monolayers from multilayers and confirming the uniformity and continuity of the grown film [60]. Figure 3:2 is a typical example of the calculated contrast as a function of MoS_2 layer number when using 300 nm SiO_2 covered Si as substrate [60].

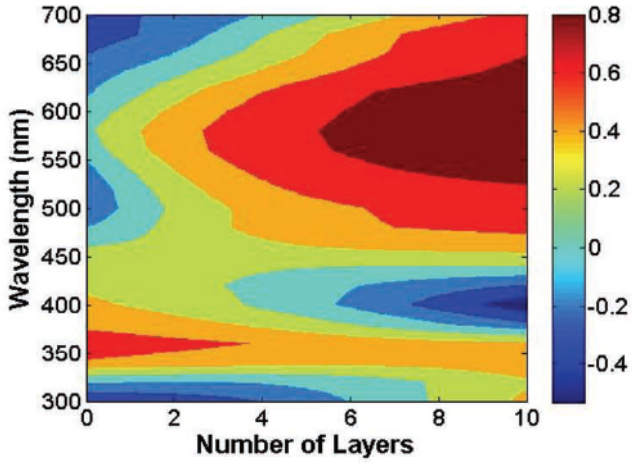

Fig. (3:2): Color contrast plot of calculated contrast as a function of the number of layers of MoS_2 ultrathin films and the illumination wavelength for 300 nm thick SiO_2/Si substrates [60].

Figure 3:3 (a-m) color optical micrograph of exfoliated 1L-15L MoS_2 on a 300 nm SiO_2/Si substrate. Figure 3:3 (n) is the measured contrast between MoS_2 and substrate as a function of layer number [61].

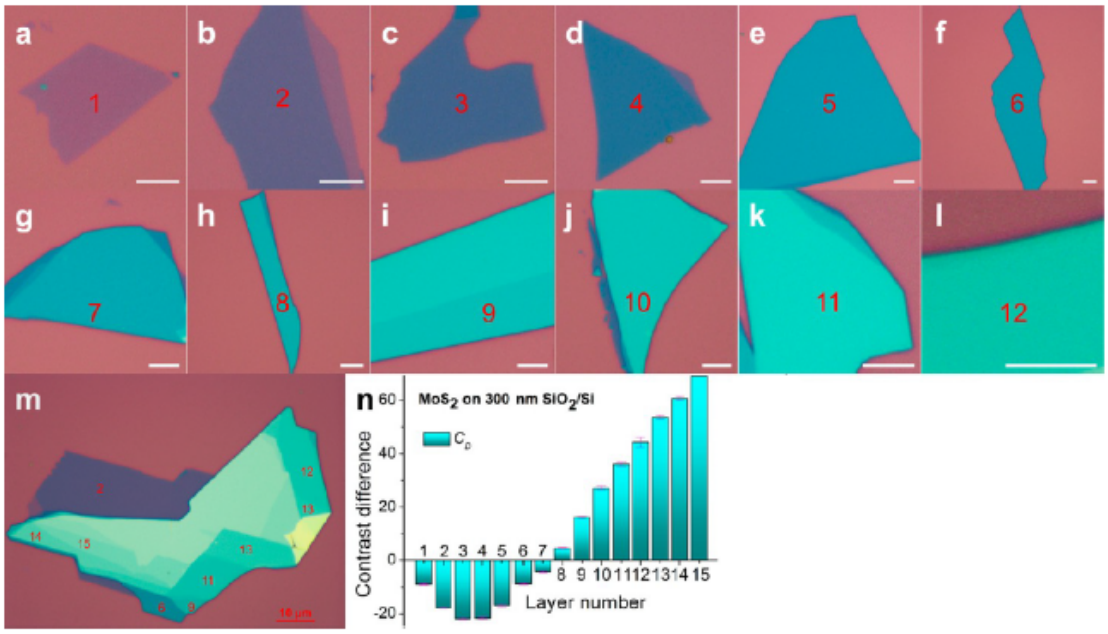

Fig. (3:3): (a–m) Color optical images of 1L–15L MoS_2 on 300 nm SiO_2/Si. The scale bars are 5 μm for images a–l and 10 μm for image m. (n) Contrast difference values of 1L–15L MoS_2 nanosheets on 300 nm SiO_2/Si [61].

3.1.2 X-ray photoelectron spectroscopy (XPS)

X-ray photoelectron spectroscopy (XPS) is a non destructive surface analysis technique that can be used to study the surface chemistry of materials. It measures the binding energy of the materials under investigation. Such measurements can be employed to find the chemical composition of sample constituents. The XPS spectra can be obtained by exposing the sample to a monochromatic soft X-ray with a certain wavelength. The incident X-ray removes core electrons which are then collected and analysed. Since the mean free path (inelastic scattering length) of the emitted electrons in solids is very short, the detected electrons originate from the top few atomic layers, making XPS a surface sensitive technique. The energy of the ejected electron represents the binding strength of the core level which is an indicator of the presence of a certain element. The emitted electrons have measured kinetic energies given by [62]:

$$KE = h\upsilon - (\Phi + BE) \qquad 3:5$$

where *KE* is the kinetic energy of the emitted electron, *h* is Planck's' constant , Φ is the work function *BE* is electron binding energy.

Furthermore, the atoms' core level binding is very sensitive to the chemical environment of the corresponding atom. For an atom in two different chemical states, the binding energy for the same core level will be different. Such variation in the binding energy results in a shift in the position of XPS peaks. This effect is called a chemical shift and can be used to study the chemical status of the elements in the sample [62]. The spectral intensity for the core level transition is proportional to the quantity of that element in the sample.

3.1.3 Photoluminescence spectroscopy (PL)

In photoluminescence spectroscopy, we use the optical emission spectrum of semiconductors to study their electronic structure.

When a semiconductor is exposed to radiation with photon energy greater that the band gap of the semiconductor, electrons are excited to the conduction band leaving holes in the valence band. When the electrons return to the ground state, they recombine with holes and emit radiation with a certain wavelength that is characteristic of the semiconductor under study [63].

Experimentally, a laser beam with an appropriate photon energy is focused by an objective lens on the sample surface and the emitted radiation is recorded after filtering the incident beam. The emission spectrum extracted provides valuable information about the type of semiconductor whether it has a direct band gap or an indirect band gap, the semiconductor quality and the presence of impurities and defects [63].

As we explained in chapter one, an MoS_2 monolayer is a direct band gap semiconductor and, due to the valence band splitting in MoS_2, there are two excitonic transitions from the valence band to the conduction band called A and B. The observed PL peaks of the two excitons are at 1.85 eV and 1.98 eV respectively [13].

In this project, we employed PL measurements for a non-destructive study of the intrinsic optical properties of our samples and evaluating the crystalline quality of the as-grown monolayer films.

3.1.4 Raman spectroscopy

When photons interact with matter, they can be transmitted, scattered or absorbed. The scattering processes have three categories depending on the frequency of the out-coming photons (v_o) which one shown in Figure 3:4. When the photons have the same frequency v_o to the incident ones, it is called Rayleigh scattering (elastic scattering). When the scattered photons have a different frequency ($v_0 \pm v_v$), the process is called Raman scattering (inelastic scattering). The intensity of Raman scattering is very weak, in the range of 10^3 to 10^6 times lower than the intensity of Rayleigh scattered photons which means the sample needs to be exposed to a laser light in the Raman spectroscopy [64], [65].

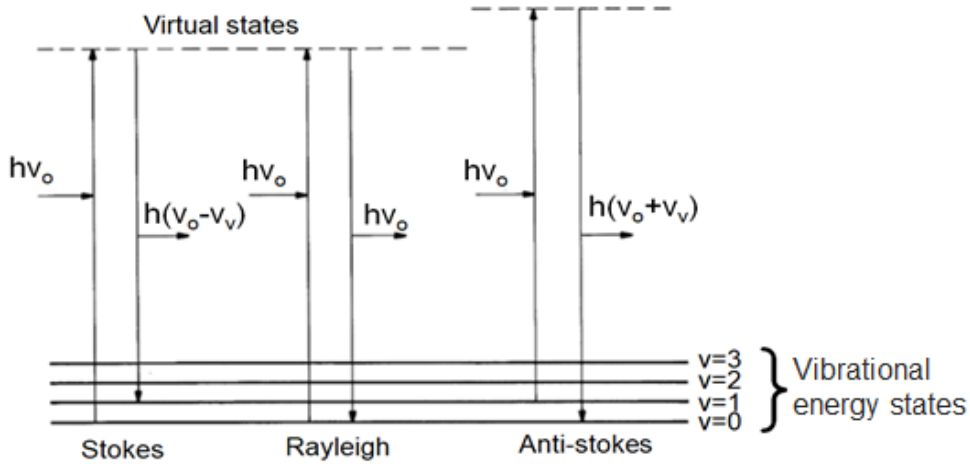

Fig. (3:4): Idealised model of Rayleigh scattering and Raman stokes and anti-stokes scattering [64].

Raman spectroscopy is a non-destructive technique based on the analysis of the inelastically scattered photons from the medium, produced by the interaction of the photon with the atomic vibrations that are also called phonons. Experimentally, the shift in frequency between the incoming and inelastically scattered photons is measured. The Raman effect was first observed in molecules by C.V. Raman in 1930, and nowadays the technique is one of the most widely used in analysing molecules and crystals [66].

Raman spectroscopy is a very powerful characterization tool in the field of 2D materials. Due to its sensitivity to symmetric carbon-carbon bonds it has been used to identify different carbon based materials: graphene, graphite, single-wall carbon nanotube (SWCNT), multi-wall carbon nanotube [67]. The G band of 1580

cm^{-1} corresponds to planar sp^2 C-C carbon in graphene, graphite and carbon nanotubes. The D band at 1350 cm^{-1} is a defect induced band corresponding to sp^2 carbon rings and its intensity is proportional to the presence of defects in the sample and it has been standardized for defect detection in graphene [68].

In our project, Raman spectroscopy is employed to assess the presence of MoS_2 crystals grown by CVD and to extract a qualitative thickness measurement as well as the growth induced strain in as grown films. For this purpose, we focus on analysing the most intense Raman modes detected from MoS_2 crystals. For bulk material, the so called the E^1_{2g} and the A^1_{1g} modes are located around 380 cm^{-1} and 405 cm^{-1} respectively. The former is due to in-plane vibrations of the atoms, while the latter results from the out of plane vibrations. It has been shown that for exfoliated MoS_2 layers as the MoS_2 is thinned down, the frequency of E^1_{2g} increased while that of A^1_{1g} decreased as shown in figure 3:5. The decrease in the latter one is attributed to a decrease in the interlayer van der Waals interaction that causes weaker restoring forces in the vibrations. The increase in the former one might arise from either long range Coulombic forces or stacking induced interlayer coupling. Therefore, this anomalous behavior is used as an indicator in identifying the number of layers present in a sample [69].

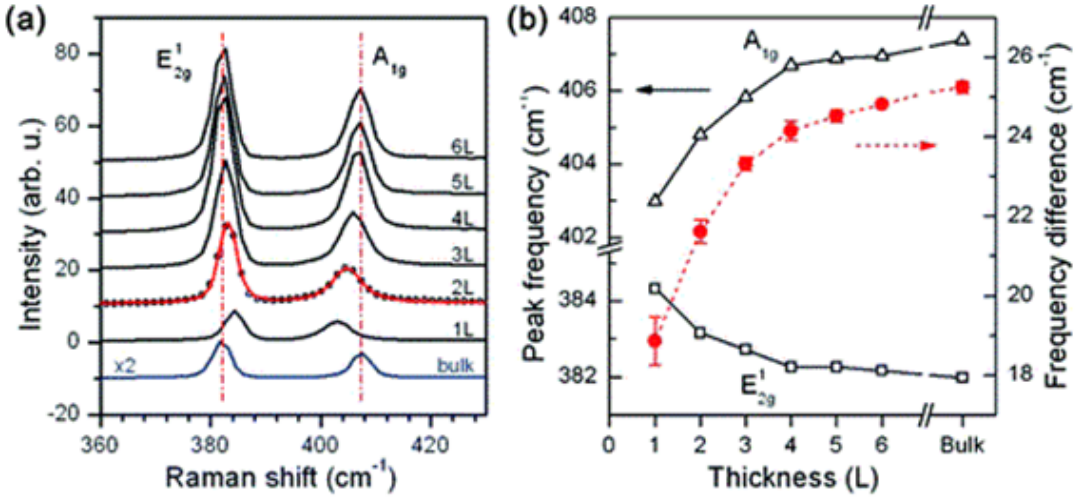

Fig. (3:5): (a) Raman spectra of thin (nL) and bulk MoS_2 films. (b) Frequencies of E^1_{2g} and A^1_{1g} Raman modes (left vertical axis) and their difference (right vertical axis) as a function of layer thickness [69].

In addition to thickness measurements, it has been found that the positions of these two peaks are very sensitive to the presence of strain in the film. In the case

of MoS_2 monolayers, a considerable shift of -2.1% strain in the E^1_{2g} mode, and a smaller, but observable shift of -0.4 % strain of the A^1_{1g} mode has been detected [70].

3.1.5 Second harmonic generation microscopy

When the intensity of the incident light is relatively low, interaction between light and matter can be assumed to be linear, and the induced polarization by the electric field is given by [71]:

$$\overline{P}(t) = \varepsilon_0 \chi^{(1)} \overline{E}(t) \qquad 3:6$$

where $\overline{P}$ is the polarization, ε_0 is the permittivity of free space, $\chi^{(1)}$ is known as the linear susceptibility and $\overline{E}$ is the electric field.

When the amplitude of the applied field is of the order of the characteristic atomic electric field strength of 5.14×10^{11} V/m, the linear relationship breaks down and the electric polarization depends on higher powers of the electric field [71]:

$$\overline{P}(t) = \varepsilon_0[\chi^{(1)}\overline{E}(t) + \chi^{(2)}\overline{E}^{\,2}(t) + \chi^{(3)}\overline{E}^{\,3}(t) + ...] \qquad 3:7$$

The quantities $\chi^{(2)}$ and $\chi^{(3)}$ are known as the second and third order nonlinear optical susceptibilities, respectively.

The second-order polarization:

$$\overline{P}^{\,2}(t) = \varepsilon_0 \chi^{(2)} \overline{E}^{\,2}(t) \qquad 3:8$$

gives rise to second harmonic generation SHG. In the SHG process, a laser beam with an electric field of [71]:

$$\overline{E}(t) = Ee^{(-i\omega t)} + cc \qquad 3:9$$

is incident upon non centrosymmetric crystals with second order susceptibility $\chi^{(2)}$ is non-zero, the nonlinear polarization created in such a crystal is given by [71]:

$$\overline{P}^{\,2}(t) = 2\varepsilon_0 \chi^{(2)} EE^* + (\varepsilon_0 \chi^{(2)}\, E^2 e^{-2i\omega t} + cc) \qquad 3:10$$

We see that the second-order polarization consists of a contribution at zero frequency (the first term) and a contribution at frequency 2ω (the second term).

According to the driven wave equation 3:10, this latter contribution can lead to the generation of radiation at the second-harmonic frequency.

MoS_2 monolayers, odd number of the 2H [72] and 3R [73] polytypes possess D_{3h} symmetry. With the D_{3h} symmetry, the second-order nonlinear susceptibility

tensor has nonzero elements of $\chi^{(2)}_{y'y'y'} = -\chi^{(2)}_{y'x'x'} = -\chi^{(2)}_{x'x'y'} = -\chi^{(2)}_{x'y'x'} = \chi^{(2)}$ where $x'y'z'$ are crystalline coordinates [71].

The relationship between the incident electric field of the pump laser and the coherently generated nonlinear polarization can be expressed as follows [74]:

$$I_{2\omega} \propto |\hat{e}_{2\omega}.(\chi^{(2)}_{x'y'z'}.\hat{e}_{\omega}).\hat{e}_{\omega}|^2 \qquad 3:11$$

where $\hat{e}_{\omega}$ and $\hat{e}_{2\omega}$ are the polarization vectors for the beams at the fundamental and the harmonic frequencies.

If the incident laser radiation is polarized along the x-direction, then x- and y-polarized SHG emission from a MoS_2 monolayer is given by [75]:

$$I^{x}_{2\omega} \propto |\chi^{(2)}.cos(3\Theta)|^2 \qquad 3:12$$

and

$$I^{y}_{2\omega} \propto |\chi^{(2)}.sin(3\Theta)|^2 \qquad 3:13$$

Here Θ is the angle of the crystal orientation, *i.e.* the angle between the orientation of incident polarized radiation and one of the mirror planes of the MoS_2 monolayer.

The orientations of each individual grain therefore can be determined as follow:

$$\Theta = \tfrac{1}{3} tan^{-1} \sqrt{\frac{I^{y}_{2\omega}}{I^{x}_{2\omega}}} \qquad 3:14$$

MoS_2 monolayers have three fold rotational symmetry, SHG without phase information can not distinguish between opposite crystal orientations and the measurable difference between grain orientations is from 0 to 30 degrees *i.e.* due to the reflection symmetry of the MoS_2 lattice, the six-fold symmetry present when using SHG [75]. Equation 3:14 has an angular resolution of about 1°, which is comparable to that achieved by TEM methods [76].

Figure 3:6(a) is an optical image of a polycrystalline MoS_2 monolayer film, with the corresponding (b) polarization resolved SHG image and (c) color coded orientation map of the same film and (d) select regions of the sample showing the actual crystal orientation vector of the grains [75].

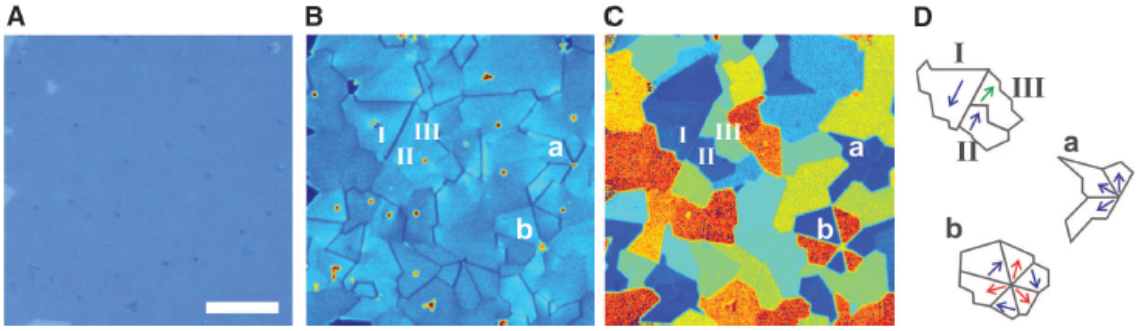

Fig. (3:6): (A) Optical image of CVD-grown monolayer MoS_2. (B) SHG image of a polycrystalline monolayer of MoS_2 of the same area showing the grain boundaries. (C) Color coded orientation map of the same area (D) Crystal orientation vectors of the grains I,II,III, b and a [75].

In this project, we used SHG for confirming the uniformity of our MoS_2 monolayer films. Polarization resolved SHG is used for finding the grain size distribution within the polycrystalline film.

3.1.6 Scanning electron microscopy (SEM) and energy-dispersive X-ray (EDX) spectroscopy

The scanning electron microscope (SEM) is a powerful instrument that permits the observation and characterization of materials on a nanometer (nm) to micrometer scale with resolving power of 1-5 nm [77].

The story of the scanning electron microscope and every other electron microscope started in 1926 when H. Busch (1926) studied the effect of electric and magnetic fields on the trajectories of charged particles in axially-symmetric fields [78] and the first prototype instrument was built by Knoll (1935) [79].

The major components of an SEM are the electron column and the control console. In the column there is an electron gun for generating electrons and electromagnetic lenses for controlling the electron path down to the sample [77].

Two different kinds of guns are used in SEM. Thermionic emission sources rely on high temperature to generate electrons such as a tungsten hairpin or lanthanum hexaboride LaB_6. The other is a field emission cathode, a sharp wire fashioned into point a (100 nm or less in radius) and supported by a tungsten hairpin [77].

The generated electrons accelerate to energies in the range 0.1-30 keV (100-30,000 electron volts) and pass through the condenser lense which de-magnifies the beam. The beam finally gets focused on the sample by an objective lens. The electron ray path is shown in figure 3:7.

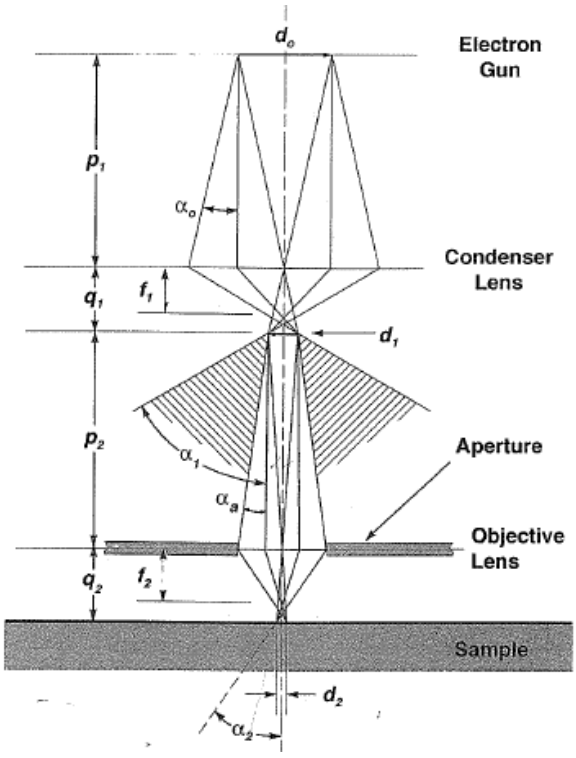

Fig. (3:7): Electron ray traces through a schematic SEM column with a condenser lens and a probe-forming or objective lens. Lens distances p and q are marked for each lens [77].

The focused electron beam interacts with sample atoms elastically or inelastically. This interaction derives many types of first and secondary emissions: elastically scattered electrons leaving the sample (sometimes via a process called "backscattering") provide an important class of information for SEM imaging. Simultaneously with elastic scattering, the incident electrons lose energy and transfer it in different ways to the target atoms giving rise to useful imaging signals such as secondary electrons (SE), visible light (chathodoluminecence, or CL), X-ray photons and Auger electrons [77].

The sample surface morphology of the sample can be determined by analysing the SE. The SE signal results from ionization of near surface sample atoms. More specifically SE are electrons ejected from the conduction band in the case of metals and the valence band in the case of semiconductors and insulators and their energy lies between (0-50) eV [77].

Backscattered electrons (BSEs) are beam electrons that are reflected from the sample at different depths by elastic scattering and their energy is very close to the incident beam. The scattering intensity of BSEs is proportional to to the atomic number of atoms existing in the sample. Heavy atoms give rise to a strong BSE

signal, therefore the BSE spectrum can be used for identification of sample composition [77].

In X-ray photon generation, the incident beam interacts with the tightly bound inner shell electrons of the target atoms. As a result, the inner shell electron gets ejected from the atom, leaving the atom in an excited state. The atom can relax to the ground state in two different ways: 1) via an Auger process in which the difference in shells energies is transferred to a valence electron ejecting it from the atom with a specific kinetic energy; 2) via X-ray generation where the difference in the shell energy is released as a characteristic X-ray photon with a sharp energy peak. By analysing the generated X-ray the elemental composition of the sample can be estimated [77].

For MoS_2 monolayers, SEM is one of the powerful tools for quick characterization of CVD samples on their growth substrates. Using the SE signal, a clear contrast between the monolayer and substrate and monolayer and multilayer can be observed. There is a weak interaction between the incident beam and 2D material monolayers and few layers because the depth of the interaction volume of secondary electrons in the 2D materials monolayers and few layers are much greater than their layer thickness. Therefore, the contrast of 2D materials with layer number might not be a result of direct interaction between the beam and 2D material. However, it is suspected that 2D materials monolayers and few layers attenuate a portion of the SE signal generated in the underlying substrate. As a result of this, increasing the thickness of the 2D material will result in a decrease in the number of the secondary electrons reaching the detector and thus a reduction of the SE signal over 2D material layers [80]. Figure 3:8 shows SE image of an as grown MoS_2 film showing monolayer, bilayer and bare substrate regions [43].

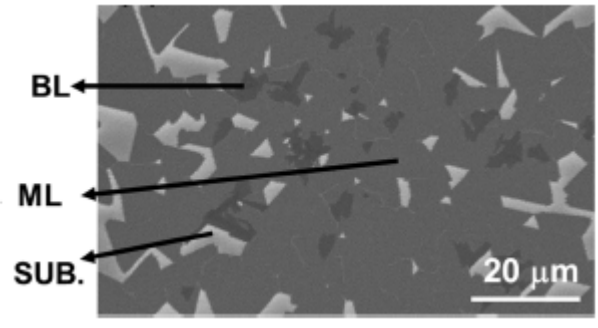

Fig. (3:8): SEM image of an MoS_2 film. Monolayer (ML), bilayer (BL) and substrate (SUB) areas are marked [43].

In addition, energy dispersive X-ray (EDX) could be the first checking point of the elemental composition of the grown film.

3.1.7 Transmission electron microscopy (TEM)

Transmission electron microscopy (TEM) is an electron based technique used for characterization of nanomaterials with resolution of 0.1 nm or better. As in the case of SEM, electrons in TEM are generated by either thermionic emission or field emission using (LaB_6) crystals and fine tungsten needles [81]. The generated electrons are accelerated by a high voltage (100-400 kV). Because of this high voltage, the electron wavelength is decreased dramatically, essential for the formation of high-resolution images [81].

Generally the image formation system in TEM consists of several lenses (electromagnetic lenses) and apertures (see figure 3:9). A condenser lens is located above the sample and it is used to produce parallel or convergent beam illumination of the sample under study. The parallel beam is usually used in TEM and convergent beam in the STEM. The objective lens sits just below the specimen to collect the electrons that pass through the specimen and are directed onto a focal plane and an image plane. The objective lens can be considered as the most important part of the TEM as microscope resolution and the image quality is largely determined by this lens. Under the objective lense there are intermediate lenses which allow either image mode or diffraction mode to be formed and control of the magnification in the case of image mode and change the camera of length in the case of diffraction mode. There are also projection lenses that project the image and diffraction pattern onto an imaging system [81].

Regarding the apertures, the condenser aperture controls the fraction of the electron beam that hits the specimen and thus controls the intensity of illumination. The objective aperture is placed in the back focal plane of the objective lens, the place at which diffraction patterns are formed. This allows one to use the objective aperture to select specific diffracted beams in diffraction contrast imaging. The selected area aperture is located in the image plane of the objective lens and allows selection of an area of interest in the conjugate sample plane. The basic image operation systems are shown in figure 3:9 [81].

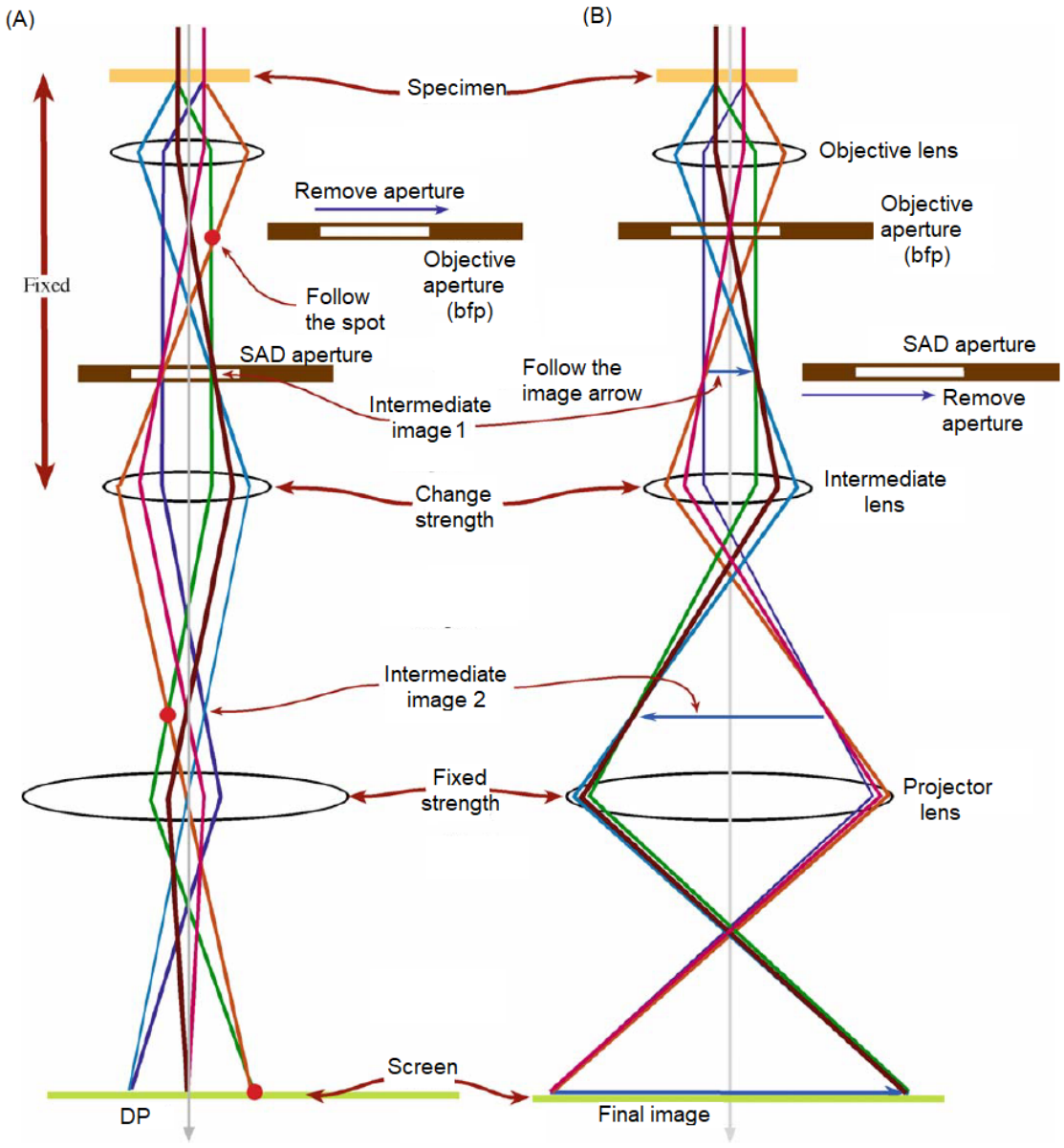

Fig. (3:9): The two basic operation modes of a typical TEM imaging system: (A) the diffraction mode: projecting the diffraction patterns (DP) onto the viewing screen and (B) the image mode: projecting the image onto the screen [81].

In our work, we used TEM to study the crystallinity of our samples using selected area diffraction patterns (SAED) as well as bright field images of large areas of the film, high resolution transmission electron microscopy (HRTEM) for atomic resolution structural imaging and scanning transmission electron microscopy (STEM) for annular dark field or Z-contrast imaging [81].

As the electron beam passes through a crystalline sample the electrons are diffracted by the atomic planes nearly parallel to the incident beam. The diffraction is described by Bragg's law [81]:

$$n\lambda = 2dsin(\theta) \qquad 3:15$$

where n is an integer called diffraction order, λ is the wavelength of the incident electrons, d is the separation between atomic planes and θ is the angle between the incident beam and the atomic planes. In the SAED, a selected area aperture is used to select an area of interest, then the intermediate lens is focused on the back focal plane of the objective the place where diffraction patterns are formed.

In bright field (BF) imaging the diffracted beams are blocked using an objective aperture and the transmitted beam is used for image formation and the image contrast depends on the amplitude of the transmitted beam. In dark field (DF) imaging, the transmitted beam is blocked and the diffracted beams are used for image formation, resulting in so called diffraction contrast imaging.

For HRTEM, the image formation is the result of the interference between the transmitted and diffracted beams in the image plane. This type of imaging is called phase contrast imaging. As the phase variations can not be detected directly, the phase modulation must be transformed into an amplitude modulation. This is done by the interference of the transmitted beam with suitably phase delayed diffracted beams. The phase difference in the sample exit wave changes into changes in the amplitude of the wave. By taking the effect of the spherical aberration and lens defocus only, the origin of the contract in HRTEM imaging can be described by a contrast transfer function (CTF):

$$CTF = sin[\pi \Delta f \lambda m^2 + \tfrac{1}{2}\pi C_s \lambda^3 m^4] \qquad 3:16$$

where Δf is the defocus of the microscope, λ is the wavelength of incident electrons, C_s is the spherical aberration and m is the spatial frequency.

In a special case when the macroscope is set to Scherzer defocus [81]. :

$$\Delta f_{Sch} = 1.2(C_s \lambda)^{0.5} \qquad 3:17$$

the point resolution of the microscope is given by:

$$r_{Sch} = 0.66 C_s^{\frac{1}{4}} \lambda^{\frac{3}{4}} \qquad 3:18$$

In STEM, the optics are different than in TEM. The electron beam is scanned over the sample using deflection coils, such that the incident beam is always parallel to the optical axis of the machine. During the scan, the STEM detectors register the scattered or transmitted beams at each probe position for a selected scattering angle. There are different types of detectors when using STEM mode. The electrons scattered at 0-10 mrad are registered using a bright field detector. For registering scattered electrons, Annular Dark Field (ADF), Medium-Angle Annular Dark Field (MAADF) and High Angle Annular Dark Field (HAADF) detectors are

used. HAADF imaging is also called Z-contrast imaging as the scattered electrons detected are mostly from Rutherford-type scattering with contrast proportional to atomic number Z.

3.1.8 Atomic force microscopy (AFM)

AFM is a particular type of scanning probe microscopy that relies on the interatomic forces between the tip and surface. AFM uses a tip typically made of silicon or silicon nitride and with a typical radius of tens of nanometers and is attached to the end of a small cantilever. By bringing the tip close to the sample surface, the forces between tip and surface cause deflection of the cantilever. There are different kinds of forces that the cantilever may experience, such as repulsive mechanical force, van der Waals force or magnetic force [82] .

In AFM, the tip scans the sample surface by using a piezoelectric scanner. The piezoelectric scanner moves the sample precisely in the *x*, *y*, and *z* directions as the piezoelectric materials used can change their shape in response to the applied voltage. A photo detector is used to detect the deflection of the cantilever during the scanning. This is done by measuring the displacement of a laser beam reflected from the back side of the cantilever. AFM generates an accurate topographic map of the features on the sample surface by using a feedback loop to control the height of the tip above the sample [83]. A schematic diagram of the basic setup of AFM is shown in figure 3:10 [84].

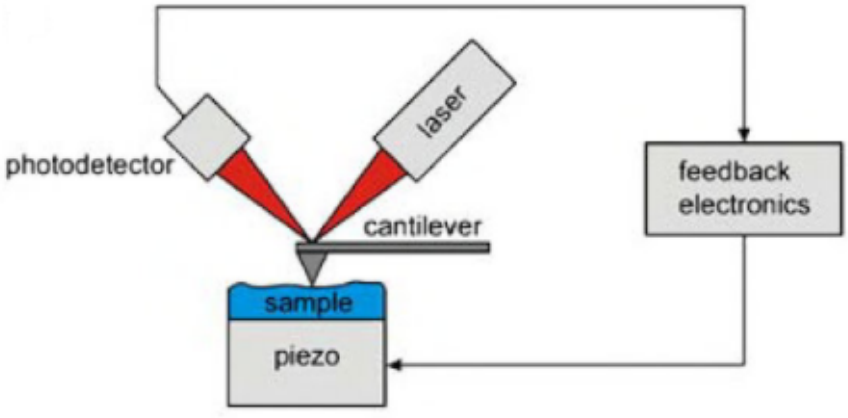

Fig. (3:10): Schematic diagram of a basic setup of AFM [84].

Depending on the distance between the tip and sample surface, three types of AFM operating modes can be distinguished: contact, non-contact and intermediate contact.

In contact mode AFM, the tip is brought very close to the sample, on the order of a few angstroms. At such distances the electronic clouds of the tip and the sample's atoms strongly repel each other due to Pauli-exclusion. This repulsive force causes the cantilever to be bent as it passes over the sample features during the scanning. The feedback loop ensures the actual cantilever deflection stays constant by comparing the actual bending with a given setpoint; if they do not coincide, the control system modulates the signal applied to the piezoelectric scanner so that the scanner retracts or extends in order to bring the deflection back to the setpoint [85].

In non-contact AFM, a cantilever vibrating at its resonant frequency is placed above the sample at a distance of tens to hundreds of angstroms. The force exerted by the sample features changes the amplitude of vibration of the cantilever with these changes used to extract the topographical data. Analogously to the contact mode, a constant amplitude is preserved by the feedback loop by changing the tip sample distance [85] .

The Intermittent contact mode, also called AC or tapping mode, is similar to the non-contact mode except that the tip is brought closer to the sample. The force is strongly repulsive when the tip touches the sample surface and attractive at the rest of the vibration cycle of the tip. Detecting both short range repulsive and long range attractive force increase the signal to noise ratio. This is an advantage compared to the non-contact mode, which relies only on the attractive long range forces [83], [85]. Figure 3:11 shows an idealized force curve between the tip and the sample with highlighted probe-sample separation regions where different AFM operating modes work.

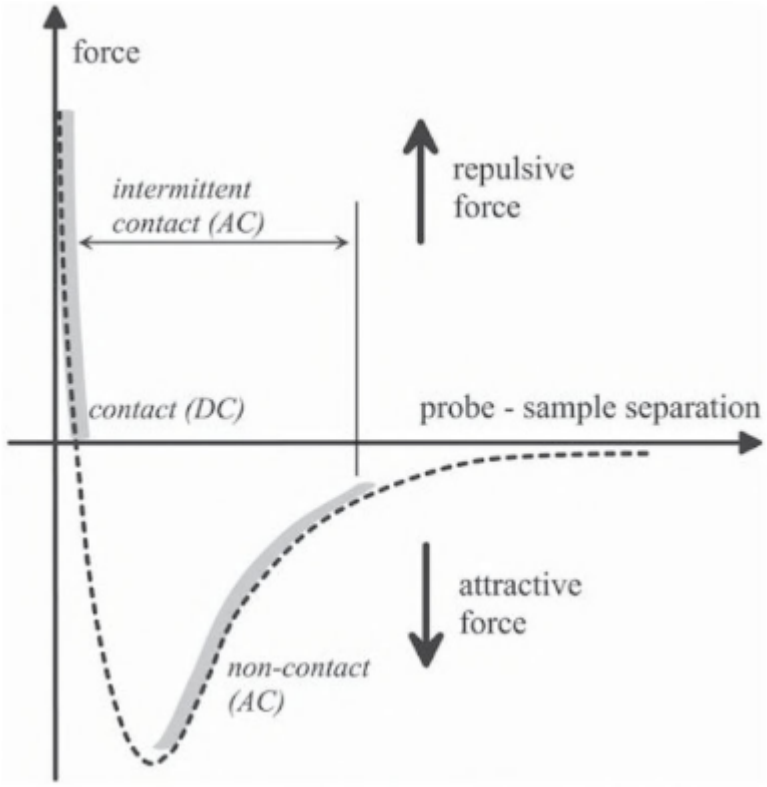

Fig. (3:11): Idealized forces between tip and sample surface highlighting where the three imaging modes are operative [83].

AFM is one of the most extensively used tools for obtaining topological images of 2D materials and their thickness measurement. Depending on the measurements conditions, the recorded AFM values of MoS_2 monolayer thickness range from 0.6 nm to 1 nm and for graphene from 0.3 nm to 1.7 nm [86].

3.1.9 X-ray diffractometry (XRD)

X-ray diffraction (XRD) is a non-destructive technique that can be used to study the atomic structure of materials, and characterize the crystallographic structure, grain size and strain in polycrystalline films [87].

In XRD experiments, an X-ray beam strikes a crystal surface and is scattered into different directions according to the crystal orientation. The scattered beams in a direction that satisfies the Bragg conditions (equation 3:15) add constructively and can be detected by an XRD detector. The beams in a direction that do not satisfy Bragg conditions interfere destructively and cancel each other [87].

A typical X-ray diffractometer consists of an X-ray source, a sample stage, and a detector. We are going to present the two configurations that have been used in this project. The first one is Bragg Brentano geometry in which the detector, the X-ray source and the sample are moved during the scanning in such

a way to guarantee the detector is always at 2θ and the sample surface is always at θ to the incident X-ray beam. In this configuration only the crystallographic planes which are nearly parallel to the sample surface can be detected. The schematic diagram of this Bragg Brentano configuration is shown in figure 3:12. The disadvantage of this configuration is that the penetration of the X-rays is large and as a result there is intense signal from the substrate and a weak signal from the surface. Therefore, it is not suitable for characterization of monolayer films [88].

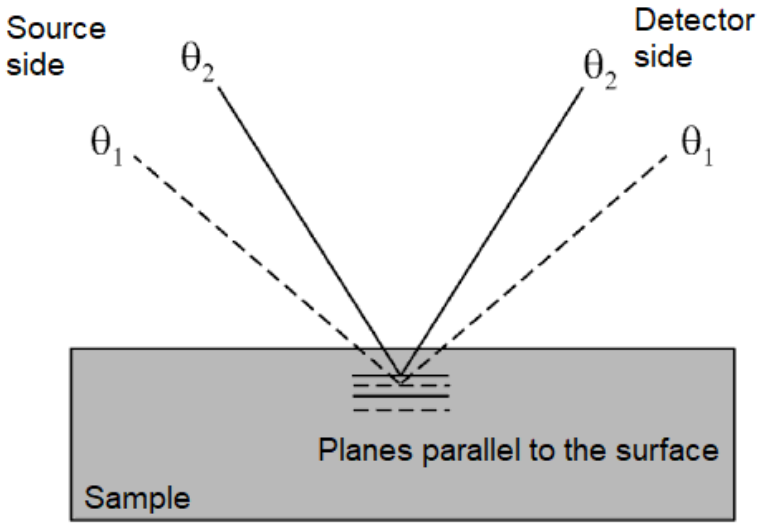

Fig. (3:12): Schematic of Bragg Brentano XRD [88].

In the case of monolayer films it is more convenient to use in-plane grazing incidence angle X-ray diffraction (GIIXRD) to maximize the signal from the monolayers. The X-ray beam is incident on the sample at very small angles (β~0) that are larger than the total internal reflection angle of the sample usually 1° or less and the detector is placed in a horizontal plane with respect to the sample surface to detect the diffracted beams from crystallographic planes which are perpendicular to the sample surface [88]. The schematic diagram of GIIXRD is shown in figure 3:13.

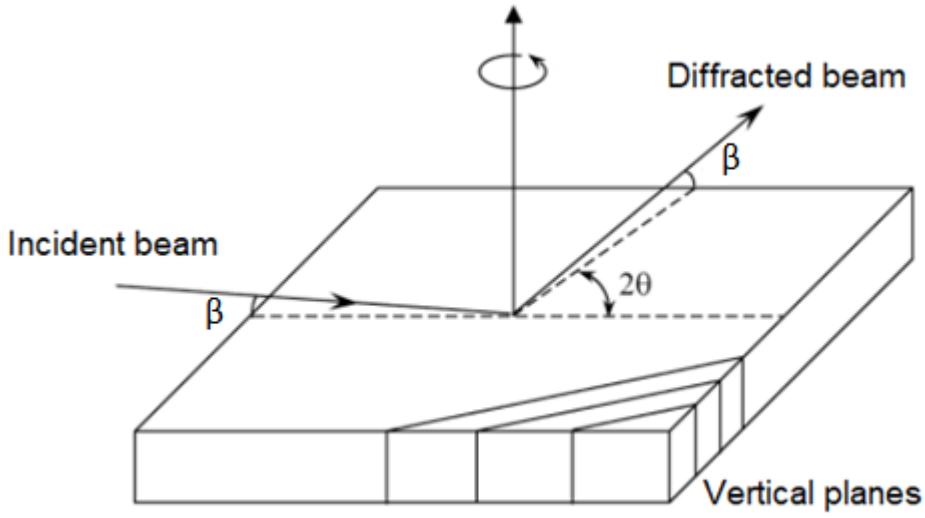

Fig. (3:13): Schematic of GIIXRD [88].

In this project, we used both types of XRD: θ-2θ scans were performed using Rigaku SmartLab diffractometer and in plane grazing angle incident X-ray diffraction GIIXRD using synchrotron radiation at Diamond Light Source.

3.2. CVD simulation using COMSOL

In our project the CVD simulations are performed by a commercial software COMSOL Multiphysics 5.2a. The COMSOL software has a powerful interactive environment for modeling and solving different kinds of scientific and engineering problems based on partial differential equations.

In our CVD simulations, the following coupling was investigated:

1- Momentum transfer - compressible Navier-Stokes equations

2- Mass transfer - convection and diffusion

3-Energy transfer - heat convection and conduction

Using the above couplings we correlate the carrier gas velocity to the pressure and temperature of the CVD system and the reactant concentration to the carrier gas velocity, pressure and temperature of the system.

The Navier-Stokes equations are the equations governing the fluid dynamics. When using these equations along with a set of boundary conditions such as the dimension of the inlets, the outlets and the walls of the system, the velocity, pressure, temperature and the density of the fluid can described inside the system. These equations are time-dependent continuity equations for the mass,

momentum and energy conservation respectively. In the case of a compressible Newtonian fluid, the momentum equation is [89]:

$$\rho(\frac{\partial u}{\partial t} + u.\nabla u) = -\nabla p + \nabla.(\mu(\nabla u + (\nabla u)^T - \frac{3}{2}\mu(\nabla.u)I) + F \qquad 3:19$$

where ρ is the fluid density, u is the velocity vector field, and μ is the fluid dynamic viscosity, T is transpose matrix and I is identity matrix. The left-hand side term corresponds to the inertial forces and the first term on the right hand side describes the differential pressure effect, the second term viscous forces and the last is external forces applied to the fluid.

Equation (3:19) is solved together with the continuity equation which describes the relationship between the temporal rate of change of mass density and the divergence of the mass flux [89].

$$\frac{\partial \rho}{\partial t} + \nabla.(\rho u) = 0 \qquad 3:20$$

The COMSOL fluid dynamics module is used to solve the above equations in our CVD system to describe the velocity profile of the carrier gas.

We also used mass transport in our CVD simulations to study the concentration profile of the reactant material inside the CVD reactor. The mass transport is coupled with velocity profile and temperature gradient along the tube furnace.

The chemical reaction engineering module of COMSOL is used for this purpose by solving the diffusion-convection equations [90]:

$$\nabla.(-D_i\nabla c_i) + u.\nabla c_i = R_i \qquad 3:21$$

$$N_i = -D_i\nabla c_i + uc_i \qquad 3:22$$

where D_i is the diffusion coefficient of the i^{th} species, c_i and R_i and N_i are the corresponding contraction, reaction rate and flux respectively.

Heat transfer is also very important in the CVD simulations since temperature gradient can affect the density of the fluid, which can affect the fluid flow and mass transfer. The heat transfer can be described through the following equation [90]:

$$\rho C_p u.\nabla.T + \nabla.q = Q \qquad 3:23$$

$$q = -k_f\nabla T \qquad 3:24$$

where C_p is the specific heat of fluid at constant pressure, T is the temperature of the system, Q are any other heat sources (chemical reaction), k_f is the thermal conductivity of the fluid, and q is the heat flux.

3.3 Summary

We have presented the characterization and simulation tools used during the course of this project. We have introduced the principles of visualising 2D materials under an optical microscope and explained how this simple tool provides valuable information about the 2D material thickness, uniformity and continuity. For the chemical analysis, the principle of XPS was introduced and its operation has been explained. Raman spectroscopy provides a qualitative MoS_2 thickness measurements and strain analysis in the CVD grown MoS_2 monolayer polycrystalline films. Its working principle was presented. The origin of the Raman modes shifting as a function of the MoS_2 thickness was explained and examples from the literature were given. Another thickness measurement method, using atomic force microscopy, was presented and the different operational modes are summarized. Second harmonic generation (SHG) microscopy was used for checking the monolayer film uniformity on a large scale and studying the grain size and orientation distribution as a function of experimental conditions. The physics behind SHG and polarization resolved SHG was outlined. The basic principles of the scanning electron microscopy were explained, with special attention given to the imaging by secondary electrons and the generation of X-rays. The imaging modes of TEM that have been used in this project such as dark field imaging, bright field imaging, HRTEM and STEM annular dark field imaging with the origin of contrast in each imaging mode were presented. For studying the crystalline nature of MoS_2 monolayers, two types of XRD, conventional XRD and GIIXRD were introduced. Finally, for CVD simulations, COMSOL software with a fluid dynamic module, a chemical engineering module, and a heat transfer module were presented.

Chapter 4: LPCVD growth of continuous MoS_2 monolayer films

Abstract

We have employed low pressure chemical vapor deposition (LPCVD) as our growth method for MoS_2 monolayers. Molybdenum dioxide (MoO_2) and sulphur (S) have been used as starting materials to achieve the growth of wafer scale uniform MoS_2 monolayers with crystal sizes up to 400 microns on SiO_2/Si substrates.

X-ray photoelectron spectroscopy (XPS) has confirmed the chemical composition of the monolayers. The thickness of the monolayers have been determined quantitatively using atomic force microscopy and the result is further corroborated by second harmonic generation and Raman spectroscopy. The uniformity of the films is verified using optical and nonlinear two photon microscopy.

Grazing incidence in-plane x-ray diffraction (GIIXRD) is used to study the growth induced strain in the as grown monolayer films as well as the monolayer thermal expansion coefficient.

The crystalline quality of the monolayers has been confirmed by transmission electron microscopy (TEM) and GIIXRD. Finally, the optical and electrical properties of the monolayers have been evaluated by photoluminescence spectroscopy and a field effect transistor respectively.

4.1 Literature review

There have been few approaches about growing continuous MoS_2 monolayers films on large scale (centimeter scale) via sulphurization of MoO_3, $MoCl_5$ and $Mo(CO)_6$. The growth of the continuous monolayer is being controlled via the partial pressure of the reactant materials which plays the major role on the final product composition and its uniformity [91]. The role of the reactant partial pressure will be discussed comprehensively in the following chapters. In the following paragraphs we will discuss the most frequent approaches that have been used by classifying them according to the Mo source being employed.

Regarding the molybdenum oxides, MoO_3 is the most extensively used. Jing Zhang *et al.* (2014), successfully grew MoS_2 monolayers on a centimeter scale using MoO_3. In their approach, the partial pressure of MoO_3 is controlled by changing the evaporation temperature of MoO_3 and growth temperature of the substrate. Although, the growth of a continuous monolayer film is successfully managed, the grown monolayer grains have relatively small sizes up 600 nm [40]. Similarly, Jaeho Jeon *et al.* (2014) used MoO_3 to grow MoS_2 monolayers, bilayers and trilayers. However, as a result of the local variation in MoO_3 concentration, the substrate was not fully covered with film and the grain size was still in the range of nanometers [40]. Finally, Shanshan Wang *et al.* (2015) used the substrate geometry to better control MoO_3 concentration in their CVD growth, however the films produced are not uniform and the grain size was few microns [92]. Despite the relatively large amount of MoS_2 monolayers grown using MoO_3, those approaches are still facing scalability issues.

To overcome scalability and have better control on the deposition, recent reports on TMD growth have focused on using alternative precursors as Mo sources, primarily transition metal halides such as $MoCl_5$ or transition metal carbonyls such as $Mo(CO)_6$.

Using $MoCl_5$, the CVD growth of MoS_2 monolayers and multilayers on a large scale is well controlled [41]. In contrast to the well defined morphological shapes of MoS_2 monolayers that can be produced using MoO_3, the monolayer produced using $MoCl_5$ are continuous and do not have well defined morphology, and the monolayers have poor crystalline quality [93].

The growth of continuous monolayer films has been achieved by MOCVD using $Mo(CO)_6$ and $C_4H_{10}S$. Using this approach, the growth of continuous monolayers is well controlled through the growth time. However, for monolayer , the growth time is quite long (26 hr) which might not be desirable from the production point of view [47]. The grain size of the produced monolayers is only few microns (up to 10 microns) [47]. Depending on the growth conditions, the grown film might contain undesirable carbon compound such Mo_2C or MoOC [94] [95]. The carbon impurities from starting material may be another issue for opto-electronic applications [91].

All in all, several attempts have been taken for growing MoS_2 monolayers on a centimeter scale using different CVD approaches. A remarkable success in the

film growth driven by controlling the partial pressure of reactants has been established, however, the uniformity, continuity and grain size of these films is still an issue and there is no standardized approach being presented for reproducible growth.

In this chapter, we are introducing an LPCVD approach using MoO_2 as a new starting material. MoO_2 has a relatively low vapor pressure compared to other Mo sources. We take and advantage of such a low vapor pressure to establish a standard approach that can be used to grow wafer scale, continuous, uniform, MoS_2 monolayers with the optimum grain size.

4.2 Experimental

4.2.1 CVD set-up, temperature dependence

The MoS_2 monolayers have been grown using a TSH 16/75/450 single zone tube furnace (from Elite Thermal Systems Limited) with a maximum operating temperature of 1600 ºC and a heating zone that is 45 cm in length, integrated with Eurotherm 2416 PID and 2116 over-temperature controllers. The gas flow through the tube furnace was controlled by an MKS Mass Flow Controller (MFC) Type 1179A with a maximum flow of 1000 Standard Cubic Centimeters per Minute (SCCM) and calibrated for argon and argon-hydrogen mixture. The MFC was controlled by a MKS PR4000 control box. The exhaust gas was passed through a sealed glass bottle half filled with water to remove particulates and prevent contaminated gas travelling up the exhaust. The setup of the furnace is shown in figure 4:1.

Fig. (4:1): The Elite thermal system used for growing MoS_2 monolayers.

The temperature distribution was measured along the tube from the center to both ends when the furnace was under vacuum (10 mbar) in order to know the temperature range that might be used in the experiments. For this purpose, a 1 m long, 0 → +1100 °C, K type thermocouple (supplied by RS) was used, with both-ends of the tube closed (without the flow of the carrier gas). The temperature profile of the furnace is shown in figure 4:2. It has a symmetrical form as expected. The central region has a constant heated zone at the designated temperature, with a width of 40 cm providing a relatively uniform temperature in the growth region where the Mo source and substrate are placed. The change to this temperature profile in the presence of the flow will be simulated using COMSOL and the result will be presented in chapter 5.

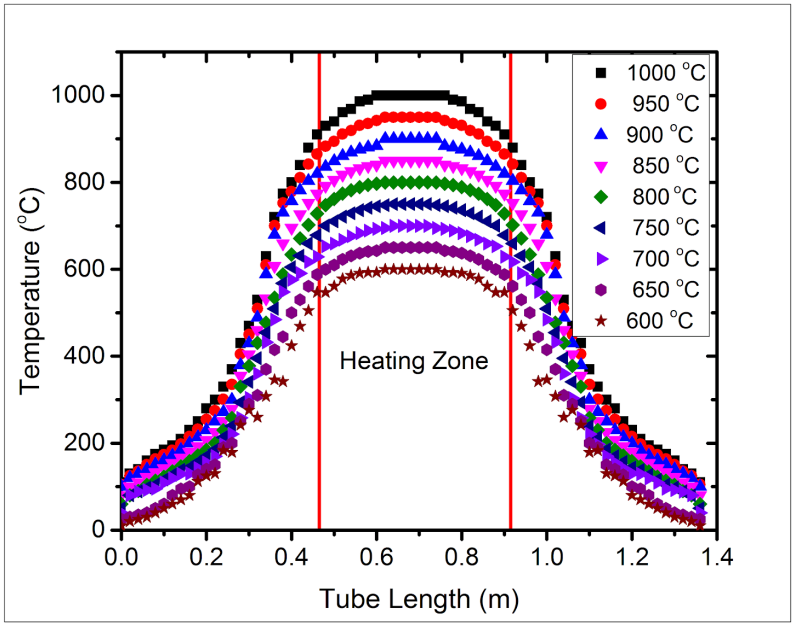

Fig. (4.2): Measured furnace temperature profiles for different set-temperature of the tube furnace.

4.2.2 Experimental procedure

In a typical two-zone CVD growth procedure, 300 mg of high purity MoO_2 powder (99% pure from Sigma Aldrich) was placed in a quartz boat. A SiO_2 covered Si wafer (5×3 cm^2 by dimension) was cleaned with acetone and ultrasonicated for 10 minutes and then placed face down on the MoO_2 container. The MoO_2 container with the substrates were then placed at the center of the 75 mm diameter tube furnace. Another boat containing 5-10 mg of sulphur powder (99.98% pure from Sigma Aldrich) was placed 42 cm away from the MoO_2, in a region where the temperature reaches 200 °C. Prior to the growth, the furnace was flushed with

Argon gas (1000 SCCM) for about 30 minutes. Then the furnace was pumped down to 10 mbar and the center was heated to 800 °C with a heating rate of 15 °C /minute in an argon flow (200 SCCM). After keeping at 800 °C for 10-20 minutes, the furnace was naturally cooled down to room temperature. The temperature of the sulphur source also rises, roughly in line with the temperature profile at the centre of the tube furnace, reaching an average of 200 °C during the 15 minutes when the sample is in the growth temperature. The temperature profiles during the growth process are summarized in figure 4:3.

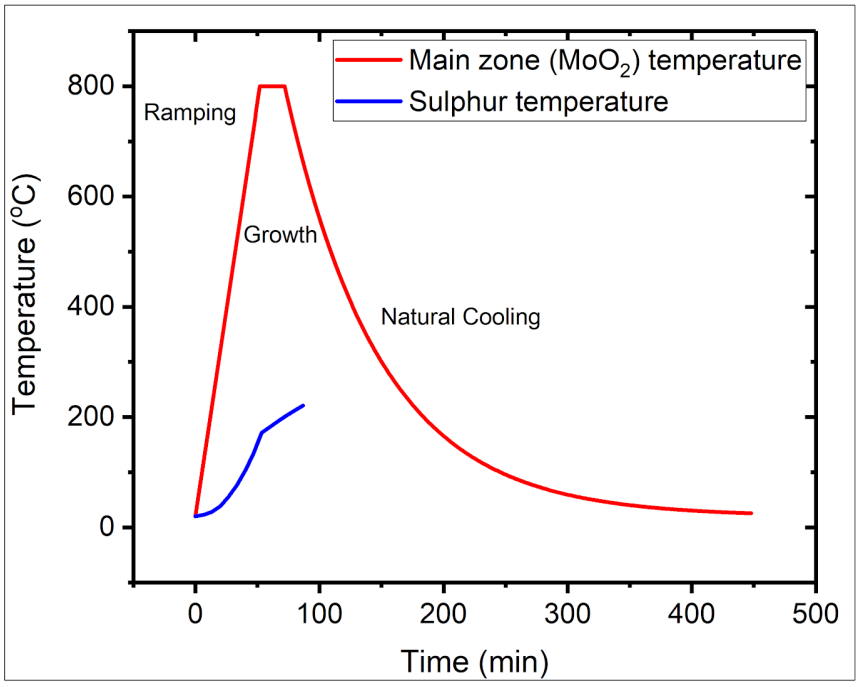

Fig. (4:3): Temperature profile for sublimation of starting materials during a typical growth run.

4.3 Results and discussion

4.3.1 Self-limiting growth of monolayer thin films

Figure 4:4 shows a low-resolution optical photograph of an as grown centimeter scale MoS_2 monolayer film (the upper purple colored part) and the bare 300 nm SiO_2/Si substrate (the lower part). There is a clear contrast for color of the area covered by the monolayer film (blue) compared to the color of the substrate (light pink). The color change is consistent with the expected light interference between the monolayer film and the 300 nm SiO_2 covered Si substrate [58], [59], [96], as we have explained in section 3.1.1. For a growth time close to 15 minutes, the whole substrate was found to be covered by a uniform monolayer thick film.

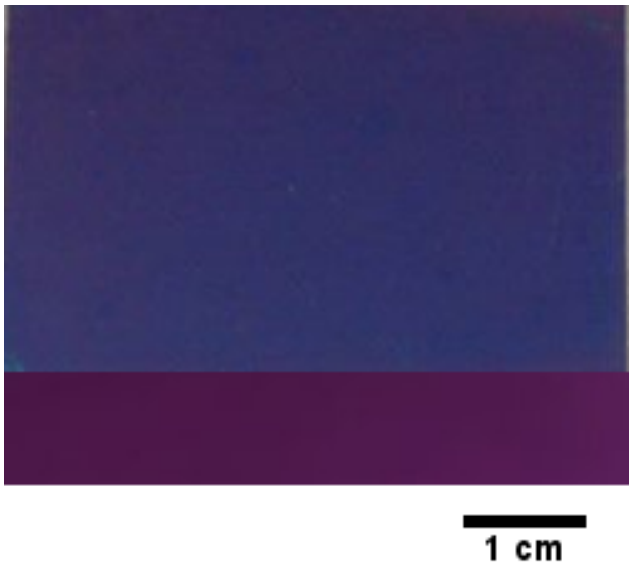

Fig.(4:4): Optical images of a centimeter scale MoS_2 monolayer (the upper part) and the bare SiO_2 covered Si substrate (the lower purple part).

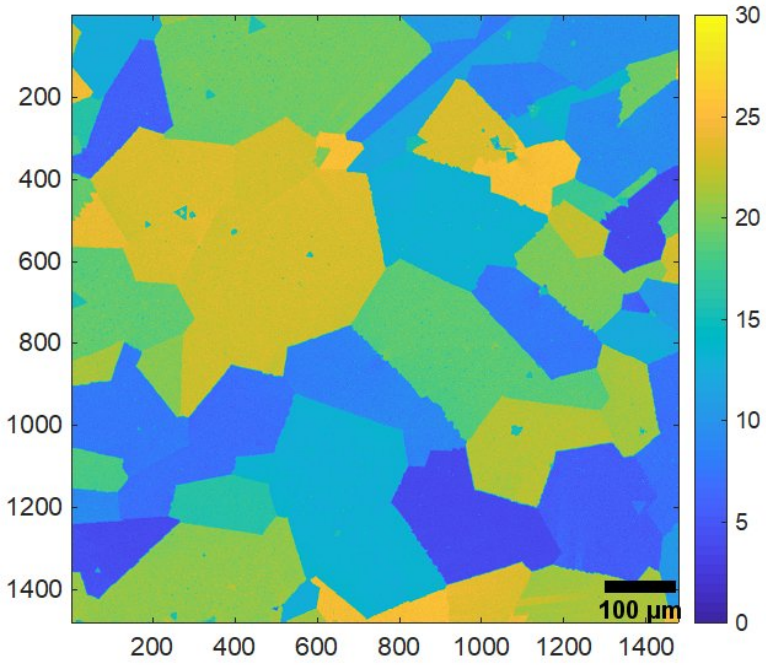

Fig. (4:5): Second harmonic generation (SHG) nonlinear two-photon microscopy revealing the polycrystalline nature of continuous MoS_2 monolayers where grains with different orientations show different color (see section 4:5 for details).

As the contrast between monolayer and multilayers of MoS_2 thin film can be quite subtle, we turn to nonlinear optical microscopy for additional confirmation as the SHG signal is both sensitive to layer thickness as well as the in-plane orientation of the crystallites [97]. Figure 4.5 shows a snapshot of our centimeter-sized monolayer. This shows that the film indeed consists of a continuous monolayer. The pseudo-color texture is due to its polycrystalline nature, as grains with different orientations showing different color (see section

3.1.5 of Chapter 3). This suggests that the film-growth, once started, can proceeded very rapidly but is self-limiting with very little evidence for pronounced secondary- or multilayer growth.

4.3.2 Chemical analysis by XPS measurements

Elemental composition and bonding in the CVD grown MoS_2 monolayers was examined with X-ray photoelectron spectroscopy (XPS). The data was taken at a base pressure of 2.5×10^{-9} mbar using an Al X-ray anode. The XPS source is the XM1000 MkII monochromator/x-ray source from Omicron (Scienta Omicron). The analyser is an Omicron EA125 hemispherical energy analyser. Survey scan was conducted at 0.5 eV per step, with a dwell time of 0.5 second at each step. Detailed scans were conducted at 0.1 eV per steps, with 1 second at each step, and an average 10 cumulative sweeps. For data analysis, the software XPSPeak 4.1 was used with the background subtraction type set to Shirley. Five elements are present in the spectra acquired. An example of the survey scan is presented in figure 4:6: Mo and S from the monolayer MoS_2, as well as Si, O from the substrate and C due to residual contamination from the samples having been in air.

In Figure 4:7 a detailed scan performed over the Mo 3d peaks and adjacent S 2s peak is presented. Clear Mo peaks corresponding to 3d 3/2 and 5/2 states are present with intensity ratio of 3:2 and an energetic position relative to the S 2s peak as expected. In our samples, the binding energy of the molybdenum doublet Mo $3d_{3/2}$ and Mo $3d_{5/2}$ appear at energies of 232.7 eV and 229.6 eV, and the sulphur S $2s_{1/2}$, S $2p_{1/2}$ and S $2p_{3/2}$ at 226.85 eV, 163.6 eV and 162.4 eV respectively. This is in good agreement with literature values for characteristic band positions of fully transformed MoS_2 grown by sulfurization of MoO_3 [98], [99] confirming complete conversion of MoO_2 to MoS_2 in our CVD growth process. Figure 4:8 zooms into the S 2p peak region where a clear doublet structure is observed with a good 1:2 ratio, as expected for emission from the corresponding $2p_{1/2}$ and $2p_{3/2}$ levels.

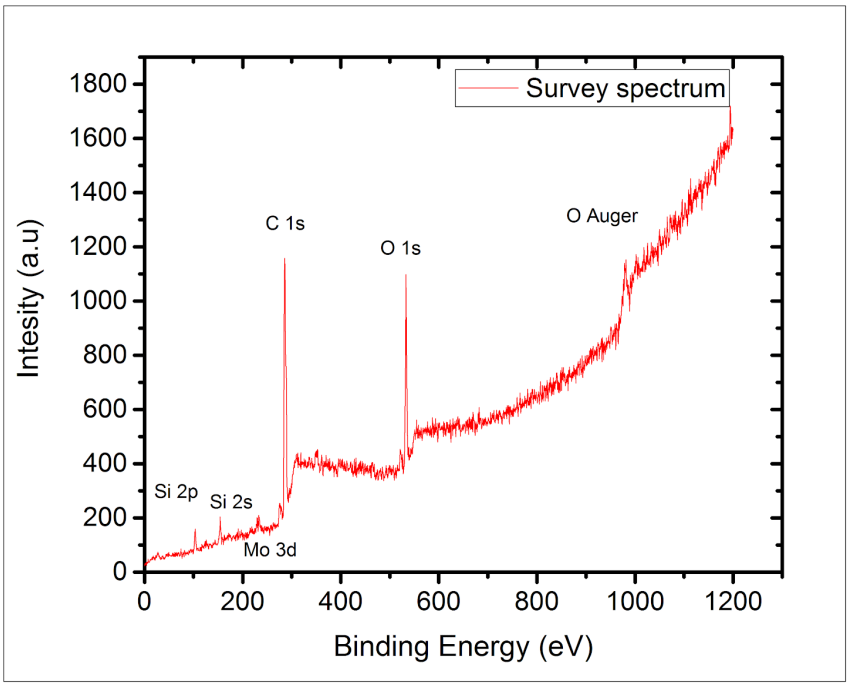

Fig. (4:6): XPS survey spectrum of MoS_2 monolayers grown on SiO_2/Si substrate.

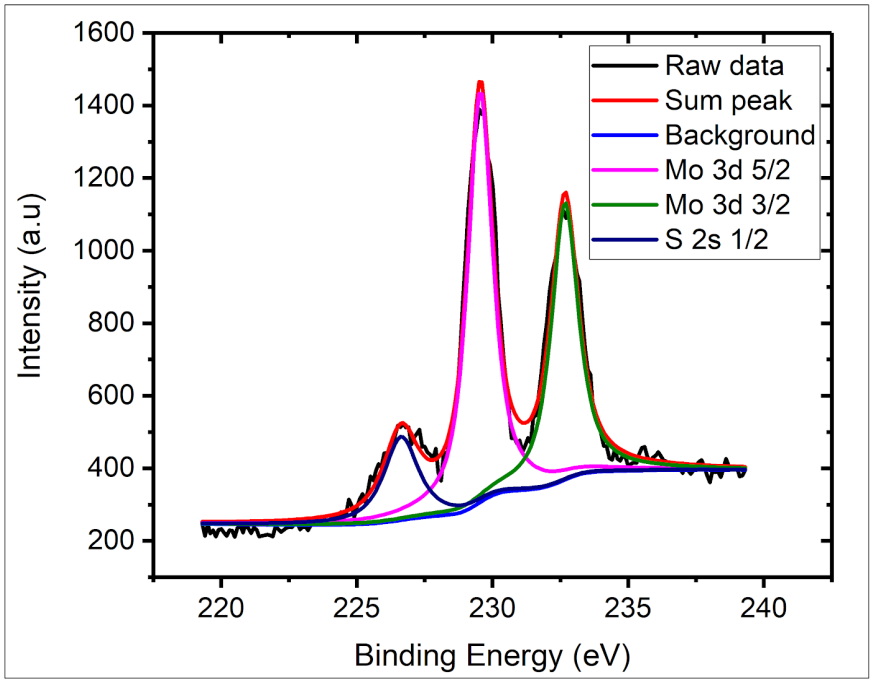

Fig. (4:7): Mo *3d* and S *2s* XPS spectrum of MoS_2 monolayers.

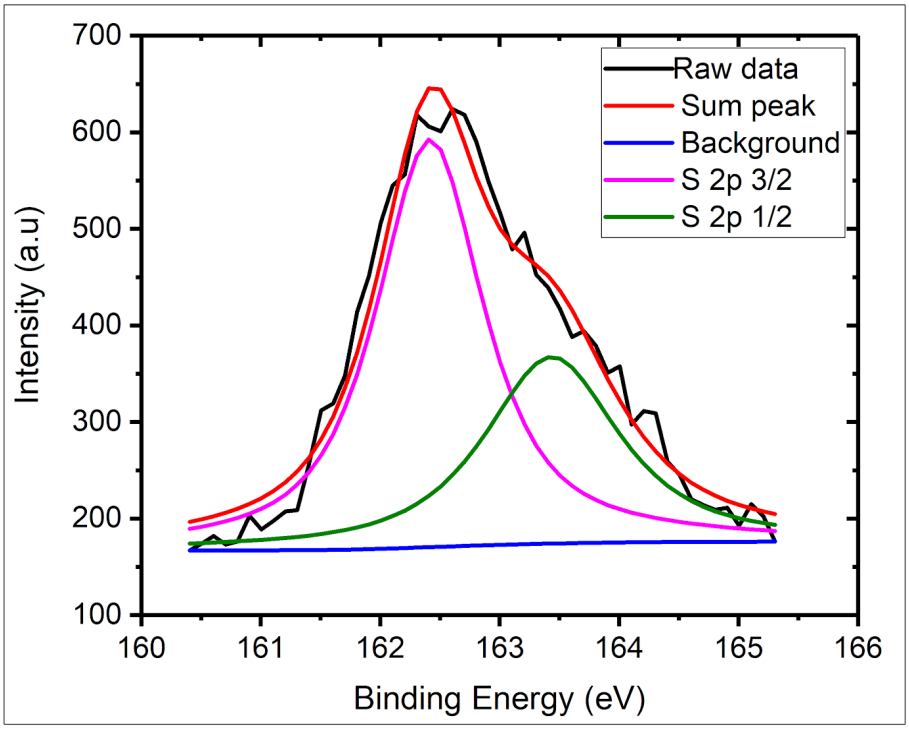

Fig. (4:8): S *2p* XPS spectra of MoS_2 monolayers.

4.3.3 Thickness measurements by AFM

For direct thickness measurements, a JEOL JSPM-5200 atomic force microscope was used. Figure 4:9 shows an AFM topography map of a single crystal region of a MoS_2 monolayer film. Figure 4:10 is a topographical measurement in a polycrystalline region of the same film showing a grain boundary. The monolayer thickness measurements were performed on the edges of the films. The edge of an isolated crystalline film is shown in figure 4:11 with the corresponding height profile displayed in figure 4:12. For a continuous film, the film is first scratched with a sharp tip and the measurements were then taken at the edges of the scratch as shown in figure 4:13 with the corresponding height profile displayed in figure 4:14. The height difference between the substrate and the crystal edge is found to be 0.9 nm and 0.85 nm for the isolated crystal and the continuous polycrystalline film respectively. These values (0.85-0.90 nm) agree well with the results from mechanically exfoliated MoS_2 monolayers reported in the literature [13].

To confirm that our films are uniform, other techniques such as Raman spectroscopy and second harmonic generation microscopy will be discussed in the next paragraphs as AFM is time consuming and continuous films have to be scratched, *i.e*. damaged.

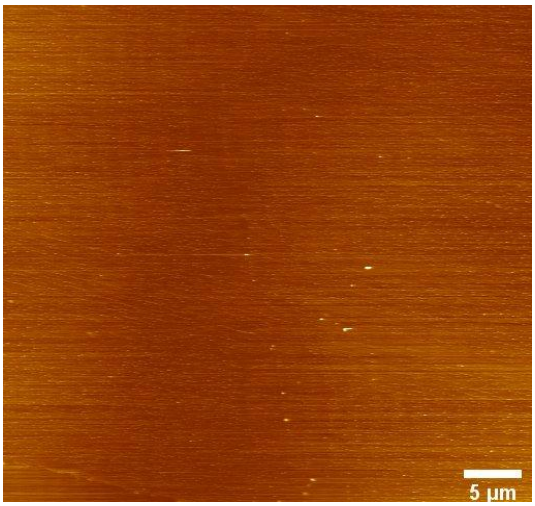

Fig. (4:9): AFM topography of a single crystalline MoS_2 monolayer.

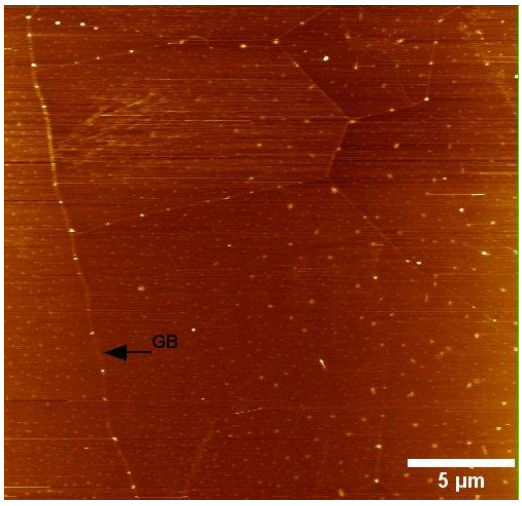

Fig. (4:10): AFM topography of a MoS_2 polycrystalline film showing grain boundaries (GB).

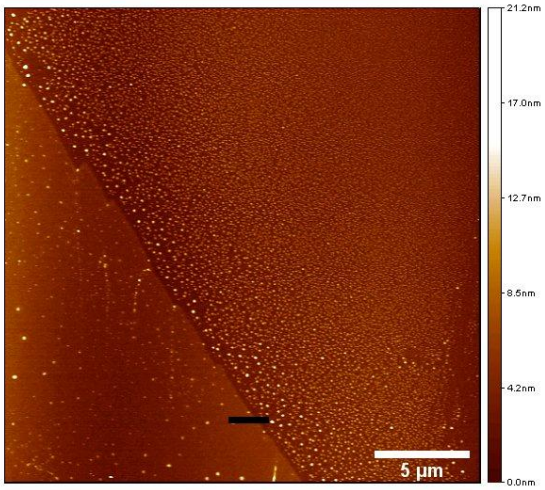

Fig. (4:11): AFM micrograph of MoS_2 single crystal monolayer edge.

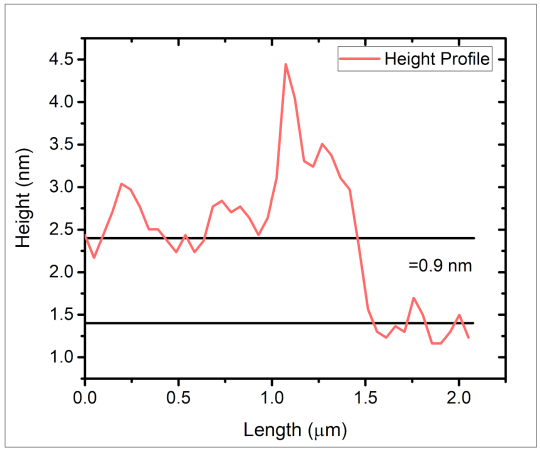

Fig. (4:12): Height profile measurements of the crystal shown in fig. (4:11); data taken along dark line.

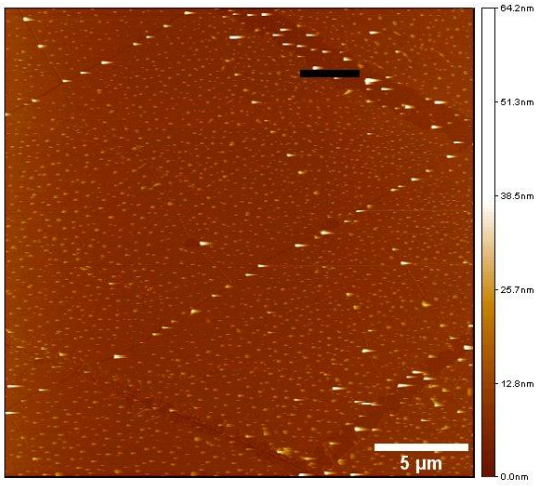

Fig. (4:13): AFM micrograph of a scratched continuous monolayer MoS_2 film.

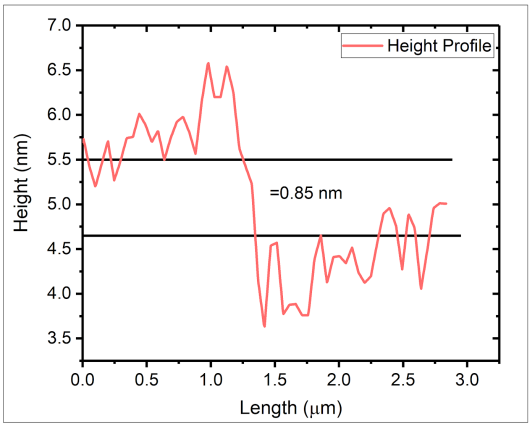

Fig. (4:14): Height profile measurements of the film shown in fig. (4:13): data taken along the dark line.

4.3.4 Uniformity of monolayer films using multiphoton microscopy

Due to the absence of the inversion symmetry in the MoS_2 monolayers, 3R stacking bulk MoS_2 and odd layers of 2H stacking, they exhibit very strong second harmonic generation (SHG) [73]. Therefore, this spectroscopic property can be employed for checking the uniformity of MoS_2 films and their stacking order. For this purpose, a confocal Zeiss LSM 780 multiphoton microscope was used for measuring second harmonic generation from MoS_2 monolayers. The measurements were performed in a reflection geometry using normal incidence excitation. The pump radiation was supplied by a mode-locked Ti:sapphire oscillator operating at an 80-MHz repetition rate. The pulses were of 140-fs duration and centered at a wavelength of 800 nm. Using a 10X objective and 20X with numerical apertures of 0.3 and 0.8 respectively. Figure (4:15) shows a SHG image of an incomplete coverage of MoS_2 monolayers on SiO_2 covered Si substrate. For this film the growth time was 5 minutes which is shorter than 15 minutes for a complete coverage. There is a clear contrast between the substrate (dark regions) and the monolayers (grey regions). This is because SiO_2 is amorphous and does not produce SHG.

Figure 4:16 (a-d) shows SHG maps of continuous polycrystalline monolayers films grown at temperatures of 700 °C,750 °C , 800 °C, 850 °C with a growth time of 15 minutes. From the SHG contrast in the images, we can confirm that the films are uniform and the slightly dark lines represent the grain boundaries [76].

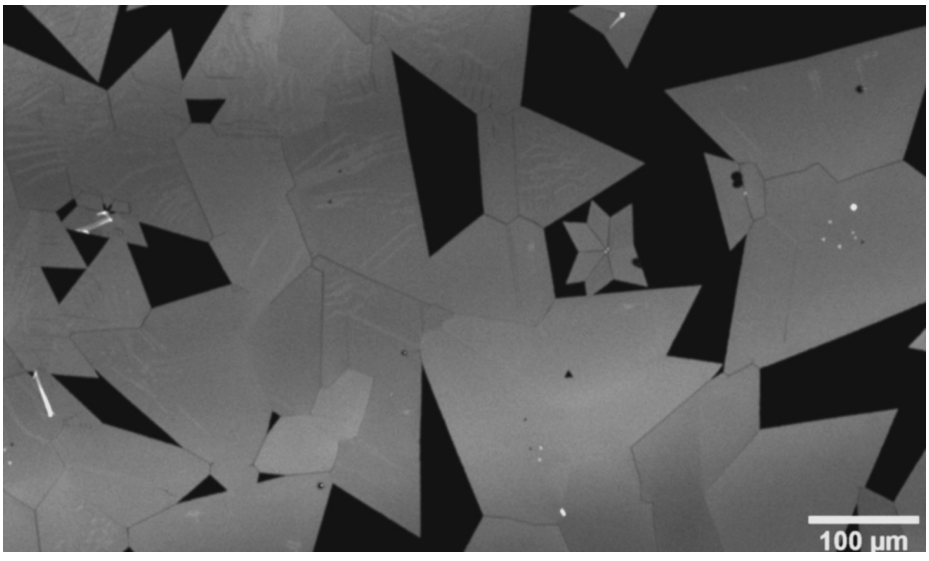

Fig. (4:15): SHG image of MoS_2 monolayers grown at 800 °C (grey regions) on a SiO_2/Si substrate (dark regions).

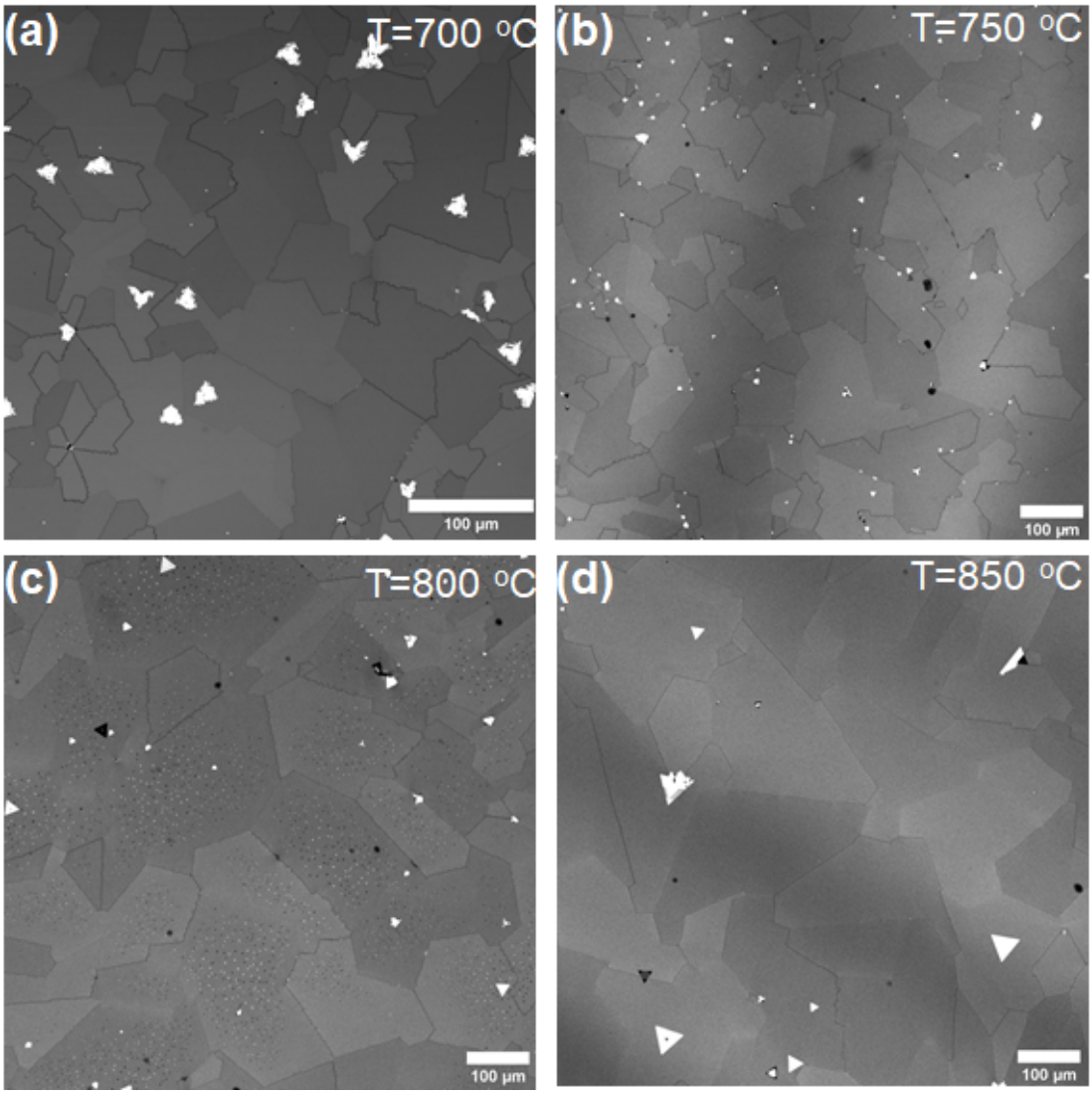

Fig. (4:16): SHG images of continuous MoS_2 monolayer films grown at growth temperatures of (a) 700 °C, (b) 750 °C, (c) 800 °C and (d) 850 °C.

Moreover, to stress that our films are monolayers we have shown a 3R stacking bilayer in figure (4:17). In this figure, there is a continuous background of monolayers. On top of that, there is a secondary nucleation of 3R stacking (bright triangles). In such a stacking there is constructive interference between SHG generated from the top and bottom layers which is why the top layer appears to be about 2.5 times brighter (the profile is shown in figure 4:18). In the case of 2H stacking bilayers as shown in figure 4:19, there is also a continuous monolayer background with triangles (dark ones) that have 2H stacking. In this case there is destructive interference between SHG generated from the top and bottom layers and the two beams completely cancel each other (profile is shown in figure 4:20). Theoretically, the total SHG from the stacking region of bilayers can be approximated as follows [97]:

$$I_t(\alpha) = I_1 + I_2 + \sqrt{I_1 I_2}\cos(3\alpha) \qquad 4:1$$

where I_t, I_1 and I_2 stand for the SH intensity in the stacking region, top grain and bottom grain respectively. α is the stacking angle between the two grains.

However, the measured SH from the stacking regions is slightly different due to the absorption and intensity variation (~10-15%) among different flakes [97].

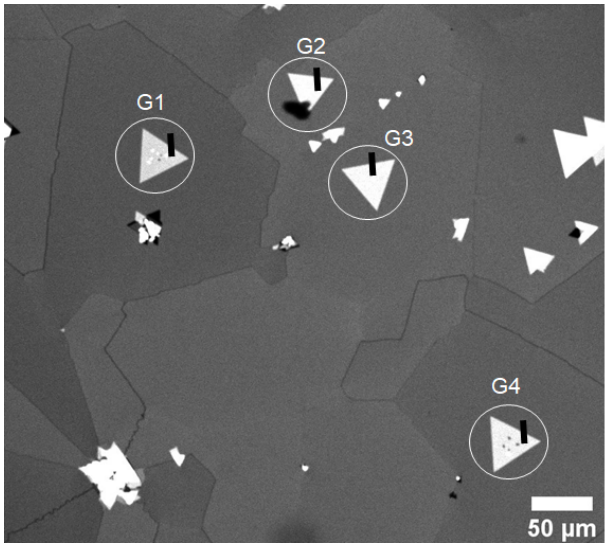

Fig. (4:17): SHG image showing 3R-Stacking MoS_2 bilayer grains G1,G2, G3 and G4 (white triangles).

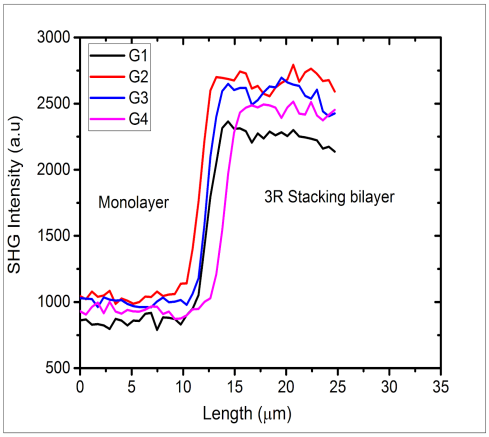

Fig.(4:18): SH intensity profile taken from MoS_2 monolayers and 3R stacking bilayer, data taken along dark lines on G1, G2, G3 and G4 shown in fig. (4:17).

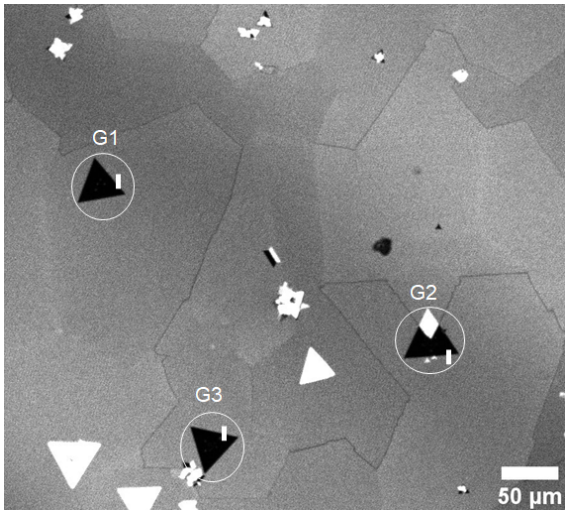

Fig.(4:19): SHG image of 2H-stacking MoS_2 bilayer grains G1, G2 and G3 (dark triangles).

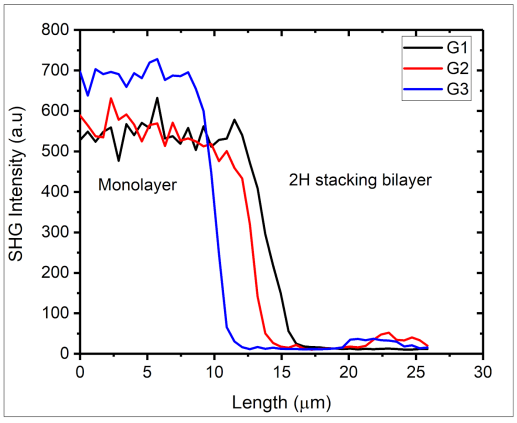

Fig. (4:20): SHG intensity from monolayer and 2H-stacking bilayer MoS_2, data taken along the white lines on G1,G2 and G3 shown in fig. (4:19).

The synthesized MoS_2 monolayers show unprecedented uniformity over a range of growth temperatures (700-850 °C). Beside the uniformity of the monolayer, the as-grown MoS_2 thin films are continuous and uniform across an

area of wafer scale. We have taken the data from different growth runs and our approach proved to be reproducible. We can consider our approach to be the starting point for mass production of MoS_2 monolayers.

4.3.5 Phase identification by Raman spectroscopy, TEM and X-ray diffraction

4.3.5.1 Raman spectroscopy

Raman spectroscopy is one of the most important characterization tools in the field of the TMDs that has been used in qualitative thickness measurements and identifying strain in the as grown films. MoS_2 exhibits two characteristics Raman peaks which are known as E^1_{2g} and A^1_{1g} modes corresponding to the in plane vibrations of Mo and S atoms and out of vibrations of S atoms. The separation between these two peaks is very sensitive to the thickness of MoS_2 film [69]. As the thin film thickness decreases, the separation between the peaks also decreases such that the E^1_{2g} peak red-shifts (phonon softens), while the A^1_{1g} peak blue-shifts (phonon stiffens), therefore such shifts in the Raman peaks can be used to determine the layer number of MoS_2 [69]. However, the real situation is complicated by the presence of growth induced strain. The separation between the two Raman peaks is affected by the presence of strain within the monolayer, especially the position of E^1_{2g}, as well as the laser wavelength that has been used for the the measurements [100], [101]. In our case, using a SiO_2 covered Si substrate, the thermal expansion coefficient of MoS_2 (10^{-5} /^{o}C) is roughly 1000 times greater than that of silicon dioxide (5.6 10^{-8} /^{o}C). Our CVD-grown MoS_2 on SiO_2/Si at elevated temperatures always suffers from a native tensile strain induced by interactions between the MoS_2 film and the substrate. In some cases the strain is strong enough to cause fracture of the monolayer, especially in fast cooling rates during CVD growth [102]. The native strain in our samples will be quantitatively analysed using XRD measurements in the following section.

For MoS_2 monolayers, the position of the E^1_{2g} peak is at about 384 cm^{-1} and the A^1_{1g} peak at about 405 cm^{-1}. There is a slight variation in this position of the two peaks depending on the method that has been used for depositing monolayers, the presence of the strain and the laser power and wavelength that has been used for characterization [41], [69], [101], [103].

In our case, Raman measurements were carried out under ambient conditions at room temperature using a JY Horiba HR800 micro-Raman system. A 532 nm wavelength laser beam with power of 0.5 mW and spot diameter of 1 μm was focused on the sample. Figure (4:21) is a typical Raman spectrum of a continuous film grown at 800 °C. The E^1_{2g} peak is located at 383.6 cm^{-1} and A^1_{1g} at 404.8 cm^{-1}, with separation about 21 cm^{-1}. These measurements agree well with values reported for CVD grown MoS_2 monolayers [41]. However, this separation is slightly larger than the one recorded for the counterpart mechanically exfoliated monolayer (separation 18 cm^{-1}) confirming the presence of strain in the CVD grown monolayers [101], [104].

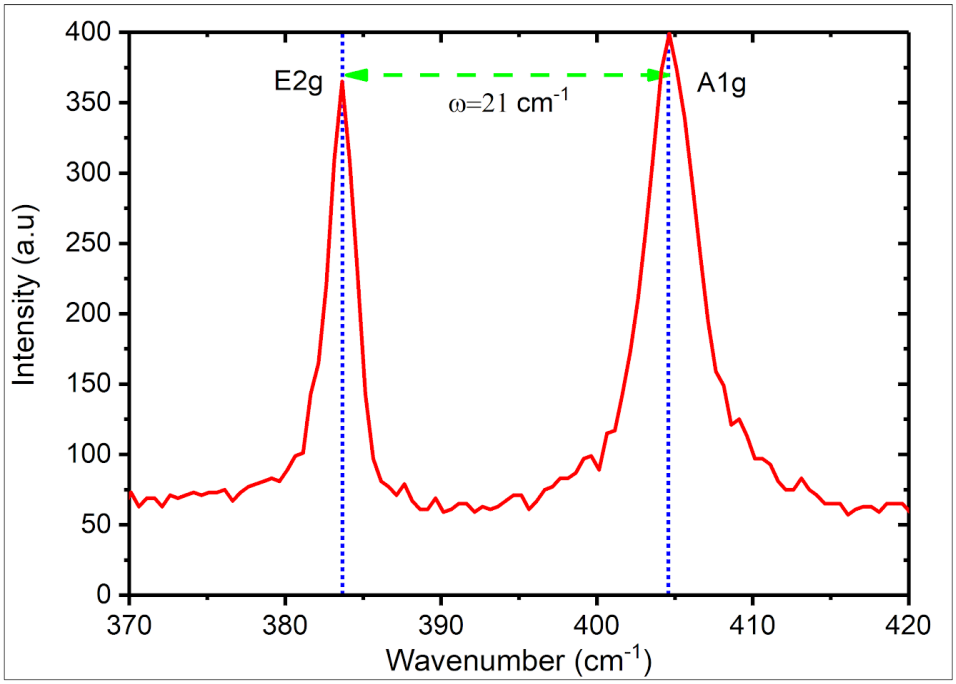

Fig. (4:21): Raman spectrum of a continuous MoS_2 monolayer film grown at 800 °C.

4.3.5.2 Transmission electron microscopy investigations

The crystal quality of the CVD grown MoS_2 was characterized at the atomic level using aberration-corrected transmission electron microscopy (TEM). Figure 4:22(a) shows a continuous MoS_2 film that was transferred to a TEM grid following a poly (methyl methacrylate) (PMMA) assisted method (see Appendix A1 for more details). The continuity of the transferred film indicated the high quality of the grown sample; folds and holes observed on the TEM specimen were caused by the transfer process. Figure 4:22(b) is an HRTEM image of the same monolayer region. Figure 4:22(c) is the corresponding selected area diffraction patterns

(SAED) with [001] zone axis. It can be seen that the monolayer exhibits high quality single crystalline nature with hexagonal lattice symmetry. Using SAED diffraction spots, we have found the value of the MoS_2 monolayer lattice constant (a=3.20 Å). This value agrees with the ones reported in literatures [41], [105].

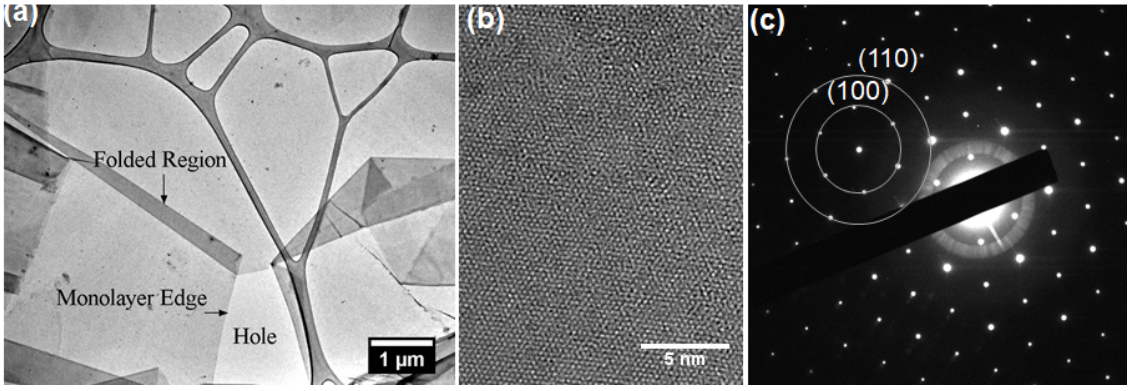

Fig. (4:22): (a) Transferred MoS_2 monolayer on lacey carbon film (b) HRTEM image of monolayer region (c) SAED from the same region in (b).

4.3.5.3 Synchrotron X-ray in-plane grazing angle diffraction GIIXRD

The crystalline structure and quality of our films is further verified using in-plane grazing incidence X-ray diffraction (GIIXRD). The measurements were done using synchrotron radiation (with a wavelength=0.65255 Å) and an incidence angle of 0.2 degree on the beam line I07 at the Diamond Light Source in Harwell Campus/(Didcot, OX11 0DE, UK). The scanning was performed at fixed substrate angle using an in-plane rotating detector. The X-ray beam was defocused on an area of 200 μm^2 and data were taken from different parts of the monolayer film. The measured data is compared with that calculated for the 1H phase (fig. 4:23). The peaks (100) and (110) have been detected on the different parts of the film and the positions of these peaks coincides with the calculated 1H phase. A zoom in scan of the two planes (100) and (110) of seven points on the sample are plotted in figure 4:24.

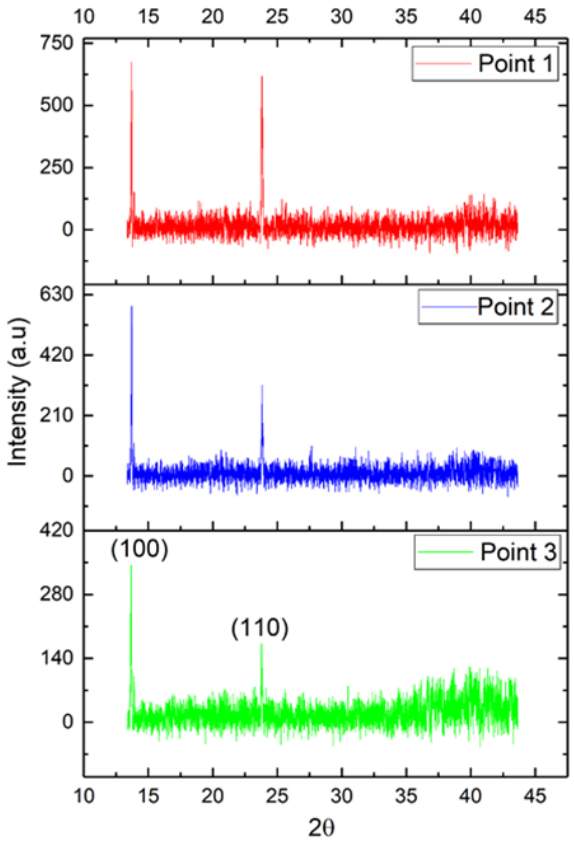

Fig. (4:23): Measured GIIXRD from a MoS_2 monolayer film.

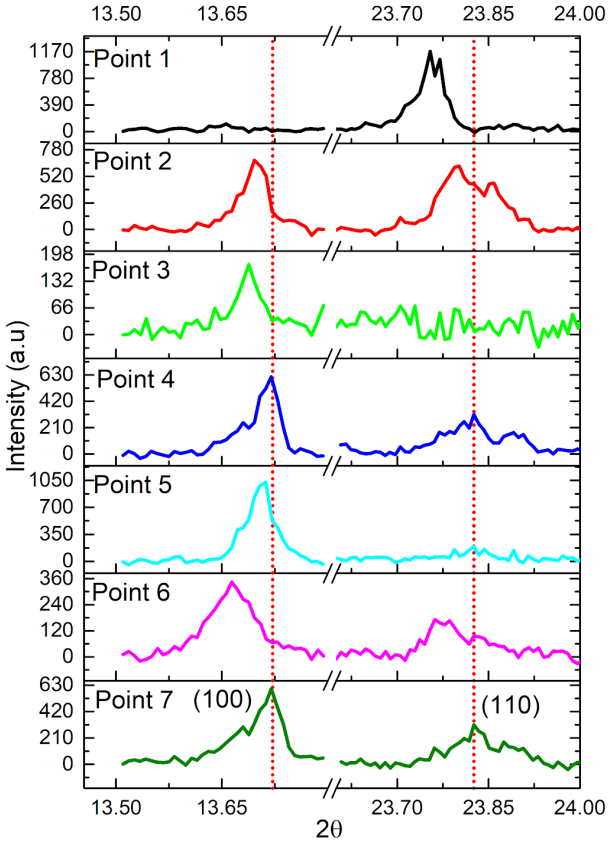

Fig. (4:24): Zoom in scan of (100) and (110) MoS_2 monolayer planes at seven different points on the sample.

The XRD peak broadening could be due to strain in the film, grain sizes and thin film thickness [106]. In our case the grain size is several hundreds of micrometers, and in the grazing incidence, the film can be assumed to be infinitely thick. Therefore the broadening in the XRD peaks can only be attributed to the strain and instrumentation. Using synchrotron monochromatic radiation, the instrumentation broadening is minimized and can be neglected.

We have investigated the growth induced strain in the films quantitatively focusing on the shift of the peak (100) that is taken from seven different positions of the film from different growth runs as shown in figure 4:24. The strain can be calculated as follows [106]:

$$\frac{\Delta d}{d} = -\Delta\theta \times cot(\theta) \qquad 4:2$$

where *d* is the lattice spacing and $\Delta\theta$ is the XRD peak broadening (FWHM).

For a hexagonal system the lattice spacing is given as:

$$\frac{1}{d^2} = \frac{4}{3}\left(\frac{h^2+hk+k^2}{a^2}\right) + \frac{l^2}{c^2} \qquad 4:3$$

where *a* is the lattice constant, *(hkl)* are Miller indice, and *c* is the lattice constant perpendicular to the basal plane.

In the case of monolayer *l*=0, therefore eq. 4:3 is reduced to:

$$\frac{1}{d^2} = \frac{4}{3}\left(\frac{h^2+hk+k^2}{a^2}\right) \qquad 4:4$$

and :

$$a = \frac{2}{\sqrt{3}} d\sqrt{h^2+hk+k^2} \qquad 4:5$$

$$\Delta a = \frac{2}{\sqrt{3}} \Delta d\sqrt{h^2+hk+k^2} \qquad 4:6$$

Dividing equation 4:6 by 4:5, we get:

$$\frac{\Delta a}{a} = \frac{\Delta d}{d} \qquad 4:7$$

$\frac{\Delta a}{a}$ represents the strain in the monolayer or the error in the lattice constant.

Figure 4:25 shows the lattice constant measurement at seven different points on the monolayer film. The variations in the lattice constant range between 3.17 to 3.156 Å. Such a variation in the lattice constant values indicate that the film is under nonuniform strain. The error bars in figure 4:25 represent the strain within a specific point, as the XRD spot was 200 μm^2, these error bars also represent the strain variation in a 200 μm^2 film area. The strain within these spots ranges between 0.5% (point 1) up to 1% (point 6). These values of strain agree with those reported in the literature using Raman spectroscopy [104].

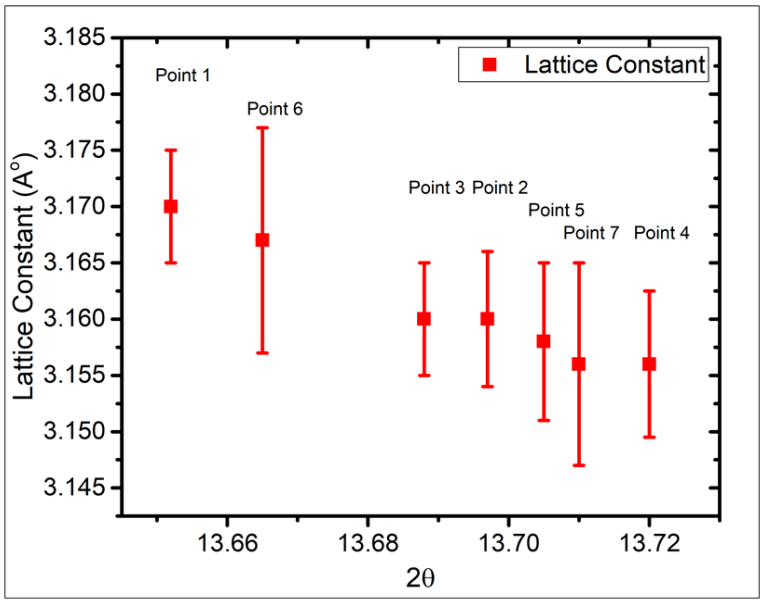

Fig. (4:25): Lattice constant variation as result of growth induced strain in the polycrystalline monolayer film.

We propose that this strain is induced by natural fast cooling of the samples at the end of the growth process. As we have mentioned, the thermal expansion coefficient of the underlying substrate (silica) is roughly 1000 times smaller than MoS_2 monolayers. A natural cooling process from the growth temperature (800 °C) could induce a significant strain in the film as a result of this mismatch in the thermal expansion coefficient. The resulted strain is not uniform across the film as shown in figure (4:25).

When the data is taken from neighboring grains that are strongly differently strained, a splitting the in peaks is expected. Figure 4:26 is an example of such an expected case. As we can see the peaks (100) and (110) are clearly splitted.

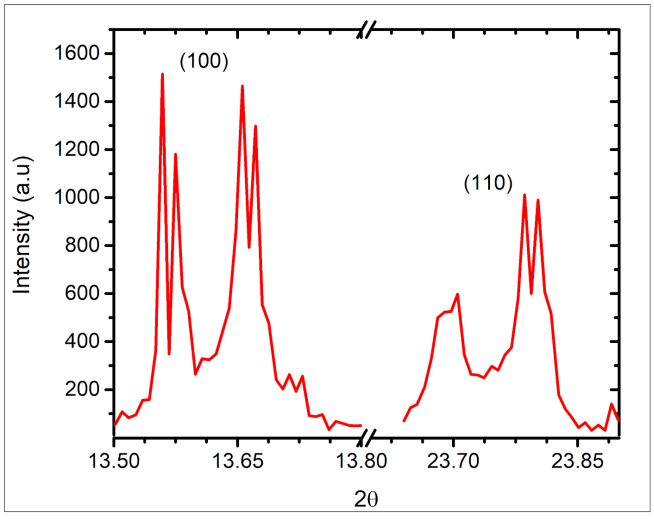

Fig. (4:26): GIIXRD peak splitting from differently strained grains.

4.3.6 In situ annealing of the MoS_2 monolayers

We have also studied the effect of temperature on the as grown monolayers. For this purpose we have tested the samples under 25, 100, 200, 300, 400, 500 and 800 °C in an ultra-high vacuum (UHV) to see how the film is affected by annealing. Figure 4:27 shows GIIXRD measurements of an in-situ annealed MoS_2 monolayer film. As we can see the film preserve its crystalline nature up to 800 °C and it is stable under this temperature only for a few minutes (t≃5 minutes).

Figures 4:28 show the details of the diffraction profile zoomed in on the (100) and (110) reflections of MoS_2 monolayer planes at different annealing temperatures.

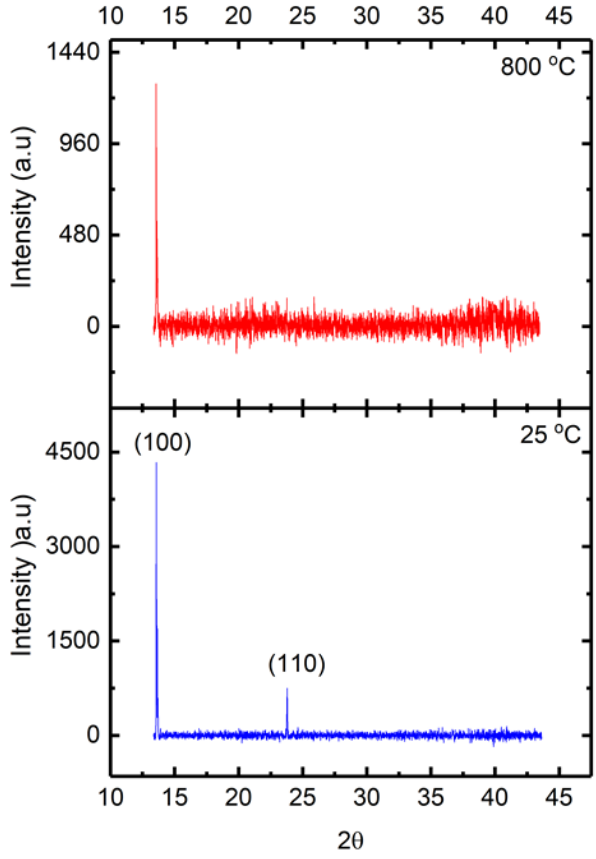

Fig. (4:27): GIIXRD of a MoS_2 monolayer at room temperature and an annealing temperature of 800 °C.

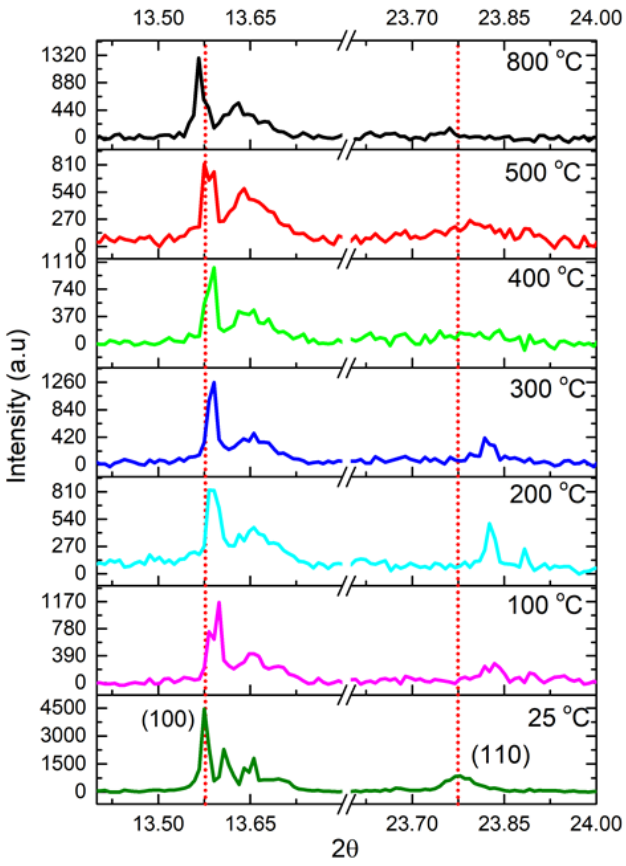

Fig. (4:28): High resolution (100) and (110) MoS_2 monolayer planes at different annealing temperatures.

The thermal expansion coefficient of MoS_2 monolayers on SiO_2/Si has been extracted from lattice constant expansion as a function of temperature as shown in figure 4:29. At room temperature the film is under tensile strain induced by the growth temperature (800 °C). The lattice constant at room temperature is found to be 3.167 Å. When the fim is heated to 100 °C, the strain is relaxed, as can be seen by the sharp drop in the lattice constant value which is 3.161 Å. Such relaxation is expected as there is a weak interaction between the film and substrate. Furthermore, this relaxation confirms that the film was under tensile strain. Similarly, strain release has been observed when transferring as grown monolayer to a fresh substrate [104].

By heating the film, the lattice constant increased linearly to reach a value of 3.170 Å at a temperature 800 °C, *i.e.* nearly reached the value of the growth temperature.

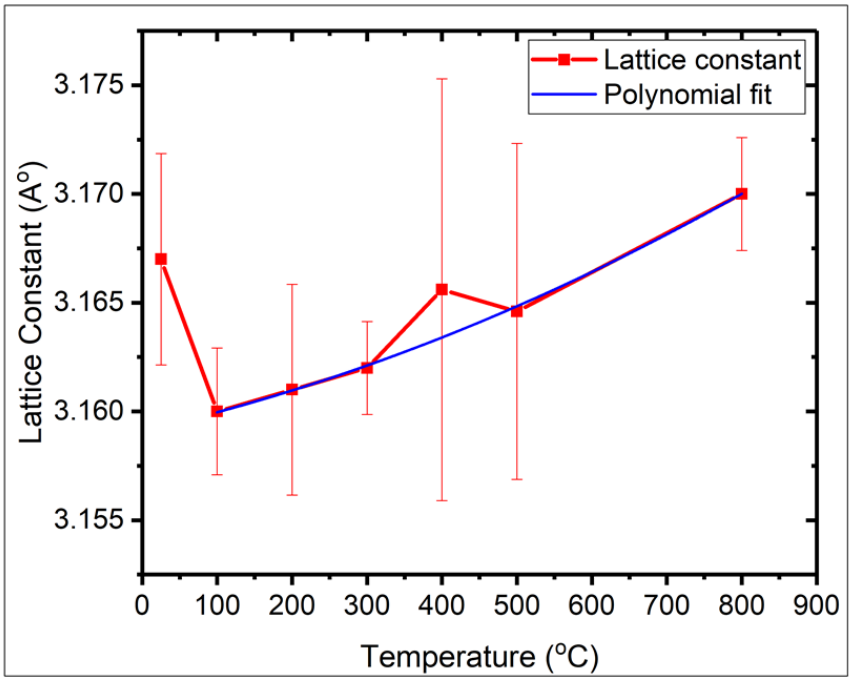

Fig. (4:29): MoS_2 monolayer lattice expansion as a function of temperature extracted from (110) plane.

The experimental data were fit with polynomial:

$$x_T = x_o + x_1 T + x_2 T^2 \qquad 4:8$$

Here T is the temperature (°C) and the ratio x_1/x_o gives the principal linear coefficient of thermal expansion in the a direction [107].

The fit through the experimental points gives the temperature dependence of the lattice constant a :

$$a = 3.160 + 7.845 \times 10^{-6} T + 7.22 \times 10^{-9} T^2 \qquad 4:9$$

The principal linear coefficients of thermal expansion is (2.5±1.2) x10^{-6} /°C. This value is slightly greater than the one reported for bulk MoS_2 powder (1.9 × 10^{-6}/°C) [107].

4.4 Physical property measurement

4.4.1 Optical properties

Photoluminescence (PL) measurements, were performed on MoS_2 monolayer samples (both continuous and isolated films) . All measurements were carried out under ambient conditions at room temperature using a JY Horiba HR800 micro-Raman system.

A 532 nm wavelength laser beam with power of 0.5 mW and spot diameter of 1 μm was focused on the sample. A typical example of PL measurements is shown in figure 4:30. There are two pronounced peaks known as A exciton and B exciton centered at 1.80 eV and 1.96 eV respectively. These two peaks are associated with direct transitions from the lowest conduction band to the spin-orbit split valence bands (see Fig. 1.6). This result agrees with PL measurements recorded from mechanically exfoliated MoS_2 monolayers [13]. The full width at half maximum (FWHM) width of A exciton is 71 meV. This is even narrower than the mechanically exfoliated MoS_2 monolayers on SiO_2 substrate and confirms the high quality of our films [108].

The A exciton peak is comprised of transitions due to neutral exciton (A^o) and trions (A^-) generated in the monolayer [109]. The PL spectra of single-layer MoS_2 fitted with three Lorentzian functions as shown in figure 4:30, with the trion peak centered at 1.78 eV and the neutral exciton peak at 1.81 eV [110].

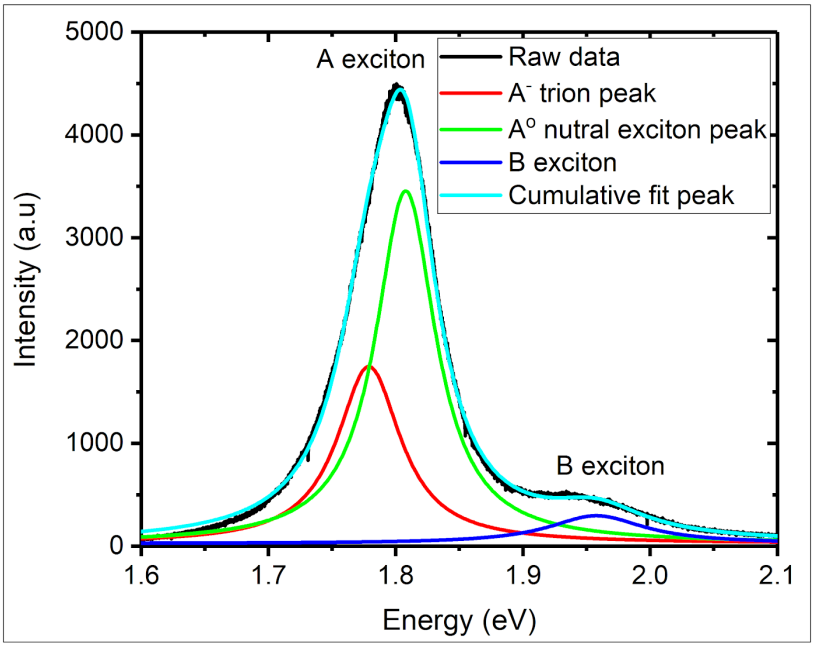

Fig. (4:30): Lorentzian peak fitting of MoS_2 monolayer PL spectra showing neutral exciton and trion peaks.

The position of the excitonic peaks can be affected by growth induced strain in the film. As we explained in the previous sections there is non uniform strain across the polycrystalline film.

The physical properties of MoS_2 monolayers are affected by the underlying substrate in the MoS_2/substrate heterostructure. It has been reported that there is a charge transfer from substrate to the monolayer and the amount of the charge transfer depends on the type of substrate. For example, the trion peak for

MoS_2/SiO_2 is found to be higher than that for MoS_2/STO, suggesting that charge injection to the MoS_2 is substrate dependent. The trion intensity is further reduced when taking PL from freestanding monolayers [110], [111].

The presence of the trion peak in our films confirms the n-type doping of the MoS_2 by charge transfer effects from the SiO_2 substrate and this result is in good agreement with previous reports [109], [111], [112].

A PL quantum yield (QE) of 1% has been recorded for an as deposited MoS_2 monolayer [113]. Such a low PL yield is mainly due to the presence of defects especially sulphur defects which act as nonradiative recombination centers and significantly quench the emission [114], [115]. This situation has been resolved by post deposition treatments and the QE can be increased to near unity (*i.e.* 100%) by treating monolayers with a non oxidizing organic superacid: bis(trifluoromethane) sulfonimide (TFSI) [116]. The mechanisms by which the acid passivates MoS_2 defects is not quite clear. The propagation of the acid can remove the surface contamination such as H_2O and hydroxyl groups that adsorbed to the surface from the environment. Such cleaning opens the active defect sites to sulphur adatoms on the surface. The presence of sulphur adatoms and clusters on the MoS_2 surface has previously been confirmed by scanning tunneling microscopy and the acid facilitates the reaction between the adatoms and active defect sites. The increase in the S/M ratio in the monolayer after treatment is confirmed using XPS indicating that the sulphur defects have filled [116].

4.4.2 Electrical properties

Figure 4:31 shows a schematic diagram of a field effect transistor FET used for electrical characterization and figure 4:32 is the IV characteristics of the FET transistor. The FET was fabricated as follows: the MoS_2 sample was covered with PMMA by spin coating at 4000 rpm, subsequent baking at 170 °C for 2 minutes followed by electron-beam lithography. After that, the sample was developed in AR 600-55 solution (a mixture of methyl isobutyl ketone and Isopropyl alcohol in the proportion of 1:3 according to the Raith company) for 2 minutes, and photographically fixed for 20 seconds in IPA (isopropyl alcohol). 5 nm of Ti and 45 nm of Au were evaporated by electron beam deposition (AXXIS Kurt J. Lesker company)with lift-off in acetone.The back gate FET devices were then fabricated. We used a Keithley 4200 semiconductor analyzer to test the electrical characteristics at room temperature. The IV characteristics of the device at

different V_{ds} are shown in figure 4:32. We extract the device mobility using the equation [7]:

$$\mu_c = \left(\frac{dI_{ds}}{dV_{bg}}\right) \times \left(\frac{L}{WCV_{ds}}\right) \qquad 4:10$$

Here μ_c is the carrier mobility, L is the channel length, W is the channel width, $C = \frac{\varepsilon_0 \varepsilon_r}{d}$ is the per unit area capacitance of the oxide layer between the back gate and the channel, ε_0= 8.85x10^{-12} F/m is the dielectric constant of vacuum, ε_r= 3.9 is the dielectric constant of SiO_2, d=300 nm is the thickness of SiO_2 [7]. Taking L=2 μm, W=26 μm in to equation (4:10), one obtains a mobility which is about 0.1 cm^{2}V^{-1}s^{-1}.

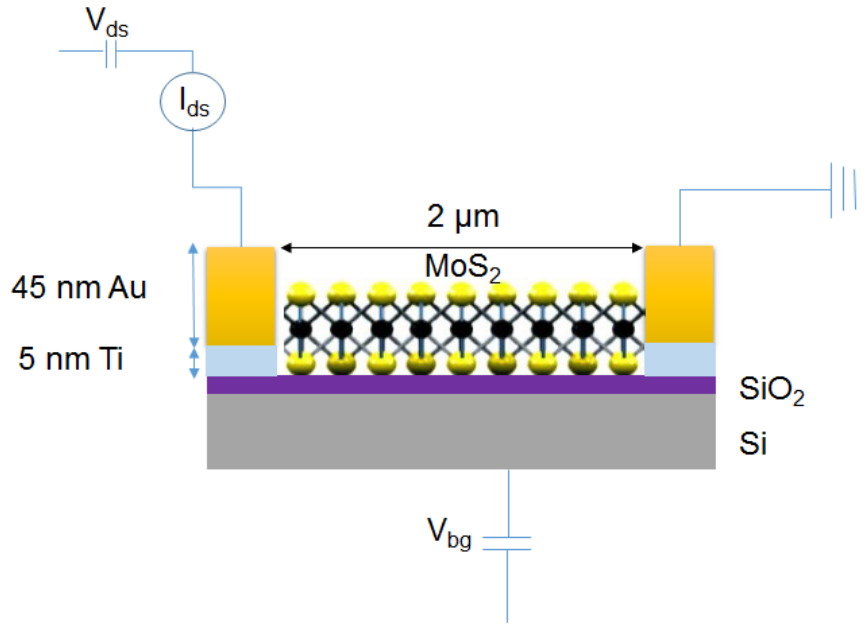

Fig. (4:31): Schematics of the FET used for electrical characterizations.

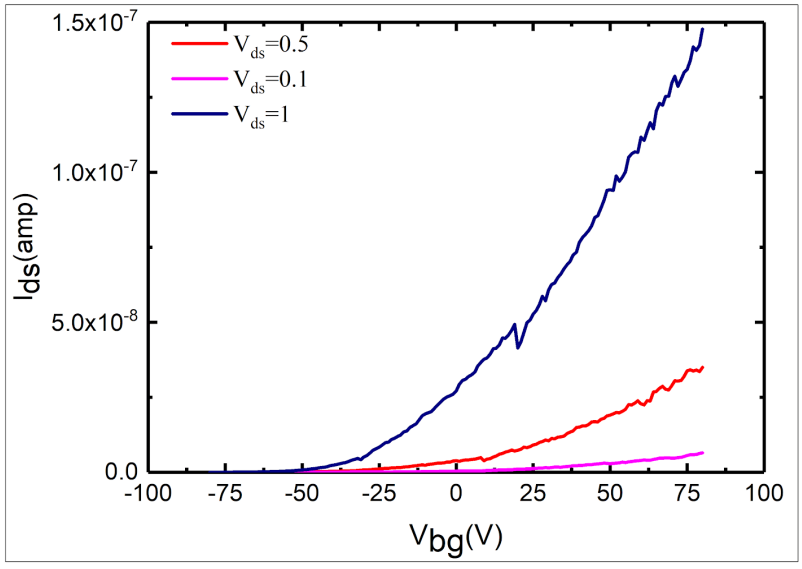

Fig. (4:32): Drain-source current I_{ds} as a function of back-gate voltage V_{bg} at different drain-source bias voltage V_{ds}=0.1V,V_{ds}=0.5 V and V_{DS}=1 V.

The mobility of our films is comparable to the mobility extracted from mechanically exfoliated films [112], [117] as well as CVD grown films [118]. The mobility of the as grown monolayers is quite low and far below the theoretically estimated value of 410 $cm^2V^{-1}s^{-1}$ [19]. There are several factors affecting the carrier mobility in MoS_2 monolayers and other 2D materials. The main ones are phonon scattering, Coulomb scattering due to the presence of impurities, and substrate roughness. In addition, large contact resistance induced by the Schottky barrier at the MoS_2-metal interface could also be another factor [9], [119]. The effect of these factors should be reduced to improve the carrier mobility to reach a level required for practical realistic applications. Several attempts have been made to improve the mobility of the as grown monolayers. A MoS_2 FET is capped with a high dielectric material like HfO_2 as a backgate, increasing the mobility to 200 $cm^2V^{-1}s^{-1}$. Such an increase is primarily due to the dielectric screening of Coulomb scattering of charged impurities. This figure of mobility is comparable to that of silicon thin films and graphene nanoribbons. This advancement in the mobility, could allow MoS_2 monolayers to be the backbone in future electronics [7]. Using metal contacts with low work function such as scandium, improves contacts with thin MoS_2 flakes, resulting in high carrier mobility compared to the counterpart metals with higher work function [119]. However, to reach the theoretical value of the mobility, intensive research on transistors is still needed.

4.5 Grain size distribution and nucleation density

Growing uniform and continuous 2D monolayer crystals with the largest possible grain size is still one of the main challenges in the field of 2D materials. As the physical properties of 2D materials are thickness dependent (as explained in Chapter One), the uniformity of the grown film is crucial. Similarly, without film continuity, making electronic devices on the film will be a difficult task. Additionally, the presence of grain boundaries in the polycrystalline film affects its physical properties such as a non uniform the PL yield and carrier mobility across the film [11], [120].

Using SHG we have shown that our films are uniform and continuous and now we discuss the grain size within the polycrystalline film. For this purpose, we have employed polarization resolved SHG for mapping grain size, orientation and boundaries. This technique has an angular resolution of of ±1° with measurable angles from 0° to 30° due to the reflection symmetry in MoS_2 [76]. Due to the loss

of phase information, the orientation (Mo-S) and (S-Mo) cannot be determined *i.e.* the technique cannot distinguish between grains in opposite directions unless the grains are grown next to each other [75], [76], [121]. For neighboring opposite grains, the SHG generation interfere destructively at the grain boundary and the boundary appears as a dark line and this will be shown later in this paragraph.

The experimental procedure for polarization resolved SHG is similar to that explained in 4.3.4, with the addition of a linear polarizer for measuring X and Y components of linearly polarized SHG. Figure 4:33 is a SHG image of the film under investigation. Figures 4:34(a) and 4:34(b) are the corresponding X-polarized and Y-polarized SHG images respectively. The orientation map of the grain sizes obtained using a Matlab script (Appendix A2) and equation (3:14) can be mapped over all intensities as shown in figure 4:35.

To evaluate the grain size distribution, we have considered grains to have elliptical shapes and the area of grains is calculated on this basis. The gains within continuous film have irregular shapes as shown in figure 4:35 and the ellipse is the closest shape.

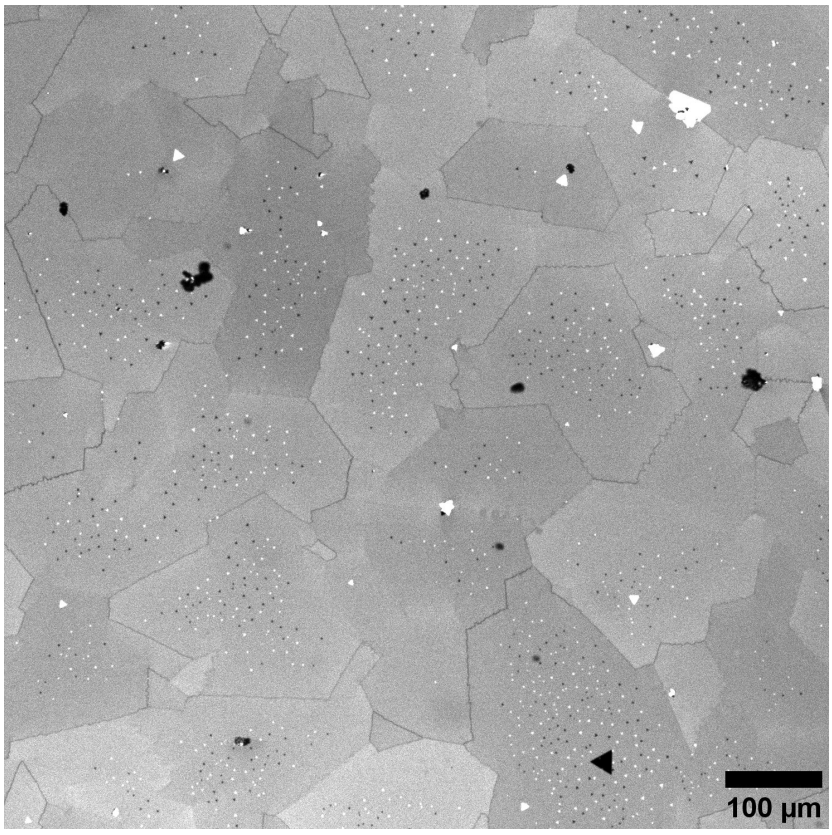

Fig. (4:33): SHG image of MoS_2 monolayer film grown at 800 °C.

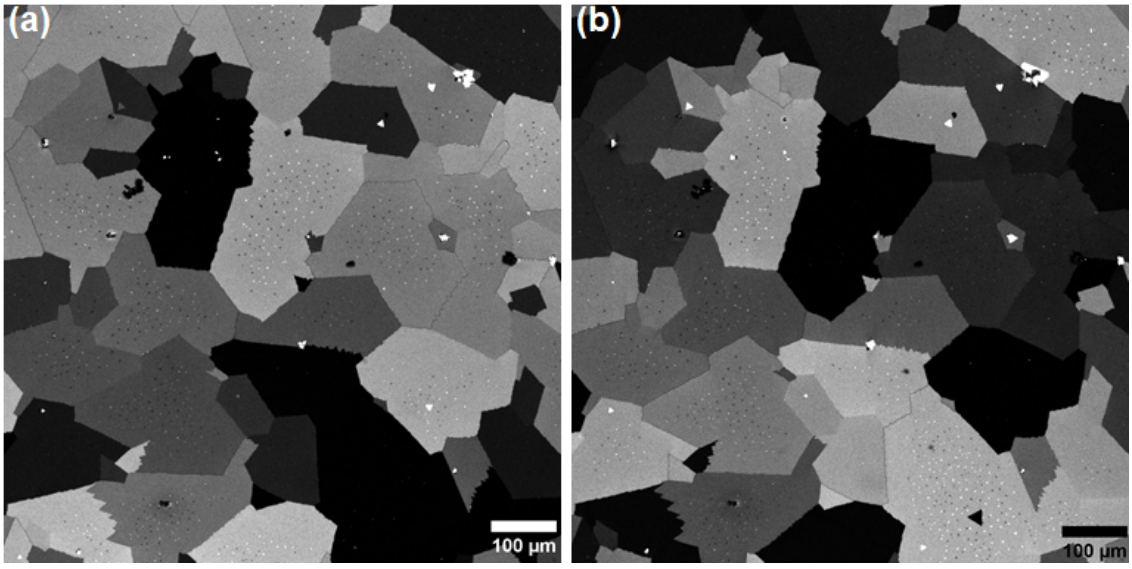

Fig. (4:34): (a) X-polarized SHG image of the film shown in fig. 4.33 (b) Y-polarized SHG image of the film shown in fig. 4.33.

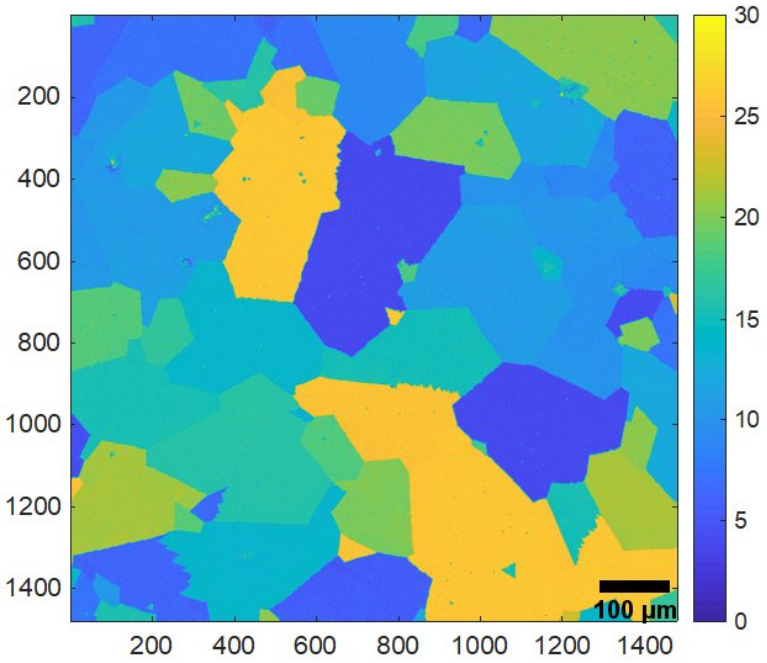

Fig.(4:35): Orientation color map of the film shown in fig. (4:33).

Figure 4:36 is a typical SHG image of neighboring opposite grains labeled as G1 and G2 with a dark line between them (destructive SHG interference at the grain boundary). Figure 4:37 shows a polarization resolved SHG image of the same area. As we can see the two grains have the same contrast and have not been resolved as two different grains. However, the presence of the dark boundary confirms that they are opposite grains. Taking data along the white arrow in figure 4:37, the intensity dramatically drops at boundaries as presented in figure 4:38.

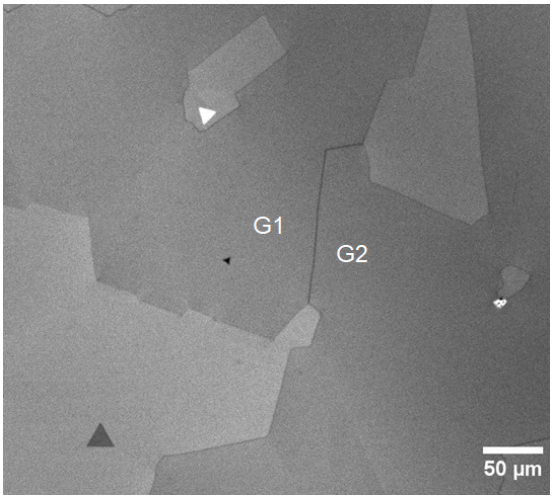

Fig. (4:36): SHG image showing two opposite grains labelled G1 and G2.

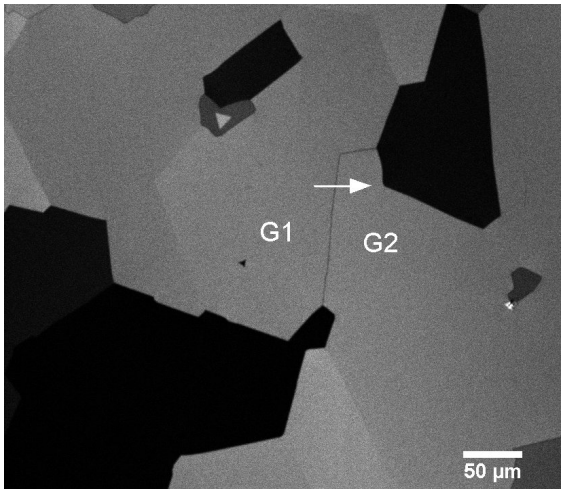

Fig. (4:37): Polarization-resolved SHG image showing two opposite grains G1 and G2.

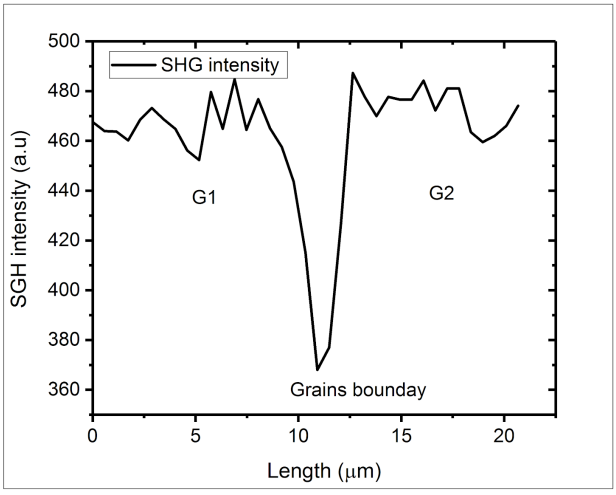

Fig. (4:38): SHG profile across the white arrow shown in fig. 4:37.

The grain size distribution versus frequency of occurring is shown in figure 4:39. The grain size ranges between 2600±515 µm^2 and 79740±9670 µm^2 with an average of 13837±1614 µm^2 and an average nucleation density of 82±9 mm^{-2}.

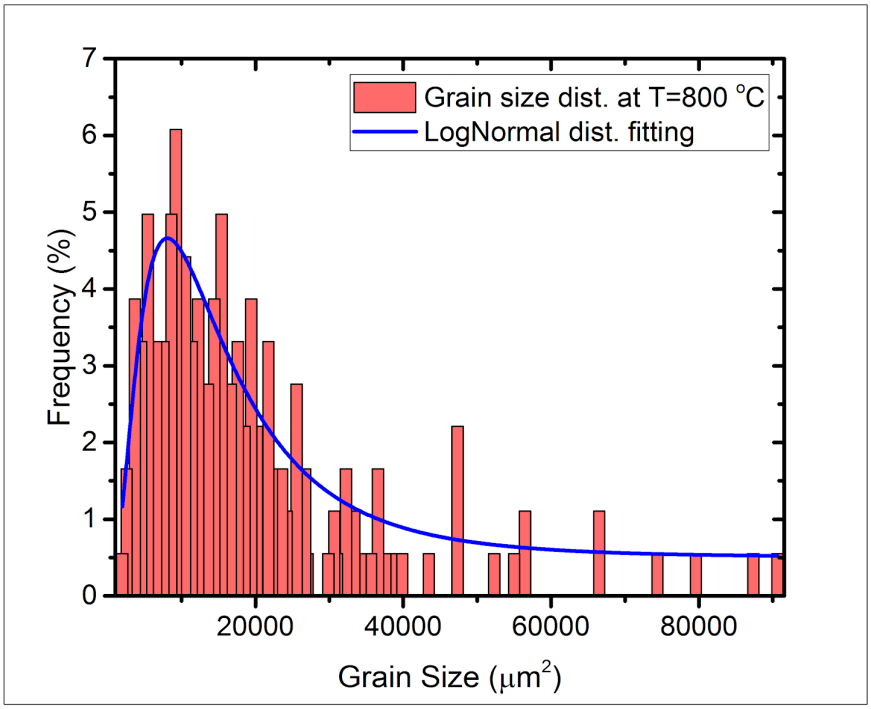

Fig. (4:39): Grain size distribution of a MoS_2 polycrystalline film.

4.6 Conclusions

The establishment of a scalable synthesis approach for growing MoS_2 monolayers is an important fundamental step towards the technology requirements in the manufacturing world. However, despite the intense research efforts towards controlled deposition of 2D MoS_2 monolayers, wafer-scale synthesis with optimum grain size, uniform and continuous films is still a challenging issue.

In this chapter we have introduced a scalable LPCVD approach using MoO_2 and S as starting materials for growing wafer scale uniform MoS_2 monolayers with grain sizes up to 400 microns.

Compared with MoS_2 monolayer growth using MOCVD which is only achievable at low temperatures and therefore imposes restrictions on the the grain size, our approach is reproducible in a range of growth temperatures and hence our grain size at an optimum growth temperature 800 °C can be 40 times greater than that achieved by MOCVD [47].

In the case of using MoO_3, the substrate is always located downstream. This means that variation in the concentration depends on the CVD system size and the growth might not be reproducible in different systems. While in our case the substrate is placed face down on the MoO_2 container, and so there is no variation in the MoO_2 concentration in the case when using different systems. Also, the

MoO_3 concentration is temperature dependent therefore the reproducibility might not be achievable at different growth temperatures. In our case, the substrate and the MoO_2 are in the same heating zone and the growth proved to be reproducible at different growth temperatures. Regarding the grain size, our grains are almost 600 times greater than those achieved using MoO_3 [40].

Our films have high crystalline quality, as confirmed by TEM, GIIXRD, Raman and PL measurements compared to the poor crystalline quality of MoS_2 monolayers produced using $MoCl_5$ [93].

We have used a range of different techniques to characterize our films. XPS is used to confirm that a complete conversion to MoS_2 occured as result of reaction between MoO_2 and S in the reaction zone. The AFM measurements confirm the monolayer nature of the film, and this was further confirmed by Raman and PL measurements.

A SHG microscopy investigation proved that the monolayers are uniform over a range of growth temperatures. The crystalline quality of the films was studied using TEM and GIIXRD and the results indicated high crystalline quality. Finally, the carrier mobility was measured using a prototype FET and the mobility value found to be in the range that has been extracted from CVD and exfoliated monolayers.

Our GIIXRD results indicate that there is a native strain in the as-grown monolayer films. This strain is growth induced strain as a result of the thermal expansion mismatch between the monolayers and the underlying SiO_2 substrate. The value of the strain is found be in agreement with the ones reported in literatures [104]. GIIXRD is further used to study the thermal expansion of the monolayers by in situ annealing. The monolayers were found to be stable up to 800 ^oC under UHV conditions and the thermal expansion coefficient is comparable with that reported for bulk MoS_2 [107].

All in all, we have established an LPCVD approach for growing MoS_2 monolayers on a wafer scale. The approach is proven to be scalable and reproducible in a range of growth temperatures. The monolayers have unprecedented size when grown at optimum temperature.

Chapter 5: Growth mechanism studies with the aid of COMSOL

Abstract

In this chapter we will present a mechanistic study of the LPCVD approach used for growing a reproducible MoS_2 monolayer on a wafer scale. We report the dependence of the MoS_2 film growth as a function of growth conditions such as MoO_2 concentration, sulphur flux, growth temperature, sulphur chemical potential and growth time. We will use COMSOL to simulate the concentration distribution at the surface of the substrate with a view to understanding the reaction conditions at the growth front.

The growth of continuous monolayer films was found to depend on the vertical distance between the substrate and MoO_2 powder. We also found that full monolayer film coverage can be obtained when the MoO_2 vapor pressure is equal to the saturation vapor pressure. A sulphur flux of at least 7×10^{-6} mol/m^{2}s is required for growing continuous monolayer films.

Our results suggest that continuous reproducible monolayer films can be grown at temperature range 650 ºC - 850 ºC with the maximum possible grain size at temperatures 800 ºC - 850 ºC and a minimum nucleation density is obtained in the same range of growth temperatures.

We further studied the growth rate of a single monolayer grain and we have found that growth occurs in the reaction limited regime at 650 ºC ≤ T< 800 ºC, and that the mass transport or feed limited regime happens at 800 ºC ≤ T ≤ 900 ºC. A desorption limited regime occurs at 900 ºC ≤ T ≤ 1000 ºC. Beyond 1000 ºC, rapid desorption occurs before the reaction of the starting materials and no growth is observed.

From a flush growth study (one minute growth) of the individual grains at temperatures of 700 ºC - 1000 ºC, it is determined that the growth rate could be as large as 710±260 μm^2/s at a growth temperature of 900 ºC. The optimum growth temperature was found to be 800 ºC. Beyond this growth temperature, the growth of additional layers is observed. The optimum monolayer growth time at 800 ºC is 15 minutes beyond which bilayers start to initiate.

Finally the morphology of the grains can be tuned using different growth temperatures: triangles with bent edges at a temperature T ≤ 700 °C to perfect triangles at 800 °C ≤ T ≤ 900 °C and perfect hexagons at 900 °C ≤ T≤ 1000 °C.

5.1 Literature review

5.1.1 CVD process

In chemical vapor deposition, the film growth rate, nucleation density, grain size, grain morphology, and thickness can be controlled via several parameters such as the composition and chemistry of the precursors and their partial pressure in the CVD system, the pressure and the design of the CVD system and the growth temperature [122] .

To understand the effect of different parameters on the film growth, the model shown in figure 5:1 (a substrate placed in the reaction zone of the CVD tube) is proposed. In this model, the mass transport of the precursors through the boundary layer depends on the mass diffusion. Therefore, there is a concentration gradient of the precursors [122]. The flux (F_1) of the precursor from the bulk gas stream to the substrate can be written as follows [122]:

$$F_1 = h_G(C_1 - C_2) \qquad 5:1$$

$$h_G = \frac{D}{\delta} \qquad 5:2$$

Assuming the special case when the chemical reaction is of first order:

$$F_2 = k_S C_2 \qquad 5:3$$

where F_1 and F_2 are the fluxes in stream and on the substrate respectively, h_G and k_S are the mass transfer rate constant and the reaction rate constant respectively, and C_1 and C_2 are the concentrations in the stream and on the substrate respectively. D is the diffusion constant of the precursor and δ is the thickness of the boundary layer.

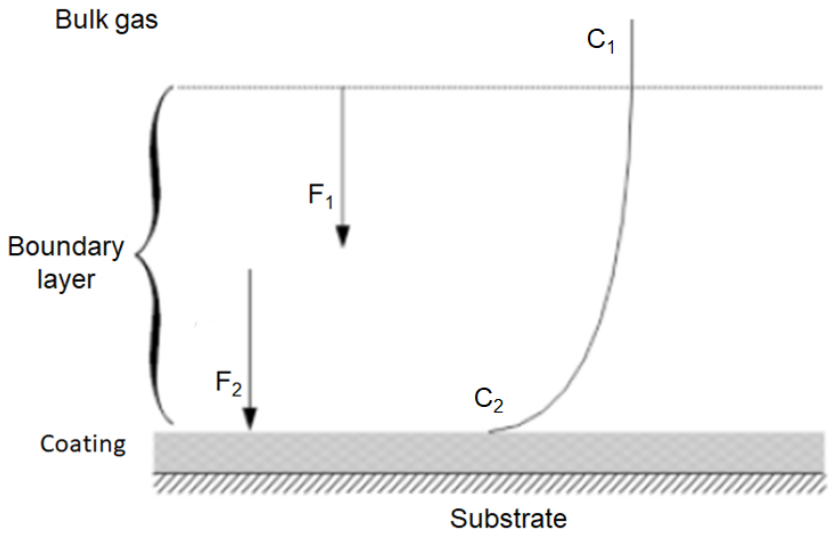

Fig. (5:1): Substrate in the reaction zone of the CVD system [122].

Under steady conditions, the flux F_1 is equal to the the flux on the substrate F_2. Then the relationship between C_1 and C_2 obtained as :

$$C_2 = \frac{C_1}{1+\frac{k_S}{h_G}} \qquad 5:4$$

When discussing the effect of the growth temperature on a CVD process, one can classify the growth process into three regimes: at relatively low temperatures $k_S \ll h_G$, the film growth is controlled by the kinetics of the chemical reactions of the precursors. Even if there is an overabundance of the reactants in the reaction zone, the growth is very slow. In this regime the growth rate is weakly affected by the partial pressure of the precursors and is strongly temperature dependent (growth rate $\propto T^{3/2}$) [123].

At moderate temperatures $k_G \ll k_S$, the growth is controlled by feed or mass transport of the reactant. The growth rate can be approximated as follows:

$$Growth\ rate = u^{0.5} T^m \frac{P}{P_s} \qquad 5:5$$

where u is the velocity of the carrier gas in the CVD tube, T is the growth temperature, P is the partial pressure of the reactant and P_s is the total pressure of the CVD system.

In the case of atmospheric pressure chemical vapor deposition (APCVD) [123], the growth rate depends on the diffusion of reactants through the boundary layer to the substrate while in the case of low pressure chemical vapor deposition, the boundary layer over the substrate is relatively thin and the growth is controlled by feed of the reactants into the CVD system [123]. In mass transport or feed

controlled regime, the growth is weakly temperature dependent and the optimum growth rate can be achieved [123].

At higher temperatures, the system is in the desorption regime. In this regime, the desorption and reaction of the starting materials are competing and the growth rate is reduced. Further increase in the temperature, a quick desorption of the precursors occurs before the reaction and the film growth cannot be achieved [123]. Each of the above mentioned growth regimes can be described by an Arrhenius equation [124]:

$$Growth\ rate = Ae^{\frac{-E_a}{kT}} \qquad 5:6$$

where A is a constant, E_a is the relevant activation energy and k is Boltzmann constant. A typical Arrhenius plot for the growth rate displaying different growth regimes is shown in figure 5:2.

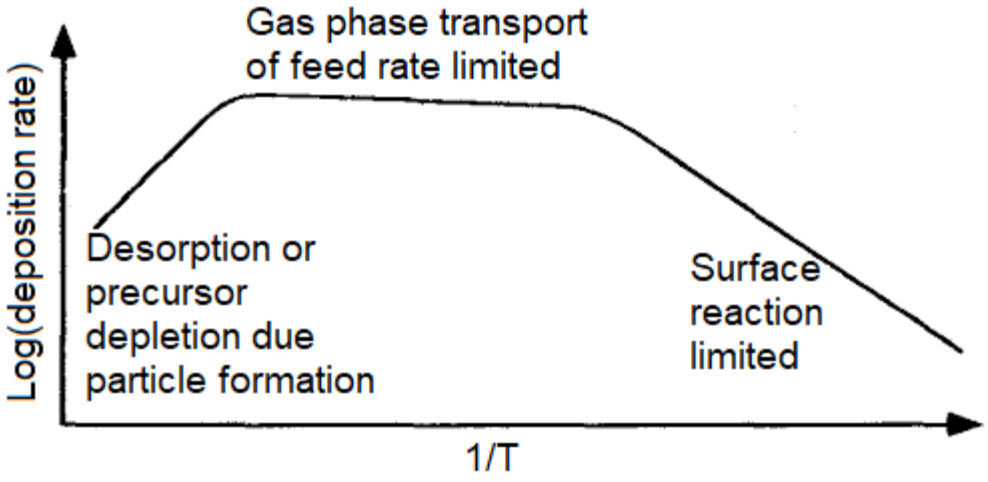

Fig. (5:2): Typical Arrhenius plot, dependence of growth rate on temperature [123].

In this chapter, we are going to present our own Arrhenius plot analysis of the LPCVD of MoS_2 monolayers to demonstrate how we employed the effect of the mentioned CVD parameters for establishing a standardized protocol for growing MoS_2 monolayers on a wafer scale.

5.1.2 Thermodynamics of CVD

The chemical reaction can be described by the Gibbs free energy of the reactants and products [125]. Gas A reacting with B to form C, as shown in the following equation [126]:

$$A_{(g)} + B_{(g)} \leftrightarrow 2C_{(g)} \qquad 5:7$$

At time t=0, A=1 mol, B=1 mol and C is absent. At any other time, t, A=1-x mol, B=1-x mol and C=2x. The Gibbs free energy, G, of the system becomes [125]:

$$G = (1-x)\mu_A + (1-x)\mu_B + 2x\mu_C \qquad 5:8$$

where μ_A is the chemical potential of A, μ_B is the chemical potential of B and μ_C is the chemical potential of C.

The derivative of G with respect to x can be positive, zero or negative. In the case of a positive derivative, the reaction in eq. 5:7 would increase the Gibbs free energy of the system which is not allowed. The product C is unstable and decomposes to A and B.

$$\frac{dG}{dx} = 2\mu_C - \mu_A - \mu_B > 0 \rightarrow \mu_A + \mu_B < 2\mu_C \qquad 5:9$$

A zero derivative means the reaction is in equilibrium:

$$\frac{dG}{dx} = 2\mu_C - \mu_A - \mu_B = 0 \rightarrow \mu_A + \mu_B = \mu_C \qquad 5:10$$

and a negative derivative means the energy of the system would decrease and the reaction would fe forward.

$$\frac{dG}{dx} = 2\mu_C - \mu_A - \mu_B < 0 \rightarrow \mu_A + \mu_B > 2\mu_C \qquad 5:11$$

For ideal gas behaviour, the chemical potential at a given temperature and pressure can be defined as follows [125]:

$$\mu(T,P) = \mu(T,P_{ref}) + kTln(\frac{P}{P_{ref}}) \qquad 5:12$$

where *T* is temperature in *K*, *P* is the gas partial pressure, Pr_{ef} is the atmospheric pressure and *k* is the Boltzmann constant. In the case of MoS_2, a more realistic empirical formula exists and is used in section 5.6.4.

In the case of MoS_2, the stable monolayer can be described as follows [127]:

$$\mu_{Mo} + 2\mu_S = \mu_{MoS_2} \qquad 5:13$$

The allowed values of the sulphur chemical potential are as follows [128]:

$$\frac{H_f}{2} \leq \mu_S \leq 0 \qquad 5:14$$

where H_f= 2.61 eV is the formation energy of MoS_2. From equation 5:14, we can see that large values of μ_S correspond to sulphur-rich conditions, whereas small values of μ_S relate to Mo-rich conditions. The maximum chemical potential μ_S is zero, corresponding to conditions at which sulphur condenses as bulk. The lower limit for μ_S is −1.30 eV. Below this limit MoS_2 monolayers are reduced to metallic body-centered cubic (bcc) Mo [128], [129].

5.1.3 Monolayer growth mechanisms

The growth of thin films can be classified into three primary modes: Frank van der Merwe, Volmer-Weber and Stranski–Krastanov modes [91]. The Volmer–Weber mode is a layer-by-layer growth mode, the Frank van der Merwe mode is an island growth mode and the Stranski–Krastanov mode is a layer-plus-island growth mode. The growth of monolayer TMDs is believed to follow the Frank van der Merwe or Stranski–Krastanov modes [91]. In the Frank van der Merwe mode, TMD islands of different thickness stitch to form a complete thin film. In the Stranski–Krastanov mode, monolayer TMD domains grow and interconnect with each other until a complete coverage and then the second layer starts to grow in the same manner [91]. Although, the TMDs monolayer growth is still a controversial topic, all our observations on the MoS_2 monolayers for different growth temperatures support Stranski–Krastanov mode as shown by the SHG images (previous chapter).

Now we focus on the growth mechanisms of MoS_2 monolayers when using MoO_2 as Mo source and sulphur powder as sulphur source. At high temperatures, MoO_2 sublimes in the form of $(MoO_2)_n$ and $(MoO_3)_n$ clusters [130] and is then deposited on the substrate that is placed face down on the MoO_2 container. Under a sulphur-rich environment, there is a probability that those clusters might partially or fully sulfurise before being deposited. However there is no concrete evidence for gas phase sulfurization yet [131]. On the substrate, the sulphur and Mo react and the MoS_2 monolayer nucleus initiates either from atomic MoS_2 monolayer clusters or unsaturated molybdenum oxysulphide (MoO_xS_{2-y}, $y \geq x$) nanoparticles. Both nucleation processes have been confirmed *ex-situ* through an electron microscopy study by Zhu *et al.* (2017) in APCVD of MoS_2 on graphene as shown in figure (5:3) [131]. In a similar study for deposition on a 20 nm thick SiO_2 membrane, JD Chain *et al.* (2016) [132] have found that a $Mo(S/Se)_2$ alloyed monolayer starts from $MoO_x(S/Se)_{2-y}$ nanoparticles deposited on the substrate in a sulphur poor environment, before the complete conversion to MoS_2 in the optimal sulphur atmosphere is achieved, resulting in the nucleation and growth of monolayers at the nanoparticle sites [132].

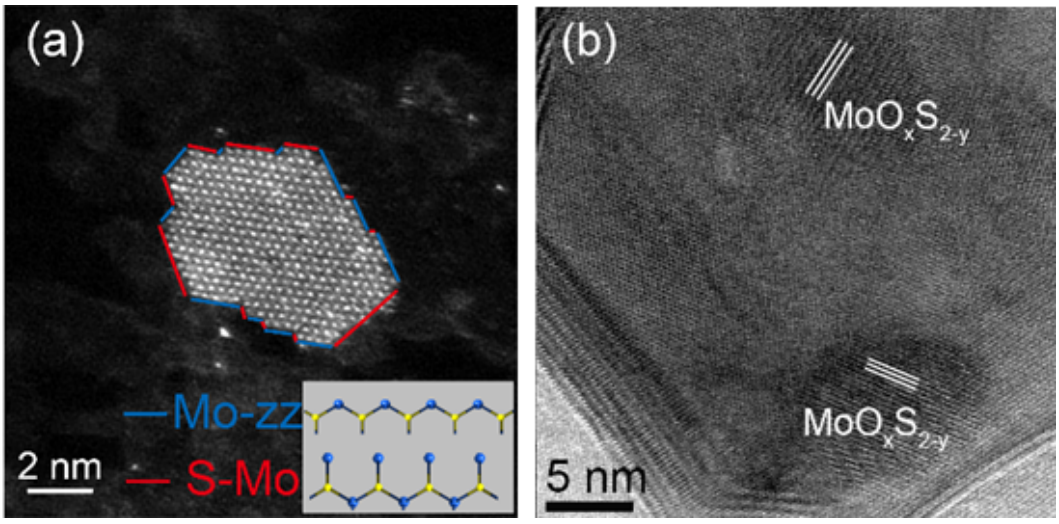

Fig. (5:3): Two possible nucleation routes for growing MoS_2 monolayers (a) MoS_2 monolayer cluster (b) molybdenum oxysulphides (MoO_xS_{2-y}, y≥x) nanoparticles [131].

All the above mentioned work on the nucleation of MoS_2 monolayers has been done using APCVD. All the evidence presented in the literature on the MoS_2 nucleation and growth mechanisms relied on post-growth studies. It is still not clear if the formation of MoO_xS_{2-y} nanoparticles happens in the gas phase or on the substrate, therefore we believe more in situ experiments based on techniques such as mass spectroscopy or TEM are still required for finding the origin of the nucleation.

5.2 Experimental investigation

5.2.1 Effect of gas flow on furnace temperature profile

The furnace temperature profile is one of the most important parameters that affect the CVD growth of thin films. We have presented our measured data of temperature profile of a closed-ended furnace in (Chapter Four). We expect the furnace temperature profile also depends on the gas flow. Here we use COMSOL's heat transfer in fluids module for simulation of the temperature profile under different flow conditions. For this purpose, we use typical growth conditions of a set temperature of 800 °C (1073 K) and a CVD tube pressure of 10 mbar to see the effect of varying the Ar flow rate (between 0 to 1000 SCCM) on the temperature variations in both the sulphur and MoO_2 zones. Figure 5:4 is a typical simulated furnace temperature profile file for the growth temperature of 1073 K and a flow rate of 100 SCCM.

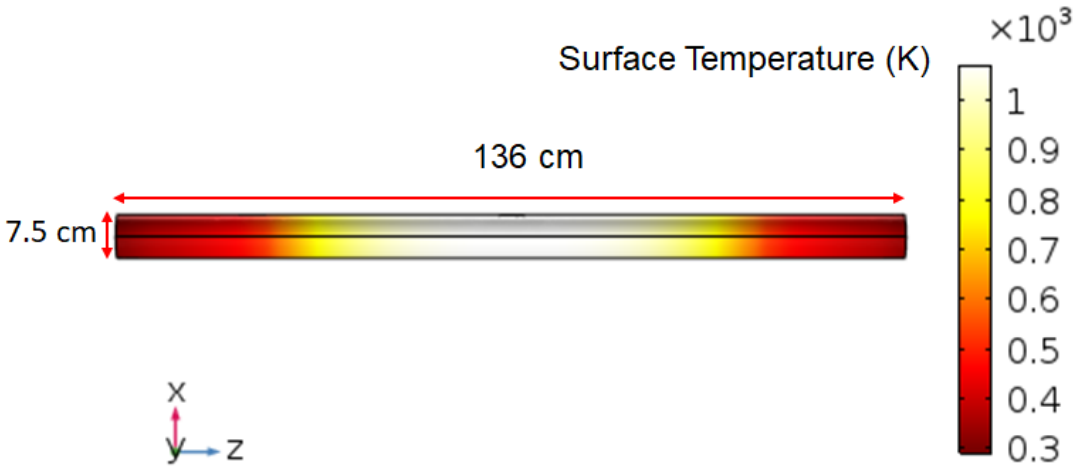

Fig. (5:4): Typical tube furnace surface temperature for a growth temperature of 1073 K and a flow rate of 100 SCCM.

The temperature profile as a function of flow rate in the main (MoO_2) zone and sulphur zone at a growth temperature 1073 K and different flow rates is shown in figures 5:5 and 5:6 respectively.

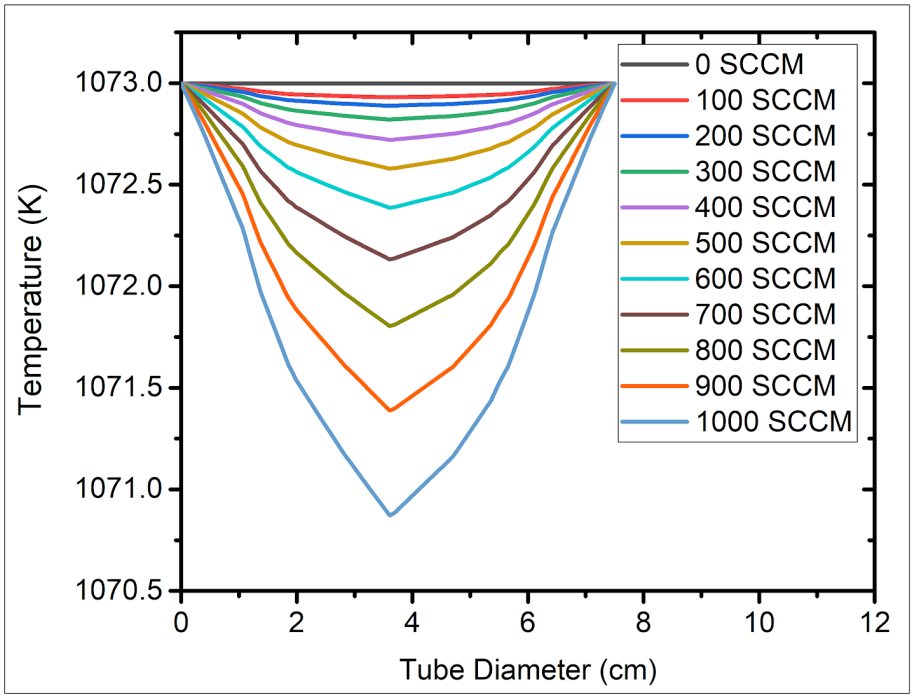

Fig. (5:5): Main (MoO_2) zone temperature profile at a growth temperature of 1073 K under different flow rates.

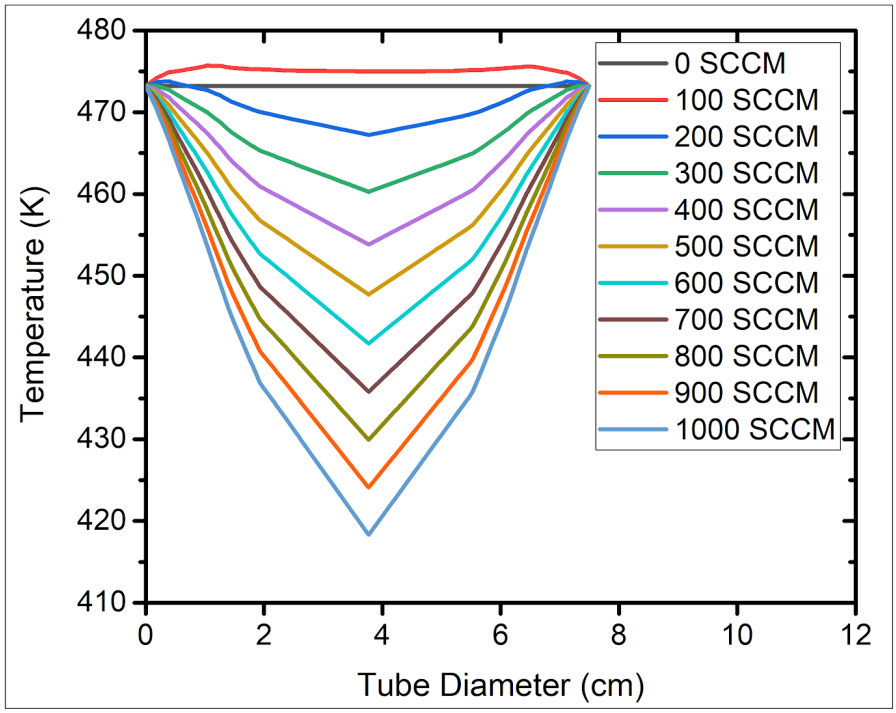

Fig. (5:6): Sulphur zone temperature profile at a growth temperature of 1073 K under different flow rates.

A typical surface temperature profiles of MoO_2 and sulphur zones at growth temperature 1073 K and flow rate of 200 SCCM are shown figures 5:7 and 5:8 respectively. The data shown in figure 5:5 and figure 5:6 is taken along the cutline shown in figure 5:9.

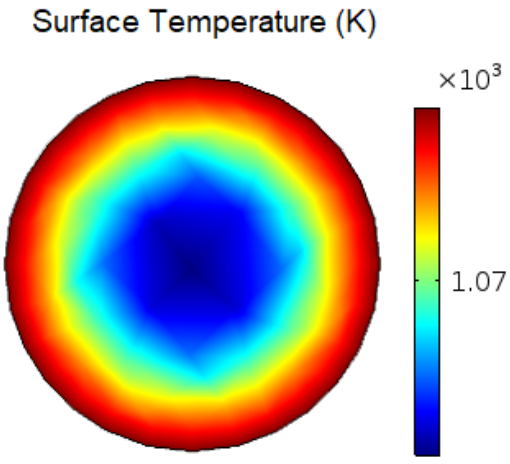

Fig. (5:7): Cross sectional temperature profile of the MoO_2 zone at a growth temperature of 1073 K under 200 SCCM.

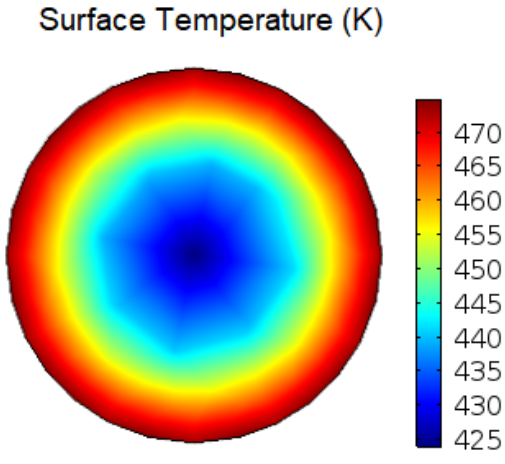

Fig. (5:8): Cross sectional temperature profile of the sulphur zone at a growth temperature of 1073 K under 200 SCCM.

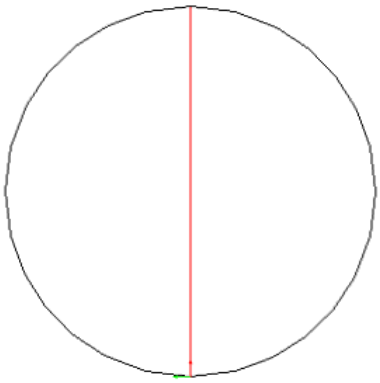

Fig. (5:9): Cutline along which the data is taken.

We have seen that there is little change in the reaction zone temperature under different flow rates while the sulphur zone temperature fall sharply when going to higher flow rates especially if the sulphur boat is placed somewhere close to the center of furnace tube. In experimental work this should be taken into consideration as the sulphur vapor pressure is very sensitive to the temperature changes. The sulphur vapor pressure as a function of temperature will be discussed later on in this chapter.

5.2.2 Starting material vapor pressure and concentration

The vapor pressure of molybdenum dioxide in the range (1620-1860) K is given in the following empirical correlation [133].

$$log\ P = -\frac{17873}{T} + 6.035 \qquad 5:15$$

where *P* is the vapor pressure in (atm.) and *T* is temperature in K.

As there are no reliable measured data in the range of our growth temperatures, we extrapolated Eq. (5:15) for finding the MoO_2 vapor pressure. Sulphur: The vapor pressure of sulphur is given by the following correlation (389 K < T < 1313 K) [134].

$$log\frac{P}{P_c} = [A(1-\frac{T}{T_c}) + B(1-\frac{T}{T_c})^{3/2} + C(1-\frac{T}{T_c})^3 + D(1-\frac{T}{T_c})^6](\frac{T}{T_c}) \qquad 5:16$$

where T is the temperature of the sulphur precursor in K, A = -7.246, *B* = 0.187, *C* = 5.271, *D* = -12.128, T_c = 1313 K, and P_c = 18208 kPa.

Assuming the validity of the ideal-gas law for a dilute vapor, the concentration is given by following equation:

$$C(T) = \frac{P(T)}{RT} \qquad 5:17$$

where *C(T)* is the concentration as a function of temperature and *R* is the universal gas constant.

5.3 Experimental results

In this section, we present our results on the effect of vertical distance between the MoO_2 powder and the substrate on the monolayer coverage. For this purpose we adopt the model presented in figure 5:10. The CVD reactor setup we used for growing uniform MoS_2 monolayer on a centimeter scale is a variation from those used by other groups. In CVD, for a uniform film growth, the substrate must be exposed to a uniform flux of the reactant materials. One way to do this is to place the substrate face down on the MoO_2 container in a place where where the Mo flux is uniform. By changing the MoO_2-substrate vertical distance, the MoO_2 concentration can be tuned such that the optimum condition for full coverage of monolayers is obtained. To cover all MoO_2-substrate distances in one go, a simple and clever method is to place the substrate at a certain angle with respect to the MoO_2 powder.

The procedure is as follows: 40 mg of high purity MoO_2 powder (99% Sigma Aldrich) was placed in a quartz boat to act as a Mo source. SiO_2 covered Si wafers (1×1.5 cm^2) were cleaned with acetone and ultrasonicated for 10 minutes and then positioned at certain angles 15°, 20°, 28°, 48° and 66° on a MoO_2 container with a typical example shown in figure 5:10. The MoO_2 container with the substrates was then placed at the center of the 75 mm diameter tube furnace. Another boat contained 5-20 mg of Sulphur powder (99.98% Sigma Aldrich) was placed, 42 cm away from MoO_2, in a region where the temperature reaches 200 °C. Prior to the growth, the furnace was flushed with argon gas (1000 SCCM) for about 30 minutes. Then the furnace was pumped down to 10 mbar and the center was heated to 800 °C with a heating rate of 15 °C /minute in an argon flow (200 SCCM). After keeping the temperature at 600-1000 °C for 10-20 minutes, the furnace was naturally cooled down to room temperature.

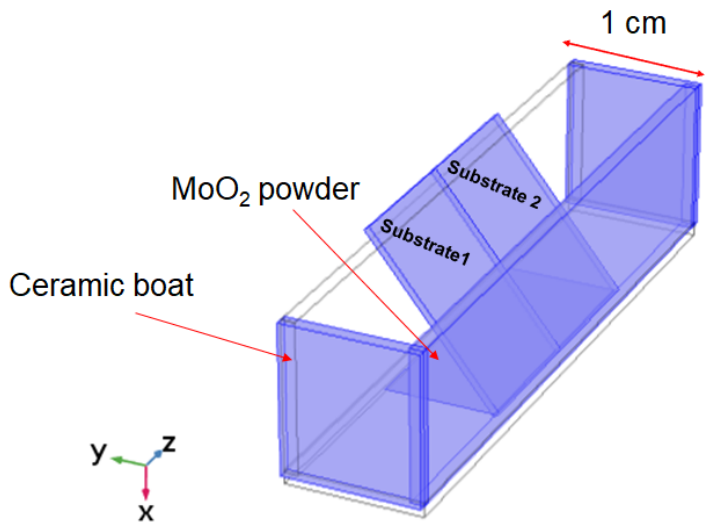

Fig. (5:10): Typical position of the substrates with respect to MoO_2 powder in the reaction boat.

5.3.1 The effect of the vertical distance between substrate and Mo source on the monolayer film coverage

Figure 5:11 shows the monolayer coverage as a function of substrate vertical distance for five different different tilt angles.

We found that the substrate is always fully covered by a continuous uniform monolayer when the MoO_2-substrate distance is less than 5 mm. Above 5 mm, the substrate is found to be partially covered with monolayers. Based on our findings, at vertical distances of 0-5 mm, our system is in a steady state with respect to Mo for the growing MoS_2 monolayers. Beyond 5 mm, the system is in the feed-limited regime. Figure 5:12 is an optical image of monolayer coverage on a SiO_2/Si substrate placed at 48°. The isolated grains and continuous film are shown in optical micrographs 5:13 and 5:14 respectively.

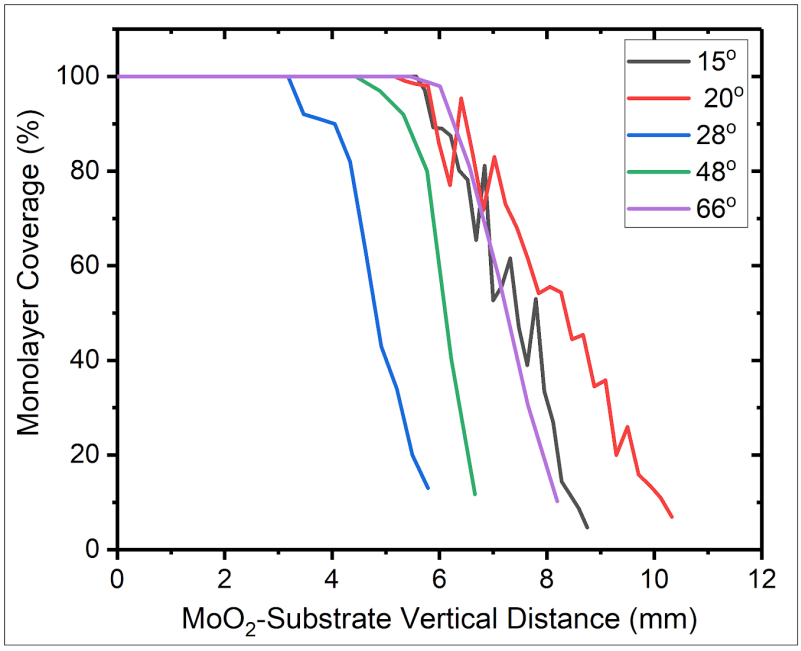

Fig. (5:11): MoS_2 monolayer coverage as a function of MoO_2-substrate distance.

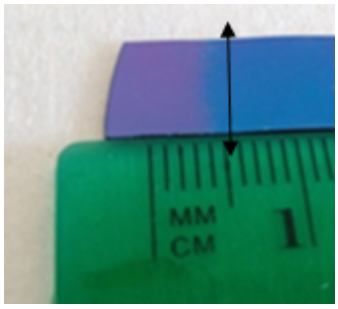

Fig. (5:12): Photograph of a continuous monolayer film (right part) and bare substrate (left part) of a typical sample grown at an angle 48°.

Fig. (5:13): Isolated grains from left side of sample shown in fig. 5:12.

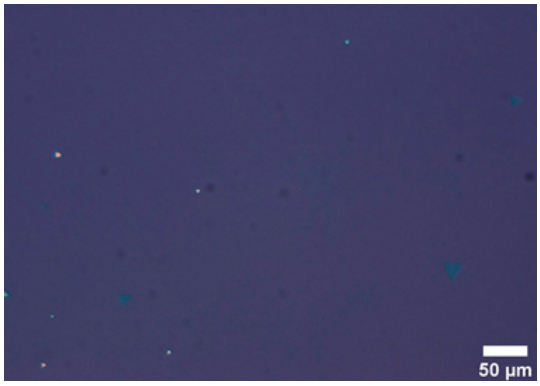

Fig. (5:14): Continuous monolayer film from right side of sample shown in fig. 5:12.

To have a better understanding of the growth mechanism we use a COMSOL software to find out the concentration profile of the reactant materials in

the furnace tube. Figure 5:15 displays the results of the simulation of MoO_2 concentration as a function of the MoO_2-substrate vertical distance.

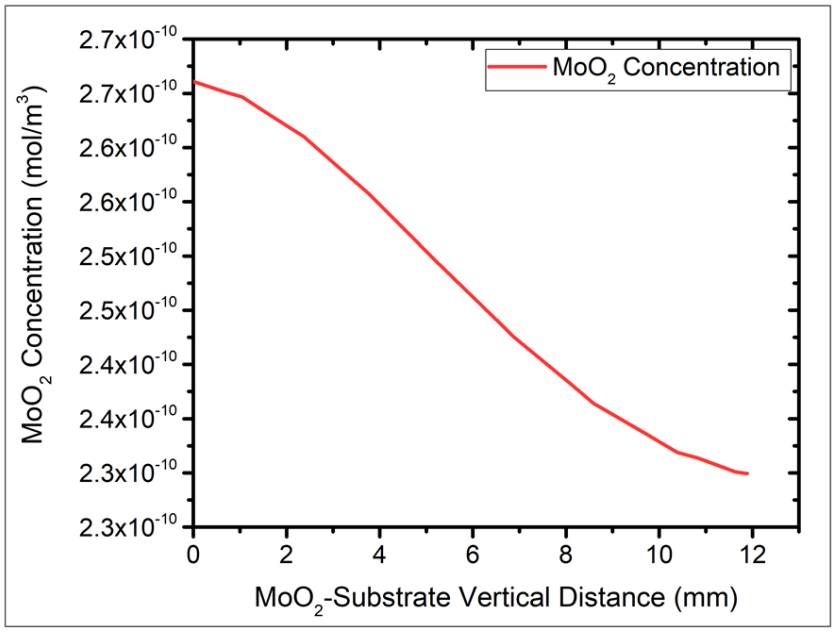

Fig. (5:15): MoO_2 concentration as function of MoO_2-substrate vertical distance at a growth temperature 1073 K and an Ar flow rate 200 of SCCM.

Figure 5:16 shows a cross-sectional MoO_2 concentration profile inside the reaction boat under the growth conditions of 1073 K and 200 SCCM flow rate.

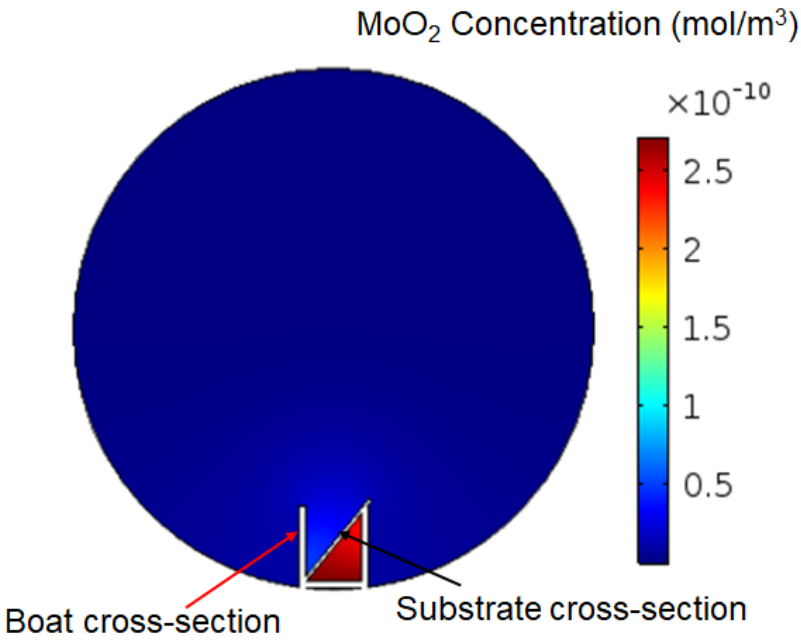

Fig. (5:16): Cross-section of MoO_2 concentration profile inside the reaction boat at a growth temperature 1073 K and an Ar flow rate of 200 SCCM.

We have presented the results at a typical growth temperature of 800 °C. We used the same design for growth temperatures between 650-1000 °C. The growth proved to be reproducible for full coverage uniform monolayers up to a 5 mm substrate vertical distance in the temperature window 650-850 °C. The results for different growth temperature will be presented later on in this chapter.

The sulphur concentration profile along the furnace tube in the ZX-plane is shown in figure 5:17. A data profile taken along cutline displayed in figure 5:17 is shown in figure 5:18. As one can see, the concentration profile becomes fully developed 10 cm away from the sulphur boat centered 23 cm from the inlet. There is a small but non negligible amount of sulphur diffusing back toward the inlet.

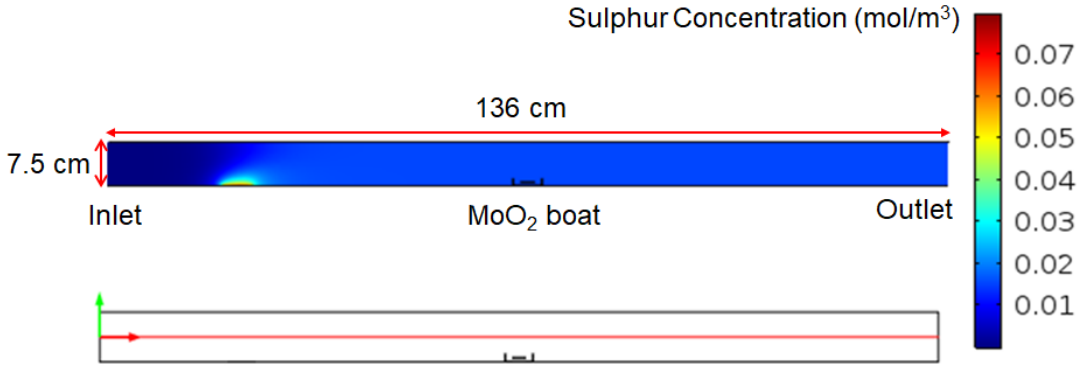

Fig. (5:17): Upper: ZX-plane, sulphur concentration profile at a growth temperature 1073 K and a flow rate of 200 SCCM. Below: cutline (red) along the tube.

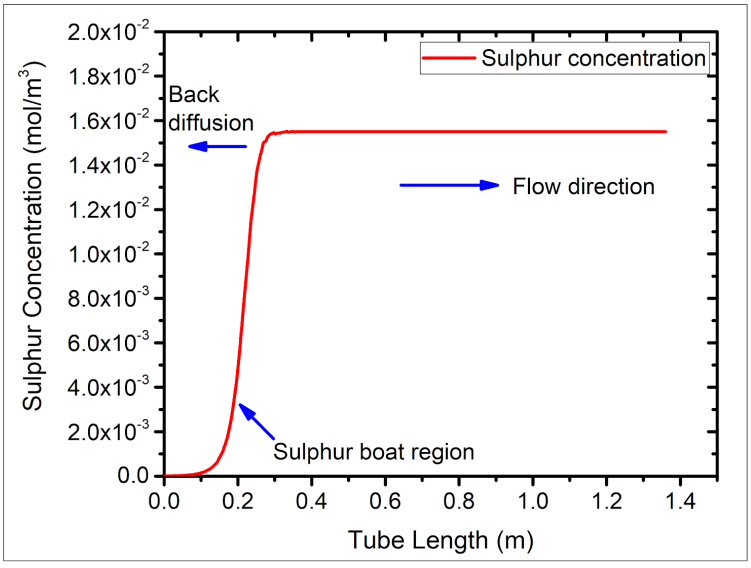

Fig.(5:18): Sulphur concentration profile taken along the cutline shown in fig. (5:17).

The velocity profile of the Ar carrier gas in the reaction boat is shown in figure 5:19 (left). The data taken along the red cutline in figure 5:19 (right) is shown in figure 5:20.

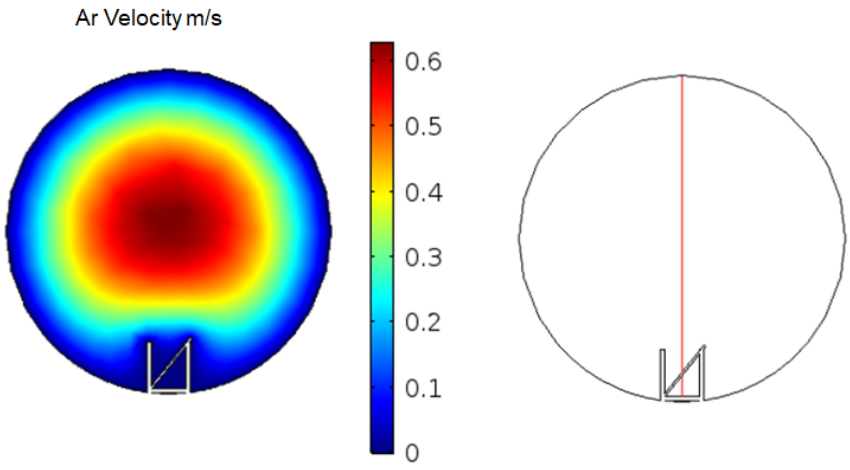

Fig. (5:19): Left: Ar velocity profile in the XY-plane at the center of the furnace tube. Right: red cutline.

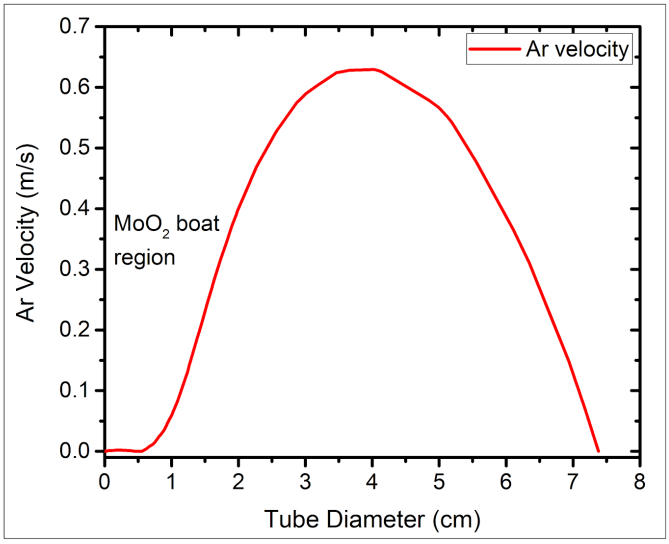

Fig. (5:20): Ar velocity profile taken along the cutline shown in figure 5:19 (right).

The average carrier velocity inside the reaction boat is 0.1 cm/s and the width of the substrate is 2 cm. The sulphur and MoO_2 diffusion coefficients under our growth conditions are 168 cm^2/s and 92 cm^2/s respectively .

We can quantify the concentration in terms of a dimensionless number called the Péclet number (Pe), which is the ratio of the contributions to mass transport by convection to those by diffusion [135]:

$$Pe = \frac{L_r U}{4D} \qquad 5:18$$

where L_r is the length of reactor, U is the mean carrier velocity and D is the diffusion constant.

In our case the Pe value for sulphur is 3×10^{-4} and for MoO_2 is 5.4×10^{-4}. If Pe <<1, the diffusion is dominant and the concentration is uniform, while for Pe >>1, there is a gradient in the species concentration [135]. For our model we have seen that Pe is <<1 and the concentration of sulphur and MoO_2 are therefore uniform. These values of Pe are as expected since we are using LPCVD where the starting materials have high diffusion constants.

5.3.2 The effect of sulphur flux on the coverage of monolayers

One of the ways to change the sulphur concentration and flux in the growth reactor is by changing the carrier gas flow rate. Depending on the size of the reactor, the flow rate can be tuned to get the optimum condition for the growth. A set of experiments have been done using the same model explained in section 5:3. In those experiments the growth temperature was set to be 800 °C, the sulphur was placed at a region where the temperature reaches 200 °C, the growth time was 15 minutes and gas flow was 10, 20, 30, 40, 50 and 200 SCCM. In such conditions, the growth rate is expected to be a function of gas flow rate only. The experimental data of monolayer film coverage as a function of the gas flow rate is shown in figure 5:21.

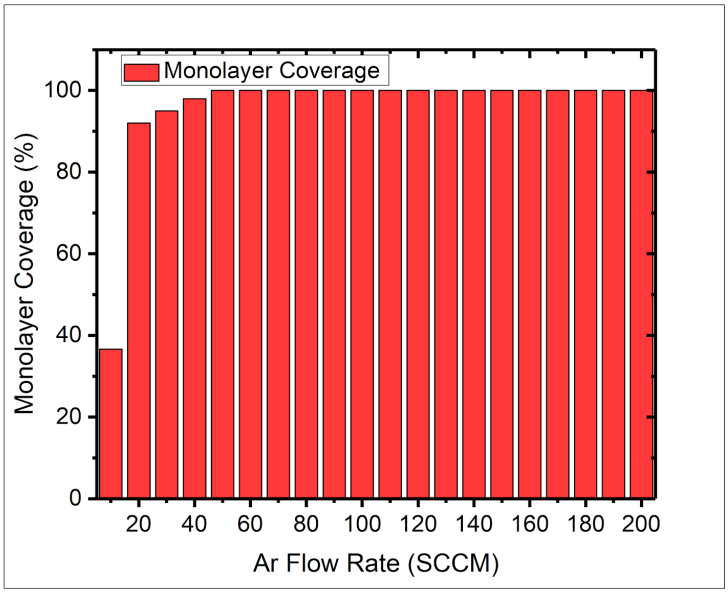

Fig. (5:21): Monolayer coverage as a function of Ar flow rate for a growth temperature 1073 K.

The sulphur concentration and flux is proportional to the carrier gas velocity inside the furnace tube which is in turn related to the tube cross section and the gas flow rate. It is better to present the monolayer coverage as a function of sulphur flux. The left subplot of figure 5:22 shows COMSOL simulations of typical sulphur convective flux at 200 SCCM at growth temperature of 1073 K. The right subplot of figure 5:22 shows the red cutline along which data is taken for different flow rates and displayed in figure 5:23.

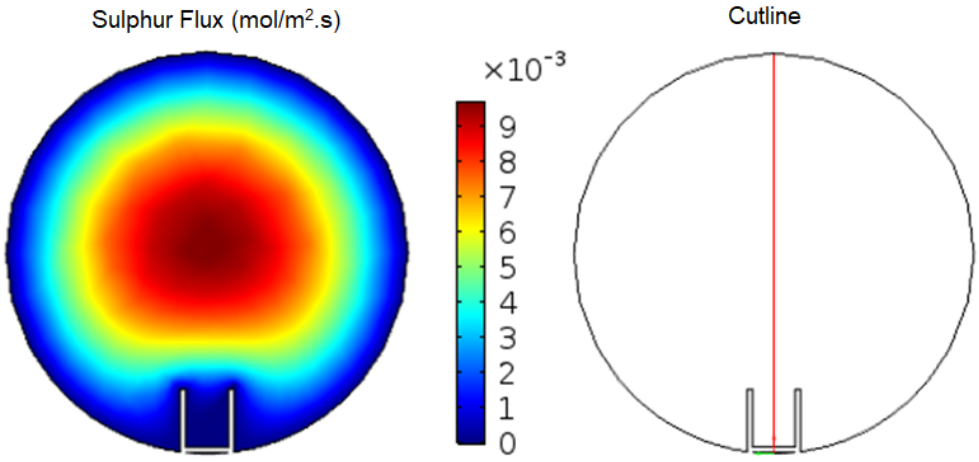

Fig. (5:22): Left: typical sulphur flux at the inlet of the growth region at a growth temperature of 1073 K and a flow rate 200 SCCM. Right: cutline along which data for different flow rates is taken.

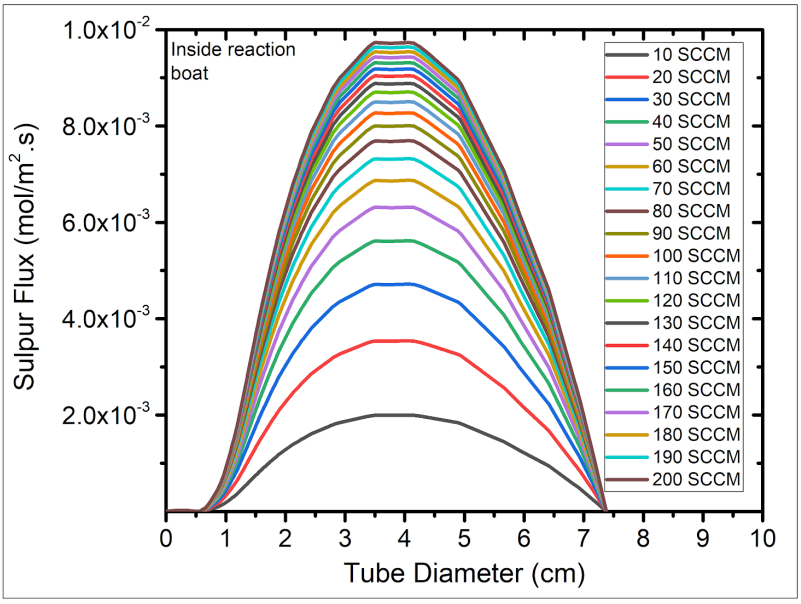

Fig. (5:23): Sulphur convective flux under different flow rates, and at a growth temperature 1073 K. Data is taken along the red cutline shown in fig 5:22,right.

The sulphur convective flux at the reaction zone inlet is magnified in the following figure (5:24)

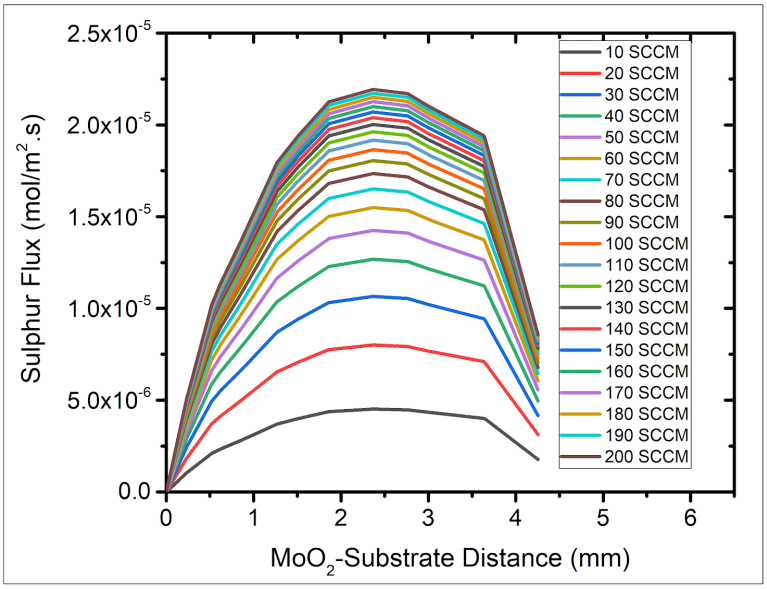

Fig. (5:24): Close-up of the sulphur flux profile at the reaction zone as a function of Ar flow rate.

We also extracted the average sulphur convective flux at the inlet of the reaction zone as displayed in figure 5:25. As we can see, the film is partially covered up to a sulphur flux of 7×10^{-6} mol/m^2.s indicating that the growth is in a feed-limited regime with respect to sulphur. Above 7×10^{-6} mol/m^2.s full coverage monolayers is obtained and the growth became in steady state regime.

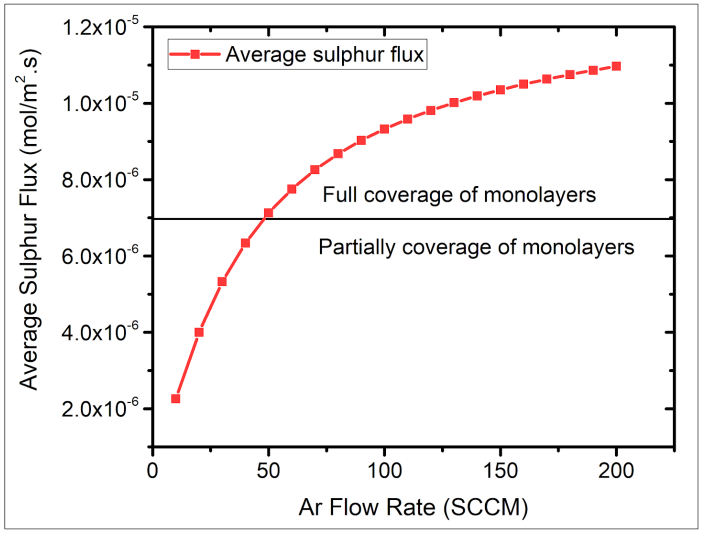

Fig (5:25): Average sulphur flux entering the reaction zone as a function of Ar flow rate.

The sulphur concentration profile as a function of flow rate at the center of the tube furnace is shown in figure 5:26.

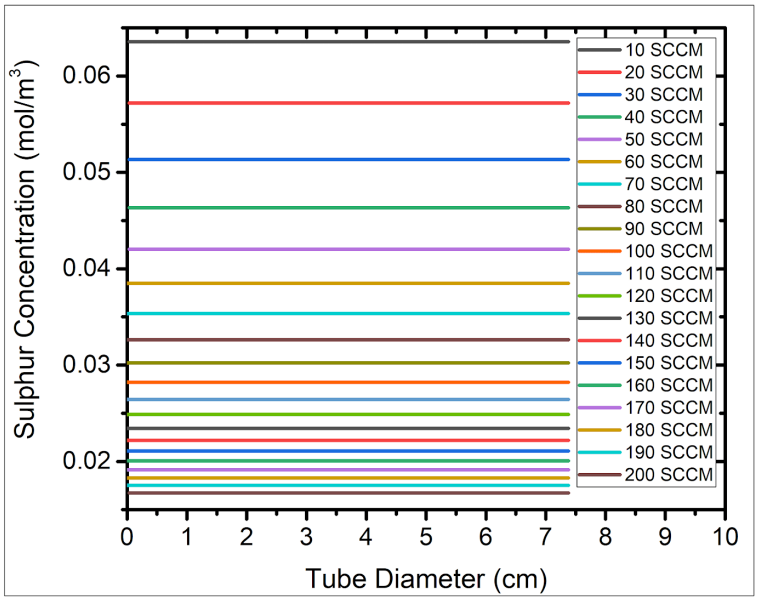

Fig. (5:26): Sulphur concentration profile as a function of Ar flow rate. Data is taken along the red cutline shown in fig. 5:22.

In this section, we studied the effect of the sulphur concentration and flux on the monolayer film growth rate. We correlate both concentration and flux to the carrier gas flow rate using COMSOL (transport of diluted species). Based on our experimental findings a sulphur flux of at least 7×10^{-6} mol/m^2.s is required to grow full coverage monolayer films. Below 7×10^{-6} mol/m^2.s, the system was in (sulphur) feed-limited regime, *i.e.* the rate of providing sulphur to the reaction zone was much lower than the rate of sulphur consumption by the reaction at the growth front. From 7×10^{-6} mol/m^2.s up to 10^{-5} mol/m^2.s, a full coverage monolayer is obtained and the system is expected to be in a steady state.

5.3.3 Grain size and nucleation density temperature dependence

We have studied the effect of temperature on the grain size distribution and nucleation density using the same experimental procedure as explained in section 5.3. The results presented here are for temperatures of 650-850 ºC that result in the growth of reproducible continuous monolayer films. The temperature dependent nucleation density and grain size distribution were carefully investigated using SHG microscopy. The reproducibility of the film growth is confirmed by several growth runs. Figures 5:27-5:31 show colored orientation maps of continuous monolayer films grown at temperatures between 850 ºC and 650 ºC respectively.

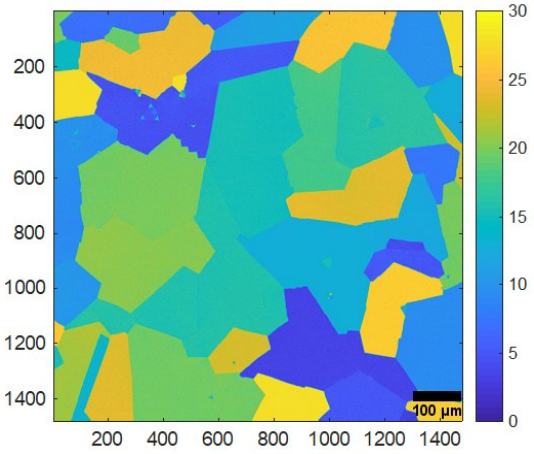

Fig. (5:27): Colored orientation map of a polycrystalline film grown at 850 °C.

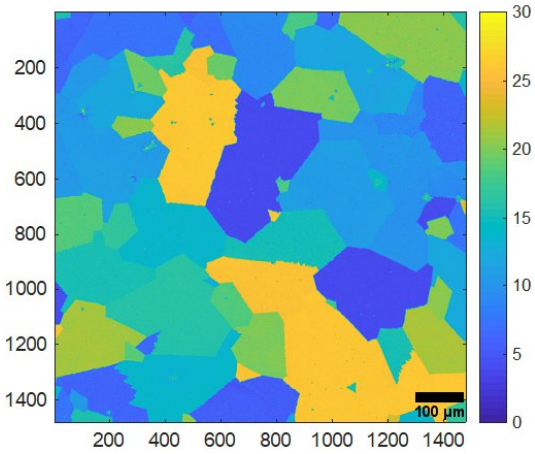

Fig. (5:28): Colored orientation map of a polycrystalline film grown at 800 °C.

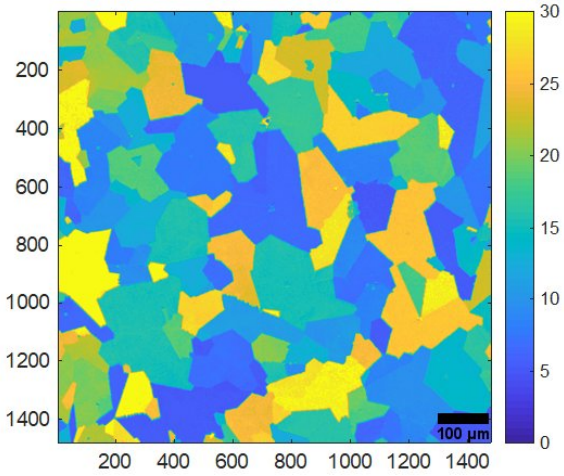

Fig. (5:29): Colored orientation map of a polycrystalline film grown at 750 °C.

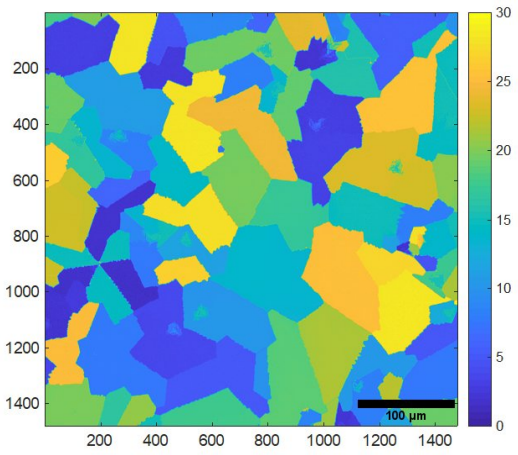

Fig. (5:30): Colored orientation map of a polycrystalline film grown at 700 °C.

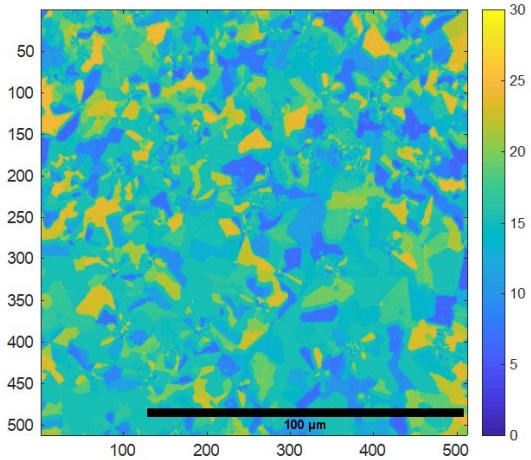

Fig. (5:31): Colored orientation map of a polycrystalline film grown at 650 °C.

The statistics of the grain size distribution as a function of temperature between 650 °C and 850 °C are shown in figures 5:32-5:36 respectively. They all appear to follow a well-defined log-normal distribution. The average nucleation density as a function of temperature is shown in figure 5:37.

At a growth temperature of 850 °C, the grain size ranges from 3030±780 μm^2 to 60560±10350 μm^2 with the peak centered at 24669±12235 μm^2 and the average nucleation density of 50±7 mm^{-2}. The figures for 800 °C are very close to that of 850 °C. At 800 °C the maximum size of gain can be as large as 79740±9670 μm^2 and minimum size 2600±515 μm^2 and the most probable size of 13837±1613 μm^2 and the nucleation density slightly increased to 82±9 mm^{-2}. A sharp change happens at the growth temperature of 750 °C, the largest grain that can be grown at this temperature 30930±6400 μm^2 is less than the half size of grain grown 800 °C. The average grain size at 750 °C was found to be 5974±706 μm^2 and the nucleation density is 180±13 mm^{-2}. A more steep change occurs when the temperature is reduced to 700 °C. At this point the grain size ranges from 4980±800 μm^2 to 500±300 μm^2 with an average of 1000±605 μm^2 and nucleation density is up to 3271±60 mm^{-2}. At 650 °C the mean grain size reduces dramatically to only 30±2 μm^2 with the average nucleation density increased to 25794±160 mm^{-2}.

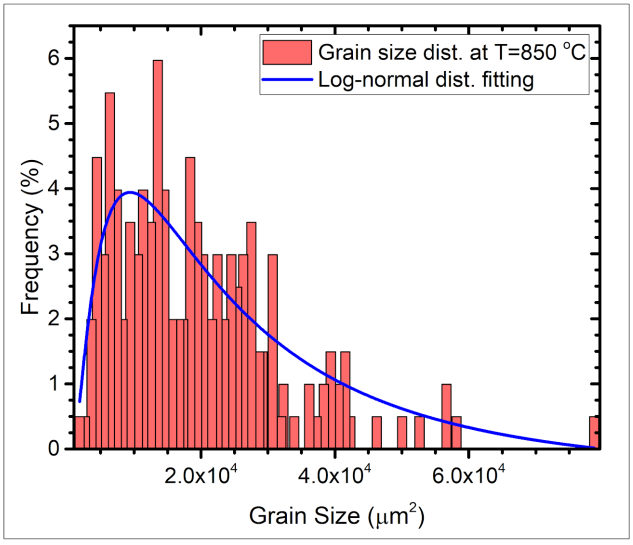

Fig. (5:32): Grain size distribution at a growth temperature of 850 °C.

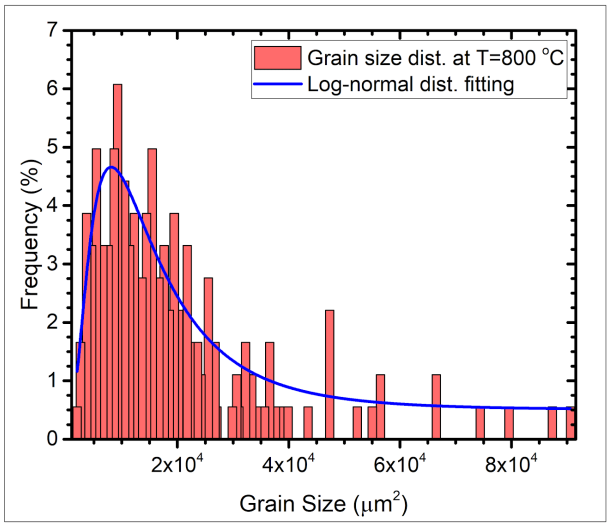

Fig. (5:33): Grain size distribution at a growth temperature of 800 °C.

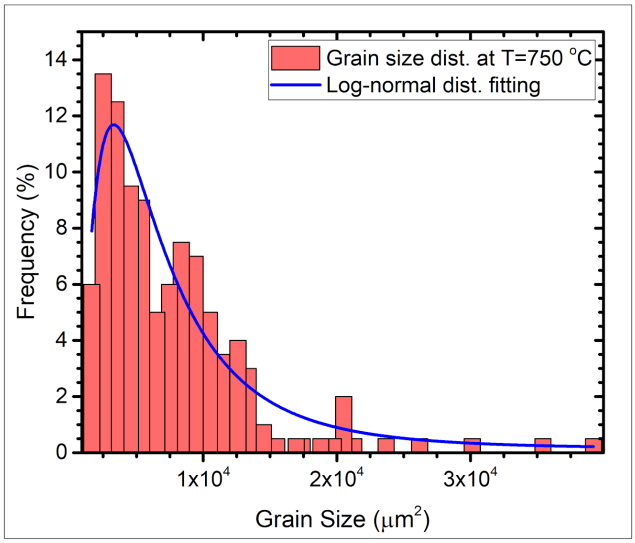

Fig. (5:34): Grain size distribution at a growth temperature of 750 °C.

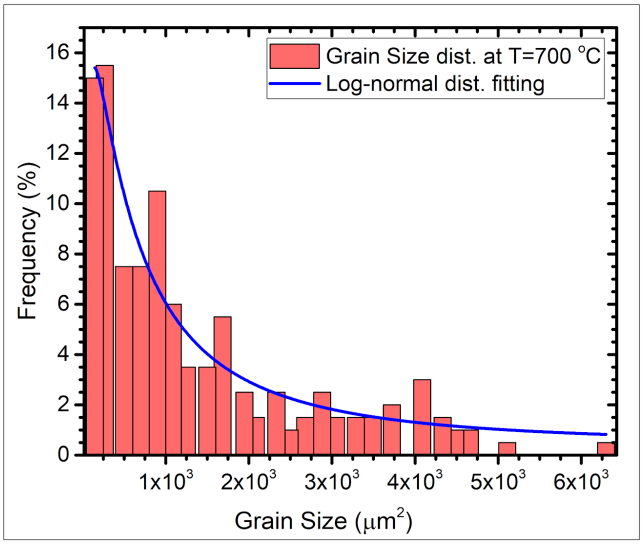

Fig. (5:35): Grain size distribution at a growth temperature of 700 °C.

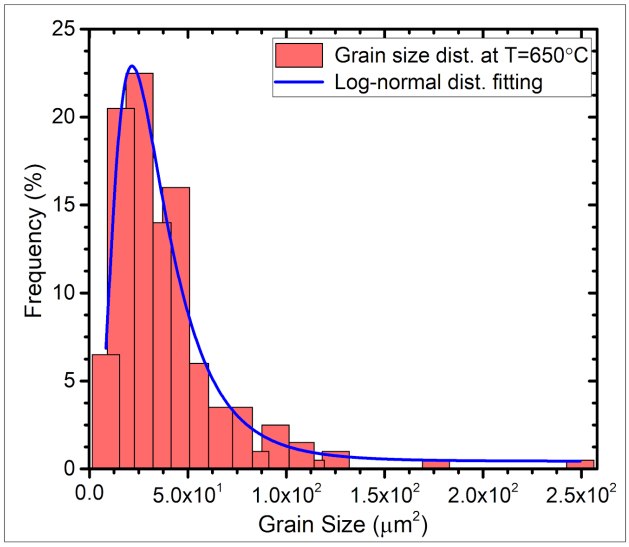

Fig. (5:36): Grain size distribution at a growth temperature of 650 °C.

By fitting our measured data with an Arrhenius equation, as shown in figure 5:37, we have found that that the nucleation density $N\alpha e^{\frac{-3.26\pm0.23}{kT}}$ where 3.26±0.23 eV is the nucleation activation energy for a growth temperature T≤ 750 °C and $N\alpha e^{\frac{-1.33\pm0.123}{kT}}$ where 1.33±0.12 eV is the nucleation activation for growth temperature T≥800 °C.

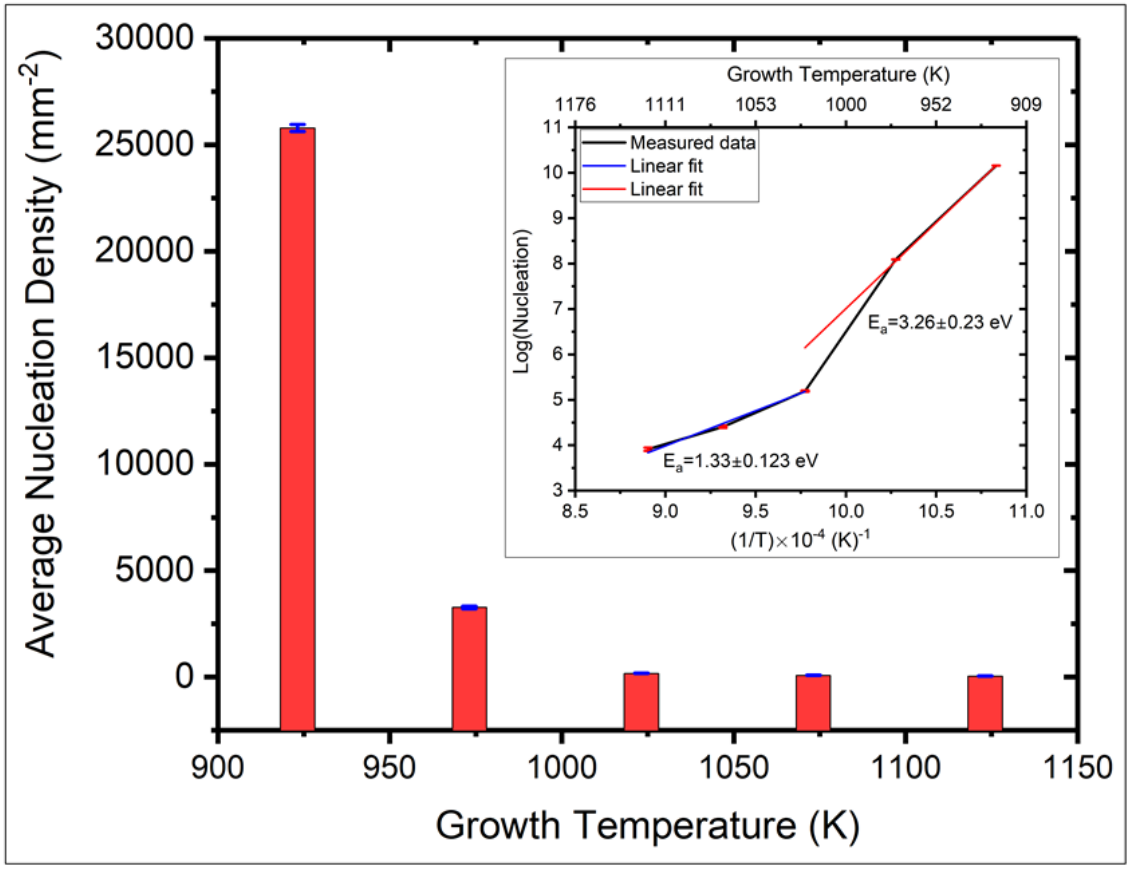

Fig. (5:37): Nucleation density as a function of growth temperature with the inset fitted with an Arrhenius equation.

The growth time for full coverage monolayers is 15 minute for all growth temperatures. Based on this fact the growth rate of the film as a whole is similar for all growth temperatures while the growth rate for single grains within the polycrystalline film is temperature dependent. At low growth temperatures T < 800 °C the nucleation probability is high as shown in figure 5:37 and the growth rate of single grains is slow. While at high temperatures T ≥ 800 °C, the nucleation is suppressed and single grain growth rate is dramatically increased.

From the kinetic theory of gases we can easily estimate the time required to form a monolayer on the target substrate. This monolayer formation time is inversely related to the impingement rate (flux). From our experimental investigations, we have found that the required time for full monolayer coverage is 15 minute for all growth temperatures. The lattice constant of the 1H MoS_2 phase is 3.16 Å and each primitive unit cell contains 1 Mo atom and 2 S atoms. This means in the case of a perfect monolayer, there are 10^{19} Mo atoms/ m^2 and 2×10^{19} S atoms/m^2 respectively. The Mo flux incorporated in the crystal growth is given by:

$$Flux = \frac{10^{19}(\,atoms/m^2)}{growth\ time\ (s)} \qquad 5:19$$

The relation between the flux and vapor pressure is given as follow:

$$Flux = \frac{P}{\sqrt{\frac{2\pi RT}{M}}} \qquad 5:20$$

Here, *P* is the partial pressure of Mo consumed in the reaction, *R* is the universal gas constant, *M* is molar mass and *T* is temperature in Kelvin.

Using equations 5:19 and 5:20 together with the experimentally observed growth time, we have found that in the steady state (when the sticking coefficient is assumed to equal to one), the required vapor pressure of the Mo source for a monolayer growth is 10^{-11} atmosphere. With the help of the vapor pressure data of different precursors, our finding suggests that choosing the right processor can be is the key for growing TMDs monolayers. The finding suggests that there should be a proper designing of CVD reactors for growing TMDs monolayers when having a precursor with high vapor pressure.

Equation 5:15 shows that the MoO_2 vapor pressure is ≥ 10^{-11} atmosphere at growth temperatures T ≥ 800 °C. Such a low vapor pressure is essential for growing monolayers on large scales. However, for growth temperatures T < 800

°C, equation 5:15 gives a vapor pressure lower that 10^{-11} atmosphere, which contradicts our experimental results indicating that extrapolation of equation 5:15 is not correct for low temperatures.

As we have seen, MoO_2 provides enough flux for growing MoS_2 monolayers at a range of growth temperatures when the substrate is placed in an appropriate place such that the whole flux generated diffuses to the substrate. The full coverage obtained at different growth temperatures in equal growth times confirms our point. The MoO_2 vapor pressure increases exponentially with temperature, which means that the substrate receives more Mo at higher temperatures, but at the same time the Mo sticking coefficient decreases with raising temperature. Therefore there is more Mo desorption from the substrate at high temperatures such that the net Mo-flux available at each temperature is critical for MoS_2 monolayer growth. In the next chapter, we will use MoO_3 as precursor, which has a much higher vapor pressure than MoO_2, to study film growth beyond such critical MoO_3 vapor pressures required for growing monolayers.

5.3.4 Temperature dependence of the initial monolayer growth rate

In this section we present a systematic study of the initial monolayer growth rate temperature dependence. Arrhenius plots under a fixed reactant concentration can be used for this purpose. In our case, we fixed the sulphur flux in the reaction zone by keeping the sulphur boat at the same sublimation temperature of 200 °C for all growth temperatures (650 °C - 1000 °C). Figure 5:38 is the average sulphur flux in the reaction zone. As we can see, the flux is slightly higher for higher temperatures due to a slightly higher carrier gas velocity at high temperatures.

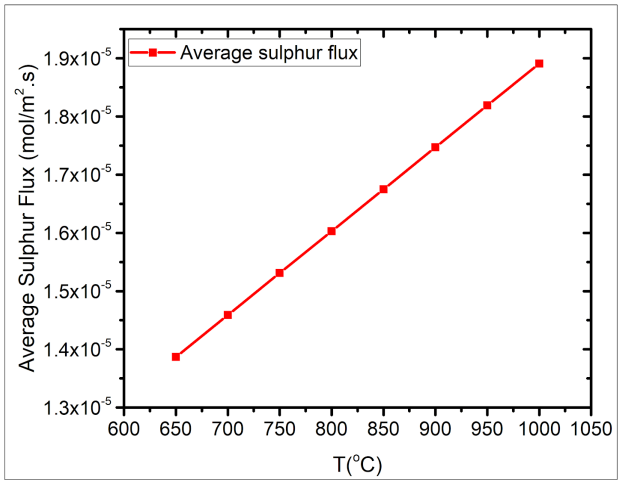

Fig. (5:38): Sulphur flux in the reaction zone at different growth temperatures.

The Mo flux is also proportional to the growth temperature via equation (5:15). However, we do not have control over it as we have control for sulphur because the MoO_2 container and the substrate are positioned in the same temperature zone. We assume that the rates of high Mo flux at high temperatures are compensated by the high rates of Mo desorption from the substrate. We base our assumption on the fact that we can get a full coverage of monolayers during a 15 minute growth run for all growth temperatures as we presented in the previous section. Therefore the amount of Mo involved in the reaction are equal for all growth temperatures.

For comparison of data from different growth temperatures, we used the size of the maximum possible grains observed at each growth temperatures. Figure 5:39 is the corresponding Arrhenius plot of the grain size as a function of growth temperature.

As we can see the growth rate follows the three classical temperature regions. At 650 ^{o}C ≤ T< 800 ^{o}C, the grain growth starts from a low level but increase sharply with temperature. This is considered to be in the surface kinetics limited regime with an activation energy of -2.6±0.4 eV. Although there is plenty of sulphur in the reaction zone (as shown in figure 5:38), the grain growth (rate) is limited by the kinetics of the chemical reactions at the surface which is strongly temperature dependent. In this regime, the supply of the reactant materials to the substrate is higher than the rate consumed by the reaction.

At 800 ^{o}C ≤ T ≤ 900 ^{o}C, the grain growth seems to have plateaued and the system is in a mass transport or feed controlled regime. In this regime the growth rate strongly depends on feed supply of the starting materials and weakly on the growth temperature.

At 900 ^{o}C ≤ T ≤ 1000^{o}C the growth is in desorption regime. As a result of high desorption of the reactants, the growth rate reduces. Beyond 1000 ^{o}C, there is a rapid desorption of the precursors from the substrate before the reaction occurs and the growth was not observable.

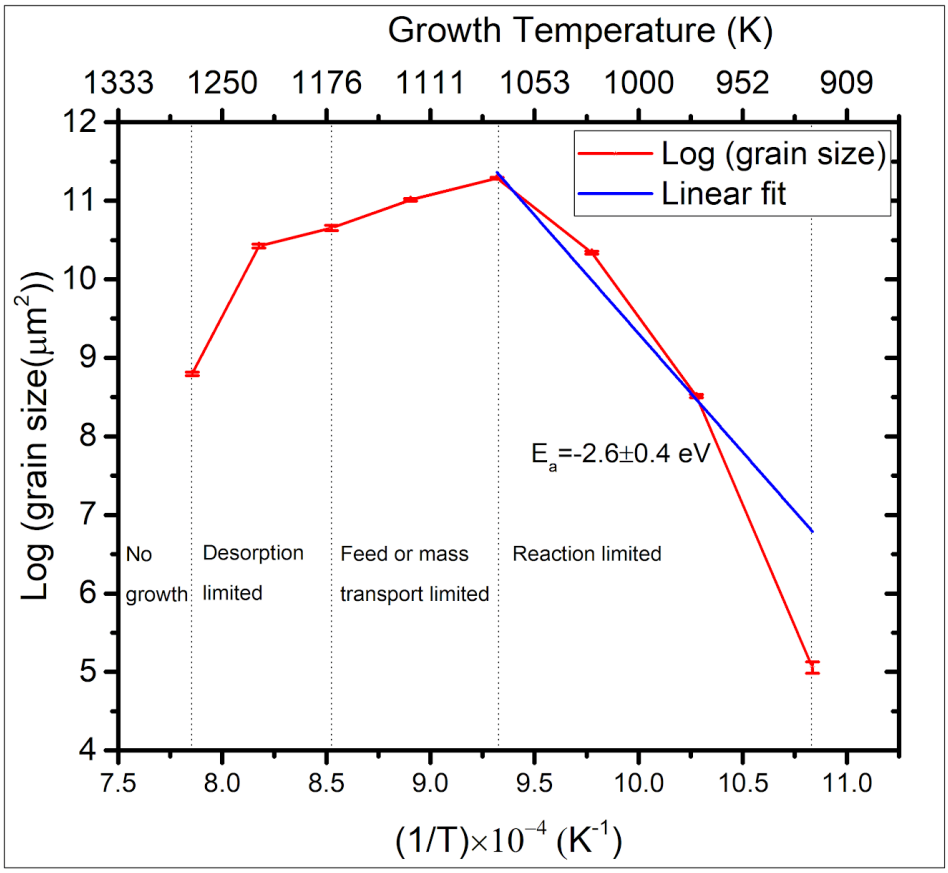

Fig. (5:39): Arrhenius plot of MoS_2 monolayer growth for 15 minutes.

5.3.5 One minute growth (flushing growth)

We further studied the growth of single grain monolayer by reducing the growth time to only one minute (flash growth). For this purpose we further increased the sulphur flux to make sure the system in a rich sulphur environment and the growth is temperature dependent. The sulphur flux for one minute growth at different temperatures is shown in figure 5:40.

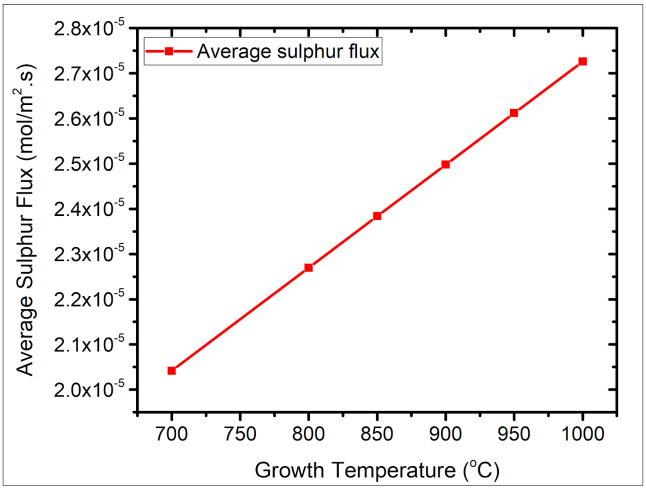

Fig. (5:40): Average sulphur flux used in the one minute growth.

When using the maximum grains found on the substrate, their growth rate is found to be 4 ±1 $\mu m^2/s$, 326±53 $\mu m^2/s$, 340±15 $\mu m^2/s$, 710±260 $\mu m^2/s$, 560±137 $\mu m^2/s$ and 110±21 $\mu m^2/s$ at growth temperatures of 700 °C, 800 °C, 850 °C, 900 °C, 950 °C and 1000 °C respectively. The arrhenius plot for flush growth is shown in figure 5:41. Again we can see that the monolayers are at a reaction limited regime at T<800 °C, a transport limited regime at 800 °C ≤ T ≤ 900 °C and a deposition limited regime at T ≥ 950 °C. These results confirm our classification for growth regimes presented in the previous section that is based on the grain size. The activation energy for the reaction limited regime is -4 eV much larger than -0.4 eV for the mass transport limited regime. This is as expected as the reaction limited regime is strongly temperature dependent while the transport regime is weakly temperature dependent.

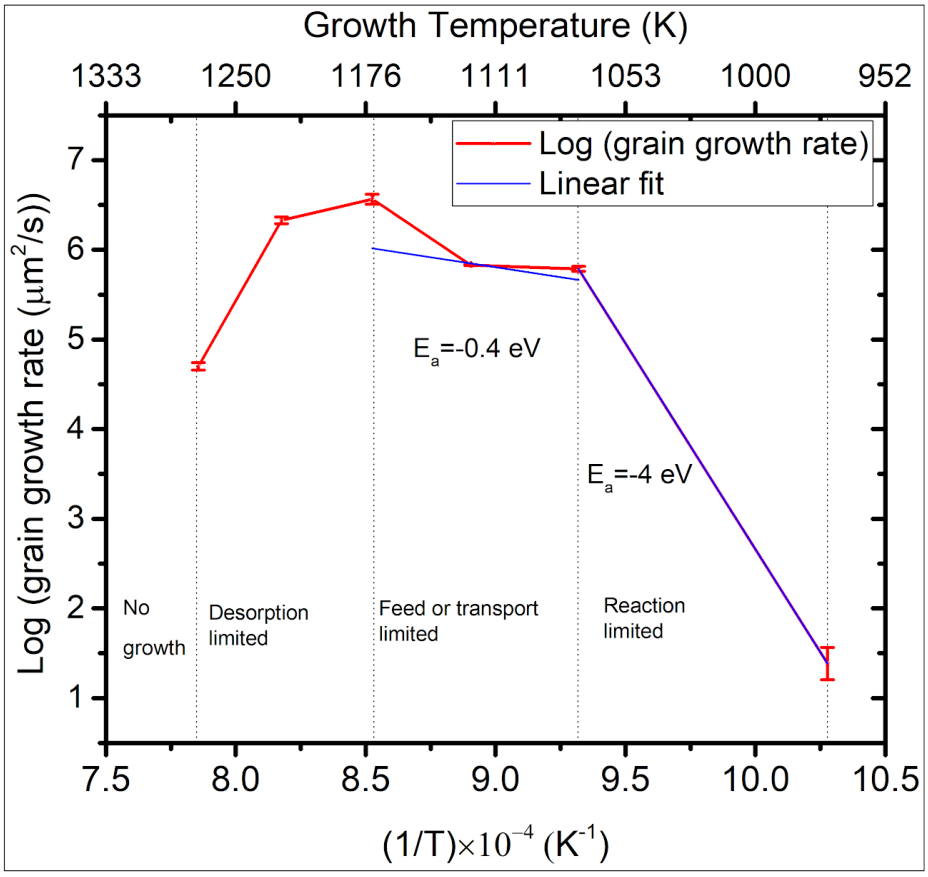

Fig. (5:41): Arrhenius plot for one minute growth.

Figure 5:42 a-e show grey style images of monolayers grown in one minute at growth temperatures of 700 °C - 1000 °C respectively.

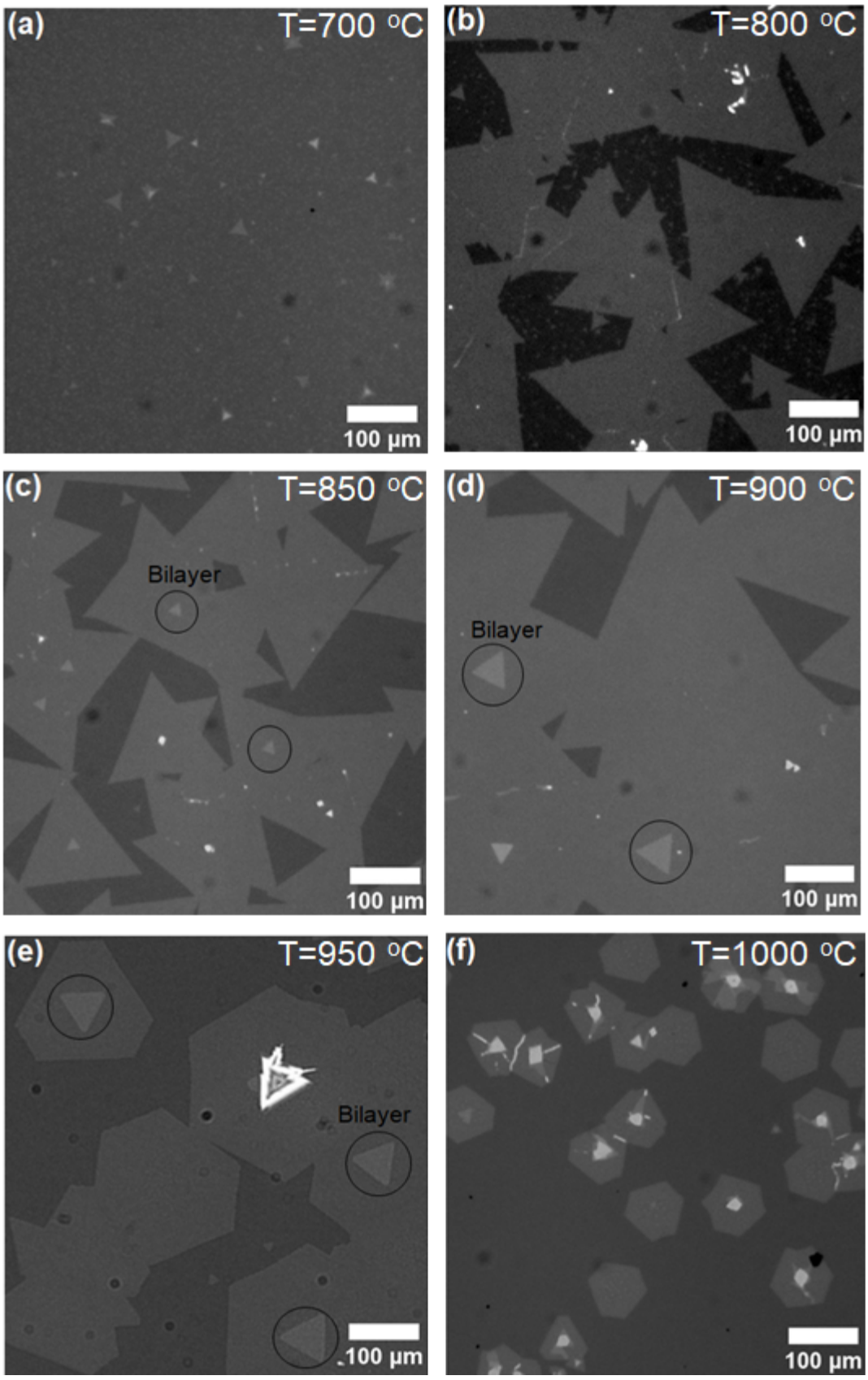

Fig. (5:42 a-f): Are the grey style images of monolayers grown in one minute at different growth temperatures between 700 ºC and 1000 ºC respectively.

From figure 5:42, we also can observe that the significant growth of additional layers increases at growth temperatures T ≥ 850 °C even for such a short growth run, as shown in the white circles (fig. 5:42 c-f). For growth of monolayers free from adlayers, the optimum growth temperature would therefore be 800 °C.

5.3.6 The effect of sulphur chemical potential on grain morphology

The precise control of the edge geometry and crystal morphology of monolayer two dimensional materials is of particular interest for their application as catalysts in hydrodesulfurization of fossil fuels [136]. In the case of MoS_2 monolayers, edge structures have two different kinds, the $(10\bar{1}0)$ Mo zigzag edge and the $(\bar{1}010)$ S zigzag edge (see Fig.1:4 in Chapter One). The Mo zigzag edge is found to be catalytically active while the S zigzag equilibrium edge structure itself is not active, and sulphur vacancies are needed for the reaction to proceed [137].

The equilibrium shape of isolated MoS_2 monolayer grains may be very different, depending on the experimental conditions of the deposition [138]. The most common parameters that have been used for determining the morphology of MoS_2 monolayers in CVD growth are temperature [139] and concentration of the starting materials [138]. However, precise control of the morphology has not been achieved yet and different shapes coexist in a single experimental run.

Wang *et al.* (2014) [138] have found that different morphologies can coexist in a single experimental run. They claimed that the growth of such patterns might be due to the local variations in Mo/S ratio on the substrate. However, they did not present a quantitative figure of the Mo/S ratio that can lead to the growth a single type of morphology.

To better control the morphology of MoS_2 monolayers, Xie *et al.* (2016) [139] used the evaporation temperature of the starting materials (MoO_3 and S) to change Mo/S in the reaction zone. They found that the MoS_2 domains are mainly round, nearly round and hexagonal, and truncated triangles grew at 760 °C, 750 °C and 730 °C respectively. However, they have not presented a clear explanation of the mechanisms of growth. In a similar work by Yang *et al.* (2017) [140], they found that at low temperature MoS_2 monolayers have a triangular shape. By increasing the temperature to 850–950 °C, hexagonal MoS_2 flakes are observed. A further increase in temperature to over 950 °C, MoS_2 rectangle shape monolayers are produced. Although, both of the mentioned works use the same type of starting

materials (MoO_3 and S), they have found different morphologies under different growth temperatures. Therefore, we believe further understanding of the growth conditions and growth mechanisms is still needed to obtain control over the reproducibility of MoS_2 monolayer morphology.

Here, we used the chemical potential of sulphur to finely tune the morphology of MoS_2 monolayers. We have produced bent triangles, perfect triangles and hexagons in a reproducible manner. Figure 5:43(a-d) shows optical micrographs of the MoS_2 monolayer grains with different morphologies grown at temperatures of 700 ^oC - 1000 ^oC respectively. The growth process of the MoS_2 monolayers can be can be summarized as follows: (1) the sublimation of sulphur powder at 200 ^oC and its transport by the carrier gas to the substrate; (2) the sublimation of MoO_2 powder at the growth temperatures and its diffusion to the substrate as the substrate is directly faced down on the MoO_2 source; (3) adsorption of the source materials (S and MoO_2) on the substrate (4) diffusion and reaction of the source materials on the substrate that lead to the nucleation of a MoS_2 monolayer; (5) desorption of the reaction byproducts to the carrier gas stream.

Based on microscopic studies, in the early stages of growth the MoS_2 monolayer starts as an irregular polygon with Mo and S terminations as depicted in figure 5:44 [131]. According to crystal growth theory [141], the different growth rates of the different crystal facets determine the final morphology of the crystal. The growth rate of a crystal face depends on the face free energy [141]. In the case of MoS_2 facets ($10\bar{1}0$) and ($\bar{1}010$) which are known as Mo-terminating and S-terminating, zigzag edges are the most commonly observed and energetically stable edges [11].

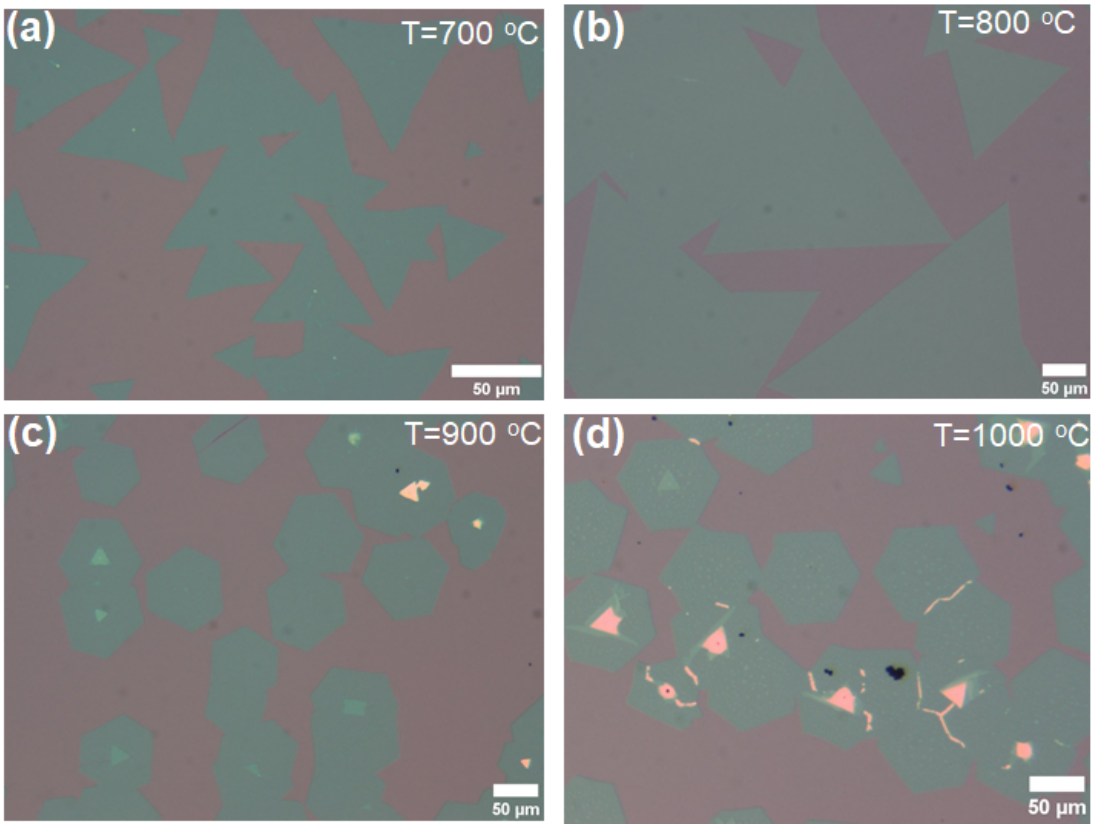

Fig. (5:43): Shape evolution of MoS_2 monolayers grown between 700 °C and 1000 °C.

Fig. (5:44): Depiction of MoS_2 monolayer nucleus in the early growth stage showing Mo and S zigzags.

The growth rates of advancing $(\bar{1}010)$ and $(10\bar{1}0)$ facets depend on the Mo and S concentrations in the reaction zone. In the case of a S-rich environment the $(\bar{1}010)$ facets advance faster and disappear and the final shape of the crystal will be bent or perfect triangle as shown in figure 5:43(a) and 5:43(b) respectively. By decreasing the sulphur concentration, the two faces $(\bar{1}010)$ and $(10\bar{1}0)$ advance

equally and the final morphology will be a hexagon as shown in figure 5:43 c and 5:43 d respectively.

Using COMSOL simulation we have found that the average sulphur concentration in the reaction zone is 0.016 mol/m^3-0.0157 mol/m^3 at growth temperatures between 700 °C - 1000 °C. This means we are growing monolayers under the same sulphur environment. Based on this data the grown monolayers should have a triangular shape at all growth temperatures. However, observation of hexagonal shaped monolayer crystals at growth temperatures above 900 °C means that the system is in sulphur poor environment.

To understand this we correlated the MoS_2 morphology to the chemical potential of the sulphur in the reaction zone. We have used the correlation given by Jackson *et al.* (2016) [142] to calculate the sulphur chemical potential as a function of growth temperature and sulphur vapor pressure:

$$\mu_S(T,P) = \tfrac{1}{2}(erfc(\tfrac{T-T_{tr}}{w}))\tfrac{\mu_{S8}}{8} + \tfrac{1}{2}(erf(\tfrac{T-T_{tr}}{w})+1)\tfrac{\mu_{S2}}{2} - aexp(-\tfrac{(T-(T_{tr}-b)))^2}{2c^2}) \qquad 5:21$$

where T_{tr} and a are represented by the polynomials in $\log_{10}(P/P_a)$.

$$T_{tr} = \sum_i x_{Ttr,i}(log_{10}(\tfrac{P}{Pa}))^i \qquad 5:22$$

$$a = a_o + a_1 log_{10}(\tfrac{P}{Pa}) + a_2(log_{10}(\tfrac{P}{Pa}))^2 \qquad 5:23$$

and μ_{S8}, μ_{S2} are pressure-corrected polynomials in T:

$$\mu_{S8} = \sum_i x_{S8,i}T^i + kTln\tfrac{P}{Pref} \qquad 5:24$$

$$\mu_{S2} = \sum_i x_{S2,i}T^i + kTln\tfrac{P}{Pref} \qquad 5:25$$

where P_{ref} is 10^5 Pa. P is equal to the pressure in Pascals and k = 8.617×10^{-5} eV K^{-1} is the Boltzmann constant. The values of all other parameters are given in Appendix (A3).

Figure 5:45 shows the sulphur chemical potential as a function of sulphur vapor pressure and growth temperature. The sulphur vapor pressure was calculated using COMSOL. We have found that for μ_S=-0.834 eV , the bent, triangles are grown, for μ_S=-0.995 eV, perfect crystals are observed and for μ_S from -1.156 eV to -1.318 eV, hexagonal monolayers are grown. Theoretically, the growth of hexagons is expected to happen at μ_S=-0.98 eV up to -0.04 eV, and the growth of triangles starts at μ_S=-0.04 up to 0 eV [143].

We have used the temperature parameter to change the chemical potential in our system. We have proved that the system could be switched from sulphur-rich to Mo-rich environment. As a consequence of this, we have a control over the morphology of the grown MoS_2 monolayers.

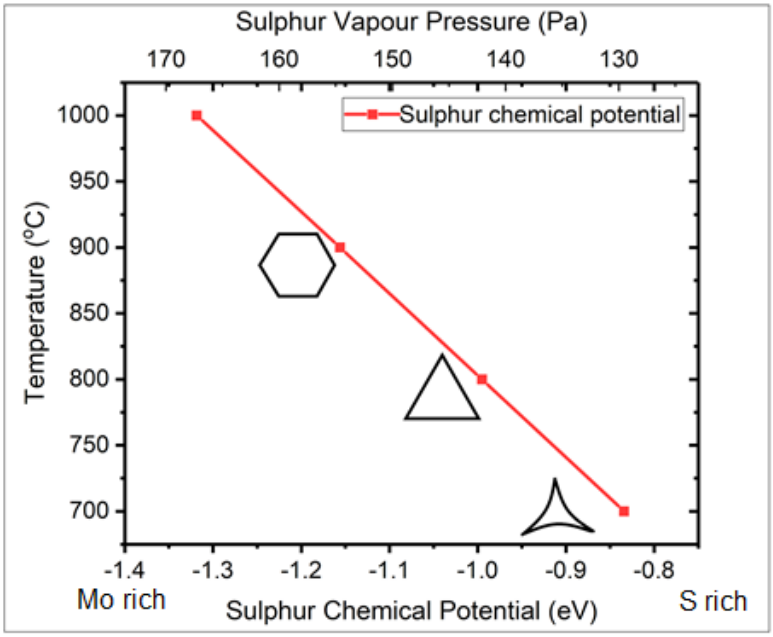

Fig. (5:45): Sulphur chemical potential as a function of growth temperature and vapor pressure indicating the morphology of MoS_2 monolayers at each growth temperature range.

5.3.7 The effect of the growth time on the film uniformity

As we have seen in the previous sections, our model is reproducible for growing full coverage monolayers under a range of growth temperatures when using typical growth time of 15 minutes. In this section we present our results when the growth time is beyond that for a full coverage monolayers (*i.e.* beyond 15 minute growth). For this purpose, we employ typical growth conditions: growth temperature 800 °C and Ar flow rate 200 SCCM.

Figure 5:46 a-b show optical micrographs of uniform MoS_2 monolayers grown at a typical growth growth time of 15 minutes and 20 minutes respectively.

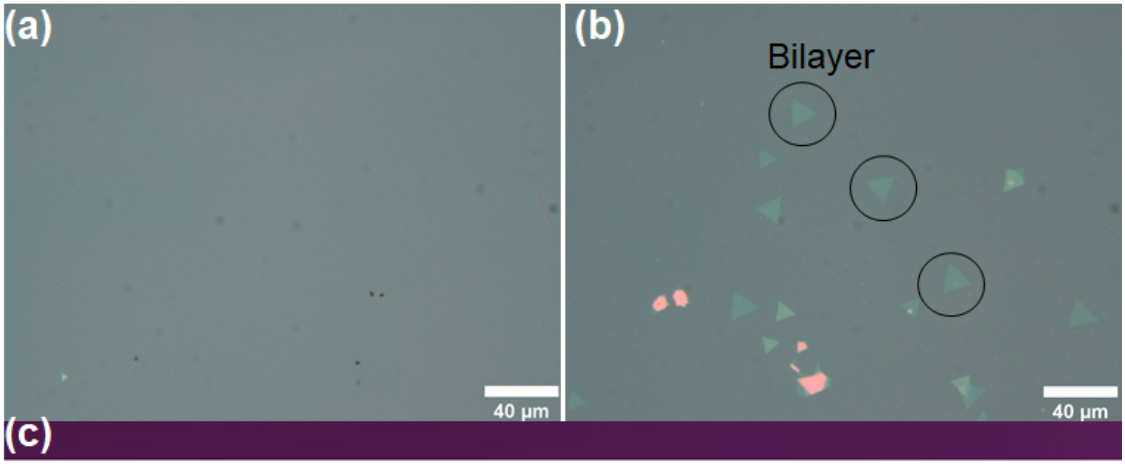

Fig. (5:46): Optical images of (a) continuous MoS_2 monolayer film grown at 15 min., (b) continuous monolayer film grown at 20 min. The initial stages of bilayer growth is shown in the dark circles. (c) bare 300 nm SiO_2/Si substrate.

As we can see from figure 5:46a, the film is continuous and there is no sign of adlayers or holes in the film. Therefore the growth time of 15 minutes can be considered as the optimized time for growing monolayers in our approach. This observation confirms that the monolayer growth is self-limiting to an extent. Further increasing the growth time to 20 minutes, we observed the growth of bilayers as shown in figure 5:46b. These bilayers have not fully covered the surface at this stage. The small triangular grains in the dark circles are the initial stage of the bilayer growing. The nucleation of the bilayers on the continuous background of monolayers confirms the layer-by-layer growth of our films. We did not continue to grow the full coverage bilayers because such growth is beyond the scope of this project. However, we can say that the growth time parameter can be used for further bilayer growth investigations.

In the long-duration growth runs, the sulphur supply must be guaranteed, otherwise the growth of MoO_2 adlayers which is usually grown in a sulphur poor environment is expected. Figure 5:47(a) is an optical micrograph of a diamond-like MoO_2 grain which is grown in a 30 minute run when the sulphur feed stoke is depleted. Our Raman measurement shown in figure 5:47(b) confirms that the diamond-like grains are MoO_2 and agree with the Raman spectra shown in the literature as in figure 5:47(c) [144].

We have shown that when using MoO_2 as the Mo source, a growth time of 15 minutes is ideal for full coverage monolayers. Beyond 15 minutes, the growth of a

bilayer is initiated in a sulphur rich environment. If the sulphur is depleted, the growth of MoO_2 adlayers is observed.

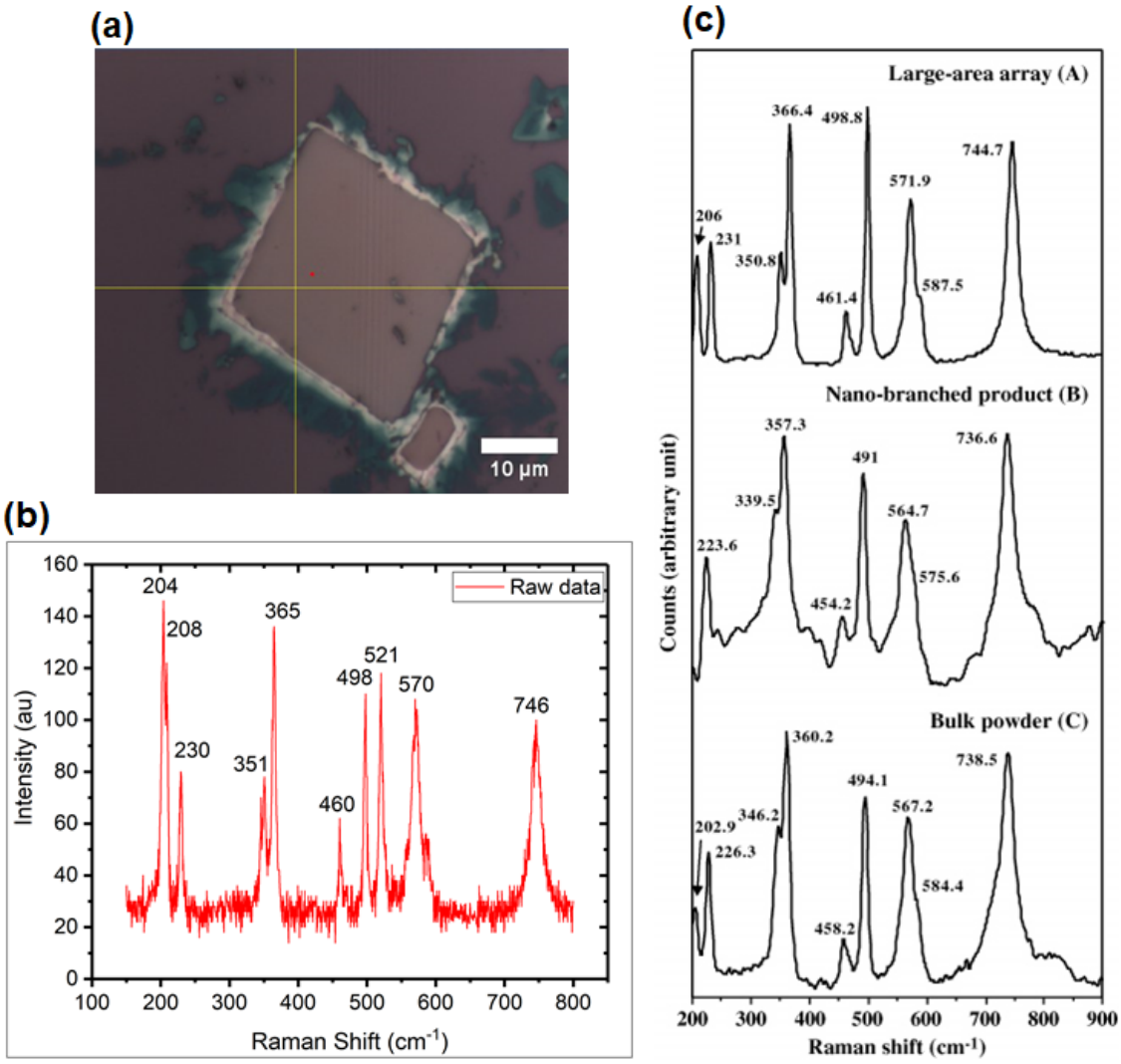

Fig. (5:47): Optical micrograph of a MoO_2 grain (b) the corresponding Raman spectrum and (c) Raman spectrum for MoO_2 from the literature [144].

5.4 Discussion and conclusion

In chemical vapor deposition, the film growth phenomena can be controlled through several parameters such as the nature of the starting materials, transport mechanisms in the reactor, the reaction temperature, and the reactor design. We will discuss the effect of all the mentioned parameters one by one and explain how we employed them in our CVD approach. Based on the mentioned parameters, we established an unprecedented LPCVD approach for growing uniform wafer scale MoS_2 monolayers on a SiO_2/Si substrate. COMSOL simulations are essential to study quantitatively the effect of different parameters on the growth.

Firstly, we presented our data of furnace temperature profile in chapter four. This data was taken under low Ar pressure with no flow conditions. Here, we employed COMSOL (heat transfer in fluids module) to study the effect of the Ar gas flow rate on the temperature profile of the tube furnace to see whether the flow has an effect on the reaction zone temperature and the sulphur zone temperature. For this purpose, we chose a growth temperature of 800 ^{o}C and flow rates of (100-1000) SCCM. We have found that the average temperature of the reaction zone (the place where the Mo source and substrate are placed) is only slightly reduced by the flow rate (up to one degree), even at the highest flow rate of 1000 SCCM. Such a negligible variation of the reaction zone temperature is expected as we use LPCVD where the density of Ar is very low. Also, the center of the reaction zone of our system is 68 cm away from the inlet and the Ar gas gains energy from the hot wall of the tube furnace as it passes such a long distance to the center. Therefore, we can say that neither the evaporation rate of MoO_2, nor the reaction rates could be affected due to the temperature variations resulting from the flow rate. However, in the sulphur zone, the situation is slightly different. The average temperature could reduce (about 10 degrees) at the highest flow rate of 1000 SCCM. Although, we never used such high flow rates in our experimental work, such changes in the temperature should be taken in to account when using low growth temperatures and high flow rates.

We have introduced an experimental set-up that predominantly resulted in the growth of MoS_2 polycrystalline monolayer films under different growth temperatures. This achievement is realized through both employing the low vapor pressure of MoO_2 as Mo source and the peculiar geometry of the reactor. As we designed our set-up such that the substrate is placed in close proximity of the Mo source, in this case the vapor pressure of the Mo source does matter. To understand how the vapor pressures of the Mo sources are important, we investigated the time needed for growing a MoS_2 monolayer.

Three different candidates are available to be used as Mo source molybdenum carbonyls such as $Mo(CO)_6$, molybdenum salts such $MoCl_5$; molybdenum oxides such as MoO_3 and MoO_2. $Mo(CO)_6$, and $MoCl_5$; have melting points of 150 ^{o}C and 194 ^{o}C and they can not be directly used in our approach because they will melt away before the system reaches growth temperature which

is typically 800 °C. Regarding the molybdenum oxides, MoO_3 has a much higher vapor pressure than MoO_2 [133].

Using MoO_3, the rate of providing MoO_3 to the substrate will always be higher than the rate of consumption in the reaction leading to the formation of pure MoS_2. As result of this, the yield on the substrate will be a mixture of nonuniform MoS_2, and molybdenum suboxides. This means that the system is in the reaction limited regime with regard to the MoO_3. In this regard there are several works that have used MoO_3 in this manner that lead to the growth of MoS_2 and Mo suboxides [138], [145], [146]. We also provide our results about using MoO_3 in the following chapter.

Now, regarding MoO_2, our experimental results confirmed that as a result of low vapor pressure, the rate of providing Mo to the substrate is nearly equal to the rate of consumption at certain heights above the Mo source. By quantifying the monolayer coverage as a function of the vertical distance between the substrate and the Mo source, we have found that the complete coverage of monolayers can only be achieved at certain heights. We used this height to guide us to place our substrate horizontally on the Mo source and we have grown wafer scale uniform monolayers as presented in chapter four.

Another key success in our approach is the simple geometry that we have adopted. The position of the substrate relative to the Mo source is the key factor for delivering a uniform Mo flux to the substrate. In the CVD tube, there is an infinite number of ways to place the substrate. In our approach, we placed the substrate at a certain angle to the Mo source for two reasons. Firstly, during the sublimation the Mo directly diffuses to the substrate, as there are no surfaces in between for Mo to deposit on. In this way, we avoided any reduction in the Mo flux and guarantee a uniform Mo concentration profile to the substrate. Secondly, on such an inclined substrate, we can study the growth as a function of Mo concentration covering the concentration variation as a function of vertical distance between the substrate and Mo source in one experimental run.

The CVD growth of MoS_2 is a multicomponent CVD and the presence of sulphur is as important as Mo. The sulphur flux in the reaction zone is another key factor through which we can control the MoS_2 film growth as it determines the rate at which we provide sulphur to the reaction. To evaluate the role of sulphur flux, we studied the effect of the flux on the monolayer coverage in a series of experiments. There are two methods to increase the sulphur flux that reaches the reaction zone.

The first one is to increase the temperature of the sulphur container that would increase the vapor pressure of the sulphur and the second one is to increase the flow rate of the carrier gas. In our work we used the second one as we wanted the sulphur to last during the experiment course. For this purpose, we increased the flow rate from 10-200 SCCM and used COMSOL to correlate the sulphur flux with the flow rate. Using sulphur flux is more convenient, as the flow rate can be interpreted differently in furnace tubes with different sizes. We have found that a minimum flux of 7×10^{-6} mol/m^2.s is required for growing continuous monolayer films. Below this value, there was an incomplete coverage of the film indicating that the rate of delivering sulphur does not keep up with the rate of sulphur consumption.

In light of the findings in the previous section and optimization of the growth conditions by varying the condition for mass transport of Mo and sulphur in our system, we next studied the effect of the growth temperature on grain size distribution and nucleation density. We have found that full coverage monolayers can be grown in the temperature range 650°C to 850°C, with a maximum possible grain size up 79740±9670 μm^2, and a minimum nucleation density of 82-50 mm^{-2} in the temperature window 800 °C-850 °C. Based on our finding, this temperature window is therefore recommended when using MoO_2 as starting material. Furthermore, we have found that, in the case of steady state monolayer growth, a Mo vapor pressure of 10^{-11} atmosphere is required for all growth temperatures.

We studied the growth of monolayers in three different regimes: the reaction limited regime, the mass transport limited regime and the desorption limited regime. Based in our findings, at temperatures of 650 °C ≤ T<800 °C, the growth is in the reaction limited regime. At temperatures of 800 °C ≤T ≤ 900 °C, we have the mass transported regime and at temperatures of 900 °C≤T≤1000 °C, growth is in the desorption or thermodynamic controlled regime. We could not grow the monolayers beyond 1000 °C, as the system is controlled by rapid desorption of starting materials from the substrate before the reaction occurs.

To find the growth rate of individual grains, we limited the growth time to only one minute and investigated the growth at temperatures of 700 °C-1000 °C. We have found that the growth rate is proportional to the temperature up to 900 °C at which the growth rate is 710±260 μm^2/s. Beyond 900 °C the growth rate is reduced and this expected as we are in the desorption limited regime. We also

found that the optimum growth temperature is 800 °C because at higher temperatures, the growth of bilayers starts to appear even for a one minute growth.

We also studied the effect of growth time on the coverage of monolayer growth. For all temperatures, the optimum growth time that can produce full coverage monolayers is found to be 15 minutes. When the growth time is increased to 20 minutes, nucleation of the bilayers is observed, indicating that the nucleation rates of monolayers and double layers are different. Our monolayer growth explores this difference. If this difference is due to different substrates for the nucleation (SiO_2 for monolayer and MoS_2 for multi-layer), then we expect that multilayer growth follows the start of the bilayer. This seems to be observed.

Finally, we used the growth temperature and sulphur vapor pressure in the reaction zone to switch chemical potential of sulphur for controlling the morphology of MoS_2 monolayers. We have produced bent triangles, perfect triangles and hexagons in a reproducible manner.

From the above discussion, we can conclude that by changing the growth parameters such as sulphur flux, MoO_3 concentration, gas flow and growth temperature we can switch our system to different growth regimes. At low temperatures of 650 °C ≤ T < 800 °C the system is controlled by the surface kinetics, *i.e.* by active species absorbed by the substrate (S and MoO_2 in our case), the reaction of MoO_2 and sulphur and the mobility of the active species on the substrate surface. The low mobility leads to short diffusion length which limits the grain growth rate and size. At moderate temperatures of 800 °C ≤ T ≤ 900 °C, the growth is controlled by the reactant supply (Mo and sulphur). At this temperature window, the residence time of S and MoO_2 on the substrate is very short and their mobility and reactivity are high. The high mobility of the species allows them to travel long distances and add at the growing edges of 2D flakes, causing high growth rates and low nucleation probability. Both are favorable for the growth of large grains. Further increases in the temperature to 900 °C ≤ T ≤ 1000 °C and the growth is controlled by the thermal stability of the MoS_2 monolayer, leading the growth to be thermodynamically controlled rather than kinetic controlled. For example, the chemical potential of sulphur becomes very low such that the sulphur prefers to be in the gas phase rather than as a solid. The low chemical potential of sulphur also causes the fast growing S-rich zigzag edge

growth rate to slow down and to be comparable to Mo-rich zigzag edges, changes the final morphology of MoS_2 grains to hexagon with Mo and S edge terminations.

All in all, in this chapter, we tried to answer five basic questions about the CVD growth of the MoS_2 monolayers. Our answers come through studying the effect of growth parameters such as reactant concentrations, temperature, carrier gas flow rate on the uniformity, continuity, grain size and morphology of the polycrystalline MoS_2 monolayer films. Our findings provide an unprecedented approach for growing wafer scale uniform monolayers that could be scaled up for industrial mass production. They also shed light on the growth mechanics involved.

Chapter 6: MoS_2/MoO_2 nanostructure growth

Abstract

In this chapter we present an alternative approach for growing MoS_2 films on a wafer scale. The approach is based on using MoO_3 as the Mo source. MoO_3 has a much higher vapor pressure than MoO_2 at the same growth temperature. This enables us to tune the S:Mo ratio to a value that is not possible with MoO_2. Since MoO_2 has a very low vapor pressure, the system is always under sulphur rich conditions. By tuning the supersaturation by varying the S:MoO_3 ratio, different structures such as laterally aligned MoS_2 monolayers, MoO_2 and vertically aligned MoS_2/MoO_2 are produced. COMSOL is used for fluid dynamics simulations and the concentration of MoO_3 and S in each growth run is comprehensively analysed and the growth mechanisms of the film growth is discussed. The growth of different structures is confirmed using XRD.

6.1 Literature review

Molybdenum trioxide (MoO_3) is one of the most extensively studied Mo sources and it has been used in growing MoS_2 films. Before monolayer of TMDs came to existence, this precursor had been used for growing MoS_2 nanoparticles and nanotubes [147]. In the pioneer experimental report for monolayers in 2012, Yi-Hsien Lee *et al.* used MoO_3 to grow laterally aligned triangular shape MoS_2 monolayers and multilayers using CVD. Afterwards, MoO_3 become the main Mo source in CVD growth of MoS_2 monolayers [148]. Beside growth of laterally aligned MoS_2 monolayers, MoO_3 has been used in producing vertically aligned MoS_2/MoO_x flakes [149].

The MoO_3 vapor pressure is given by the following empirical relations [150] for 600 °C ≤ T ≤ 795 °C :

$$4.576 \log P(MoO_3)_n = -\frac{75400}{T} + 62.3 \qquad 6.1$$

For 795 °C <T ≤ 1155 °C:

$$4.576 \log P(MoO_3)_n = -\frac{35200}{T} + 24.6 \qquad 6.2$$

where *P* is pressure in atm. and *T* is temperature in K.

When using MoO_3 and S as starting material, the growth protocol is as follows: the MoO_3 and S are placed in an appropriate place where the

temperatures are high enough for their evaporation. Usually S is placed in the upstream and MoO_3 is placed in the downstream. The S is transported by the carrier gas to the reaction zone and MoO_3 vapor is partially reduced by sulphur to MoO_{3-x} and deposits on the substrate as nanoparticles [151]. The possible kinetics as result of MoO_3 and S reaction are [152]:

$$MoO_3 + \tfrac{x}{2}S \rightarrow MoO_{3-x} + \tfrac{x}{2}SO_2 \qquad 6:3$$

$$MoO_{3-x} + \tfrac{7-x}{2}S \rightarrow MoS_2 + \tfrac{3-x}{2}SO_2 \qquad 6:4$$

For a value of x = 1, the reaction proceeds as follows [147]:

$$MoO_3 + \tfrac{1}{2}S \rightarrow MoO_2 + \tfrac{1}{2}SO_2 \qquad 6:5$$

The growth of undesired MoO_2 is possible at high MoO_3 concentrations used in the CVD as we will discuss in the rest of this chapter.

Although the growth mechanisms of MoS_2 using MoO_{3-x} and S are still not fully understood, two possible routes are being proposed: (1) The MoO_{3-x} species diffuse to the substrate and further react with sulphur to form MoS_2; (2) The MoO_{3-x} and S might fully react in the gas phase, and the resulting MoS_2 clusters adsorb, and nucleate on the substrate. The two routes are shown in figure 6:1a.

The partial pressure of MoO_3 and S can be controlled by the temperature which subsequently governs the adsorption and surface-bound reactions on the substrate. According to the ternary Mo–O–S phase diagram shown in figure 6:1b, poor sulphur conditions result in low-valence-state oxide or oxysulphide nanoparticles, thus preventing the direct formation of MoS_2 [153], while sulphur-rich conditions could suppress the volatilization of MoO_3, leading to a low yield of monolayer growth. Therefore a moderate sulphur environment is recommended during the monolayer growth [151].

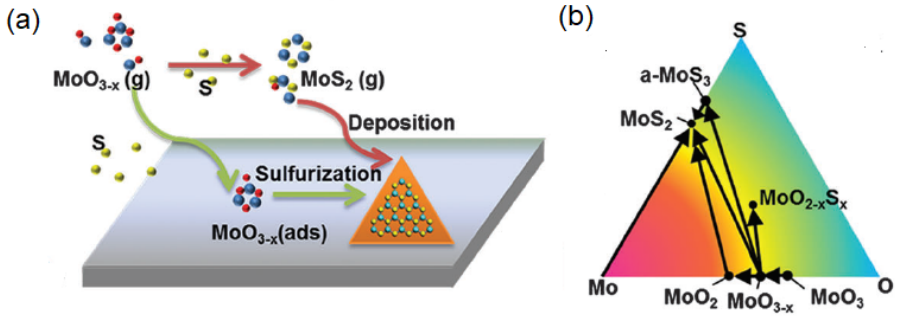

Fig. (6:1):(a) Possible growth processes of MoS_2 by the reaction of MoO_{3-x} and S. (b) The Mo–O–S ternary phase diagram, in which the labelled arrows indicate reaction pathways for the CVD growth of MoS_2 from MoO_3 precursors [151].

6.2 Experimental investigation

The experimental work with MoO_3 as one of the starting materials for growing MoS_2 monolayers started with a rectangular duct with walls as shown in figure 6:2 and a rectangular duct with pillars (see fig. 6:3). The duct is made of a molybdenum foil with a thickness of 0.1 mm and purity of 99.99% (Sigma Aldrich). The MoO_3 powder was spread on the bottom surface of the duct and the SiO_2/Si substrate placed on the top of the duct, facing down to the MoO_3 powder. The duct height was varied between 1-5 cm and the duct was placed in the center of the tube furnace. The sulphur powder was placed in a ceramic boat and loaded into the upstream of the furnace in a place where the temperature reaches 200 °C.

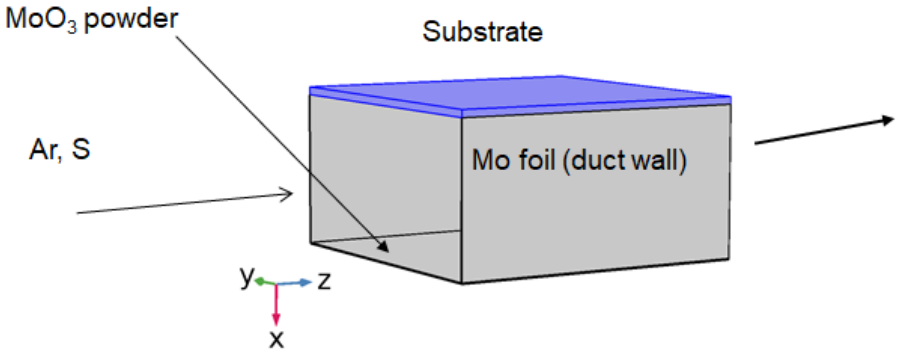

Fig. (6:2): Rectangular duct for MoS_2 growth.

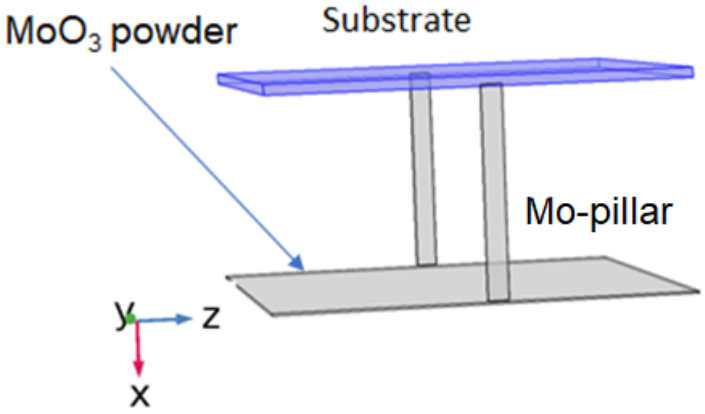

Fig. (6:3): Duct with pillars for MoS_2 growth.

6.3 Results and Discussion

6.3.1 Effect of non-uniform MoO_3 concentration on the grown film

In our preliminary work, we used ducts with walls. We found that, as a result of the walls, the MoO_3 arriving of the substrate is not uniform, resulting in the non-uniform film growth. Figure 6:4a is a photograph of the film using a duct with walls. There is a clear color change from the center to the edges. This color change is due to thickness changes in the film as will be shown in a series of SEM images. To overcome the concentration nonuniformity on the substrate, we designed ducts without walls. The duct is designed such that it leaves very thin pillars in the middle for fixing the substrate. Figure 6:4b is a photograph of the films grown using the duct with pillars. It is obvious from the color change that the film is much more uniform compared to the duct with walls. The experimental conditions for both cases are the same and as follows: the MoO_3-substrate distance is 1 cm, the growth temperature is 650 °C, and the Ar flow rate is 200 SCCM.

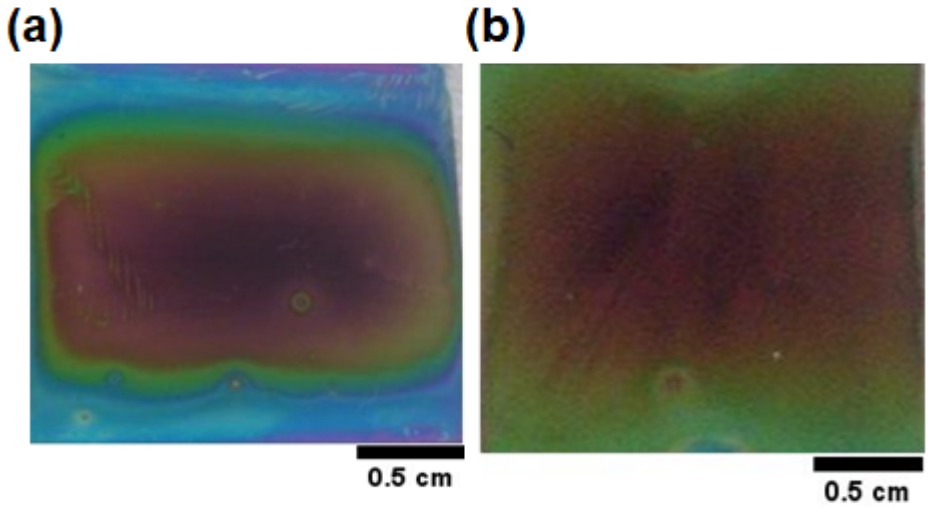

Fig. (6:4): Optical image of MoS_2-MoO_2 film grown using a duct with (a) walls (b) pillars.

Figure 6:5 (a-f) shows a series of SEM images taken from the edge of the sample grown with the duct with walls. They clearly demonstrate thickness nonuniformity as well as morphology changes. At the edge of the sample, isolated MoS_2 monolayer grains are observed. Toward the center, there are a number of different MoO_2 and MoS_2/MoO_2 structures whose crystalline structure will be analysed later using the XRD technique.

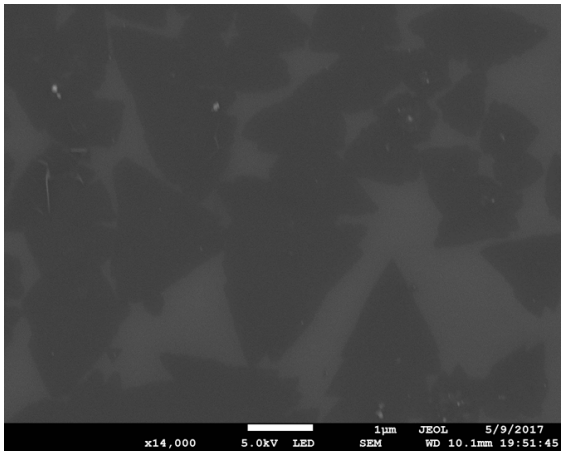

Fig. (6:5a): Edge of the sample MoS_2 monolayers.

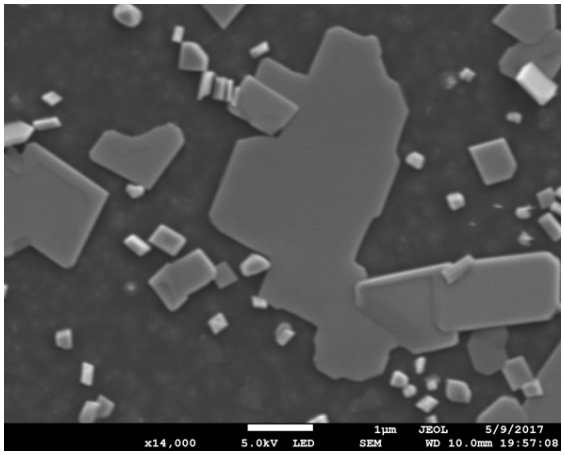

Fig. (6:5b): 1 mm from the edge, MoO_2 crystals.

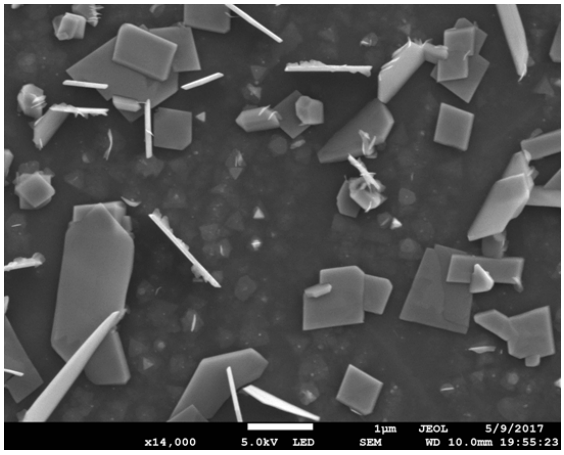

Fig. (6:5c): 2 mm from edge, MoO_2 crystals and vertically aligned MoS_2/MoO_2

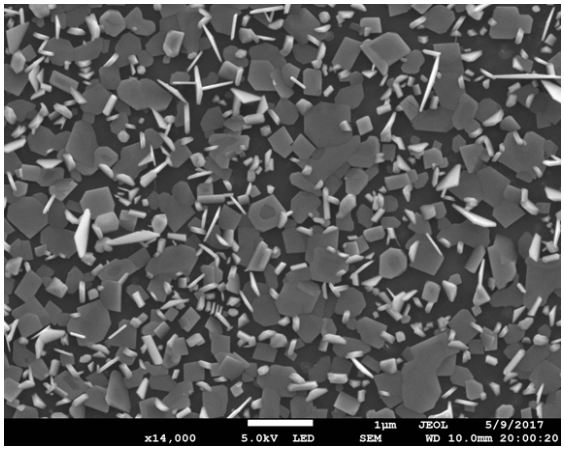

Fig. (6:5d): 2.5 mm from edge, MoS_2 film and vertically aligned MoS_2/MoO_2.

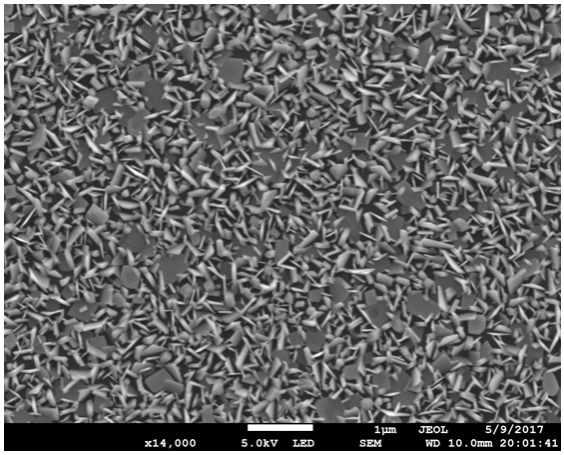

Fig. (6:5e): 3 mm from edge, mostly vertically aligned MoS_2/MoO_2.

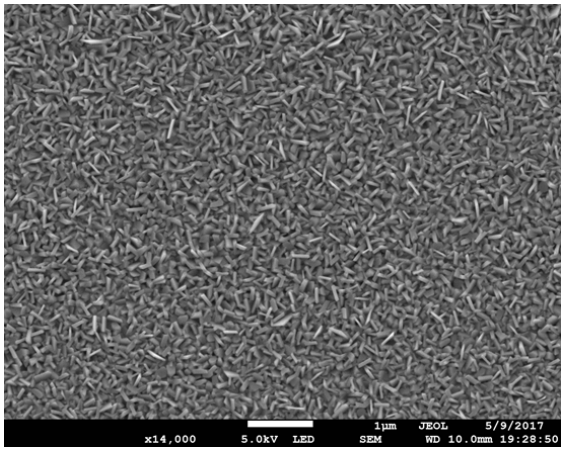

Fig. (6:5f): 4 mm from edge, vertically aligned MoS_2/MoO_2.

Regarding the duct with pillars, the film shows more uniformity all over the the substrate. Only MoS_2/MoO_2 crystals are grown as shown in the following SEM images (Fig. 6: (a-d)).

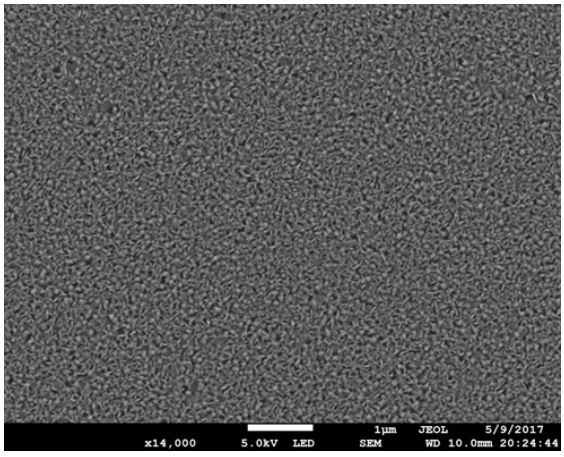

Fig. (6:6a): Edge of the sample, vertically aligned MoS_2/MoO_2.

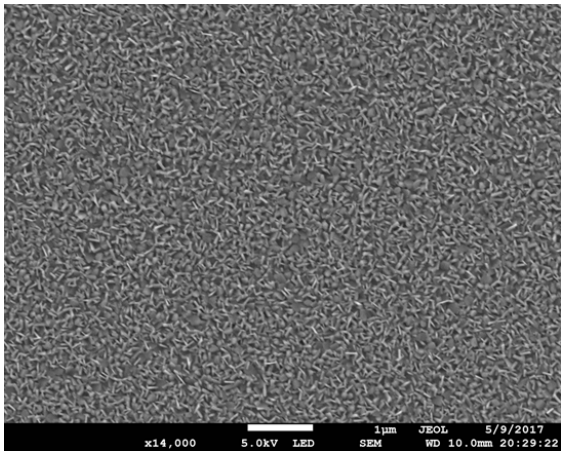

Fig. (6:6b): 1 mm from edge, vertically aligned MoS_2/MoO_2.

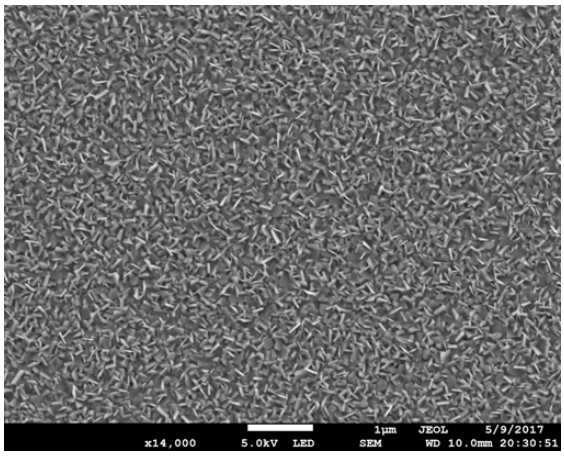

Fig. (6:6c): 2 mm from edge, vertically aligned MoS_2/MoO_2.

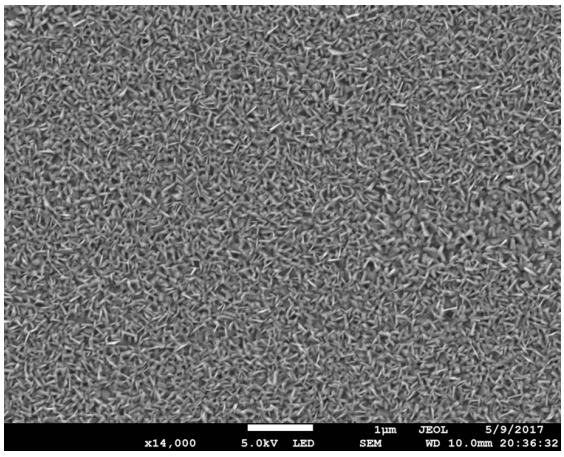

Fig. (6:6d): 4 mm from edge, vertically aligned MoS_2/MoO_2.

To understand the non uniformity of the film growth, we used COMSOL simulations for finding the MoO_3 concentration profile on the substrate in both mentioned cases. In the case of the duct with walls, MoO_3 reacts with S and deposit on the duct walls causing a concentration gradient. Because we do not know the experimental reaction rate on the walls, we used a reactive sticking coefficient of 1. Quantitatively, this figure of sticking coefficient may be very crude, but qualitatively it will be helpful to understand the changes in the MoO_3 concentration profiles. Figures 6:7(a-c) show the MoO_3 concentration profile on the substrate when using the duct with walls with a sticking coefficient of 1 and zero

and the duct with pillars, respectively. Figures 6:8(a-c) are the corresponding cross-sectional concentration profiles. Figure 6:9 is a plot of the concentration profile on the substrate in the three cases.

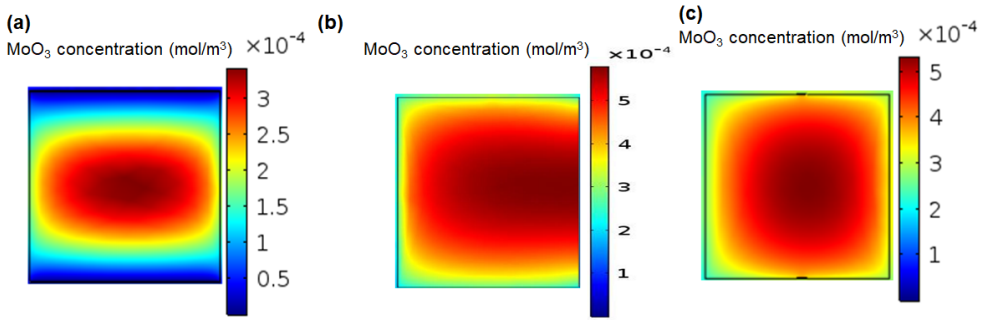

Fig. (6:7): MoO_3 concentration profile on the substrate when using a duct with (a) walls sticking coefficient of one, (b) wall sticking coefficient of zero (c) pillars.

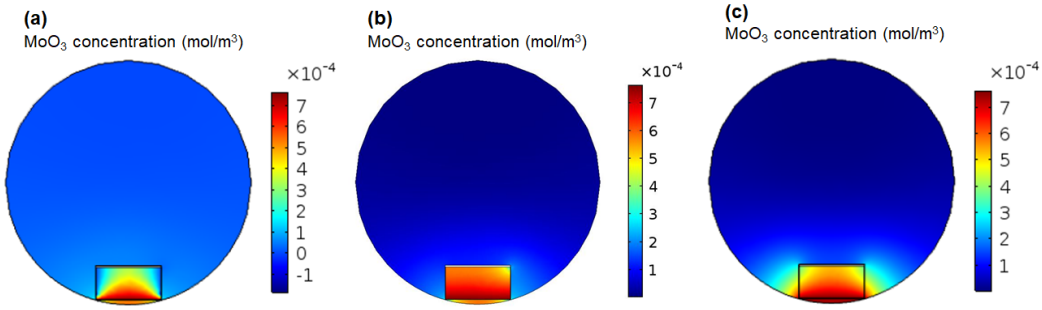

Fig. (6:8): Cross-sectional view of MoO_3 concentration profile in the center of the reaction zone when using duct with (a) wall sticking coefficient of one (b) wall sticking coefficient of zero (c) pillars.

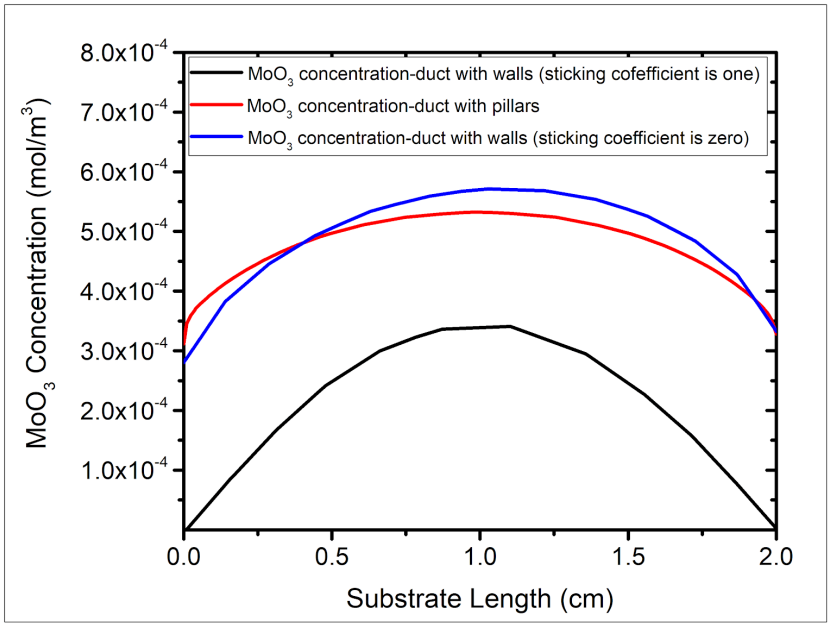

Fig. (6:9): MoO_3 concentration profile on the substrate in the three cases :duct with walls with a sticking coefficient of one and zero, and a duct with pillars.

The duct wall before and after deposition is shown optically in figure 6:10 (a-b) with a clear sign of deposition after the experiment run.

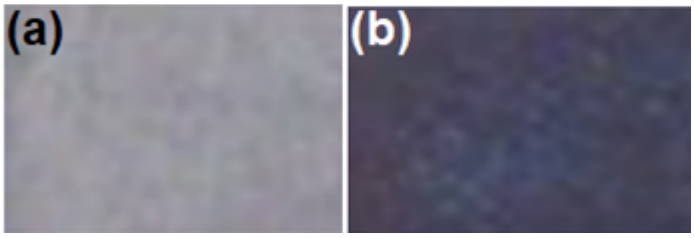

Fig. (6:10): Duct walls (a) before and (b) after deposition.

The configuration in which a duct or a boat with walls is placed with the substrate facing down on the MoO_3 powder is the most commonly used one in CVD of TMDs [138], [154]–[157]. Our experimental and simulation results have shown that this configuration will result in MoO_3 concentration nonuniformity on the substrate which in turn causes nonuniformity in the film grown. To overcome this problem we suggest designing ducts with pillars in TMDs CVD growth.

6.3.2 The effect of MoO_3 concentration on the film growth at constant temperature

Here we study the effect of MoO_3 concentration on the structure and morphology of the grown film. The concentration is changed by changing the vertical distance between the Mo source and the substrate. To avoid deposition on the MoO_3 container walls, we use a duct with pillars as shown in figure 6:3. In typical experimental procedure, 5 mg of MoO_3 powder was loaded in the duct and the duct is placed in the center of the reaction zone of our furnace. A ceramic boat containing 10 mg of sulphur was placed in the upstream of the tube furnace in a position where the temperature reaches 200 °C. Prior to the growth, the furnace was flushed with argon gas (at 1000 SCCM) for about 30 minutes. Then the furnace was pumped down to 10 mbar and the center part of the tube wall was heated to 650 °C with a heating rate of 15 °C /minute in an argon flow (at 200 SCCM). After keeping the temperature at 650 °C for 15 minutes, the furnace was naturally cooled down to room temperature. The temperature of the sulphur source also rises, roughly inline with the temperature profile at the centre of the tube furnace, reaching an average of 200 °C during the 15 minutes when the sample is at the growth temperature. Figures 6:11(a-e) show SEM images of the films grown on substrate whose vertical distances from the MoO_3 source are 1-5 cm

respectively. At 1-3 cm vertical distance, the film consists mostly of MoS_2/MoO_2 grains grown vertically. At 4 cm vertical distance, some planner MoO_2 crystals start to be observed on a continuous MoS_2 multilayer background. A complete coverage of multilayer MoS_2 film is only obtained at a distance of 5 cm. The characterization of those films will be discussed later on in this chapter.

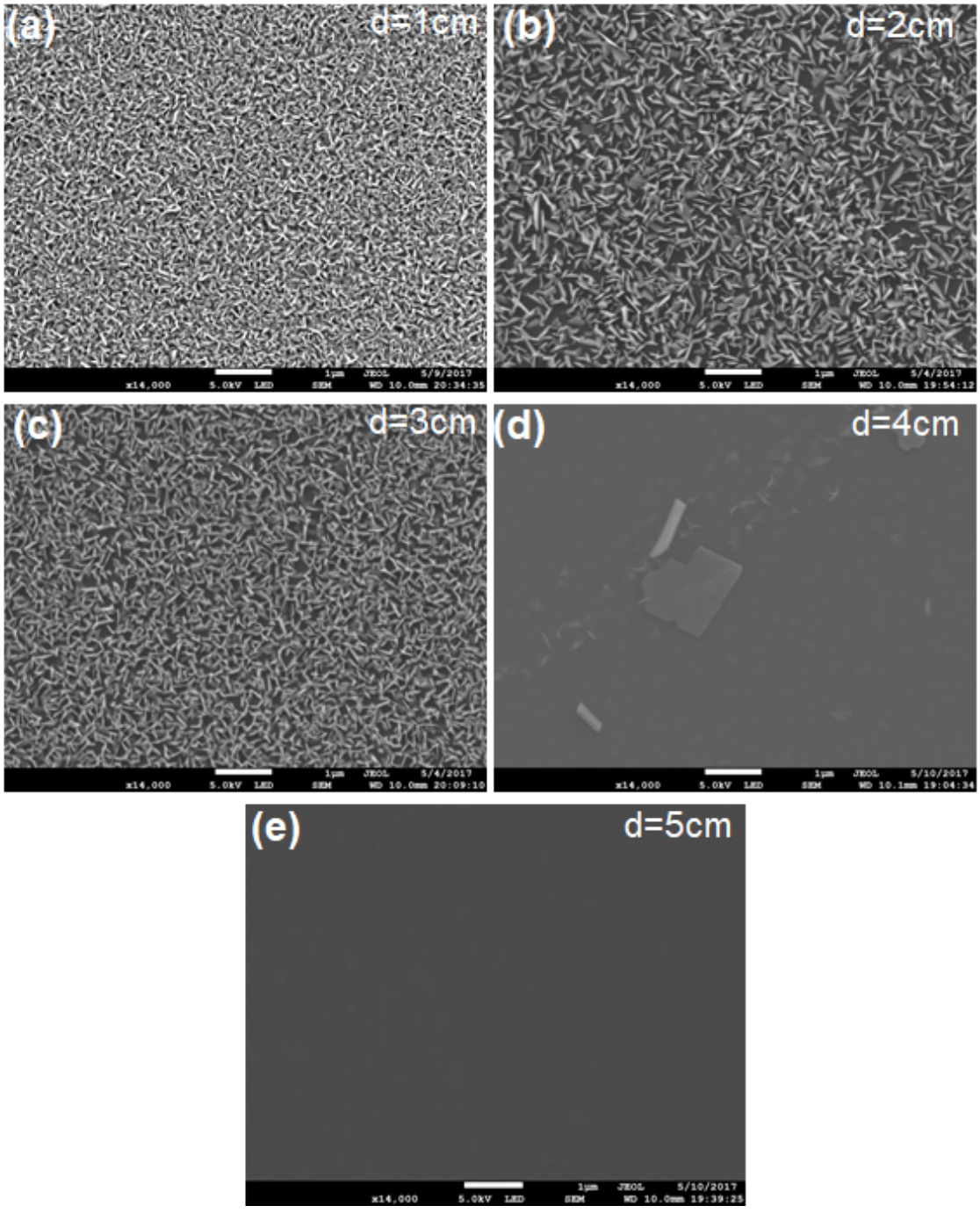

Fig. (6:11): SEM images of MoS_2-MoO_2 films grown at T=650 °C and MoO_3-substrate vertical distances of (a) 1 cm (b) 2 cm (c) 3 cm (d) 4 cm and (e) 5 cm.

The (COMSOL calculated) concentration profile of MoO_3 on the substrate is shown in figure 6:12 as a function of vertical distance. It can be seen that the

concentration is uniform across the substrate. At 1 cm, the average concentration 4.41 $\times 10^{-4}$ mol.m^{-3}, much higher than what is essential to grow MoS_2 monolayers. Instead, vertically aligned MoS_2 /MoO_2 grains are grown. At 2 and 3 cm, the concentration is reduced to 2×10^{-4} mol.m^{-3} and 7.4×10^{-5} mol.m^{-3} respectively and the films still have the same structure as in the previous case. At a concentration of 2×10^{-5} mol.m^{-3} (4 cm vertical distance), no further vertically aligned grains are seen and laterally-aligned MoO_2 crystals on a continuous MoS_2 film are grown. A continuous multilayer MoS_2 film is deposited at a concentration of 7.4 $\times 10^{-6}$ mol.m^{-3} (5 cm vertical distance).

We have seen that at a constant growth temperature of 650 °C, a vertically aligned MoS_2/MoO_2 grains can be grown in the MoO_3 concentration range from 4.41×10^{-4} mol.m^{-3} to 7×10^{-5} mol.m^{-3} and multilayer MoS_2 is realized at a MoO_3 concentration of 7.4×10^{-6} mol.m^{-3}.

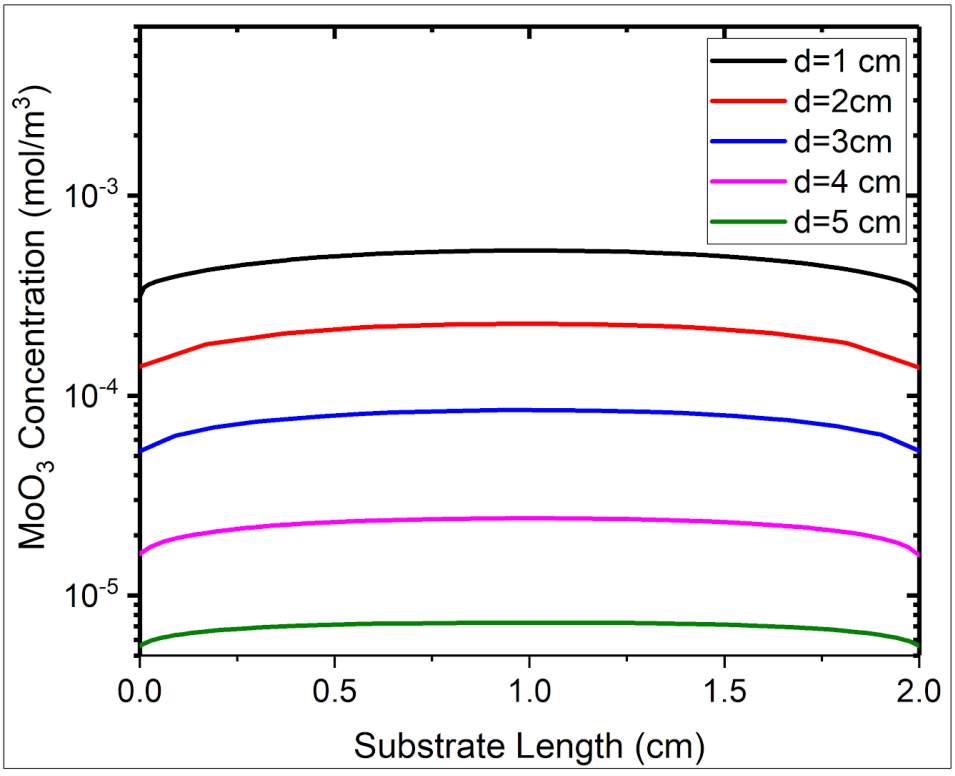

Fig. (6:12): Calculated MoO_3 concentration on the substrate as a function of vertical distance at a growth temperature of 650 °C.

6.3.3 The effect of MoO_3 concentration on the film growth at different growth temperatures

In this section we present the effect of temperature on MoO_3 concentration and the structure of the grown films. The experimental procedure is as presented in 6.3.2 except we kept the substrate at a vertical distance of d=5 cm and we changed the growth temperature from 650 °C to 800 °C by increments of 50 °C. The sulphur concentration at the substrate for all growth temperatures is estimated by COMSOL to be 0.02 mol/m^3. Figure 6:13(a-d) are SEM micrographs of the films grown at 650 °C, 700 °C, 750 °C, and 800 °C, respectively.

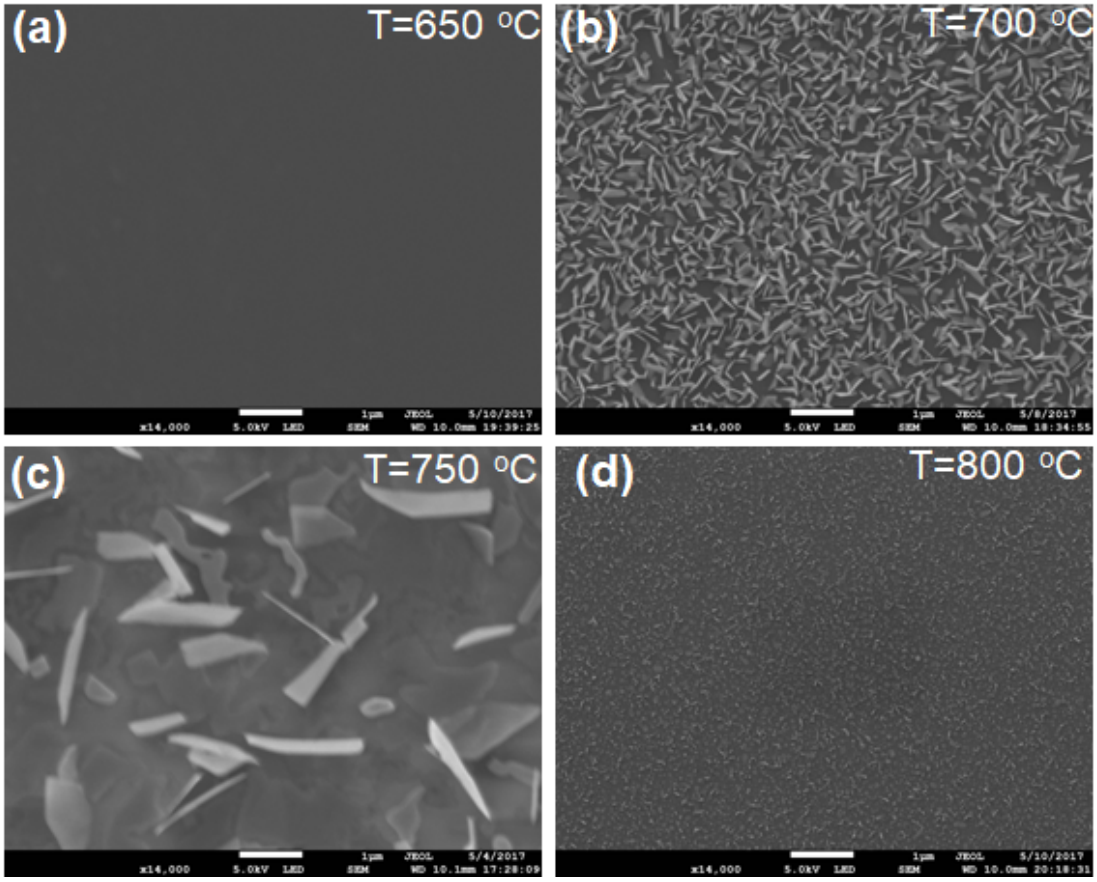

Fig. (6:13): SEM images of MoS_2-MoO_2 films grown at (a) 650 °C (b) 700 °C (c) 750 °C and 800 °C.

The concentration profile of MoO_3 at different growth temperatures on a substrate placed at a vertical distance of 5 cm is shown in figure 6:14 below.

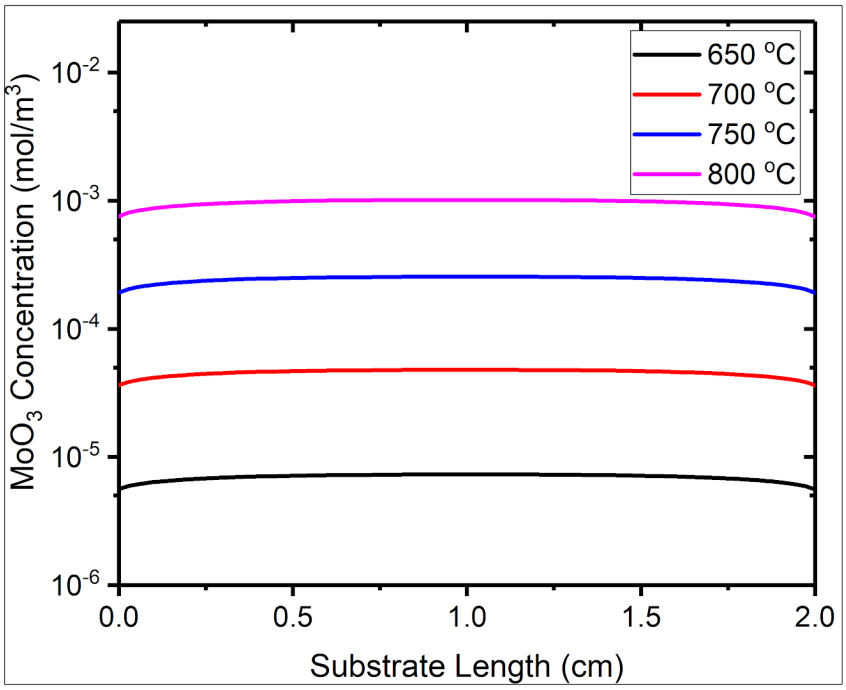

Fig. (6:14): MoO_3 concentration profile at different growth temperatures on a substrate placed at a vertical distance 5 cm.

The composition and morphology of the films shown in figures 6:12a-d will be discussed in the next section as investigated using XRD.

6.3.4 Film characterization using XRD and TEM

The XRD measurements were performed using a Rigaku SmartLab diffractometer (*Cu Kα1* wavelength=1.5405 Å) and θ/2θ scan Bragg Brentano geometry (as explained in fig. 3:12).

The results for the films grown at 650 °C, 700 °C, 750 °C and 800 °C are shown in figures 6:15-6:18 respectively.

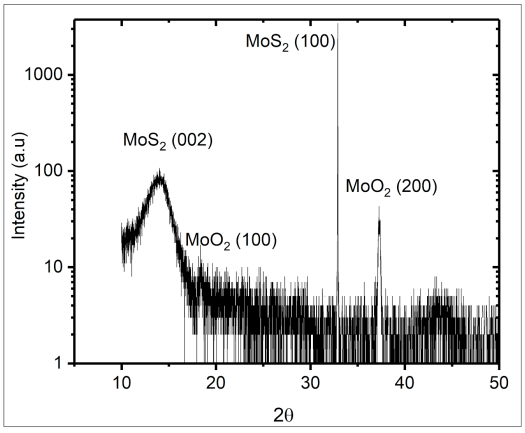

Fig. (6:15): XRD data for a film grown at T=650 °C.

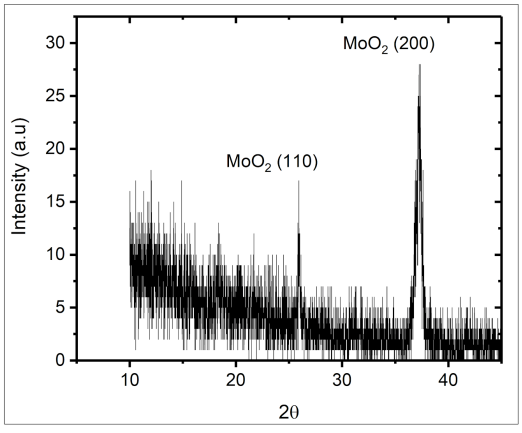

Fig. (6:16): XRD data for a film grown at T=700 °C.

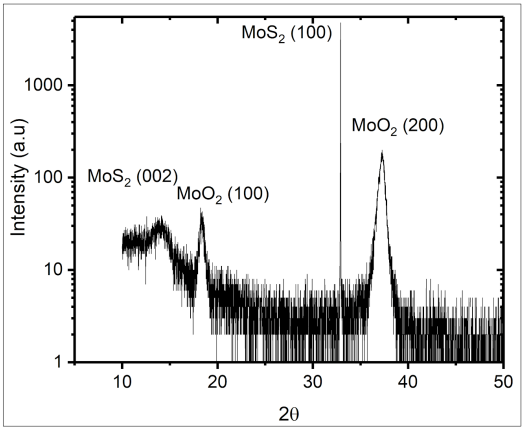

Fig. (6:17): XRD data for a film grown at T=750 ºC.

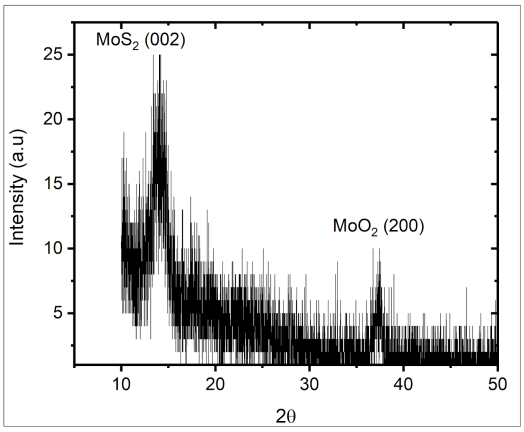

Fig. (6:18): XRD data for a film grown at T=800 ºC.

XRD data from different growth temperatures indicate the coexistence of MoS_2 and MoO_2 in the samples and there is no sign for unreacted MoO_3. This means that MoO_3 is partially reduced by sulphur to MoO_2 or fully reduced to MoS_2. The presence of the MoS_2 (002) peak confirms that the MoS_2 structure is multilayer as no such peak should be observed in the case of monolayer growth (experimentally it is indeed hardly detected) [48]. The sharpness of the (002) MoS_2 reflection also means that the crystallites are large in the c-axis dimension. The presence of the MoS_2 (100) peak confirms that there are vertically aligned MoS_2 grains. The MoS_2 (100) plane is perpendicular to the basal plane (001) and in our scanning geometry such a peak can not be detected unless there is vertically aligned grains. The observation of a MoO_2 (200) peak indicates that the MoO_2 crystals are monoclinic with the orientation relationship of MoO_2(100) parallel to the substrate surface. The presence of a MoS_2 (100) reflection and a MoO_2 (200) reflection suggests that the vertically aligned grains are not pure MoS_2 but MoO_2 wrapped by MoS_2 *i.e.* the grain core is MoO_2 and the shell is MoS_2. This result agrees with those reported in the literature [158], [159] indicating that those grains are firstly grown as MoO_2 and then the shell is sulphurized to MoS_2. The sulphurization of the MoO_2 crystals is further confirmed using TEM. Figure 6:19(a-b) show TEM images of two typical vertically standing MoS_2/MoO_2 crystals showing the MoS_2 shell. The interlayer distance of MoS_2 flakes was ~ 0.62 nm which corresponds to the (002) crystal plane of the MoS_2 nanosheets.

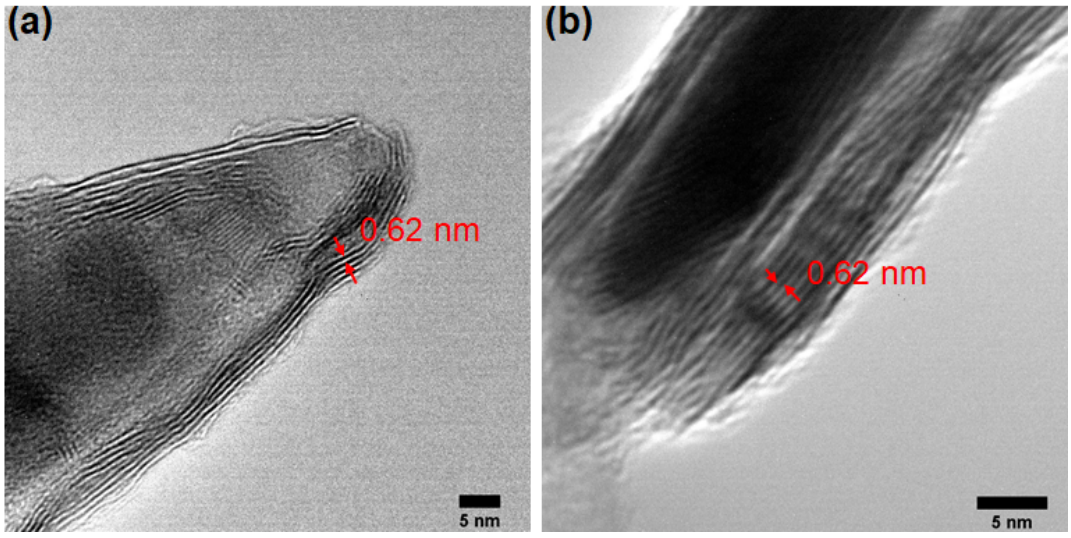

Fig. (6:19): (a-b): TEM image of typical MoS_2/MoO_2 crystals showing MoS_2 planes at the edges.

6.4 The effect of S/MoO_3 ratio on the film growth mechanisms

In this section, we study the effect of S/MoO_3 concentration ratio on the grown fim. For this purpose we used growth temperatures of 650 °C - 700 °C, the sulphur concentration is set to 0.02 mol/m^3 and the MoO_3 is changed by varying the vertical distance between the MoO_3 and substrate.

In contrast to using MoO_2 which always led to growth of MoS_2 monolayers (nothing but monolayers) as studied in the previous chapter, using MoO_3 as the Mo source, and based on our experimental result, we can classify the CVD growth products in to three different types: planar MoS_2 monolayers, vertically aligned MoS_2/MoO_2 crystals and planar MoO_2 crystals, as shown in figure 6:20 a-c respectively. Our results agree with those reported in the literature [152], [160], [161].

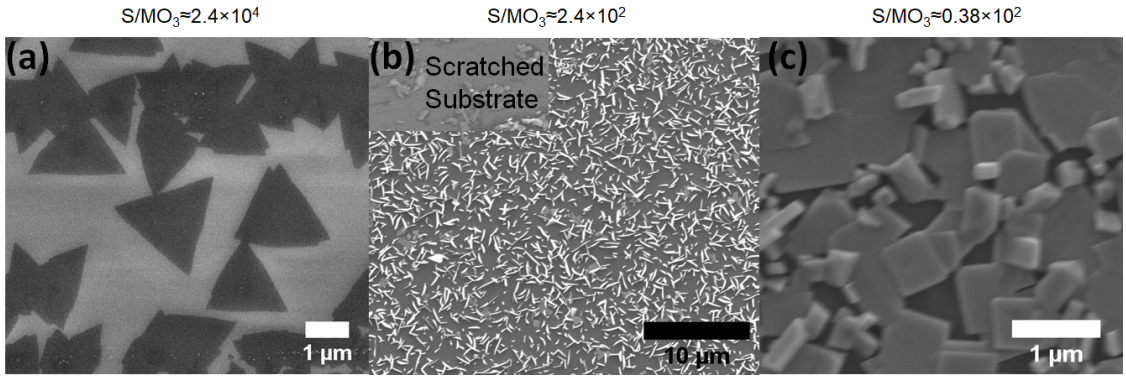

Fig.(6:20): MoS_2-MoO_2 structures grown at 650 °C, (a): MoS_2 monolayers, (b): vertically aligned MoS_2/MoO_2 crystalts, (c): planar MoO_2 crystals.

The growth of monolayers (Fig. 6:20a) is only possible at the very diluted MoO_3 concentration limit ($MoO_3 \lesssim 8.45\times10^{-7}$ mol/m^3, $S/MoO_3=2.4\times10^4$) *i.e.* at a MoO_3 partial pressure of 6.4×10^{-8} atm. A similar value of $Mo(CO)_6$ 1.3×10^{-7} atm. is found to be crucial to grow MoS_2 monolayers using MOCVD [47], however the experimental time required for MOCVD to achieve monolayers is 26 hr which is much longer than our typical growth run of 15 minute indicating that $Mo(CO)_6$ has a much lower reactive sticking coefficient than MoO_3 [47]. Increasing the value of MoO_3 vapor pressure to 6.4×10^{-6} atm ($S/MoO_3= 2.4\times10^2$), vertically aligned MoS_2/MoO_2 crystals are observed as shown in figure 6:20b. At a high MoO_3 vapor pressure of 4×10^{-5} atm and in a weakly reducing atmosphere ($S/MoO_3=0.38\times10^2$), the growth of planar MoO_2 was observed as shown in figure 6:20c. This observation agrees with our previous results in chapter five when using MoO_2 as Mo sources under poor sulphur conditions as shown in figure 5:47.

Figure 6:21 summarize the effect of $S:MoO_3$ ratio on the film composition at a typical growth growth temperature 650 °C.

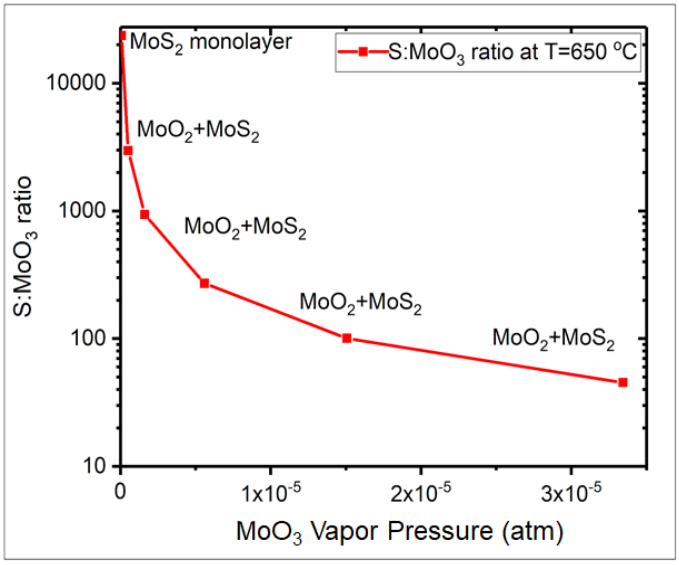

Fig. (6:21): Film composition at different $S:MoO_3$ ratios at a growth temperature of 650 °C.

It has been assumed that the vertically aligned MoS_2/MoO_2 structures are formed via mechanical collision or distortion of planar MoS_2 islands [146]. However, this assumption is invalid here as we have found growth of MoS_2/MoO_2 on bare substrate as shown in figure 6:22.

Figure 6.22 shows the edge area of a sample grown at 700 °C. The image shows partially covered planar MoS_2 monolayers, vertically aligned MoS_2/MoO_2 structures and the initial stages of MoS_2/MoO_2 structures .

As one can see in figure 6:22 (blue arrow), the MoS_2/MoO_2 structures first nucleate as a nanowire and grow in the vertical direction. Our XRD data confirmed that the shell of such vertically aligned structures is MoS_2 and the core is MoO_2. Based on this, we can assume that under high MoO_3 partial pressures (2×10^{-7} atm), those structures in the early stages are pure MoO_2, and that MoO_2 keeps growing in the vertical direction, while, simultaneously the shell is sulphurized into MoS_2.

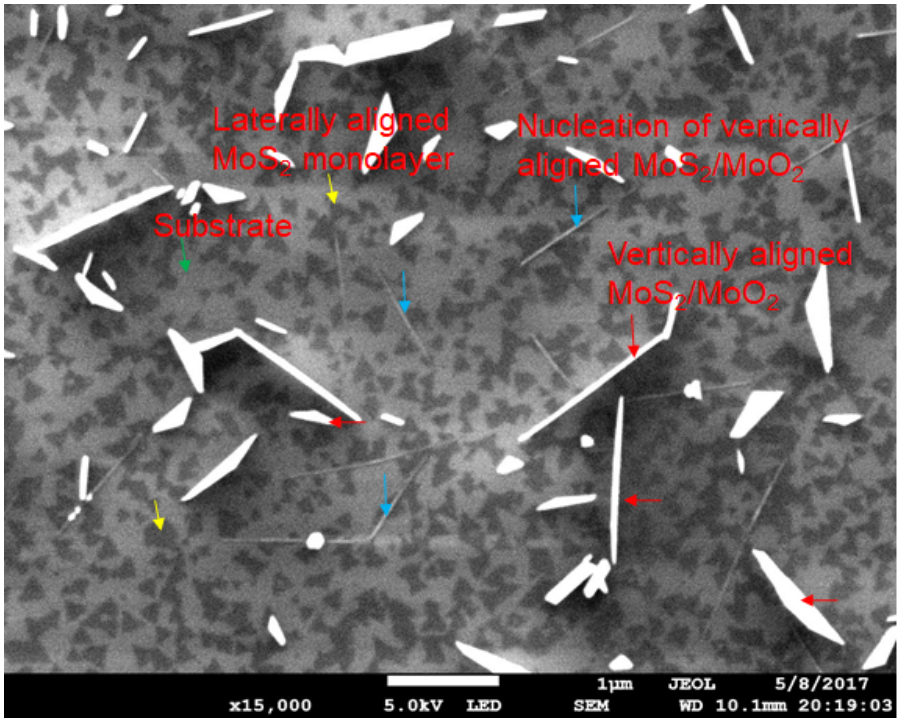

Fig. (6:22): Partially covered planar MoS_2 monolayers, vertically aligned MoS_2/MoO_2 grains and nucleation of the vertically aligned MoS_2/MoO_2 grains.

6.5 Conclusion

In this chapter we have introduced an LPCVD approach using MoO_3 as the Mo source for growing wafer scale planar MoS_2 monolayers and vertically aligned MoS_2/MoO_2 crystals.

In our preliminary work, we used a MoO_3 container with walls, observing that such a container design resulted in a nonuniform growth of the film on the substrate. Such nonuniformity is due to the deposition of Mo structures on the

container walls causing a concentration gradient on the substrate such that the concentration on the substrate edges is much lower than the center. The variation of the MoO_3 concentration is confirmed using COMSOL simulations. To overcome this problem we removed the container walls leaving very thin pillars (1 mm) to fix the substrate face down to the MoO_3 powder. Such a design resulted in more uniform films and again the MoO_3 concentration profile become more uniform.

There are typically two types of designs when growing 2D materials using powders as transition metal sources. The first one is by placing the substrate face down on the transition metal compound container and the second one by placing the substrate downstream in the CVD tube at a certain distance from the container. In both cases the deposition on the walls (container walls in the first case and CVD tube walls in the second case) is unavoidable. Therefore, for better uniform growth, the substrate placed face down on the powder container having no walls is recommended.

After solving the problem of the design, we studied the effect of concentration of MoO_3 and S/MoO_3 ratio on the film growth. The concentration of the gaseous species can be controlled by the temperature of S and MoO_3 or by changing the the distance between the substrate and the source powder. At a constant growth temperature of 650 °C and a constant sulphur concentration of 0.02 mol/m^3, we tuned the MoO_3 concentration by changing the vertical distance between the substrate and MoO_3 powder. We have found that the growth of vertically aligned MoS_2/MoO_2 is dominant at MoO_3 concentrations between 4.4×10^{-4} $mol.m^{-3}$ and 7.4×10^{-5} $mol.m^{-3}$ and the growth of monolayers is only realized at $MoO_3 \lesssim 8.45\times10^{-7}$ mol/m^3, $S/MoO_3=2.4\times10^4$ while the growth of planar MoO_2 grains is achieved at high MoO_3 concentration 2.6×10^{-4} mol/m^{-3} and poor sulphur conditions of $S/MoO_3 = 0.38\times10^2$.

We further studied the effect of growth temperature on the film growth by fixing the substrate at a vertical distance of 5 cm above the the MoO_3 powder and changing the growth temperature from 650 °C to 800 °C. Again we tuned the MoO_3 concentration from 7.3×10^{-6} mol/m^{-3}, 4.8×10^{-5} mol/m^{-3}, 2.6×10^{-4} mol/m^{-3} and 1×10^{-3} mol/m^{-3} and S/MoO_3 ratio from 2735, 417,78 and 19 for growth temperatures of 650 °C, 700 °C, 750 °C and 800 °C respectively. Under these conditions we have observed the growth of MoS_2 multilayer films coexisting with vertically-aligned MoS_2/MoO_2 structures which has been confirmed using XRD measurements.

Chapter 7: Conclusion and Future Work

7.1 Conclusion

Monolayer MoS_2 is an ultra-thin 2D semiconductor with a direct band gap of 1.9 eV. It is proposed as a potential candidate for nanoscale electronics and optoelectronic devices [12]. Due to its mechanical flexibility, MoS_2 monolayers could also be integrated in flexible and wearable devices. The broken inversion symmetry monolayer and strong spin-orbit coupling also make monolayers a promising candidate for spintronic, valleytronic and piezoelectric devices [16], [18].

For practical applications of these monolayers, scalable and controlled synthesis of monolayers on a wafer scale is required. Thickness uniformity and grain size are also major concerns for the fabrication of opto-electronic devices.

In this research project, we have focused on establishing an LPCVD approach for scalable synthesis of MoS_2 monolayers using MoO_2 and Sulphur as the starting materials and Si coated with 300 nm of SiO_2 as the substrate and argon as the carrier gas. When growing monolayer crystals, the starting materials can be considered one of the most important parameters affecting the growth.

In the case of MoS_2 monolayer crystals, sulphur has a very high vapor pressure even at relatively low temperatures, therefore it can not be placed in the growth zone with a typical temperature of 800 ^oC. Therefore the sulphur is usually kept upstream in the CVD tube furnace in a place where the temperature reaches about 200 ^oC and the sulphur flux toward the growth zone is controlled by the carrier gas flow rate. This is an economical alternative to the two furnace set-ups being reported in the literature. In case of the Mo source, the situation is different, with the non-toxic Mo sources being Mo oxides such as MoO_3 and MoO_2. These oxides have relatively low vapor pressures and need a higher temperature to produce enough vapor for significant film growth. Therefore, they are usually placed in the growth zone and the substrate is placed downstream a few centimeters away from the Mo source. One of the most challenging issues in the uniform fim growth is delivering a uniform flux of reactant materials across the substrate. The second challenge is that of bringing the growth into a steady state *i.e.* the amount of reactant delivered to the substrate must be equal to the amount

of reactant participating in the monolayer growth. As we have mentioned, the sulphur flux can be controlled by varying the carrier gas flow, so our main task was to find an appropriate Mo source. We have found among the Mo oxides MoO_2 has the lowest vapor pressure. Our experimental results confirmed that the vapor pressure of MoO_2 is low enough to achieve steady state growth in a range of growth temperatures when adapting the design we have mentioned. The third task was to adopt a design for growing scalable monolayer films. This calls for uniform delivery of reactive species. In our design we have placed the substrate face down to the Mo source such that all the generated Mo vapor diffuse relatively uniformly to the substrate.

With the above-mentioned design and MoO_2 as the Mo source, we could grow MoS_2 monolayers on a wafer scale. Our XPS measurements confirmed that a complete conversion to MoS_2 occured as result of reaction between MoO_2 and S in the reaction zone. The AFM measurements showed that the thickness of the grown film is in the monolayer range. SHG images from different parts of the film proved that the film is uniform. Techniques such as Raman spectroscopy, PL measurements, TEM, XRD and GIIXRD showed the high crystalline quality of the films.

We used GIIXRD to study the growth-induced strain in the as-grown monolayers and thermal expansion coefficient of the monolayers. As a result of the thermal expansion mismatch between the MoS_2 monolayers and the underlying substrate, a tensile strain up to 1% was observed in the as-grown monolayer. This value of the strain is comparable with the ones reported in the literature [104]. By in situ annealing of monolayers under UHV conditions, we have found the monolayers are stable up 800 ^{o}C and their thermal expansion coefficient is found to be comparable with that of bulk MoS_2 [107].

We have tested our approach in different growth temperatures and it is found that one can reproducibly grow uniform monolayers in the temperature window of 650 ^{o}C-850 ^{o}C.

Our second goal was to optimize the growth conditions with the help of COMSOL simulations to produce films with the optimum grain size and to understand the film growth mechanisms. For this purpose we have studied the effect of different growth parameters such as MoO_2 concentration, sulphur flux, growth temperature, sulphur chemical potential and growth time on the film growth.

We have related the monolayer coverage to the MoO_2 concentration and sulphur flux. We have tuned the MoO_2 concentration by changing the vertical distance between the substrate and MoO_2 powder. Our results indicated that the full monolayer coverage can be achieved at certain distances where the entire generated Mo flux diffuses to the substrate. We also quantified the monolayer coverage as a function of the sulphur flux, by changing the Ar gas flow rate which subsequently changes the sulphur flux at the reaction zone. We have found that a minimum flux of 7×10^{-6} mol/m^2.s is required for achieving full coverage monolayers. Below this value, the substrate was partially covered with monolayers indicating that our system is in the feed limited-regime with respect to sulphur. At this stage, we have optimum conditions for growing full coverage monolayers.

Next, we used the aforementioned optimum conditions to investigate the effect of growth temperature on the grain size distribution and nucleation density. We have found that a maximum possible grain size of up to 79740±9670 μm^2 can be grown at growth temperatures between 800 °C and 850 °C and that the nucleation density is suppressed to only 82-50 mm^{-2} at the same temperature range. Based on this finding, this temperature window is recommended when using MoO_2 as the starting material.

We further studied the effect of temperature on the film growth, and we have found that the growth can be classified into three distinct regimes with respect to the Mo species. At growth temperatures of 650 °C ≤ T < 800 °C, the growth is in the reaction limited regime, *i.e.* the grain growth rate is temperature dependent. At temperatures of 800 °C ≤ T ≤ 900 °C we have the mass transport regime. In this regime the grain growth rate is weakly temperature dependent. At temperatures of 900 °C ≤ T ≤ 1000 °C, there was the desorption or thermodynamic controlled regime. There is a high desorption rate in this regime and a large fraction of the reactants desorb before the reaction occurs. Beyond 1000 °C, we did not observe any monolayer growth as the growth is completely inhibited by desorption.

To find out the growth rate of individual grains, we limited the growth time to only one minute for a range of growth temperatures from 700 °C to 1000 °C. The growth rate was found to be proportional to the temperature and a peak of growth rate of 710±260 μm^2/s occurred at 900 °C beyond which the growth rate is reduced as the system entered the desorption regime. This follows the classical description of the CVD processes.

For all growth temperatures, we have found the optimum growth time is 15 minutes, beyond which the nucleation of bilayers appeared on the films. This suggests that the growth is layer-by-layer due to the different rates of nucleation on the bare substrate and on the MoS_2 monolayer. We speculate that the tendency for monolayer growth can be enhanced for substrates interacting strongly with MoS_2.

We employed the growth temperature and sulphur partial pressure to tune the sulphur chemical potential and subsequently tune the morphology of the monolayer MoS_2 grains. We have found that triangular shaped monolayer crystals are grown at sulphur chemical potentials of μ_S=-0.834 eV to -0.995 eV, and hexagonal shaped monolayer crystals are produced for μ_S=-1.156 eV to -1.318 eV. As the non-equivalent edges of the hexagonal shaped monolayer crystals can have different catalytic behaviours, the ability to tune the morphology also means that we can potentially tune the chemical reactivity of these crystals.

Finally, we have also compared our approach with an LPCVD approach based on MoO_3 as the Mo source. MoO_3 has a higher vapor pressure than MoO_2 which was previously used. Again, we studied the effect of MoO_3 concentration on the film growth by changing the vertical distance between the MoO_3 and the substrate. Then we studied the effect of growth temperature on the film growth. We could tune the S:MoO_3 ratio, to grow planar MoS_2 monolayer, vertically aligned MoS_2/MoO_2 and planar MoO_2 crystals.

In summary, we have established two LPCVD approaches for growing MoS_2 monolayers. The first approach is used for growing uniform MoS_2 monolayers on a wafer scale and the second approach can be adopted for growing vertically aligned MoS_2/MoO_2 crystals.

7.2 Future work

As we have seen we have developed a standardized approach for growing MoS_2 monolayers over a range of growth temperatures. So far we have used our approach to grow MoS_2 monolayers only. By switching the chalcogen source to selenium (Se) or tellurium (Te), we can expect to grow $MoSe_2$ and $MoTe_2$ monolayers which are also direct band gap monolayer semiconductors. Furthermore, we can employ the existed model to produce more complicated structures such as TMDs heterostructures such as MoS_2-$MoSe_2$ and MoS_2-$MoTe_2$ and TMDs alloys. 2D novel heterostructures have already been prepared which

led to the exploration of numerous exciting physical phenomena and novel nano electronic and optoelectronic applications such as light emitters [162], photodetectors [163] new generation field effect transistors [164], and memory devices [165]. However, 2D heterostructure preparation still mostly depends on the mechanical exfoliation and a scalable method such as CVD is required. We can realize the growth of such heterostructures by switching between the chalcogen sources *i.e.* first, growing partially-covered MoS_2 monolayers and then switching the chalcogen source to Se or Te to grow horizontally-aligned heterostructures or growing the full coverage of film and then switching the chalcogen source to grow vertical stacking heterostructures.

Alloying in TMDs monolayers can be used to tune the band gap of the monolayers. The alloying can be done by annealing the as-grown MoS_2 monolayers in a chalogen rich environment such as Se [166] or by supplying different chalcogen and transitional metal sources to the CVD system [167]. It has been reported that by selenization of MoS_2, the band gap is tuned from 1.85 eV for pure MoS_2 to 1.57 eV for $MoS_{2x}Se_{2(1-x)}$ [166].

Although we have grown films with optimum grain size, the film is still polycrystalline with a large number of grain boundaries that affect the electrical and optical properties of the film. So far we have only employed temperature to get large grain size. Another way to get larger grain sizes and reduce the grain boundary numbers is by epitaxial growth using hBN or graphene as a substrate. In such epitaxial growth the MoS_2 grains are expected to grow in only two prefenced orientations (0^o and 60^o). At the grain boundary the grains have similar orientations and will merge eliminating the grain boundary producing larger grains.

Another approach is growing the monolayers on other substrates rather than SiO_2/Si. SiO_2 is a good substrate, with very small defects that can be responsible for heterogeneous nucleation. Optically, the layer thickness can also be adjusted to make monolayer crystals visible for easy inspection. Well-developed methods exist for transferring the monolayer films to a substrate of interest. However, it does suffer from mismatch of the thermal expansion with MoS_2, resulting in thermal cracks. Alternative substrates with smaller thermal expansion coefficients will be useful for the production of low-stress MoS_2 monolayer films. Crystalline substrates with lattice dimensions comparable with MoS_2 can also be used to study the heteroepitaxial growth of the MoS_2 and investigating the effect of the

lattice mismatch strain induced on the film properties. Using insulating substrates with different dielectric constants, one can tune the optical properties of the MoS_2 monolayers. As we have mentioned in the main text, the optical emission of MoS_2 is excitonic, and the binding energy of the excitons depends on the dielectric properties of the surroundings.

We believe that all the aforementioned proposals are feasible with our current approaches. We might need a slight modification to feed different reactants, but in principle we have developed a framework approach to achieve them.

Our study is also helpful to our understanding of the growth mechanism involved. Our results suggest that growth is consistent with the monolayer growth being activated with nucleation of MoO_2 or related oxide/oxysulfide particles on the film. The growth speed of the monolayer can be very large compared with that of the multilayer. This is the key, together with the low nucleation density on silica surface, that allowed us to grow the monolayer MoS_2 crystalline films with minimal presence of multilayers. However, we do not know why there are such huge differences between monolayer growth and multilayer growth. One possibility could be attributed to the nature of oxide nanoparticles seen at the growing edge of the crystals. Further in-situ experiments, particularly those at atomic resolution, can shed light on the detailed chemical and physical processes at the nucleation and growth and allow us to understand the CVD parameters from first principles so that we can rationally design the optimal CVD process to produce desired films for different applications.

Appendix

A1: MoS_2 monolayers transferring method

MoS_2 monolayer films grown on SiO_2/Si substrate were transferred onto the TEM grid as follows:

1: Polymethyl methacrylate (PMMA) film is spin coated on the monolayers/SiO_2/Si and then baked at 120 ^oC for 5 minute.

2: PMMA/Monolayer/SiO_2/Si were immersed into the boiling sodium hydroxide solution (1 mol L^{-1}), to etch away the underneath SiO_2 layer.

3: The floating PMMA film was picked up with a clean piece of glass and then immersed in a distilled water to wash away the surface contaminations.

4: The PMMA film was lifted out by a TEM grid covered with lacey carbon film and left it to dry in ambient temperature.

5: This TEM grid was heated at 120 ^oC for 5 minuet in air and then immersed into acetone for about 24 h, to dissolve the PMMA.

6: The film is annealed at 300 ^oC under Ar environment to remove the PMMA residues .

A2: Polarization resolved SHG and grain orientation (Matlab script)

```
A=imread('XP1.tif'); XP1 is X-polarized SH image.
figure (1);
imagesc(A);
B=imread('YP1.tif'); YP1 is Y-polarized SH image.
imagesc(B),
figure (2);
D=uint8(A);
E=sqrt(double(D));
F=uint8(B);
G=sqrt(double(F));
H=(G./E);
I=atand(H);
```

```
J=(1/3).*I;
figure (3);
imagesc (J);
axis image;
colorbar;
title('Orientation image');
```

A3: Sulphur chemical potential parameters [142]:

Parameter	Value	Unit
$X_{S8,0}$	7.62×10^{-1}	eV/atom
$X_{S8,1}$	-2.457×10^{-3}	eV/atom. K
$X_{S8,2}$	-4.012×10^{-6}	eV/atom. K^2
$X_{S8,3}$	1.808×10^{-9}	eV/atom. K^3
$X_{S8,4}$	-3.81×10^{-13}	eV/atom. K^4
$X_{S2,0}$	1.207	eV/atom
$X_{S2,1}$	-1.848×10^{-3}	eV/atom. K
$X_{S2,2}$	-8.566×10^{-7}	eV/atom. K^2
$X_{S2,3}$	$4.001\times10-^{10}$	eV/atom. K^3
$X_{S2,4}$	$-8.654\times10-^{14}$	eV/atom. K^4
$X_{Ttr,0}$	5.077×10^{2}	K
$X_{Ttr,1}$	7.272×10^{1}	K
$X_{Ttr,2}$	-8.295	K
$X_{Ttr,3}$	1.828	K
a_0	1.465×10^{-2}	eV/atom
a_1	-2.115×10^{-3}	eV/atom
a_2	6.905×10^{-4}	eV/atom
b	10	K
c	80	K
w	100	K

Symbols and abbreviations

Symbol	Description
n	Refractive index
r	Relative refractive index
R(n)	Reflectivity
eV	Electron volt
kV	Kilovolt
KE	Kinetic energy
h	Planck constant
v	Frequency
λ	Wavelength
ω	Wavenumber
Φ	Work function
$\overline{P}$	Polarization
ε_0	Permittivity of free space
χ	Susceptibility
$\overline{E}$	Electric field
θ	Diffraction angle in XRD
Θ	Angle between between the incident electric field of the laser beam and MoS_2 armchair
α	Staking angle of MoS_2 bilayers
$I_{2\omega}^{x}$	Intensity of second harmonic radiation in x-direction.
$I_{2\omega}^{y}$	Intensity of second harmonic radiation in y-direction.
Δf	Electron microscope defocus
Δf_{Sch}	Scherzer defocus
C_s	Spherical aberration aberration correction

m	Spatial frequency
r_{Sch}	Transmission electron microscope point resolution
β	Grazing incident angle
ρ	Density
μ	Fluid dynamic viscosity
u	Fluid velocity
U	Mean fluid velocity
D_i	Diffusion constant of species (i)
c_i	Concentration of species (i)
R_i	Reaction rate of species (i)
N_i	Flux of species (i)
C_p	Specific heat of fluid
k_f	Thermal conductivity of fluid
Q	Heat sources
q	Heat flux
T	Temperature
p	Pressure
P_{ref}	Atmospheric pressure
P_s	System pressure
P	vapor pressure of precursor
nm	Nanometer
$Å$	Angstrom
a	Lattice constant

μ_c	Carrier mobility
L	Transistor channel length
w	Transistor channel width
C	Capacitance
V_{bg}	Transistor back gate voltage
V_{ds}	Transistor drain-source voltage
I_{ds}	Transistor drain-source current
F_1	Precursor flux from bulk gas
F_2	Precursor flux on the substrate
h_g	Mass transfer constant
k_s	Reaction rate constant
C_1	Concentration of precursor in stream
C_2	Concentration of precursor on substrate
δ	Boundary layer thickness
E_a	Activation energy
k	Boltzmann constant
Pe	Péclet number
L_r	Reactor length
μ_S	Sulphur chemical potential
H_f	MoS_2 Formation energy

Abbreviation	Description
2D	Two dimensional materials
ADF	Annular dark field
AFM	Atomic force microscopy
ALD	Atomic layer deposition
APCVD	Atmospheric pressure chemical vapor deposition
BSE	Backscattered electrons
CTF	Contrast transfer function
CL	Chathodoluminecence
CVD	Chemical vapor deposition
EDX	Energy- dispersive X-ray
FET	Field effect transistor
FWHM	Full width at half maximum
GIIXRD	Grazing incidence in-plane X-ray diffraction
HAADF	High angle annular dark field
HRTEM	High resolution transmission electron microscopy
LPCVD	Low pressure chemical vapor deposition
MAADF	Medium angle annular dark field
MBE	Molecular beam epitaxy
MOCVD	Metalorganic chemical vapor deposition
PL	Photoluminescence
PVD	Physical vapor deposition
QE	Quantum yield
Rheed	Reflection high energy electron diffraction
SAED	Selected area diffraction
SCCM	Standard cubic centimeter per minute
SE	Secondary electrons
SEM	Scanning electron microscopy

SHG	Second harmonic generation
STEM	Scanning transmission electron microscopy
SWCNT	Single wall carbon nanotube
TEM	Transmission electron microscopy
TMD	Transition metal dichalcogenide
UHV	Ultra high vacuum
XPS	X-Ray Photoelectron Spectroscopy
XRD	X-ray diffractometry

References

[1] S. Z. Butler *et al.*, “Progress, challenges, and opportunities in two-dimensional materials beyond graphene,” *ACS Nano*, vol. 7, no. 4, pp. 2898–2926, Apr. 2013.

[2] P. Miró, M. Audiffred, and T. Heine, “An atlas of two-dimensional materials,” *Chem. Soc. Rev.*, vol. 43, no. 18, pp. 6537–6554, Sep. 2014.

[3] K. S. Novoselov, V. I. Fal’ko, L. Colombo, P. R. Gellert, M. G. Schwab, and K. Kim, “A roadmap for graphene,” *Nature*, vol. 490, no. 7419, pp. 192–200, Oct. 2012.

[4] M. Dvorak, W. Oswald, and Z. Wu, “Bandgap opening by patterning graphene,” *Sci. Rep.*, vol. 3, p. 2289, 2013.

[5] W. Zhang, J. K. Huang, C. H. Chen, Y. H. Chang, Y. J. Cheng, and L. J. Li, “High-gain phototransistors based on a CVD MoS_2 monolayer,” *Adv. Mater.*, vol. 25, no. 25, pp. 3456–3461, 2013.

[6] M. Chhowalla, H. S. Shin, G. Eda, L. J. Li, K. P. Loh, and H. Zhang, “The chemistry of two-dimensional layered transition metal dichalcogenide nanosheets,” *Nat. Chem.*, vol. 5, no. 4, pp. 263–275, Apr. 2013.

[7] B. Radisavljevic, A. Radenovic, J. Brivio, V. Giacometti, and A. Kis, “Single-layer MoS_2 transistors,” *Nat. Nanotechnol.*, vol. 6, no. 3, pp. 147–150, Mar. 2011.

[8] J. A. Wilson and A. D. Yoffe, “The transition metal dichalcogenides discussion and interpretation of the observed optical, electrical and structural properties,” *Adv. Phys.*, vol. 18, no. 73, pp. 193–335, May 1969.

[9] Q. H. Wang, K. Kalantar-Zadeh, A. Kis, J. N. Coleman, and M. S. Strano, “Electronics and optoelectronics of two-dimensional transition metal dichalcogenides,” *Nat. Nanotechnol.*, vol. 7, no. 11, pp. 699–712, Nov. 2012.

[10] G. Eda, T. Fujita, H. Yamaguchi, D. Voiry, M. Chen, and M. Chhowalla, “Coherent atomic and electronic heterostructures of single-layer MoS_2,” *ACS Nano*, vol. 6, no. 8, pp. 7311–7317, Aug. 2012.

[11] A. M. van der Zande *et al.*, “Grains and grain boundaries in highly crystalline monolayer molybdenum disulphide,” *Nat. Mater.*, vol. 12, no. 6, pp. 554–561,

May 2013.

[12] K. F. Mak, C. Lee, J. Hone, J. Shan, and T. F. Heinz, “Atomically thin MoS_2: a new direct-gap semiconductor,” *Phys. Rev. Lett.*, vol. 105, no. 13, p. 136805, Sep. 2010.

[13] A. Splendiani *et al.*, “Emerging Photoluminescence in Monolayer MoS_2,” *Nano Lett.*, vol. 10, no. 4, pp. 1271–1275, Apr. 2010.

[14] Y. Li, C. Y. Xu, J. Y. Wang, and L. Zhen, “Photodiode-like behavior and excellent photoresponse of vertical Si/monolayer MoS_2 heterostructures,” *Sci. Rep.*, vol. 4, p. 7186, Nov. 2014.

[15] M. L. Tsai *et al.*, “Monolayer MoS_2 heterojunction solar cells,” *ACS Nano*, vol. 8, no. 8, pp. 8317–8322, Aug. 2014.

[16] D. Xiao, G. B. Liu, W. Feng, X. Xu, and W. Yao, “Coupled Spin and Valley Physics in Monolayers of MoS_2 and Other Group-VI Dichalcogenides,” *Phys. Rev. Lett.*, vol. 108, no. 19, p. 196802, May 2012.

[17] R. Suzuki *et al.*, “Valley-dependent spin polarization in bulk MoS_2 with broken inversion symmetry,” *Nat. Nanotechnol.*, vol. 9, no. 8, pp. 611–617, Aug. 2014.

[18] H. Zhu *et al.*, “Observation of piezoelectricity in free-standing monolayer MoS_2,” *Nat. Nanotechnol.*, vol. 10, no. 2, pp. 151–155, Dec. 2014.

[19] K. Kaasbjerg, K. S. Thygesen, and K. W. Jacobsen, “Phonon-limited mobility in n-type single-layer MoS_2 from first principles,” *Phys. Rev. B Condens. Matter*, vol. 85, no. 11, p. 115317, Mar. 2012.

[20] S. Bertolazzi, J. Brivio, and A. Kis, “Stretching and Breaking of Ultrathin MoS_2,” *ACS Nano*, vol. 5, no. 12, pp. 9703–9709, Dec. 2011.

[21] B. C. Brodie, “On the Atomic Weight of Graphite,” *Philosophical Transactions of the Royal Society of London*, vol. 149, no. 9, pp. 249–259, 1859.

[22] K. S. Novoselov *et al.*, “Electric field effect in atomically thin carbon films,” *Science*, vol. 306, no. 5696, pp. 666–669, 2004.

[23] A. Castellanos Gomez *et al.*, “Deterministic transfer of two-dimensional materials by all-dry viscoelastic stamping,” *2D Mater.*, vol. 1, no. 1, p. 011002, Apr. 2014.

[24] Y. Chen *et al.*, “Mechanically exfoliated black phosphorus as a new saturable absorber for both Q-switching and Mode-locking laser operation,” *Opt. Express*, vol. 23, no. 10, pp. 12823–12833, May 2015.

[25] G. Z. Magda, J. Pető, G. Dobrik, C. Hwang, L. P. Biró, and L. Tapasztó,

"Exfoliation of large-area transition metal chalcogenide single layers," *Sci. Rep.*, vol. 5, p. 14714, 2015.

[26] K. S. Novoselov, "Nobel Lecture: Graphene: Materials in the Flatland," *Rev. Mod. Phys.*, vol. 83, no. 3, pp. 837–849, 2011.

[27] H. Li *et al.*, "Fabrication of Single- and Multilayer MoS_2 Film-Based Field-Effect Transistors for Sensing NO at Room Temperature," *Small*, vol. 8, no. 1, pp. 63–67, Jan. 2012.

[28] V. Nicolosi, M. Chhowalla, M. G. Kanatzidis, M. S. Strano, and J. N. Coleman, "Liquid Exfoliation of Layered Materials," *Science*, vol. 340, no. 6139, p. 1226419, 2013.

[29] J. N. Coleman *et al.*, "Two-dimensional nanosheets produced by liquid exfoliation of layered materials," *Science*, vol. 331, no. 6017, pp. 568–571, 2011.

[30] R. J. Smith *et al.*, "Large-scale exfoliation of inorganic layered compounds in aqueous surfactant solutions," *Adv. Mater.*, vol. 23, no. 34, pp. 3944–3948, 2011.

[31] G. Eda, H. Yamaguchi, D. Voiry, T. Fujita, M. Chen, and M. Chhowalla, "Photoluminescence from Chemically Exfoliated MoS_2," *Nano Lett.*, vol. 11, no. 12, pp. 5111–5116, 2011.

[32] S. L. Nos, P. Joensen, R. F. Frindt, and S. R. Morrison, "Single-layer MoS_2," vol. 21, no. c, pp. 457–461, 1986.

[33] H. L. Tsai, J. Heising, J. L. Schindler, C. R. Kannewurf, and M. G. Kanatzidis, "Exfoliated - Restacked Phase of WS_2," *Chem. Mater.*, vol. 9, no. 96, pp. 879–882, 1997.

[34] N. Liu, P. Kim, J. H. Kim, J. H. Ye, S. Kim, and C. J. Lee, "Large-Area Atomically Thin MoS_2 Nanosheets Prepared Using Electrochemical Exfoliation," *ACS Nano*, vol. 8, no. 7, pp. 6902–6910, 2014.

[35] M. Bosi, "Growth and synthesis of mono and few-layers transition metal dichalcogenides by vapour techniques: a review," *RSC Adv.*, vol. 5, no. 92, pp. 75500–75518, Sep. 2015.

[36] Y. H. Lee *et al.*, "Synthesis and Transfer of Single-Layer Transition Metal Disulfides on Diverse Surfaces," *Nano Lett.*, vol. 13, no. 4, pp. 1852–1857, Apr. 2013.

[37] Q. Ji *et al.*, "Epitaxial monolayer MoS_2 on mica with novel photoluminescence,"

Nano Lett., vol. 13, no. 8, pp. 3870–3877, Aug. 2013.

[38] J. Shi *et al.*, “Controllable growth and transfer of monolayer MoS_2 on Au foils and its potential application in hydrogen evolution reaction,” *ACS Nano*, vol. 8, no. 10, pp. 10196–10204, Oct. 2014.

[39] J. Jeon *et al.*, “Layer-controlled CVD growth of large-area two-dimensional MoS_2 films,” *Nanoscale*, vol. 7, no. 5, pp. 1688–1695, 2015.

[40] J. Zhang *et al.*, “Scalable Growth of High-Quality Polycrystalline MoS_2 Monolayers on SiO_2 with Tunable Grain Sizes,” *ACS Nano*, vol. 8, no. 6, pp. 6024–6030, Jun. 2014.

[41] Y. Yu, C. Li, Y. Liu, L. Su, Y. Zhang, and L. Cao, “Controlled Scalable Synthesis of Uniform, High-Quality Monolayer and Few-layer MoS_2 Films,” *Sci. Rep.*, vol. 3, p. step 01866, May 2013.

[42] Y. C. Lin *et al.*, “Wafer-scale MoS_2 thin layers prepared by MoO_3 sulfurization,” *Nanoscale*, vol. 4, no. 20, pp. 6637–6641, Oct. 2012.

[43] P. Taheri *et al.*, “Growth mechanism of large scale MoS_2 monolayer by sulfurization of MoO_3 film,” *Mater. Res. Express*, vol. 3, no. 7, p. 075009, Jul. 2016.

[44] Y. Lee *et al.*, “Synthesis of wafer-scale uniform molybdenum disulfide films with control over the layer number using a gas phase sulfur precursor,” *Nanoscale*, vol. 6, no. 5, pp. 2821–2826, Feb. 2014.

[45] Y. Zhan, Z. Liu, S. Najmaei, P. M. Ajayan, and J. Lou, “Large-Area Vapor-Phase Growth and Characterization of MoS_2 Atomic Layers on a SiO_2 Substrate,” *Small*, vol. 8, no. 7, pp. 966–971, Apr. 2012.

[46] M. R. Laskar *et al.*, “Large area single crystal (0001) oriented MoS_2,” *Appl. Phys. Lett.*, vol. 102, no. 25, p. 252108, Jun. 2013.

[47] K. Kang *et al.*, “High-mobility three-atom-thick semiconducting films with wafer-scale homogeneity,” *Nature*, vol. 520, no. 7549, pp. 656–660, Apr. 2015.

[48] K. K. Liu *et al.*, “Growth of Large-Area and Highly Crystalline MoS_2 Thin Layers on Insulating Substrates,” *Nano Lett.*, vol. 12, no. 3, pp. 1538–1544, Mar. 2012.

[49] S. K. Lee, J. B. Lee, J. Singh, K. Rana, and J. H. Ahn, “Drying-Mediated Self-Assembled Growth of Transition Metal Dichalcogenide Wires and their Heterostructures,” *Adv. Mater.*, vol. 27, no. 28, pp. 4142–4149, Jul. 2015.

[50] S. Wu, C. Huang, G. Aivazian, J. S. Ross, D. H. Cobden, and X. Xu,

"Vapor–Solid Growth of High Optical Quality MoS_2 Monolayers with Near-Unity Valley Polarization," *ACS Nano*, vol. 7, no. 3, pp. 2768–2772, Mar. 2013.

[51] L. K. Tan, B. Liu, J. H. Teng, S. Guo, H. Y. Low, and K. P. Loh, "Atomic layer deposition of a MoS_2 film," *Nanoscale*, vol. 6, no. 18, pp. 10584–10588, Aug. 2014.

[52] L. Zhan, W. Wan, Z. Zhu, T.-M. Shih, and W. Cai, "MoS_2 materials synthesized on SiO_2/Si substrates via MBE," *J. Phys. Conf. Ser.*, vol. 864, no. 1, p. 012037, Aug. 2017.

[53] L. Jiao *et al.*, "Molecular-beam epitaxy of monolayer $MoSe_2$: growth characteristics and domain boundary formation," *New J. Phys.*, vol. 17, no. 5, p. 053023, May 2015.

[54] R. Yue *et al.*, "Nucleation and growth of WSe_2: enabling large grain transition metal dichalcogenides," *2D Mater.*, vol. 4, no. 4, p. 045019, Sep. 2017.

[55] D. Fu *et al.*, "Molecular Beam Epitaxy of Highly Crystalline Monolayer Molybdenum Disulfide on Hexagonal Boron Nitride," *J. Am. Chem. Soc.*, vol. 139, no. 27, pp. 9392–9400, July. 2017.

[56] H. C. Diaz, R. Chaghi, Y. Ma, and M. Batzill, "Molecular beam epitaxy of the van der Waals heterostructure $MoTe_2$ on MoS_2: phase, thermal, and chemical stability," *2D Mater.*, vol. 2, no. 4, p. 044010, Nov. 2015.

[57] R. Yue *et al.*, "$HfSe_2$ thin films: 2D transition metal dichalcogenides grown by molecular beam epitaxy," *ACS Nano*, vol. 9, no. 1, pp. 474–480, Jan. 2015.

[58] P. Blake *et al.*, "Making graphene visible," *Appl. Phys. Lett.*, vol. 91, no. 6, p. 063124, Aug. 2007.

[59] M. M. Benameur, B. Radisavljevic, J. S. Héron, S. Sahoo, H. Berger, and A. Kis, "Visibility of dichalcogenide nanolayers," *Nanotechnology*, vol. 22, no. 12, p. 125706, Feb. 2011.

[60] D. J. Late, B. Liu, H. S. S. R. Matte, C. N. R. Rao, and V. P. Dravid, "Rapid Characterization of Ultrathin Layers of Chalcogenides on SiO_2/Si Substrates," *Adv. Funct. Mater.*, vol. 22, no. 9, pp. 1894–1905, May 2012.

[61] H. Li *et al.*, "Rapid and reliable thickness identification of two-dimensional nanosheets using optical microscopy," *ACS Nano*, vol. 7, no. 11, pp. 10344–10353, Nov. 2013.

[62] J. C. Vickerman, and I. S. Gilmore, Eds., *Surface analysis : the principal techniques*, 2nd ed. Chichester, U.K.: Wiley, 2009.

[63] E. N. Kaufmann, *Characterization of Materials*. John Wiley & Sons, Incorporated, 2012.

[64] D. J. Gardiner and P. R. Graves, Eds., *Practical Raman Spectroscopy*. Springer, 1989.

[65] P. Larkin, *Infrared and Raman Spectroscopy: Principles and Spectral Interpretation*. Elsevier, 2011.

[66] M. Cardona and R. Merlin, “Light Scattering in Solids IX,” in *Light Scattering in Solid IX*, Springer, Berlin, Heidelberg, 2006, pp. 1–14.

[67] J. Hodkiewicz - Thermo Scientific Application Note and 2010, “Characterizing carbon materials with Raman spectroscopy,” 2010.

[68] E. H. Martins Ferreira *et al.*, “Evolution of the Raman spectra from single-, few-, and many-layer graphene with increasing disorder,” *Phys. Rev. B Condens. Matter*, vol. 82, no. 12, p. 125429, Sep. 2010.

[69] C. Lee, H. Yan, L. E. Brus, T. F. Heinz, J. Hone, and S. Ryu, “Anomalous lattice vibrations of single- and few-layer MoS_2,” *ACS Nano*, vol. 4, no. 5, pp. 2695–2700, May 2010.

[70] C. Rice *et al.*, “Raman-scattering measurements and first-principles calculations of strain-induced phonon shifts in monolayer MoS_2,” *Phys. Rev. B Condens. Matter*, vol. 87, no. 8, p. 081307, Feb. 2013.

[71] R. W. Boyd, *Nonlinear Optics, Third Edition*, 3rd ed. Academic Press, 2008.

[72] Y. Li *et al.*, “Probing symmetry properties of few-layer MoS_2 and h-BN by optical second-harmonic generation,” *Nano Lett.*, vol. 13, no. 7, pp. 3329–3333, Jul. 2013.

[73] M. Zhao *et al.*, “Atomically phase-matched second-harmonic generation in a 2D crystal,” *Light: Science & Applications*, vol. 5, no. 8, p. lsa2016131, Aug. 2016.

[74] T. F. Heinz, M. M. Loy, and W. A. Thompson, “Study of Si(111) surfaces by optical second-harmonic generation: Reconstruction and surface phase transformation,” *Phys. Rev. Lett.*, vol. 54, no. 1, pp. 63–66, Jan. 1985.

[75] X. Yin *et al.*, “Edge nonlinear optics on a MoS_2 atomic monolayer,” *Science*, vol. 344, no. 6183, pp. 488–490, May 2014.

[76] S. N. David *et al.*, “Rapid, all-optical crystal orientation imaging of two-dimensional transition metal dichalcogenide monolayers,” *Appl. Phys. Lett.*, vol. 107, no. 11, p. 111902, Sep. 2015.

[77] J. I. Goldstein, D. E. Newbury, J. R. Michael, N. W. M. Ritchie, J. H. J. Scott, and D. C. Joy, *Scanning Electron Microscopy and X-Ray Microanalysis*. Springer, 2017.

[78] H. Busch, “Berechnung der Bahn von Kathodenstrahlen im axialsymmetrischen elektromagnetischen Felde,” *Ann. Phys.*, vol. 386, no. 25, pp. 974–993, Jan. 1926.

[79] C. W. Oatley, “The early history of the scanning electron microscope,” *J. Appl. Phys.*, vol. 53, no. 2, pp. R1–R13, Feb. 1982.

[80] K. Shihommatsu, J. Takahashi, Y. Momiuchi, Y. Hoshi, H. Kato, and Y. Homma, “Formation Mechanism of Secondary Electron Contrast of Graphene Layers on a Metal Substrate,” *ACS Omega*, vol. 2, no. 11, pp. 7831–7836, Nov. 2017.

[81] D. B. Williams and C. Barry Carter, *Transmission Electron Microscopy: A Textbook for Materials Science*. Springer Science & Business Media, 2009.

[82] G. Haugstad, “Atomic Force Microscopy: Understanding basic modes and advanced applications. 2012,” *Published by John Wiley & Sons, Inc*.

[83] P. C. Braga and D. Ricci, *Atomic Force Microscopy: Biomedical Methods and Applications*. Springer Science & Business Media, 2004.

[84] P. Samori, *STM and AFM Studies on (Bio)molecular Systems: Unravelling the Nanoworld*. Springer Science & Business Media, 2009.

[85] W. Richard Bowen and N. Hilal, *Atomic Force Microscopy in Process Engineering: An Introduction to AFM for Improved Processes and Products*. Butterworth-Heinemann, 2009.

[86] C. Musumeci, “Advanced Scanning Probe Microscopy of Graphene and Other 2D Materials,” *Crystals*, vol. 7, no. 7, p. 216, July. 2017.

[87] Y. Waseda, E. Matsubara, and K. Shinoda, *X-Ray Diffraction Crystallography: Introduction, Examples and Solved Problems*. Springer Science & Business Media, 2011.

[88] M. Lee, *X-Ray Diffraction for Materials Research: From Fundamentals to Applications*. CRC Press, 2016.

[89] T. C. Rebollo and R. Lewandowski, *Mathematical and numerical foundations of turbulence models and applications*. Springer, 2014.

[90] R. B. Bid and S. En, *Transport Phenomena” revised 2nd edition*. john Wiley & Sons, 2007.

[91] P. Avouris, T. F. Heinz, and T. Low, *2D Materials*. Cambridge University Press, 2017.

[92] S. Wang, M. Pacios, H. Bhaskaran, and J. H. Warner, “Substrate control for large area continuous films of monolayer MoS_2 by atmospheric pressure chemical vapor deposition,” *Nanotechnology*, vol. 27, no. 8, p. 085604, Feb. 2016.

[93] S. Ganorkar, J. Kim, Y. H. Kim, and S. I. Kim, “Effect of precursor on growth and morphology of MoS_2 monolayer and multilayer,” *J. Phys. Chem. Solids*, vol. 87, pp. 32–37, 2015.

[94] H. Suhr, R. Schmid, and W. Stürmer, “Plasma reaction of group VI metal carbonyls,” *Plasma Chem. Plasma Process.*, vol. 12, no. 2, pp. 147–159, Jun. 1992.

[95] J. Mun *et al.*, “Low-temperature growth of layered molybdenum disulphide with controlled clusters,” *Sci. Rep.*, vol. 6, p. 21854, Feb. 2016.

[96] I. Jung *et al.*, “Simple Approach for High-Contrast Optical Imaging and Characterization of Graphene-Based Sheets,” *Nano Lett.*, vol. 7, no. 12, pp. 3569–3575, Dec. 2007.

[97] W. T. Hsu *et al.*, “Second Harmonic Generation from Artificially Stacked Transition Metal Dichalcogenide Twisted Bilayers,” *ACS Nano*, vol. 8, no. 3, pp. 2951–2958, Mar. 2014.

[98] A. M. de Jong *et al.*, “Sulfidation mechanism by molybdenum catalysts supported on silica/silicon(100) model support studied by surface spectroscopy,” *J. Phys. Chem.*, vol. 97, no. 24, pp. 6477–6483, June. 1993.

[99] J. H. Nielsen *et al.*, “Combined spectroscopy and microscopy of supported MoS2 nanoparticles,” *Surf. Sci.*, vol. 603, no. 9, pp. 1182–1189, May 2009.

[100] H. J. Conley, B. Wang, J. I. Ziegler, R. F. Haglund Jr, S. T. Pantelides, and K. I. Bolotin, “Bandgap engineering of strained monolayer and bilayer MoS_2,” *Nano Lett.*, vol. 13, no. 8, pp. 3626–3630, Aug. 2013.

[101] H. Li *et al.*, “From Bulk to Monolayer MoS_2: Evolution of Raman Scattering,” *Adv. Funct. Mater.*, vol. 22, no. 7, pp. 1385–1390, Apr. 2012.

[102] S. Hao, B. Yang, and Y. Gao, “Quenching induced fracture behaviors of CVD-grown polycrystalline molybdenum disulfide films,” *RSC Adv.*, vol. 6, no. 64, pp. 59816–59822, 2016.

[103] L. Yang *et al.*, “Lattice strain effects on the optical properties of MoS_2

nanosheets," *Sci. Rep.*, vol. 4, p. 5649, Jul. 2014.

[104] Z. Liu *et al.*, "Strain and structure heterogeneity in MoS_2 atomic layers grown by chemical vapour deposition," *Nat. Commun.*, vol. 5, p. 5246, Nov. 2014.

[105] Y. L. Huang *et al.*, "Bandgap tunability at single-layer molybdenum disulphide grain boundaries," *Nat. Commun.*, vol. 6, p. 6298, Feb. 2015.

[106] B. D. Cullity, *Elements of X-ray Diffraction*. Addison-Wesley Publishing Company, 1978.

[107] S. H. El-Mahalawy and B. L. Evans, "The thermal expansion of 2H-MoS_2, 2H-$MoSe_2$ and 2H-WSe_2 between 20 and 800°C," *J. Appl. Crystallogr.*, vol. 9, no. 5, pp. 403–406, Oct. 1976.

[108] D. Sercombe *et al.*, "Optical investigation of the natural electron doping in thin MoS_2 films deposited on dielectric substrates," *Sci. Rep.*, vol. 3, p. 3489, Dec. 2013.

[109] K. F. Mak *et al.*, "Tightly bound trions in monolayer MoS_2," *Nat. Mater.*, vol. 12, no. 3, pp. 207–211, Mar. 2013.

[110] Y. Li *et al.*, "Photoluminescence of monolayer MoS_2 on $LaAlO_3$ and $SrTiO_3$ substrates," *Nanoscale*, vol. 6, no. 24, pp. 15248–15254, Dec. 2014.

[111] N. Scheuschner, O. Ochedowski, A. M. Kaulitz, R. Gillen, M. Schleberger, and J. Maultzsch, "Photoluminescence of freestanding single-and few-layer MoS_2," *Phys. Rev. B: Condens. Matter Mater. Phys.*, vol. 89, no. 12, p. 125406, 2014.

[112] Z. Yin *et al.*, "Single-layer MoS_2 phototransistors," *ACS Nano*, vol. 6, no. 1, pp. 74–80, Jan. 2012.

[113] L. Yuan and L. Huang, "Exciton dynamics and annihilation in WS_2 2D semiconductors," *Nanoscale*, vol. 7, no. 16, pp. 7402–7408, Apr. 2015.

[114] M. Amani *et al.*, "High Luminescence Efficiency in MoS_2 Grown by Chemical Vapor Deposition," *ACS Nano*, vol. 10, no. 7, pp. 6535–6541, Jul. 2016.

[115] J. Hong *et al.*, "Exploring atomic defects in molybdenum disulphide monolayers," *Nat. Commun.*, vol. 6, p. 6293, Feb. 2015.

[116] M. Amani *et al.*, "Near-unity photoluminescence quantum yield in MoS_2," *Science*, vol. 350, no. 6264, pp. 1065–1068, Nov. 2015.

[117] K. S. Novoselov *et al.*, "Two-dimensional atomic crystals," *Proc. Natl. Acad. Sci. U. S. A.*, vol. 102, no. 30, pp. 10451–10453, Jul. 2005.

[118] X. Wang, H. Feng, Y. Wu, and L. Jiao, “Controlled synthesis of highly crystalline MoS_2 flakes by chemical vapor deposition,” *J. Am. Chem. Soc.*, vol. 135, no. 14, pp. 5304–5307, Apr. 2013.

[119] S. Das, H.-Y. Chen, A. V. Penumatcha, and J. Appenzeller, “High performance multilayer MoS_2 transistors with scandium contacts,” *Nano Lett.*, vol. 13, no. 1, pp. 100–105, Jan. 2013.

[120] T. H. Ly *et al.*, “Misorientation-angle-dependent electrical transport across molybdenum disulfide grain boundaries,” *Nat. Commun.*, vol. 7, p. 10426, Jan. 2016.

[121] J. Cheng *et al.*, “Kinetic Nature of Grain Boundary Formation in As-Grown MoS_2 Monolayers,” *Adv. Mater.*, vol. 27, no. 27, pp. 4069–4074, Jul. 2015.

[122] X. T. Yan and Y. Xu, *Chemical Vapour Deposition: An Integrated Engineering Design for Advanced Materials*. Springer Science & Business Media, 2010.

[123] T. T. Kodas and M. J. Hampden Smith, *The Chemistry of Metal CVD*. John Wiley & Sons, 2008.

[124] A. C. Jones and P. O’Brien, *CVD of Compound Semiconductors: Precursor Synthesis, Development and Applications*. John Wiley & Sons, 2008.

[125] N. M. Hwang, *Non-Classical Crystallization of Thin Films and Nanostructures in CVD and PVD Processes*. Springer, 2016.

[126] N. M. Hwang, in *Non-Classical Crystallization of Thin Films and Nanostructures in CVD and PVD Processes*, N. M. Hwang, Ed. Dordrecht: Springer Netherlands, 2016, pp. 21–50.

[127] H. P. Komsa and A. V. Krasheninnikov, “Native defects in bulk and monolayer MoS_2 from first principles,” *Phys. Rev. B: Condens. Matter Mater. Phys.*, vol. 91, no. 12, p. 125304, 2015.

[128] P. Raybaud, J. Hafner, G. Kresse, S. Kasztelan, and H. Toulhoat, “Ab Initio Study of the H2–H_2S/MoS_2 Gas–Solid Interface: The Nature of the Catalytically Active Sites,” *J. Catal.*, vol. 189, no. 1, pp. 129–146, Jan. 2000.

[129] H. Schweiger, P. Raybaud, G. Kresse, and H. Toulhoat, “Shape and Edge Sites Modifications of MoS_2 Catalytic Nanoparticles Induced by Working Conditions: A Theoretical Study,” *J. Catal.*, vol. 207, no. 1, pp. 76–87, Apr. 2002.

[130] R. P. Burns, G. DeMaria, J. Drowart, and R. T. Grimley, “Mass

Spectrometric Investigation of the Sublimation of Molybdenum Dioxide," *J. Chem. Phys.*, vol. 32, no. 5, pp. 1363–1366, May 1960.

[131] D. Zhu *et al.*, "Capture the growth kinetics of CVD growth of two-dimensional MoS_2," *npj 2D Materials and Applications*, vol. 1, no. 1, p. 8, May 2017.

[132] J. D. Cain, F. Shi, J. Wu, and V. P. Dravid, "Growth Mechanism of Transition Metal Dichalcogenide Monolayers: The Role of Self-Seeding Fullerene Nuclei," *ACS Nano*, vol. 10, no. 5, pp. 5440–5445, May 2016.

[133] P. E. Blackburn, "The vapor pressures of molybdenum oxides and tungsten oxides," PhD, Graduate School of The Ohio State University, 1954.

[134] D. Y. Peng and J. Zhao, "Representation of the vapour pressures of sulfur," *J. Chem. Thermodyn.*, vol. 33, no. 9, pp. 1121–1131, Sep. 2001.

[135] D. M. Dobkin and M. K. Zuraw, *Principles of Chemical Vapor Deposition*. Springer, 2003.

[136] P. Zhang and Y. H. Kim, "Understanding Size-Dependent Morphology Transition of Triangular MoS_2 Nanoclusters: The Role of Metal Substrate and Sulfur Chemical Potential," *J. Phys. Chem. C*, vol. 121, no. 3, pp. 1809–1816, Jan. 2017.

[137] P. G. Moses, B. Hinnemann, H. Topsøe, and J. K. Nørskov, "The hydrogenation and direct desulfurization reaction pathway in thiophene hydrodesulfurization over MoS_2 catalysts at realistic conditions: A density functional study," *J. Catal.*, vol. 248, no. 2, pp. 188–203, Jun. 2007.

[138] S. Wang *et al.*, "Shape Evolution of Monolayer MoS_2 Crystals Grown by Chemical Vapor Deposition," *Chem. Mater.*, vol. 26, no. 22, pp. 6371–6379, Nov. 2014.

[139] S. Xie *et al.*, "A high-quality round-shaped monolayer MoS_2 domain and its transformation," *Nanoscale*, vol. 8, no. 1, pp. 219–225, Jan. 2016.

[140] X. Yang, Y. Wang, J. Zhou, and Z. Liu, "Temperature-dependent morphology of chemical vapor grown molybdenum disulfide," *J. Phys. D Appl. Phys.*, vol. 50, no. 16, p. 164002, Mar. 2017.

[141] J. J. De Yoreo and P. G. Vekilov, "Principles of Crystal Nucleation and Growth," *Rev. Mineral. Geochem.*, vol. 54, no. 1, pp. 57–93, Jan. 2003.

[142] A. J. Jackson, D. Tiana, and A. Walsh, "A universal chemical potential for sulfur vapours," *Chem. Sci.*, vol. 7, no. 2, pp. 1082–1092, Jan. 2016.

[143] D. Cao, T. Shen, P. Liang, X. Chen, and H. Shu, “Role of Chemical Potential in Flake Shape and Edge Properties of Monolayer MoS_2,” *J. Phys. Chem. C*, vol. 119, no. 8, pp. 4294–4301, Feb. 2015.

[144] L. Kumari *et al.*, “X-ray diffraction and Raman scattering studies on large-area array and nano branched structure of 1D MoO_2 nanorods,” *Nanotechnology*, vol. 18, no. 11, p. 115717, Feb. 2007.

[145] L. Ling *et al.*, “Controlled growth of MoS_2 nanopetals and their hydrogen evolution performance,” *RSC Adv.*, vol. 6, no. 22, pp. 18483–18489, Feb. 2016.

[146] H. Li, H. Wu, S. Yuan, and H. Qian, “Synthesis and characterization of vertically standing MoS_2 nanosheets,” *Sci. Rep.*, vol. 6, p. 21171, Feb. 2016.

[147] X. L. Li and Y. D. Li, “Formation of MoS_2 Inorganic Fullerenes (IFs) by the Reaction of MoO_3 Nanobelts and S,” *Chem. Eur. J.*, vol. 9, no. 12, pp. 2726–2731, Jun. 2003.

[148] Y. H. Lee *et al.*, “Synthesis of Large-Area MoS_2 Atomic Layers with Chemical Vapor Deposition,” *Adv. Mater.*, vol. 24, no. 17, pp. 2320–2325, May 2012.

[149] G. Zhou *et al.*, “Vertically aligned MoS_2/MoO_x heterojunction nanosheets for enhanced visible-light photocatalytic activity and photostability,” *CrystEngComm*, vol. 16, no. 38, pp. 9025–9032, Sep. 2014.

[150] E. A. Gulbransen, K. F. Andrew, and F. A. Brassart, “Vapor Pressure of Molybdenum Trioxide,” *J. Electrochem. Soc.*, vol. 110, no. 3, pp. 242–243, Mar. 1963.

[151] Q. Ji, Y. Zhang, Y. Zhang, and Z. Liu, “Chemical vapour deposition of group-VIB metal dichalcogenide monolayers: engineered substrates from amorphous to single crystalline,” *Chem. Soc. Rev.*, vol. 44, no. 9, pp. 2587–2602, May 2015.

[152] N. K. Perkgoz and M. Bay, “Investigation of Single-Wall MoS_2 Monolayer Flakes Grown by Chemical Vapor Deposition,” *Nano-Micro Lett.*, vol. 8, no. 1, pp. 70–79, Jan. 2016.

[153] Y. Feldman, E. Wasserman, D. J. Srolovitz, and R. Tenne, “High-Rate, Gas-Phase Growth of MoS_2 Nested Inorganic Fullerenes and Nanotubes,” *Science*, vol. 267, no. 5195, pp. 222–225, Jan. 1995.

[154] X. Ling *et al.*, “Role of the seeding promoter in MoS_2 growth by chemical

vapor deposition," *Nano Lett.*, vol. 14, no. 2, pp. 464–472, Feb. 2014.

[155] Z. Lin *et al.*, "Controllable growth of large–size crystalline MoS_2 and resist-free transfer assisted with a Cu thin film," *Nature Scientific Reports*, 2015.

[156] J. Chen *et al.*, "Chemical Vapor Deposition of High-Quality Large-Sized MoS_2 Crystals on Silicon Dioxide Substrates," *Adv. Sci.*, vol. 3, no. 8, Aug. 2016.

[157] X. Wang *et al.*, "Chemical vapor deposition growth of crystalline monolayer $MoSe_2$," *ACS Nano*, vol. 8, no. 5, pp. 5125–5131, May 2014.

[158] D. Wu *et al.*, "Epitaxial Growth of Highly Oriented Metallic MoO_2 and MoS_2 Nanorods on C-sapphire," *J. Phys. Chem. C*, vol. 122, no. 3, pp. 1860–1866, Jan. 2018.

[159] Z. P. DeGregorio, Y. Yoo, and J. E. Johns, "Aligned MoO_2/MoS_2 and MoO_2/$MoTe_2$ Freestanding Core/Shell Nanoplates Driven by Surface Interactions," *J. Phys. Chem. Lett.*, vol. 8, no. 7, pp. 1631–1636, Apr. 2017.

[160] R. A. Vilá *et al.*, "Bottom-up synthesis of vertically oriented two-dimensional materials," *2D Mater.*, vol. 3, no. 4, p. 041003, Oct. 2016.

[161] F. Zhang *et al.*, "Controlled synthesis of 2D transition metal dichalcogenides: from vertical to planar MoS_2," *2D Mater.*, vol. 4, no. 2, p. 025029, Feb. 2017.

[162] W. Xu *et al.*, "Correlated fluorescence blinking in two-dimensional semiconductor heterostructures," *Nature*, vol. 541, no. 7635, pp. 62–67, Jan. 2017.

[163] N. Huo, J. Kang, Z. Wei, S. S. Li, J. Li, and S. H. Wei, "Novel and Enhanced Optoelectronic Performances of Multilayer MoS_2–WS_2 Heterostructure Transistors," *Adv. Funct. Mater.*, vol. 24, no. 44, pp. 7025–7031, Nov. 2014.

[164] M. H. Doan *et al.*, "Charge Transport in MoS_2/WSe_2 van der Waals Heterostructure with Tunable Inversion Layer," *ACS Nano*, vol. 11, no. 4, pp. 3832–3840, Apr. 2017.

[165] Y. Liu, N. O. Weiss, X. Duan, H. C. Cheng, Y. Huang, and X. Duan, "Van der Waals heterostructures and devices," *Nature Reviews Materials*, vol. 1, p. 16042, Jul. 2016.

[166] S. H. Su *et al.*, "Controllable Synthesis of Band-Gap-Tunable and Monolayer Transition-Metal Dichalcogenide Alloys," *Front. Energy Res.*, vol. 2,

p. 193107, Jul. 2014.

[167] S. Susarla *et al.*, “Quaternary 2D Transition Metal Dichalcogenides (TMDs) with Tunable Bandgap,” *Adv. Mater.*, vol. 29, no. 35, Sep. 2017.